Department of Mechanical Engineering

The University of Sheffield

Damage Investigation in Dual-Phase 1000 Steel and Behaviour Prediction Using Microstructure Based Modelling

Research Thesis

In Partial Fulfilment of the
Requirements for the Degree of Doctor of Philosophy
(December 2015)

By: Khaled Alharbi

Submitted to
The University of Sheffield

Department of Mechanical Engineering

The University of Sheffield

Damage Investigation in Dual-Phase 1000 Steel and Behaviour Prediction Using Microstructure Based Modelling

By:

Khaled Alharbi

The research thesis was done under the supervision of

Dr. Christophe Pinna

in the department of Mechanical Engineering

Acknowledgment

I would like to thank the supervisor Dr. Christophe Pinna and anyone else helped me completing this research.

I would like also to acknowledge TATA Steel in IJmuiden, The Netherlands for providing the material sheets of DP1000 steel.

The generous financial help of Taibah University is gratefully acknowledged.

I want to thank my wife Hanan Alharbi for her encouragement that she gave me to finish this project and for her patience.

Table of contents

Table of contents

Table of contents

Table of contents

Table of contents

List of figures

List of figures

List of figures

List of figures

List of figures

List of figures

List of figures

List of figures

List of figures

List of figures

List of figures

List of tables

List of tables

ABSTRACT

Dual phase (DP) steels are advanced high strength steels that are being progressively used in the automotive industry in order to reduce weight while enhancing safety. The development of the next generation DP steels requires better understanding of the deformation and damage development at the scale of their microstructure in order to predict their mechanical response, especially work-hardening up to the Ultimate Tensile Strength and elongation to fracture. A combined methodology of experimental measurements and modelling at micro-scale was used in this project to investigate deformation and damage in DP1000 steels. A digital image correlation (DIC) experimental technique was used to measure deformation of the microstructure. The displacement results of DIC were extracted and used as boundary conditions for microstructure simulation. The uniqueness of this method is to ensure deformation of modelling matches the actual deformation, which thus allows further investigation for strain and stress values at the damage locations. The method was then used to investigate a crack initiation criterion in the martensite phase and predict crack propagation. A critical maximum principal stress value of 1700 MPa is suggested to initiate damage in the martensite phase of DP1000 steel. Additionally, a continuum-based damage model, namely Gurson, was used for the ferrite phase in order to predict the stress/strain curve of the material. A new approach based on microstructure simulations was used to adjust the Gurson damage parameters. The transferability of these parameter values was examined using different specimen geometries with different stress triaxiality, including a notch bar of DP1000 steel. The results showed a reasonable agreement between stress predictions from microstructure simulations and experimentally measured true stress values. The method of using combined DIC results and microstructure simulation for damage

initiation criterion in the martensite and for calibrating damage model parameters for the ferrite phase is then discussed, and the significance of the results obtained in this work for the prediction of overall stress/strain curves of advanced high strength steels is then drawn.

List of symbols and abbreviations

In this thesis, many symbols and abbreviations were used. The description given in the text and the summary is as follow:

α	Constant in the empirical model of a dislocation based strain hardening approach [0.33]
M	Taylor factor
μ	Shear modulus, in GPa
b	Burger's vector, in m
L	Related to the dislocation mean free path
K	The recovery rate
Δσ	The strengthening due to carbon and precipitations
σ_0	The yield stress in the empirical model of a dislocation based strain hardening approach
ε_{eq}^{p}	Equivalent plastic strain
σ_{3D}	Stress value of the 3D RVE
σ_{2D}	Stress value of the 2D microstructure simulation
σ_{eq}	The equivalent stress; $\sigma_{eq} = \sqrt{\frac{1}{2}\left[(\sigma_1 - \sigma_2)^2 + (\sigma_2 - \sigma_3)^2 + (\sigma_3 - \sigma_1)^2\right]}$
σ_m	The mean stress; $\sigma_{m} = (\sigma_1 + \sigma_2 + \sigma_3)/3$
$\sigma_{triaxiality}$	The stress triaxiality, $\sigma_{triaxiality} = \sigma_m / \sigma_{eq}$
D	Rousselier adjustable damage variable
σ_1	Rousselier adjustable damage variable

σ_y The yield stress

f_0 The initial volume fraction of voids

$H(\epsilon_{eq}^p)$ Function to describe material hardening in Rousselier model

β Scalar variable of Rousselier damage model

Φ The yield surface for the material

σ_{kk} The trace of stress tensor (i.e. $\sigma_{11} + \sigma_{22} + \sigma_{33}$)

V_{tot} The total volume of the material

V_m The matrix volume; i.e. excludes the voids

f Value of porosity; $f = \frac{V_{tot} - V_m}{V_{tot}}$

q_1, q_2, q_3 Gurson model parameters; $q_3 = q_1^2$

f_N The volume fraction of the second phase particles where voids can be nucleated

ε_N The strain value for which 50% of the particles are damaged

S_N The standard deviation of the void nucleation strain

f^* The effective porosity at failure introduced by Tvergaard and Needleman to Gurson model

f_c The critical voids volume fraction at the beginning of the voids coalescence process

δ The multiplication factor introduced by Tvergaard and Needleman to accelerate void growth

c The cross correlation coefficient for the DIC subset at a given location; $c(\Delta x, \Delta y)$

c' The normalized correlation coefficient for the DIC subset at a given location; $c'(\Delta x, \Delta y)$

I_1 The pixel intensity in the reference image for the DIC analysis

I_2 The pixel intensity in the deformed image for the DIC analysis

A Function of the normalized autocorrelation technique

u A variable displacement

$\bar{\sigma}$ The average stress

V The total volume

ω The forming limit stress diagram condition, the initiation of damage start when the value reaches unity between the maximum principal stress of an element to the critical value of the maximum principal stress

1. Introduction

Advanced High Strength Steels (AHSS) have generated much interest in the automotive industry due to their good combination of strength to weight ratio and formability. Recently, there has been particular interest in dual-phase (DP) steels, owing to their mechanical properties, as compared to other high strength steels. With two phases only, DP-steels have the advantage of continuous yielding, high early strain hardening, high ultimate tensile strength (UTS) and large deformation to fracture. This combination currently makes DP-steels preferred materials in the automotive industry, where early yielding and high strain hardening is essential for metal forming, while the high UTS value provides good crash resistance and enables weight reduction for reduced fuel consumption. Even though transformation-induced-plasticity (TRIP) steels have higher ductility with similar UTS (Figure 1-1), manufacturing problems such as high alloy cost, casting issues and difficulties in welding make them less interesting than DP-steels. However development of next generation DP-steels requires better understanding of deformation and damage mechanisms at the micro-scale in order to predict the resulting overall stress/strain response.

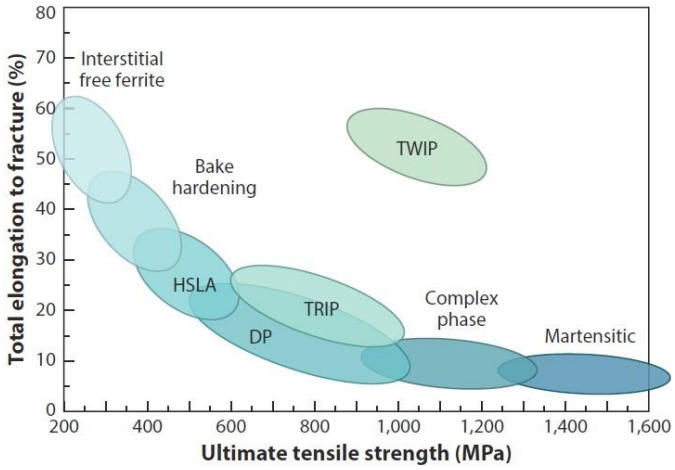

Figure 1-1: Comparison of total elongation against ultimate tensile strength for DP-steels among other high strength steels [1]. TRIP, transformation-induced-plasticity. HSLA, high strength low alloy. DP, dual-phase. TWIP, twinning-induced plasticity.

In the past three decades, several attempts have been made to investigate damage in DP-steels. Voids nucleated near the interface between the constituents and martensite fracturing have been found in several studies for DP-steels [2-11]. However, there has been no detailed investigation on the prediction of damage initiation in DP steels to provide insight into the development of physically-based multi-scale models. Most studies in the field of DP-steels have only focused on experimental observation of damage mechanisms and measurement of deformation, or microstructure simulation. However, far too little attention has been paid to combining experimental observation and modelling at the micro-scale to investigate damage locally for DP-steels. As a result, there is a clear lack of physically-based damage models in the literature aimed at predicting with confidence the overall strain/stress response needed in the steel industry.

This work therefore aims to bring new knowledge to the research field through a novel approach which combines experimental tensile testing inside a scanning electron microscope up to fracture and microstructure modelling informed by experimental results, through

Digital Image Correlation measurements, in order to set realistic boundary conditions and optimise the local unknown phase behaviour (stress/strain curves). Moreover the new approach enables the simulation of small regions of interest in the microstructure with reasonable accuracy in order to predict the appearance of very local events such as damage formation. Results from the local microstructural model are then used to inform a micro-macro damage model of a Representative Volume Element (RVE) of the material with damage parameters optimised using DIC measurements and experimental stress/strain curves. The predictability of the model in terms of overall stress/strain curve is then tested using specimens with different geometries and levels of stress triaxiality (mean stress/equivalent stress).

The following chapter reviews the relevant literature on DP-steels including the deformation and damage mechanisms commonly observed as well as a description of some continuum-based damage models applicable to this work. Chapter 3 begins by explaining the material used and the detailed procedure employed for obtaining the experimental results, including an in-situ test and DIC techniques. The fourth chapter is concerned with the methodology used for all simulations carried out in this project for macro-specimens and microstructure simulations. The fifth chapter presents the experimental results. Simulation results are divided into two sections in chapter 6; section 6.1, which illustrates the multi-scale simulation results including macro-modelling of the specimens; and section 6.2, which is focused on microstructure simulation, damage initiation and development in the martensite phase, and section 6.3 shows the RVE modelling results. Chapter 7 analyses and discusses the results obtained experimentally and numerically. Damage mechanisms observed on the DP1000 surface and deformation patterns were compared to results reported in the literature.

Uncertainties in stress calculations carried out by the microstructure simulation are then discussed. The new methodology of combining DIC results and microstructure simulation to infer damage initiation criteria is then reviewed and the prediction of the RVE model using the new calibration method for the damage model parameters used in this study is discussed. The last chapter draws the main conclusions, highlighting the novelty of this work and provides recommendation for future work.

2. Literature Review

Steels are among the most important structural materials that allow development in various engineering fields, such as infrastructure, transportation and energy. Breakthroughs in these fields have resulted from the development of Advanced High Strength Steels (AHSS). Engineering and scientific interest in AHSS is justified by the pronounced demand in the automotive industries for crash resistance materials and fuel efficiency. Dual-phase (DP) steels are one of the earliest known types of AHSS. Research and publications regarding DP-steels showing a full understanding of the material behaviour have not yet been achieved. The complex microstructures of DP-steels constituents raise open scientific questions. This chapter reviews the literature and is divided into five sections. It starts with an overview of DP-steels by showing their properties and manufacturing issues. The following sections describe damage and characterisation at the micro-scale. After this, a section deals with findings on the results of damage and microstructure modelling of DP-steels. Finally, the fifth section presents a damage model to simulate voids nucleation and growth in ductile materials that will be used in this research.

2.1 Dual Phase Steels

The terms ductility and formability will be used in this research. Definitions of these terms are presented here. Ductility is an important mechanical property of the material. It is the measurement of the plastic deformation that the material can sustain to fracture. The quantity can be given from a uniaxial tensile test. It is expressed in either percentage of elongation ($\frac{L_f - L_0}{L_0} \times 100$) or percentage of reduction in the area ($\frac{A_0 - A_f}{A_0} \times 100$). L_0 and L_f are the initial and final length of the specimen gauge section, respectively. A_0 and A_f are the initial and final cross sectional area of the specimen, respectively. Damage mechanism in ductile material includes voids initiation, growth and coalescence [12-14]. Formability can be defined as the ease in which the material can be changed permanently to a desirable shape without being damaged or fractured. It depends on the material properties (e.g. ductility and yield strength) and working conditions (e.g. temperature and stresses). The tests to measure material formability include complex loading conditions such as swift cup test [13, 14].

Dual Phase (DP) steels are high strength steels which combine the advantages of high strength and high total elongation to fracture (ductility). The stress/strain behaviour of DP-steels differs from that of other steels, such as High Strength Low Alloy (HSLA) steels as shown in Figure 2-1 (a). They have the capacity to undergo continuous deformation, with no yield point, and have high ultimate tensile strength (UTS), high strain hardening and, in some cases, low yield strength. These properties mean DP-steels have better formability and are excellent for sheet forming, making them preferable for use in the automobile industry, where formability and strength are important and desirable (i.e. for parts like car panels, etc…).

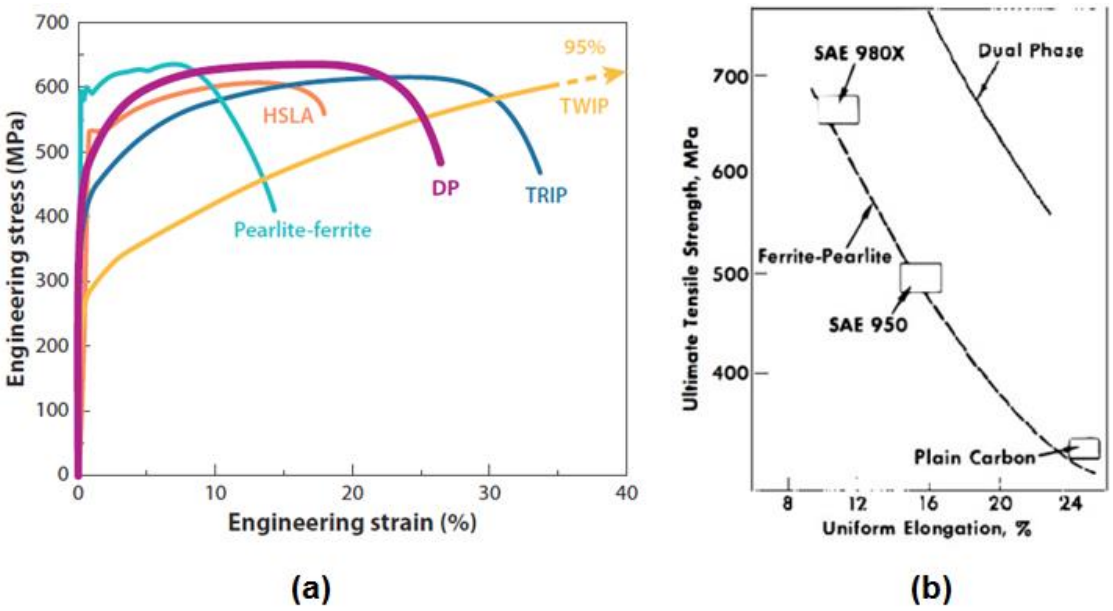

Figure 2-1: (a) Stress/strain curves of different types of AHS steels [1], and (b) ductility and strength relationship of DP-steels as compared to ferrite/pearlite steels [15]

Figure 2-1 compares DP-steels and ferrite-pearlite steels. As can be seen, when exposed to a similar uniform elongation, DP-steels have a higher UTS value than pearlite steels. The strength/ductility curve of DP-steels falls into distinct data compared to ferrite/pearlite steels. As a result, in the same manufacturing process, DP-steels afford better strength than ferrite/pearlite steels; consequently, it is possible to reduce weight, which is desirable in the automotive industries.

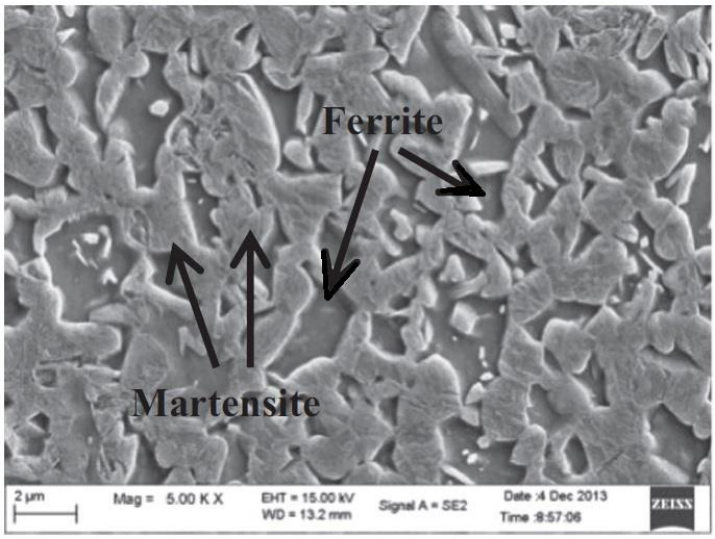

Figure 2-2: Scanning Electron Microscopy (SEM) image of DP1000 steel microstructure, showing the ferrite phase (in dark) and martensite (in bright) [8]

DP-steels microstructure consists of two main phases, ferrite and martensite, as shown in Figure 2-2. Ferrite is the soft phase, and can improve material ductility, while martensite is the hard phase, which can enhance the material's strength. DP-steels can be manufactured using the Intercritical annealing process. Ferritic steel anneals at an Intercritical temperature (750^{o}C) for a controlled period of time, to form the austenite phase beside the ferrite phase; it is then quenched to room temperature, so that the austenite transforms into martensite (although in some cases a small percentage of austenite is retained). Another method includes controlling the quenching rate of fully austenitic steels (above 800^{o}C in Figure 2-3) so that some austenite is transformed into ferrite, while the remaining becomes martensite. The temperatures at which austenite begins to transform upon heating (A_{c1}) and completes its transformation (A_{c3}) are compositions dependent. Figure 2-3 shows a schematic chart of the Intercritical annealing process [1]. The process is complex, as multiple factors can affect the produced DP-steel, such as the annealing temperature, annealing time, quenching rate and chemical composition.

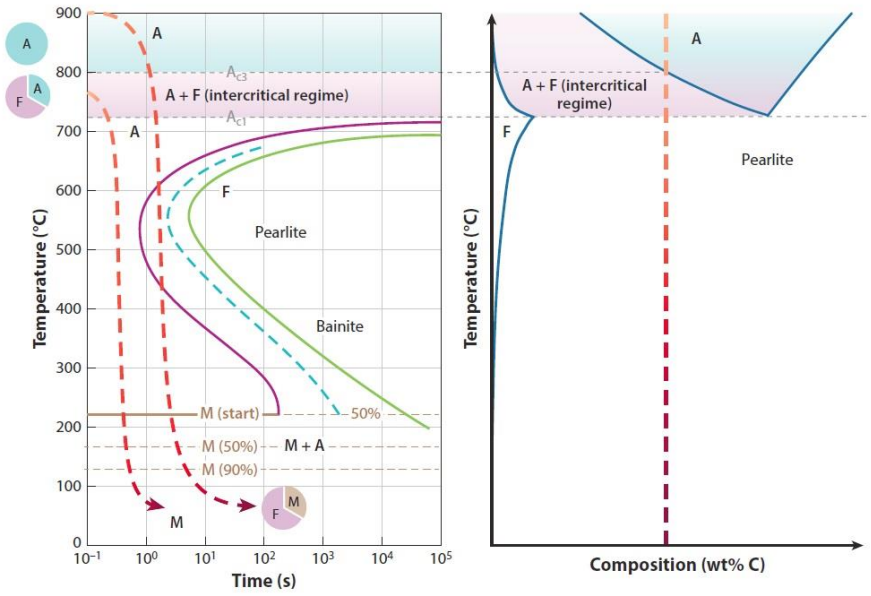

Figure 2-3: Intercritical annealing process for manufacturing DP steels. Abbreviations: M, martensite, F, ferrite, and A, austenite [1]

It is noteworthy that the mechanical properties of DP-steels are not only dependent on the manufactured microstructures, such as the distribution and volume fraction between martensite and ferrite; indeed, additional factors can influence the properties of DP-steels, such as chemical composition [16]. However, the microstructures of DP-steels play a crucial role in the damage mechanisms, thereby affecting the overall mechanical properties.

The manufacturing process plays a major role in the formation of the microstructure of DP-steels, which consequently affects the damage behaviour and development at micro-scale. Using different manufacturing processes can lead to the production of a variety of DP-steels; thus, each produced steel has distinct mechanical properties. For example, Zhao et al. in 2014 [8] investigated the effect of annealing temperature on the DP-steels produced. Elevating the annealing temperature increases the martensite volume fraction with coarser microstructures. Some researchers have tried to link manufacturing processes and their

effects on the mechanical properties of DP-steels. Kang et al. [17] studied the effect of tempering on DP600, with a 20% martensite volume fraction. Tempered specimens (i.e. heating the samples up to 450^{o}C after quenching, then cooling to room temperature) had larger carbides within the microstructure, as compared to non-tempered samples. It has been found that tempering slightly reduces the yield strength of DP600 steels, but enhances the ductility to fracture, and has a small effect on work hardening. Saeidi et al. [18] examined two types of grain morphology; ultra-fine and coarse-grained DP-steels, with a martensite volume fraction of around 50%, as shown in Figure 2-4. They reported that grain morphology has a small effect on yield stress and on the ultimate strength of tested DP-steels. However, there are noticeable effects on uniform strain and total elongation to fracture. Ultra-fine grained DP-steels have a higher uniform elongation and ductility compared to coarse ones.

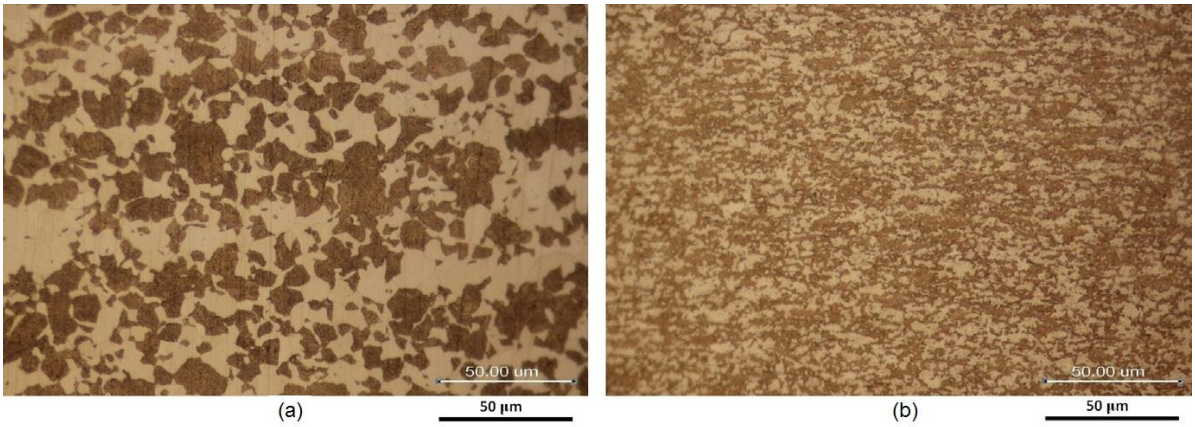

Figure 2-4: Optical microscopy images of (a) coarse-grained and (b) ultra-fine DP-steel used in [18]; ferrite in white while martensite in dark

Ramazani et al. [19] studied the effect of banding on the mechanical properties of DP-steels. Banding refers to martensite particles that are lined up in the microstructure, rather than having a uniform or random distribution of the martensite. In their research, different heat

treatment conditions were used to produce DP-steel samples. Both the faster heating rate and the increased annealing temperature can lead to a banded microstructure. The results show that banding leads to a decrease in yield strength, work hardening and tensile strength. Banding also leads to microstructural inhomogeneity, causing damage in the early stages of deformation and a reduction in the uniform elongation of DP-steels. Park et al. [20] studied the effect of microstructure morphology in DP-steels, focusing mainly on martensite distribution. They tested two types of microstructures; chained martensite, where ferrite grains are surrounded by martensite particles, and isolated randomly distributed martensite, as shown in Figure 2-5. Chaining improves hardenability, and reduces necking deformability, but does not affect total elongation.

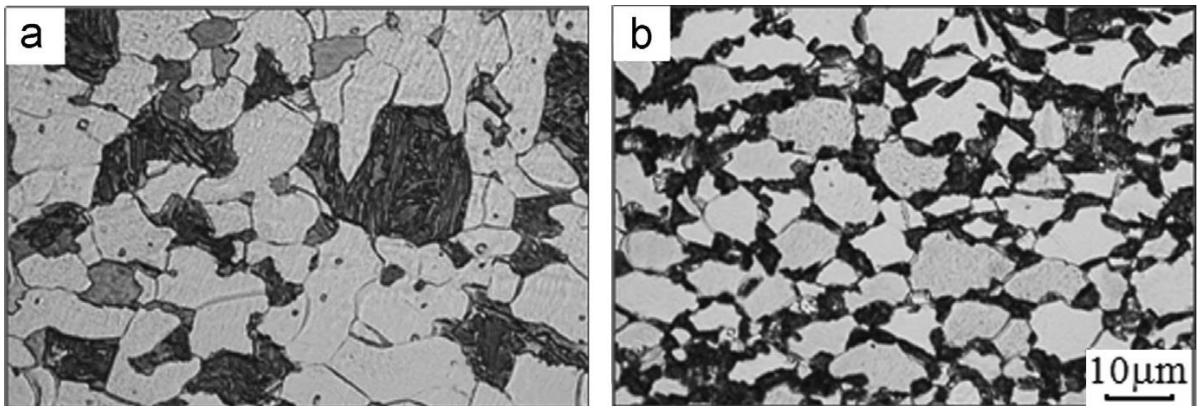

Figure 2-5: DP-steel morphology obtained using optical microscope from etched specimens of (a) isolated martensite and (b) chained martensite used by Park et al. [20]; martensite in dark while ferrite in white

Interesting results from Pierman et al. [16] showed the effect of three microscopic parameters on the mechanical behaviour of DP-steels: (i) the volume fraction of martensite, (ii) the carbon content of the martensite, and (iii) the morphology of martensite islands. Increasing the martensite volume fraction with a constant carbon content reduces the ferrite grain size and raises the interface strength, because of a high density of dislocations located

at the interface during the austenite transformation process. Consequently, the yield stress, ultimate strength and uniform elongation of DP-steels are enhanced. In addition, the microstructure includes equiaxed martensite islands (i.e. the length and width of particles are relatively uniform), leading to higher yield stress and ultimate strength and ductility when compared to fined elongated martensite particles. With equiaxed martensite, the load transfer between phases improved, and thus the ferrite plastic flow was better restricted than that of DP-steel with elongated martensite. The authors claimed that carbon content has a lesser impact on the ferrite phase compared to martensite. It was also found that microstructures with higher carbon content (keeping martensite volume fraction constant) developed better hardening, improved ultimate strength, and produced more uniform elongation, with no effect on yield stress. This is due to the enhancement in interface strength as dislocations condense near the interface. The results appear to contradict what is commonly reported in the literature; however, previous investigations focused on one particular grade of DP-steels only, i.e. the martensite volume fraction increased with a decreasing carbon content, as was also observed by Pierman et al. [16]. For example, Sodjit et al. [21] claimed that increasing the martensite volume fraction reduces ductility. However, this reduction in ductility can be explained by a reduction in carbon content in the martensite particles, leading to weaker martensite, and thus increasing the probability of earlier damage. Pierman et al. [16] were able to examine each factor independently without overlap, in order to separate the effect of each microstructural features.

For modelling purposes, martensite and ferrite phase properties have to be identified. Phase properties have been reported in the literature, as in Figure 2-6, which shows the flow curves of martensite and ferrite determined by Uthaisangsuk et al [22] as a function of the chemical

composition of DP600. However, the reported flow curves should be used with caution as they depend on carbon content, martensite volume fraction, morphology and chemical compositions which are likely to differ between DP steels and especially at the scale of the microstructure.

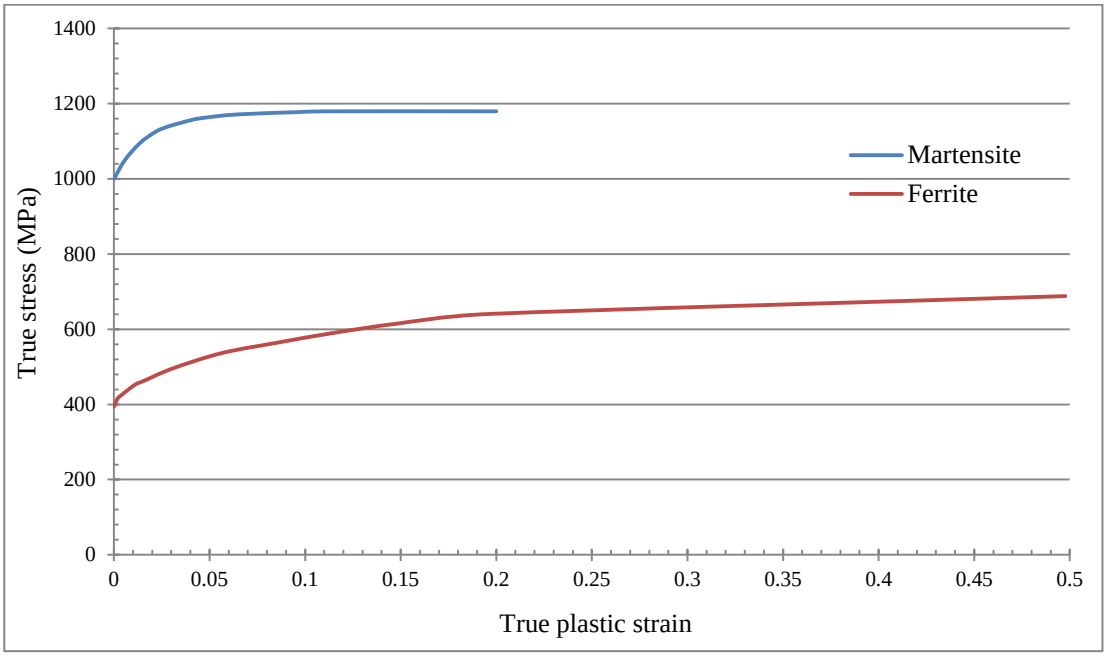

Figure 2-6: Flow curves by Uthaisangsuk et al for martensite and ferrite of DP600 steel [22]

Another method to predict the flow curves of phases is the empirical model of a dislocation based strain hardening approach [23]. The phases' flow curves can be predicted using the following expressions:

$$\sigma = \sigma_0 + \Delta\sigma + \alpha . M . \mu . \sqrt{\frac{1 - \exp(-M.k.\varepsilon^p)}{k.L}} \quad (1)$$

$$\sigma_0 = 77 + 80 \times \%Mn + 750 \times \%P + 60 \times \%Si + 80 \times \%Cu + 45 \times \%Ni + 60 \times \%Cr + 11 \times \%Mo + 5000 \times N_{ss} \quad (2)$$

where α is a constant with a value of 0.33. The terms M, μ and b are the Taylor factor, shear modulus and Burger's vector with the values of 3, 80 GPa and 2.5 E-10 m, respectively. The terms L is related to the dislocation mean free path; 'k' is the recovery rate; and Δσ is the strengthening due to carbon and precipitations. The values for ferrite of L, k and Δσ are 5E-6, 2 and 100, while for martensite these values are 3.8E-8, 41 and 1500 respectively, according to Kadkhodapour et al 2011 [23].

The previous discussion has demonstrated that the mechanical properties and behaviour of DP-steels correlate strongly with microstructures. Investigation of the microstructure deformation is important to understand the behaviour of the material and help the development of next generation DP-steels. Consequently, the characterisation of deformation and damage mechanisms at the micro-scale are essential for any DP-steel. These will be discussed further in the following sections. Additionally, the mechanical properties of DP-steels constituents have to be identified properly in order to simulate microstructure deformation and damage.

2.2 Damage Mechanisms in DP-steels

Damage mechanisms are crucial for the understanding of the behaviour of DP-steels and to improve their properties. DP-steels are ductile materials, and damage includes voids initiation, growth and coalescence, especially in a quasi-static state. Several researchers have investigated damage in DP-steels, as will be discussed in this section. Some of these studies have focused on experimental observations of the microstructure, while others have combined experimental measurements with microstructure simulations.

Steinbrunner et al. [2] reported on decohesion and martensite fracture as damage mechanisms affecting DP-steels, with a 20% martensite volume fraction, and with a weight percentage of 0.08 for carbon content. Their findings were based on scanning electron microscope (SEM) observations of failed specimens. Maire et al. [3] observed the same mechanisms for DP600, with a 10% martensite volume fraction and 0.08 wt% carbon. A proportion of 50% for each mechanism has been reported. An illustration of these mechanisms is shown in Figure 2-7 (a). An interesting finding is that the fraction of martensite fracture at the surface was low at the surface. X-ray tomography results of the necking region of a tensile specimen revealed that the percentage of voids increased when approaching the centre of the specimen in the necking region, as shown in Figure 2-8. This relates to stress triaxiality in the centre of the specimen, which was higher than at the surface. Stress triaxiality plays a major role in void growth [3].

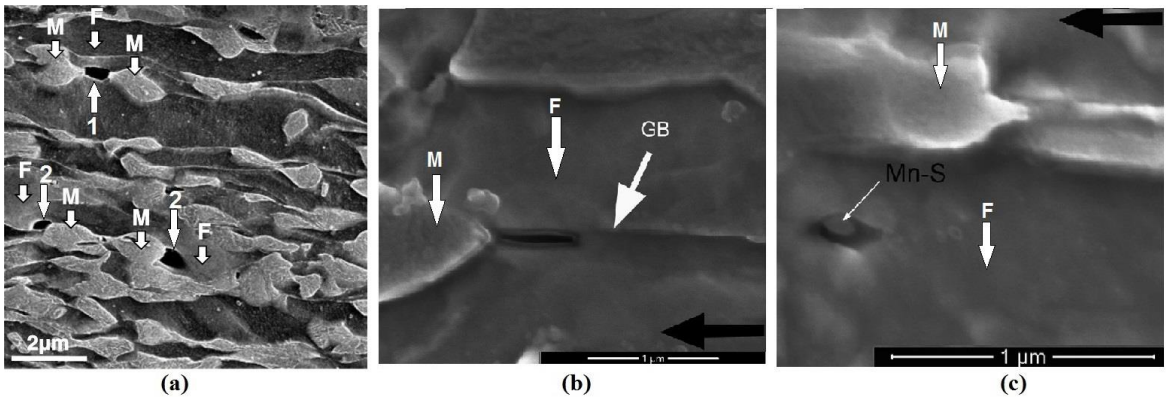

Figure 2-7: Damage mechanisms in DP-steels: (a) 1. martensite cracking and 2. decohesion between the ferrite-martensite interface [10], (b) separation along ferrite-ferrite grains, and (c) void due to inclusion failure in Ferrite [24]. Abbreviations: M, martensite, F, ferrite, and GB, grain boundary

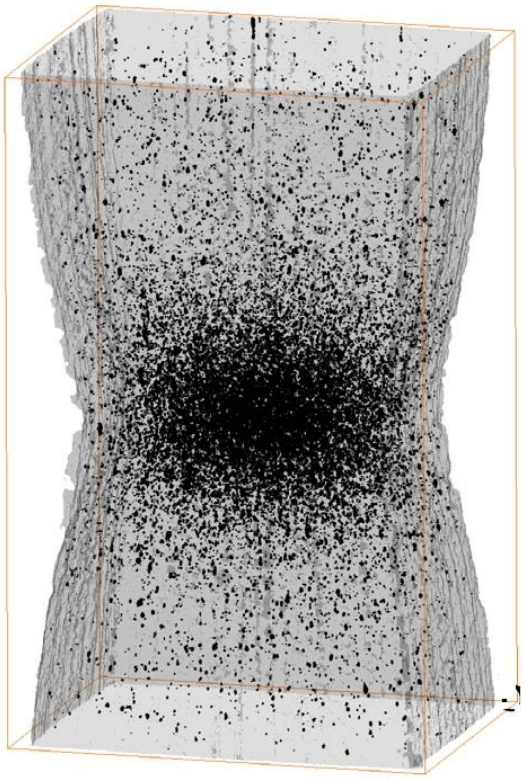

Figure 2-8: X-Ray tomography of DP600, adapted from Maire et al. [3], showing damage condenses in the centre of the necking region

However, in DP-steels, the observation of failed specimens near the fracture surface reveals that the dominant void nucleation mechanism is the decohesion of ferrite and martensite

interface, as reported in [4-10]. Moreover, in 2013, Lian et al. [11] investigated the microstructure of failed DP-steels specimens. They found that the majority of voids were generated in the ferrite phase between fragmented martensite particles. Martensite fracture was also reported in [4, 7, 10, 11] but had a small contribution to the overall damage process, whereas inclusion failure was rarely seen. Previously, in 2010, Ghadbeigi et al. [25] observed damage to DP1000 steel microstructures. Localised bands of deformation were observed in large ferrite areas. Further deformation led to damage propagation through both the ferrite and martensite phases, as well as at the interface. Martensite separation was also captured at the specimens' surface. No voids in the ferrite were reported at the surface for DP1000 steels. Choi et al. [10] investigated DP980/1000 steel specimens and observed three damage mechanisms: (i) decohesion at the interface, (ii) separation of the adjacent martensite region near the deformed ferrite phase, and (iii) martensite cracking. In 2013, Ghadbeigi et al. [24] investigated damage in DP600 steels, finding that martensite islands deformed according to three different modes; shear, tension and bending. They also reported the separation of martensite, but this did not initiate voids, as the separated particles moved within the matrix. Sub-micron voids were found to initiate at a region near the interface, which then propagated along the interface. Voids initiated at inclusions in the ferrite were also reported [24], and some voids were observed along the ferrite-ferrite grain boundaries. These voids elongated along the loading direction. Figure 2-7 (b) and (c) show voids initiated along the ferrite grains, and at inclusions.

In summary, the literature reports four main mechanisms of damage in DP-steel microstructures: decohesion near the interface between ferrite matrix and martensite particles; martensite fracturing; failure at inclusions in the ferrite; and voids nucleated along

ferrite-ferrite grain boundaries. Decohesion of the interface was preceded by micro-cracks near the interface in the ferrite phase, which then elongated along the interface and formed a void. Voids were formed in the ferrite phase or at the location where martensite fracture starts. Martensite fracture itself does not form a void.

Observations in the literature have been mostly based on post-fracture investigation. Studies following damage development and especially the history of damage development as a function of strain localisation have hardly been reported in the literature. This work is therefore aimed at filling this gap in knowledge to enhance the physical understanding of damage initiation and development in DP steels.

2.3 Characterisation at the micro-scale

There are different damage mechanisms in DP-steels, as discussed in the previous section, and it is important to analyse damage at the micro-scale. This includes studying local strains and stresses, the history of the damage, and other factors that might affect deformation and damage, such as the distribution of phases in the microstructure. Poruk et al. (2008) [26] claimed that the nucleation of voids for DP-steels occurs for an average applied strain of 0.9 ±0.05. The applied strain is the strain calculated at the macro-scale for the whole specimen. This might be useful for damage models; however, it can differ from the local strains at the micro-scale, where the void or damage is nucleated. Kim et al. [27] found the local strain in the ferrite phase exceeded the applied strain three fold, so studying the strain locally is important to find a reliable nucleation criterion.

Ghassemi-Armaki et al. [28] studied the behaviour of ferrite and martensite in DP-steels, using statistical representative indentation tests. Their results demonstrated variable hardness and strength within the ferrite phase. Near the ferrite-martensite interface, the ferrite is harder and stiffer than in the interior of the ferrite grain. When applying deformation to DP-steels, the interior of the ferrite phase tends to harden, while it softens near the vicinity of the interface. Ferrite phase starts to deform plastically in the microstructure before martensite. The plastic deformation in Ferrite starts at DP-steels yielding point while the martensite begins to deform plastically during the hardening part after the ferrite but before attaining the ultimate strength of DP-steels. This insight suggests that caution is necessary when modelling deformation of the microstructure, in order to take into account the variations in phase properties within the grain.

Microstructure deformation and damage can be analysed using scanning electron microscope (SEM) images. Detection of microstructure damage can be carried out during a test, by installing a special tensile stage inside the microscope chamber. This is termed in situ tensile testing. The advantage of this method is that the researcher can track the development of any damage at the micro-scale. However, it requires a big SEM chamber, and the test can take a long time to run and analyse, in addition to the significant cost and training required. Another option is to apply a certain amount of deformation in a conventional test to make it possible to investigate the microstructure with SEM images.

Ghadbeigi et al. (2010) [25] observed the deformation of a DP1000 microstructure, using an in-situ tensile test inside the chamber of a SEM combined with DIC. Strain results revealed localised bands at 45^{o} to the loading direction in the large ferrite phase. Localisation led to damage propagation through the ferrite, martensite, and along the interface. However Ghadbeigi et al. [24] did not observe strain bands in DP600 (with a martensite volume fraction of about 15%), when compared to DP1000, as shown in Figure 2-9.

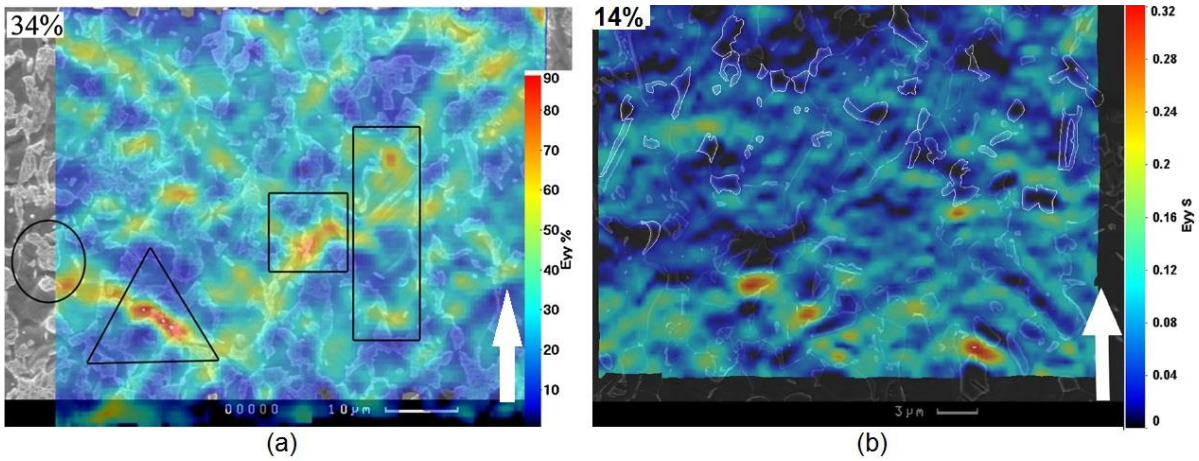

Figure 2-9: DIC strain results for (a) DP1000 showing strain bands at 45^0 to loading direction shown in white arrow [25], and (b) DP600 with no strain bands [24]

Shear bands were reported by Kadkhodapour et al. [29] for DP600 (with a martensite volume fraction of about 31%) using microstructure simulations. Trapped ferrite islands between martensite usually have strain localisation and are capable of generating micro-crack initiation. Shear bands and voids were indeed found to occur in the ferrite phase in the vicinity of martensite particles. Ghadbeigi et al.'s [24] observations appear to contradict those of Kadkhodapour et al. [29], as both studies were using DP600 steels. However, the chemical compositions differed, as did the martensite volume fraction, which leads to different deformation and damage mechanisms. An explanation was given by Sodjit et al. [21], who examined microstructure simulation results of two different DP-steels with martensite volume fractions of 25% and 60%. For the smaller martensite volume fraction (i.e. 25%), several short shear bands appeared in the microstructure, while long, continuously localised bands were observed in specimens with a high martensite volume fraction (i.e. 60%). This suggests that martensite volume fraction should be considered when analysing strain bands in the microstructure of DP-steels.

Kang et al. [17] utilised DIC method to study strain partitioning between ferrite and martensite for DP600. They found that strain heterogeneity emerges when the ratio between ferrite size to martensite is greater than three, which is not the case with the DP1000 analysed by Ghadbeigi et al. [25], whose analysis of strain partitioning in DP1000 steels showed that both phases deformed similarly, with slightly higher values in the ferrite phase, as illustrated in Figure 2-10.

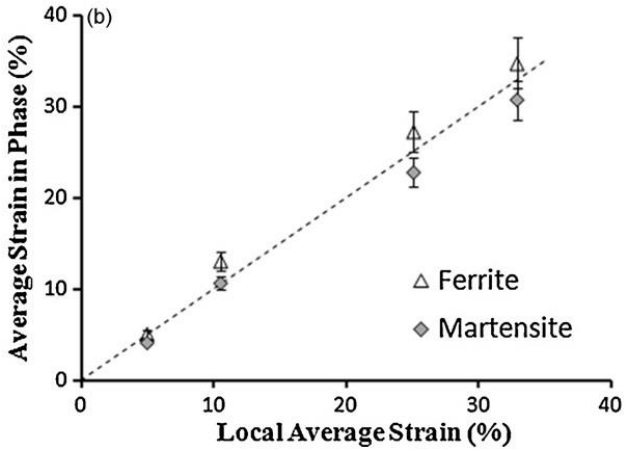

Figure 2-10: Strain results measured locally at phases using DIC against local average strain of DP1000 steel [25]

Han et al. [30] utilised micro-grid to quantify strain in the microstructure of DP-steels. The produced results suggesting that the microstructure morphology determines strain localisation. They found that large ferrite grains surrounded by martensite particles with similar size exhibit strain localisation, while ferrite grains surrounded by small martensite islands show no localisation as the neighbouring ferrite cushions the strain. Some researchers have used microstructure modelling to study strain partitioning. Paul et al. [31] added to the influence of the microstructure morphology, the effect of differences in the flow curve in both phases. Their results showed that deformation is localised in the ferrite phase. Local stress triaxiality builds up as a result of constrained deformation in the ferrite

phase, caused by martensite particles. Park et al. [20] reported that the martensite strain is higher in a chained microstructure than in a distributed martensite microstructure, which leads to a reduction in strain partitioning between phases.

Tasan et al. [32] investigated localisation in DP600 and DP800, using DIC and CPFEM. A coarse microstructure with a large ferrite phase, leads to early damage formation after early localisation of plastic deformation. However, the microstructure with fine ferrite grains and martensite islands developed lower strain localisation than the other microstructure and thus delayed any damage formation, as shown in Figure 2-11. As can be seen from Figure 2-11 (b_3), there was no location where the von Mises strain exceeded 0.4, whereas different locations (shown in whites) with values above 0.4 can be observed in Figure 2-11 (a_3)Saeidi et al. [18] argued that, in ultra-fine DP-steels, the larger number of small martensite phase particles leads to a greater total interface area between the ferrite and martensite, and thus better load transition between the phases. This results in strain relaxation within the microstructure. Consequently, ultra-fine grained DP-steels show higher plasticity in the martensite and lower strain partitioning, resulting in an improvement of DP-steels ductility.

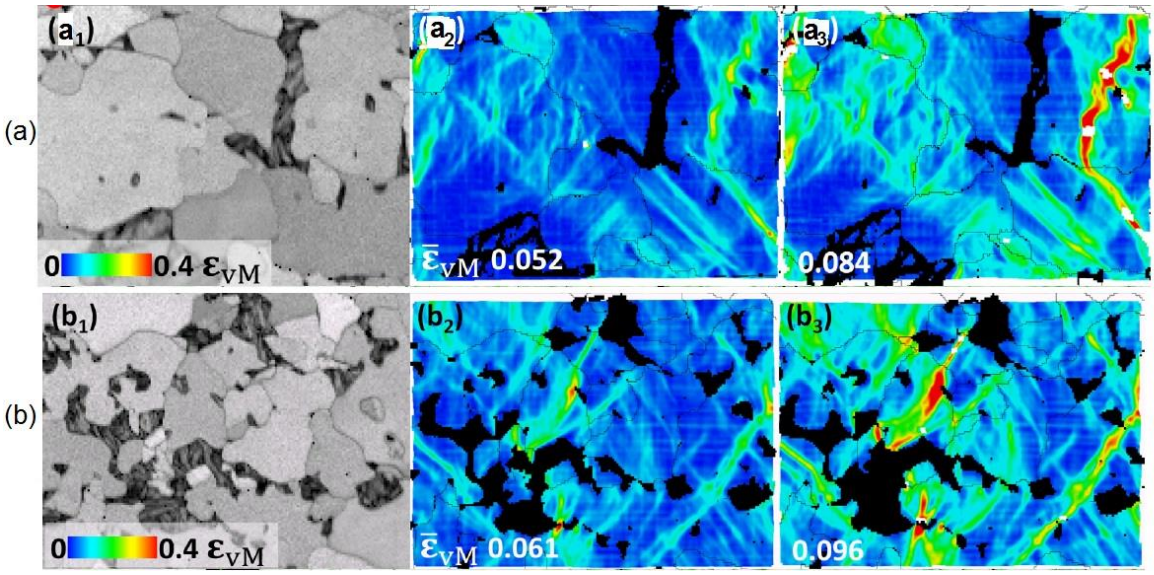

Figure 2-11: Tasan et al. [29] von Mises strain results for (a) large martensite microstructure as compared to (b) fine martensite and ferrite grains. (a1) and (b1) image quality map of microstructure with ferrite in white and martensite in dark. (a2) and (b2) are von Mises strain results at 0.65 applied true strain. (a3) and (b3) von Mises strain results at 0.85 applied true strain. Averaged von Mises strain results shown bottom left of (a) and (b). Martensite strain results excluded from results and shown in black

It is notable that, in DP-steels, martensite particles can deform plastically. This means that martensite particles are not brittle, and therefore a hardening behaviour representative of that in the actual material must be introduced in the simulations for reliable prediction of the deformation of the microstructure. Ghadbeigi et al. [25] utilised DIC to measure local strain values. For DP1000 steels, a value up to 130% was measured in the ferrite phase at an applied strain of 42%. The results showed that the martensite particles deformed plastically. A strain value of 110% was reported in martensite particles for DP1000, as opposed to 80% for DP600 [24, 25]. A further study by Ramazani et al. in 2014 [33] showed that the macro strain for martensite cracking was higher in microstructures that comprise equiaxed particles (i.e. width and length are fairly similar, as shown in Figure 2-12), compared to a banded microstructure. The strain increased from 0.06 and the critical effective stress (computed from stress/strain curve of the martensite phase) from 1652 MPa for a banded microstructure

to a strain of 0.085 and a critical effective stress of 1737 MPa for equiaxed morphology. Regarding the interface strength between the ferrite and martensite, this is estimated at between 1.2 GPa [5] and 2.4 GPa [26]. This variation relates to differences in microstructure distribution, chemical composition and other factors, such as the martensite volume fraction.

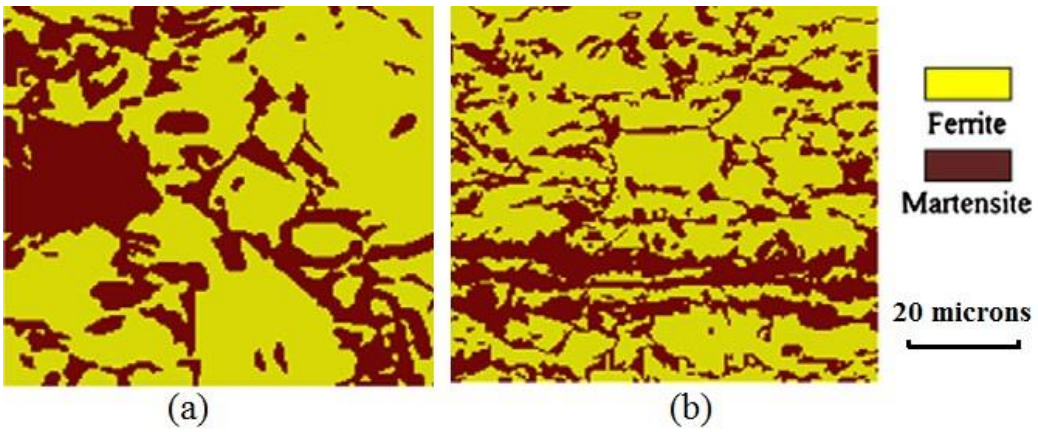

Figure 2-12: DP-steels microstructure with (a) equiaxed martensite particles and (b) banded microstructure used in Ramazani investigation [33].

From the previous results, it can be said that randomly distributed phases with finer particles are preferred for DP-steels, in order to reduce strain partitioning, improve load transfer between phases and delay damage that leads to better strength and ductility. Martensite can, in these conditions, undergo large plastic deformation. Microstructure morphology, martensite volume fraction and chemical composition should be taken into account when comparing different results from different studies for DP-steels, as these factors show a remarkable effect on deformation and damage development in the microstructure.

Despite all results reported in the literature on DP steels at the scale of microstructures, studies about criteria for damage nucleation in ferrite or martensite could not be found.

2.4 Microstructure and Damage Modelling

Microstructure simulation is a powerful modelling technique that can be used to investigate damage in DP-steels, and to predict material behaviour. The main advantage of using a microstructure simulation is to determine stress values; which cannot be measured experimentally. In the literature, two main models are used, as shown in Figure 2-13. These include a 2D model generated from the actual SEM image of the microstructure of the DP-steel and a 3D model with random distribution of the phases, built to have a similar martensite volume fraction as in the real material, termed a Representative Volume Element (RVE).

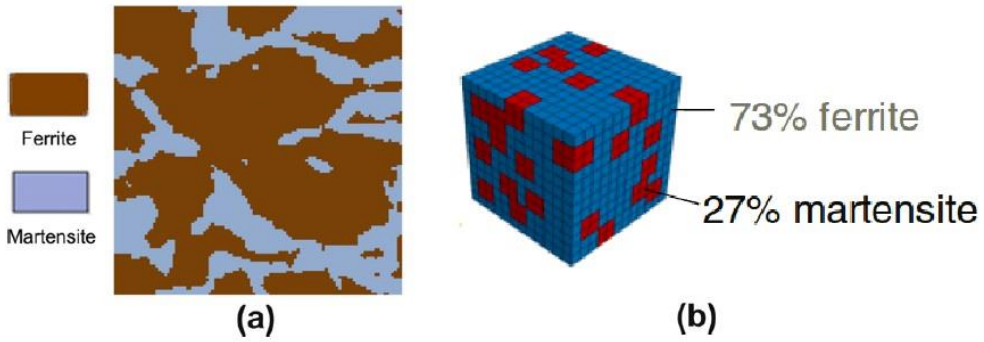

Figure 2-13: Models from the literature: (a) 2D generated from SEM image [19], and (b) 3D RVE [22]

Sun et al.'s [34] results showed that the 2D microstructure modelling reports inhomogeneity in the strain distribution between ferrite and martensite. Additionally, results of two 2D models, generated from different areas of the actual microstructure with similar martensite volume fraction and morphology, revealed a very comparable macroscopic stress/strain behaviour of DP980 steel. It is worth noting that 3D models usually give better predictions of the macroscopic response of a specimen compared to 2D plane strain models, which underestimate the response [35-37]. Iung et al. [35] relate errors when using 2D plain strain

to the mechanical and geometrical restrictions introduced in the model. Plain strain conditions assume no deformation in the third direction, and an extrusion of the 2D mesh in the third direction, which is not representative of the real microstructure. After investigating DP600 with different martensite volume fractions, Ramazani et al. [37] introduced a function to correct the stress estimation from a 2D plane strain model, according to the martensite volume fraction and equivalent plastic strain. The function was validated by the results obtained for different grades of DP-steels; DP500, DP600, DP800 and DP1000. The formula was also used in [33], and the corrected stresses were found to match the experimental results. The function is given as follows:

$$\frac{\sigma_{3D}}{\sigma_{2D}} = 2\times10^{-4}\times(\varepsilon_{eq}^{p})^{2}\times V_m^3 - 1\times10^{-7}\times\left(\varepsilon_{eq}^{p}\right)\times V_m^3 + 1\times10^{-7} \times V_m^3 + 0.0218\times\left(\varepsilon_{eq}^{p}\right)^{2}\times V_m^2 - 0.0015\times\left(\varepsilon_{eq}^{p}\right)\times V_m^2 + 7\times10^{-5}\times V_m^2 + 0.18\times\left(\varepsilon_{eq}^{p}\right)^{2}\times V_m + 0.007\times\left(\varepsilon_{eq}^{p}\right) \times V_m + 0.0036\times V_m\times\left(\varepsilon_{eq}^{p}\right)^{2} + 1 \quad (3)$$

Uthaisangsuk et al. [22] used a 3D RVE model to predict the formability of DP600 steel. Although the forming limit curves from the RVE calculations matched the experimental results, there was no comparison made at a scale of the microstructure to validate the model at that scale.

Furthermore, microstructure modelling can be used to study the effect of morphology on the behaviour of DP-steels. For instance, Ramazani et al. 2012 [19] utilised 2D models to study

the effect of martensite banding on DP-steels' behaviour. The results showed that banding increases heterogeneity, and thus decreases yield strength and uniform elongation, as discussed in Section 2.1. Sun et al. [38] investigated the effect of the martensite volume fraction on ductility, using a microstructure simulation for DP-steels, with different fractions, ranging from 7% to 44%. The results showed that, for up to 15% volume fraction of martensite, the presence of microvoids had a significant influence on ductility. However, with larger fractions, inhomogeneity between the ferrite and martensite resulted in deformation stability, which primarily governs the ductility of DP-steels. Paul et al. [31] relate inhomogeneity in strain distribution in a microstructure to microstructural heterogeneity, and differences in the flow curve between soft ferrite and hard martensite.

Microstructure modelling is also useful to investigate localisation and damage in the microstructure of DP-steels. Several studies have suggested that the localisation of plastic strain in DP-steels microstructures is related to heterogeneity at the micro-scale [7, 11, 30, 31, 39] and strain path [11]. The importance of analysing strain localisation rises in relation to DP-steels' formability [27]. Kim et al. [27] found that, for DP-steels with 49% martensite volume fraction, the martensite undergoes large plastic deformation, reducing strain localisation, which delays failure of the specimen.

Hosseini et al. [40] examined the use of large and small deformation theories to model the deformation of DP600 microstructures. After the ultimate tensile strength, (i.e. necking takes place), large deformation, displacements, and rotations develop in the ferrite phase, and transmit to martensite particles. As a result, modelling based on small deformation theory cannot predict the stress-strain response of DP-steels, especially, when specimens start

necking. Choi et al. [10] examined the effect of crystallographic orientation on the deformation behaviour of DP-steels microstructures during tensile testing. The predicted stress distribution using elasto-plastic continuum-based FEM is narrower than that obtained with a crystal-plasticity FEM (CPFE), as illustrated by the distribution charts in Figure 2-14, with maximum stress values increasing by 14% in martensite and 8% in the ferrite phase when using a CPFE model compared to the continuum-based model. Results therefore showed the strong influence of crystal orientations in the ferrite phase on deformation and damage in the microstructure of the investigated DP steels. Vajragupta et al. [41] and Tasan et al. [42] investigated strain localisation within the ferrite phase of DP-steels, using crystal plasticity and finite element modelling (CPFEM). Results showed that plastic strain concentration was related to grain boundary heterogeneity. Results for the literature have therefore shown that crystallographic and texture effects can therefore significantly influence the local response of DP steels at the scale of the microstructure. In addition, Sirinakorn et al. [43] studied the effect of geometrically necessary dislocations (GND) along the interface, on local deformation of DP1000 steels. Models with GND showed a higher value of local stress and strain in the early stages of plastic deformation, as compared to the model without a GND effect. However, both models predicted reasonably well the overall stress and strain behaviour of the material.

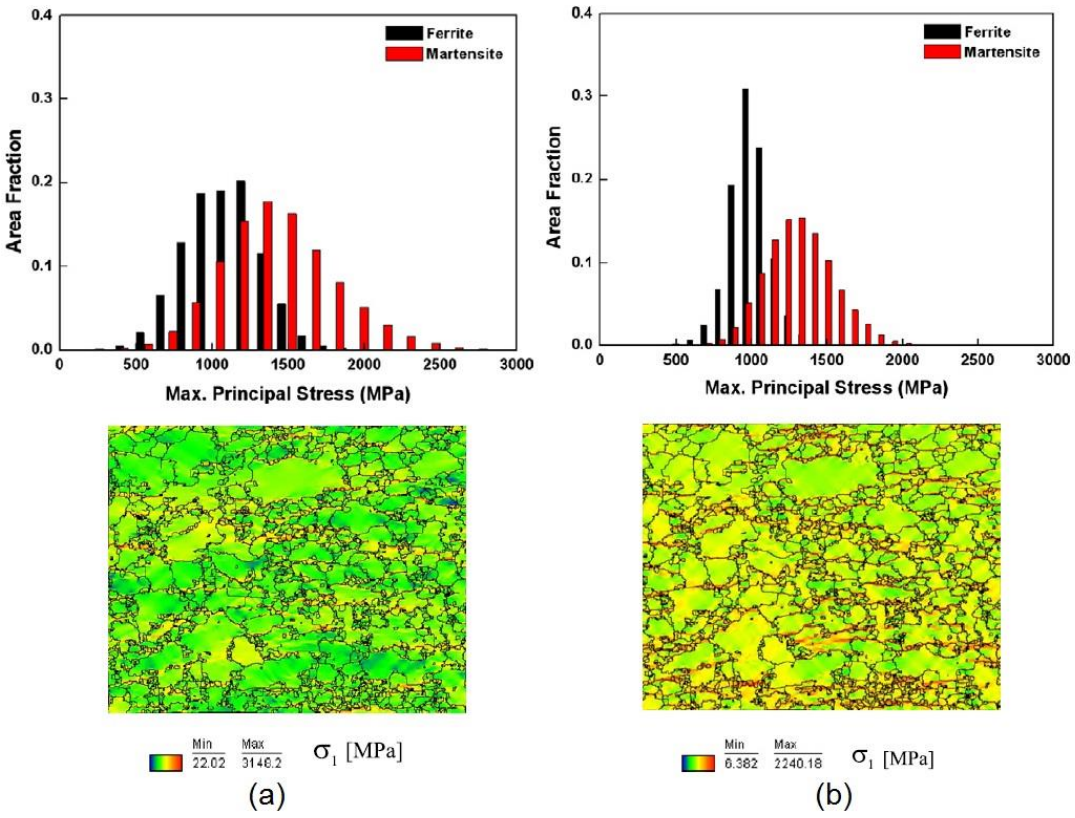

Figure 2-14: Stress results and charts of distribution for DP-steels using: (a) CPFEM and (b) continuum-based Elasto-plastic modelling [10]

Sun et al. [34] argued that the ductile failure mode depends on the size of the area of interest in the DP-steels' microstructure model. Apart from the modelling results showing a good correlation with the experimental observations for DP980 steels, their findings suggest that the failure mode relates to stress state and lateral constraints. The failure mode changes from the shear mode under plane stress state to failure perpendicular to the loading direction, if the lateral boundaries of the microstructure model are constrained (i.e. biaxial loading condition).

Kadkhadpour [44] used microstructure simulations to predict damage nucleation in DP-steels. The results show that locations of shear strain localisation and maximum hydrostatic pressure are not necessarily the same, and that any of them can lead to void nucleation. As a

result, strain or stress criteria could not be decided upon void nucleation. Lian et al. [7] concluded that initiation of damage arises at the interface, where severe plastic strain is localised as a result of deformation incompatibility between the ferrite and martensite. Simulation results showed that the damage initiation locus depends on stress triaxiality and Lode angle. Saeidi et al. [9] claimed that specimen stress triaxiality affects voids growth, whereas voids initiation is not affected. The kinematics of voids growth are faster in smooth specimens, with lower triaxiality than for notched specimens. Ramazani et al. [45] estimate a critical stress value of about 1370 MPa, and plastic strain of 0.018 for martensite cracking of DP-steel, with a 46% martensite volume fraction when prepared in the lab. However, the estimation of these values was not validated through observations of the microstructure to determine damage locations. The strain value was calculated from microstructure modelling loaded to the macro strain value of 0.065 where damage of martensite was observed. The stress value was computed from the stress/strain response of martensite. The results are shown in Figure 2-15.

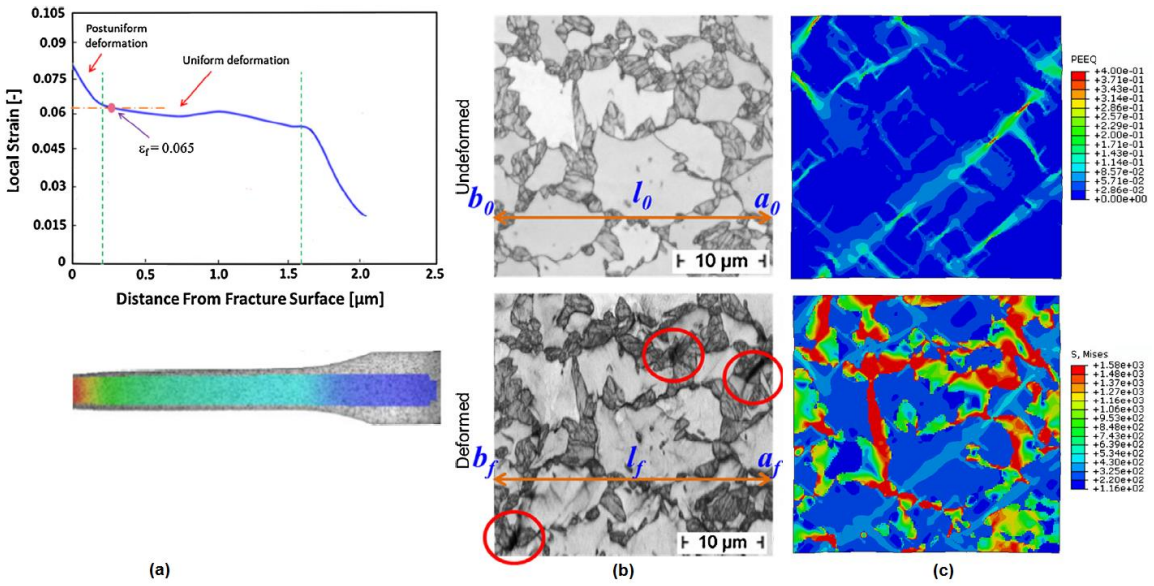

Figure 2-15: Results reported by Ramazani et al [45] to estimate critical stress and strain values for martensite cracking; (a) DIC strain distribution of the DP specimen, (b) SEM image of the microstructure before and after deformation with locations of damage highlighted with red circles, and (c) equivalent strain (top) and von Mises stress results of the 2D microstructure simulation.

Asgari et al. [39] compared a real microstructure model with a simplified model, with one martensite circular island surrounded by a ferrite phase with a similar volume fraction to that of the real model. The real microstructure-based models predicted the behaviour of the material better than the simplified model. The effect of mesh size and smoothness in the definition of phase boundaries on results from microstructural simulations was studied. Jagged or stepper mesh along the phase boundaries are usually obtained using square or rectangular elements while a smoother definition of the phase boundaries is obtained using triangular elements. These mesh types are illustrated in Figure 2-16.

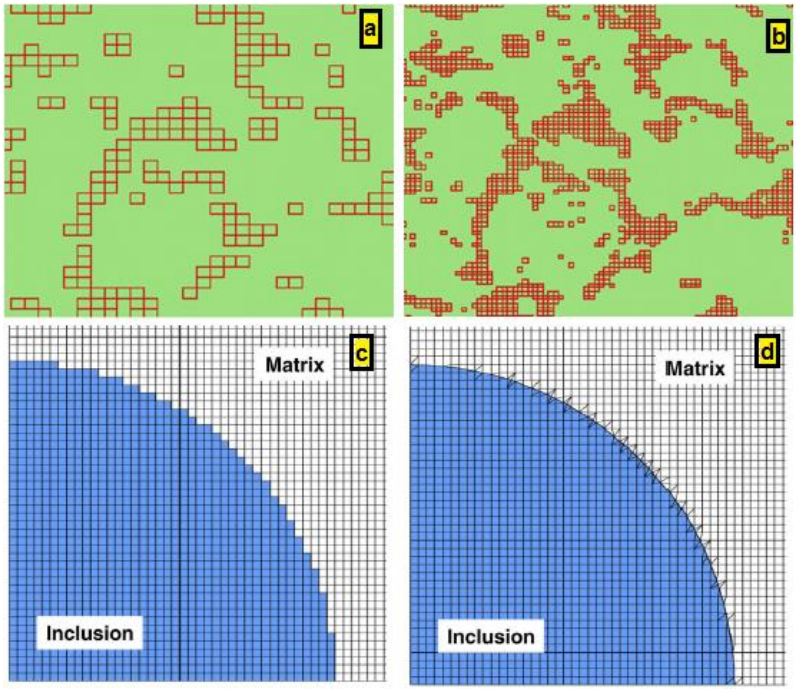

Figure 2-16: different mesh types used in the literature; top images showing different element sizes (a) coarse mesh and (b) fine mesh, and bottom images showing different levels of smoothness of the grain boundaries [36] (c) stepper or jagged mesh and (d) smooth mesh [27]

A 2D microstructure model with fine mesh converges better than with a coarse mesh in terms of prediction of experimental stress/strain curves of DP steels however deviations are small as shown in Figure 2-17 (c) [23, 34, 36]. Sun et al. 's results [34] showed that using a finer mesh within the ferrite grains has negligible effect on stress/strain prediction of DP980 steel compared to the effect of using a finer mesh along the phases boundaries. Kadkhodapour et al. [23] showed that martensite stress distribution is affected when using a coarser mesh as shown in Figure 2-17 (a) and (b). Kim et al. [27] examined the effect of smoothing the mesh along the boundary as shown in Figure 2-16 (c) and (d) on stress calculated along the boundary. Results showed that a smooth mesh predicted the analytical stress better than the stepper mesh as shown in Figure 2-17 (d).

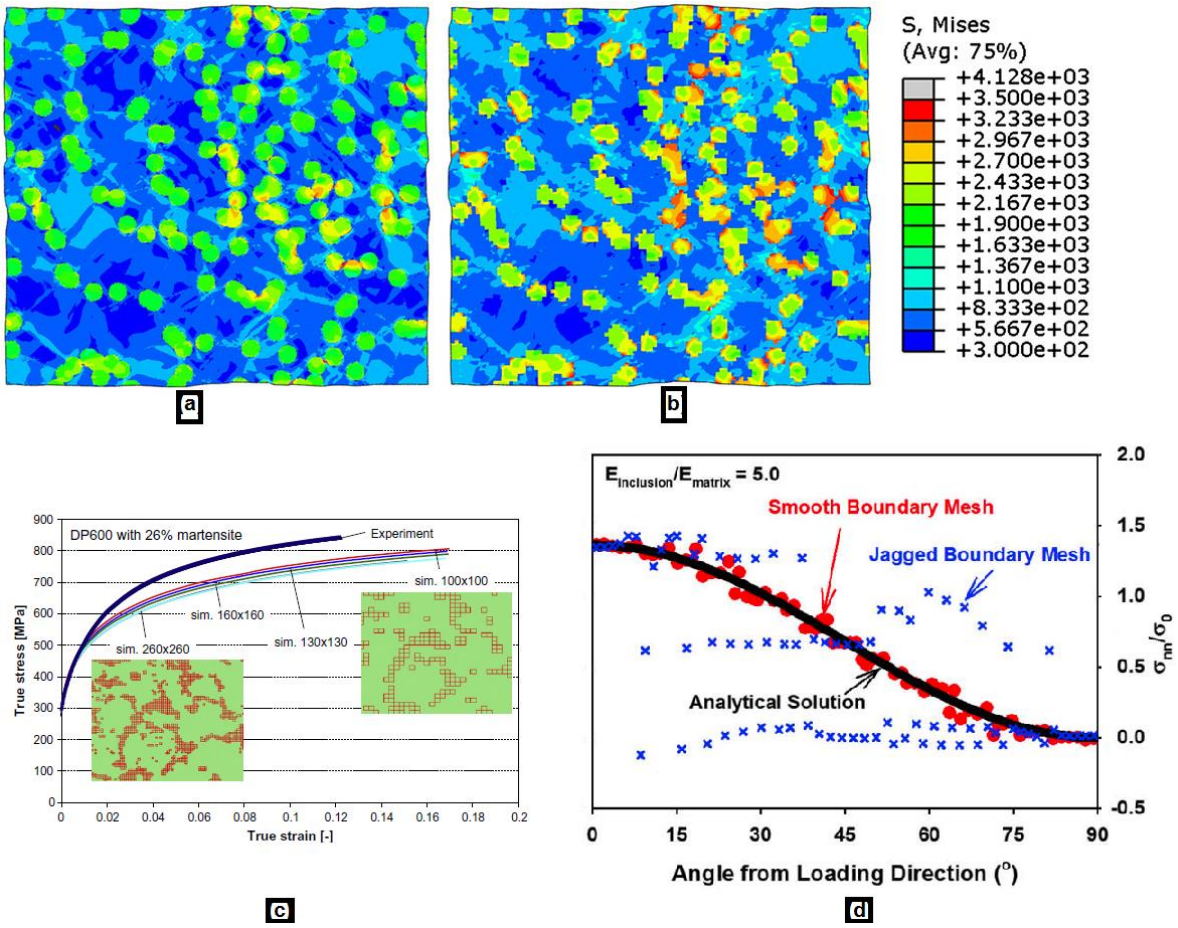

Figure 2-17: Stress distribution in the 2D microstructure model (a) using a fine mesh and (b) a coarse mesh [23], (c) stress/strain prediction with different element sizes [36], and (d) results showing the effect of smoothing the phase boundaries [27]

In summary, microstructure modelling was used as a tool to understand the behaviour, deformation and damage at the micro-scale. It can save time and cost of experiments by adjusting parameters such as morphology or martensite volume fraction, and enable the understanding of their effect on the material mechanical properties. Caution should be taken as the calculated stress values using 2D plane strain modelling could underestimate the actual stresses in the real material. A mathematical function had been suggested to correct the calculated stresses of 2D microstructure modelling. Elasto-plastic isotropic model results can vary from models that include the effect of texture by using the CPFEM method.

However, none of the modelling studies compared/validated results in terms of strain distributions at the scale of the microstructure. No study could either be found about nucleation criteria for damage nucleation at the scale of microstructure.

2.5 Continuum-Based Damage Modelling

The presence of voids affects the stress/strain behaviour of ductile materials. The process includes nucleation, growth and coalescence of voids, leading to the final fracture. In most ductile materials, the growth of voids is a key stage preceding fracture. Some of the major damage models for ductile failure are described in the following subsections.

2.5.1 Rice and Tracey model

The analyses of dilatational growth of a single spherical void in a material loaded with uniform stress at infinity were undertaken by Rice and Tracey in 1969 [46]. A classical simple equation was derived to describe void growth under high stress triaxiality as follows:

$$D = 0.283 \times exp^{\left(1.5 \frac{\sigma_m}{\sigma_{eq}}\right)} \tag{4}$$

where σ_{eq} and σ_m stand for the equivalent and mean stresses, respectively. D in equation (4) is the ratio between strain rate on the void surface and the strain rate at infinity.

The Rice and Tracey model is probably the simplest equation for void growth, which is the major advantage of the model. Practically, the model has limited applications due to the fact that it takes no account of interaction between voids, it cannot estimate fracture strain, and, in a pure shear state, the model cannot describe ductile failure. However, the model inspired Gurson, Section 2.5.3.

2.5.2 Rousselier model

Rousselier (1981) [47] proposed a thermodynamically consistent theory for ductile damage, as follows:

$$\frac{\sigma_{eq}}{\rho} - H\left(\epsilon_{eq}^{p}\right) + B\left(\beta\right) \times D \times exp^{\left(\frac{\sigma_m}{\rho\sigma_1}\right)} = 0 \tag{5}$$

where; $H\left(\epsilon_{eq}^{p}\right)$ describes the material hardening properties and usually relates to the yield stress (σ_y) of undamaged material, D and σ_1 are adjustable damage variables.

$$H\left(\epsilon_{eq}^{p}\right) = \sigma_y\left(\epsilon_{eq}^{p}\right) \tag{6}$$

β is a scalar variable of the damage and its rate defined by:

$$\dot{\beta} = \dot{\epsilon}_{eq}^{p} \times D \times exp^{\left(\frac{\sigma_m}{\rho\sigma_1}\right)} \tag{7}$$

ρ is a dimensionless density that increases with a decrease in β with the following relation:

$$\rho\left(\beta\right) = \frac{1}{1 - f_0 + f_0 \times exp^{\beta}} \tag{8}$$

f_0 is the initial volume fraction of voids. The damage function B is defined as:

$$B\ (\beta) = \frac{\sigma_1\ \times f_0\ \times exp^{\beta}}{1 -\ f_0 +\ f_0\ \times exp^{\beta}} \tag{9}$$

2.5.3 Gurson model

The first Gurson model is based on a material with a hollow sphere to represent the growth of voids. It was introduced in 1977 as a micromechanical model, and couples damage and deformation in ductile materials. A damage variable was used to describe the growth of the void, in order to describe material softening. The model was then improved and used to draw the plastic flow, by estimating the yield surface for porous metals. The following expression provides the yield surface (Φ) for a given material:

$$\Phi\ = \frac{\sigma_{eq}^2}{\sigma_y^2} + 2f\cosh\left(\frac{1}{2}\frac{\sigma_{kk}}{\sigma_y}\right) - 1 -\ f^2 = 0 \tag{10}$$

where σ_{eq} is the von Mises equivalent stress, σ_y is the yield stress and σ_{kk} is the trace of stress tensor (i.e. $\sigma_{11} + \sigma_{22} + \sigma_{33}$).

$$\sigma_{eq} = \sqrt{\frac{1}{2}\left[(\sigma_1 -\ \sigma_2)^2 +\ (\sigma_2 -\ \sigma_3)^2 +\ (\sigma_3 -\ \sigma_1)^2\right]} \tag{11}$$

The value of porosity (*f*) can be given by:

$$f = \frac{V_{tot} - V_m}{V_{tot}} \tag{12}$$

Where V_{tot} is the total volume of the material, and V_m is the matrix volume; i.e. it excludes the voids. In the case of $f = 0$, the material has no voids, and the yield surface function for this undamaged material can be written as $\Phi = (\sigma_{eq} / \sigma_y)^2 - 1 = 0$, which is simplified into a von Mises material. It is agreed that the model should represent the material behaviour, up to failure. In this case, the material has zero stress capacity at failure. From equation (10) with $\sigma_{kk} = 0$ and $\sigma_{eq} = 0$, the equation becomes $\Phi = 2f - 1 - f^2 = 0$, which means that failure occurs at $f = 1$, i.e. it is a completely voided material. This is not the actual process for materials failure, and thus the model requires modification for better predictability.

In 1981, Tvergaard et al. [48] introduced the constants q_1, q_2 and $q_3 = q_1^2$, which can be adjusted to improve the prediction of the original Gurson model. The yield surface in equation (10) was extended to the following expression:

$$\Phi = \frac{\sigma_{eq}^2}{\sigma_y^2} + 2q_1 f \cosh\left(\frac{q_2}{2}\frac{\sigma_{kk}}{\sigma_y}\right) - 1 - q_3 f^2 = 0 \tag{13}$$

One can retrieve the original Gurson model in equation (10), by setting the constants in equation (13) to unity [49]. From the literature, the constant, q_1, ranges from 1.0 to 1.5, while $q_2 = 1.0$ for typical metals [50].

The Gurson model describes the growth stage only, and the model needs to be extended to include the nucleation and coalescence stages of material failure. Nucleation of the voids

relates to the formation of new defects during the deformation of the material, such as the cracking of second phase particles or decohesion at the interface between the matrix and the particles. It is accepted that void nucleation can be a strain controlled, or stress controlled, process. Stress control is not widely used; thus, strain controlled will be discussed. Void nucleation is a continuous phenomenon, which can be expressed as follows:

$$\dot{f}_n = A_n \dot{p} \tag{14}$$

where p is the state variable and A_n is a function of the state variable p. It can be assumed that the plastic strain of the matrix (ε^{pl}_m) governs the nucleation, as used in ABAQUS. The following formula can be used to evaluate A_n:

$$A_n = \frac{f_N}{S_N \sqrt{2\,\pi}} \exp\left(-\frac{1}{2} \left(\frac{p - \varepsilon_N}{S_N} \right)^2 \right) \tag{15}$$

where f_N is the volume fraction of the second phase particles where voids can be nucleated; ε_N is the strain value for which 50% of the particles are damaged; and S_N is the standard deviation of the nucleation strain [49]. The following ranges are suggested by ABAQUS users, as reported in the literature for metals: $f_N = 0.04$, $\varepsilon_N = 0.1$ to 0.3, and 0.05 to 0.1 for S_N [50].

The micromechanism of void coalescence can be presumed to correspond to a criterion to predict the onset of ductile rupture. Tvergaard and Needleman [51] (1984) suggested a multiplication factor, δ, which theoretically accelerates void growth in order to simulate the

quick loss of stress conveyancing capacity once coalescence starts. They introduced an effective porosity f^*:

$$f^* = \begin{cases} f, & f < f_c \\ f_c + \delta\,(f - f_c), & otherwise \end{cases} \quad (16)$$

where f_c is the critical voids volume fraction at the beginning of the voids coalescence process. The parameter f_c can be considered to be a material property, and in this case, it can be determined through experimental tests. Another approach is to consider f_c as a stress dependent parameter. The multiplication factor δ ranges between 3 and 8, as reported and used in the literature. The exact values of these parameters are difficult to evaluate and are usually obtained by best fitting experimental stress/strain curves. The yield surface is still applied during the voids coalescence process, and the equation (13) can be rewritten as:

$$\Phi = \frac{\sigma_{eq}^2}{\sigma_y^2} + 2q_1 f^* \cosh\left(\frac{q_2}{2}\frac{\sigma_{kk}}{\sigma_y}\right) - 1 - q_3 f^{*2} = 0 \quad (17)$$

The process of accelerating void growth can be interrupted when values are large (i.e. 0.95 to 0.99) and the material is considered broken [49].

The Rousselier model described in Section 2.5.2 and the GTN model described here have the same advantages and drawbacks [52]. They are continuum models for damage in the material and can be used to prescribe growth of microcavities as constitutive models; and the models can be used to simulate propagation leading to fracture in numerical modelling. However, since only volumetric growth of voids is considered, the models have a weakness

in that they are not able to simulate shear fracture. The GTN model is embedded in Abaqus 6.10 and can be used directly. This advantage makes the GTN model the preferred choice and will be used in this research to describe void nucleation and growth in DP1000 steel.

2.6 Summary

The properties of DP-steels can be enhanced through better understanding of their microstructure and manufacturing processes. For better yield stress, tensile strength and ductility, it is preferable to increase the martensite volume fraction. Producing a normally distributed martensite phase with a fine grain size can give better load transition between the phases and reduce strain partitioning, as opposed to the banded microstructure or large martensite particles. Four damage mechanisms were reported: decohesion between ferrite and martensite, martensite separation, non-metallic inclusion failure, and void nucleation between ferrite grains. The first two mechanisms are the dominant mechanisms whereas the last two have been less observed. Shear bands can be found in the microstructure with a high martensite volume fraction as a result of strain localisation found in the large ferrite grains. DP1000 steel is a relatively new material and is not well understood. Even though some investigations at the micro-scale in this material have been reported in the literature [25, 53], no information about the conditions leading to damage formation and development could be found. Microstructure simulation can be used to investigate damage at the micro-scale. Additionally, predictions of the overall material behaviour at the macroscopic scale, which is of direct relevance to the steel industry, can be achieved using multi-scale modelling. However, Ramazani et al. [45] stated that simulating the complex microstructures of DP-steels is not an easy task. There are multiple methods for predicting damage evolution, where predefined voids or cracks are normally introduced in the model. However, the process by which an undamaged microstructure deforms and initiates damage is not well understood. Experimentally based damage nucleation criteria could not be found in the literature for any DP steels.

The focus of this research is therefore to develop a novel physically-based model of damage development in DP1000 by combining observations of the deformation of the microstructure and the development of damage through tensile testing carried out inside the chamber of a SEM. These tests will be combined with full-field strain measurements, obtained using DIC, at the micro-scale in order to analyse the formation of damage as a function of strain localisation. Finite element simulations of the deformation of the microstructure will also be carried out to analyse damage in terms of stress distributions. Furthermore, a modelling strategy to link the microstructural simulations to the response of the material at the macroscopic scale will be developed through the use of a Representative Volume Element (RVE).

3. Experimental Procedure

Different authors have investigated DP-steels experimentally in order to understand the behaviour and damage of microstructures. Quantitative measurement of strain distributions at the microstructural scale was carried out for DP1000 steel in this research to analyse damage development. This chapter is divided into four sections, explaining the experimental work done in this research and specimens' dimensions. The first section describes the material used, which is DP1000 steel and its properties. The procedure to investigate deformation and follow the history of deformation of the microstructure is described using an in situ tensile test inside the chamber of a SEM. Images of deformed microstructure were acquired during the test to visualise the formation of damage instantaneously. After this, an experimental strain measurement tool is explained using the Digital Image Correlation (DIC) technique. In situ tensile test images and DIC were combined in order to evaluate strain distribution over DP1000 steel surface. The last section talks about the procedure followed here in order to obtain the phases' mechanical properties.

3.1 Material

Material used in this study was dual phase steel (DP1000). DP-steels consist of two main phases: martensite islands embedded in ferrite matrix. The material was provided by Tata Steel in IJmuiden, The Netherlands, in the form of an uncoated sheet with a 1.5 mm thickness. The chemical composition of the material used is shown in Table 3-1. The volume fraction of martensite is around 51%.

Table 3-1: Weight percentage (wt%) of chemical composition of DP1000 steel

C	Mn	Si	Cr	V	Ni	Nb
0.152	1.53	0.474	0.028	0.011	0.033	0.014

To reveal the microstructure of DP1000 steel, surface preparation has to be carried out first. This includes mechanical polishing of the specimen's surface, followed by chemical etching. Silicon carbide grinding papers were used to grind and smooth the surface. After this, fine polishing, using 6 micron and down to 1 micron diamond paste, was used to achieve a good smooth surface before applying chemical etching.

Once the surface is prepared, it can be etched. Etching is a controlled corrosion process that helps the Scanning Electron Microscope (SEM) to distinguish between phases. The process started with cleaning the surface of DP1000 steels carefully with soft cotton and soap to ensure that the surface was free from any polishing sands and diamond particles. After this, specimens were washed under running water and dried using isopropanol for fast drying. Different chemicals can be used to etch the surface. Two procedures were used to etch DP1000 steel. The first method was prepared according to the procedure used by Ghadbeigi

et al [25]. The polished specimens were immersed in a 2% Nital solution for up to 5 seconds. The specimens were placed in the solution face down so that the metal corroded flakes fell down into the solution, which can help to prevent bubbles forming and inhibit the etching process. Next, the specimens were removed and washed with plenty of running water to ensure all Nital was removed from the surface and to prevent surface burning. Then they were cleaned with soap using cotton pads and washed with water and then dried with the aid of isopropanol. Next, the specimens were immersed again in aqueous solution of sodium meta-bisulfite (SMB) at 10% concentration for 10 to 15 seconds. The SMB corrodes the surface slower than the Nital and thus better control of the etching process can be achieved. After this, the specimens were washed using the same procedure as with Nital. The second etching method was adapted from the first one. Instead of using 2% Nital solution and SMB, 5% Nital solution was only used for up to 6 seconds. This is simpler and faster. However, timing is crucial as specimen may corrode if left for any more seconds. This is not the case in the first method, where the concentration of chemicals used was less; and thus extra immersion time may not cause over etching. The revealed microstructure for both etching processes was the same.

Ferrite is the soft phase, and thus it corroded more than martensite in the etching process. As a result, when an electron beam of the Scanning Electron Microscope was directed to the surface, more secondary electrons emitted from the surface were detected from the martensite as compare to the number of electrons detected from the ferrite phase. Different levels of brightness are registered on the monitor depending on the number of secondary electrons reached the detector. Consequently, martensite appears in the images with a bright contrast and ferrite with a dark contrast. Figure 3-1 illustrates the revealed microstructure of

DP1000 steel using SEM. As can be seen from Figure 3-1, martensite was randomly distributed with no banding along the rolling direction. The average size of ferrite phase was around 7 microns.

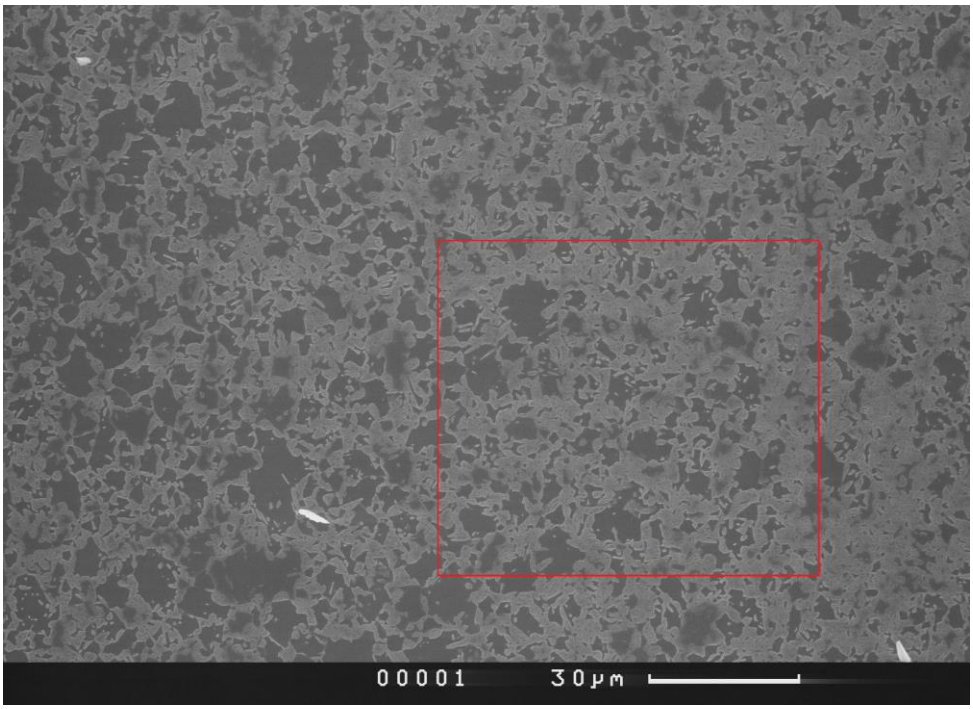

Figure 3-1: SEM image of undeformed microstructure of DP 1000 steel; ferrite in dark; martensite in white; red square is area of interest which will be used for microstructural simulation in Section 4.2

3.2 Tensile Tests

Three sets of specimens have been manufactured. The first set of eight in situ tensile test specimens will be discussed in Section 3.2. A second set of four standard geometry specimens were designed according to ASTM [54]. These specimens were used to measure the flow curve of DP1000 material and later to validate microstructure simulation prediction. The third set of four specimens were prepared with notched geometry and used to validate microstructure modelling prediction. Notched specimens have higher stress triaxiality than smooth standard geometry and are used to investigate notch sensitivity of the material [12].

3.2.1 Conventional Tensile Testing

Standard geometry specimens [54] with gauge width 6 mm were used to measure the stress strain response of DP1000 steel and are shown along with the geometry of notched specimens in Figure 3-2. A conventional tensile machine Mayes was used to apply a tensile load to the specimens. The tests were displacement controlled with a speed of 0.1 mm per minute. A digital image correlation (DIC) method was used to measure extension and overall strain of the gauge section. The method is described in detail in Section 3.3. For this purpose, the surface of the specimens was painted to create a speckle pattern. Figure 3-3 shows the broken specimen with the speckle pattern of the surface. The elongation was measured from the gauge section with 24 mm in length. Notch specimens' dimensions are shown in Figure 3-2. The specimens were tested in the same procedure as the standard specimens and the speckle pattern is shown in Figure 3-3. However, for notch specimens, the width reduction of the notch area (i.e. the smallest width in the specimen) was also measured using DIC and used instead of elongation, as in the standard specimens.

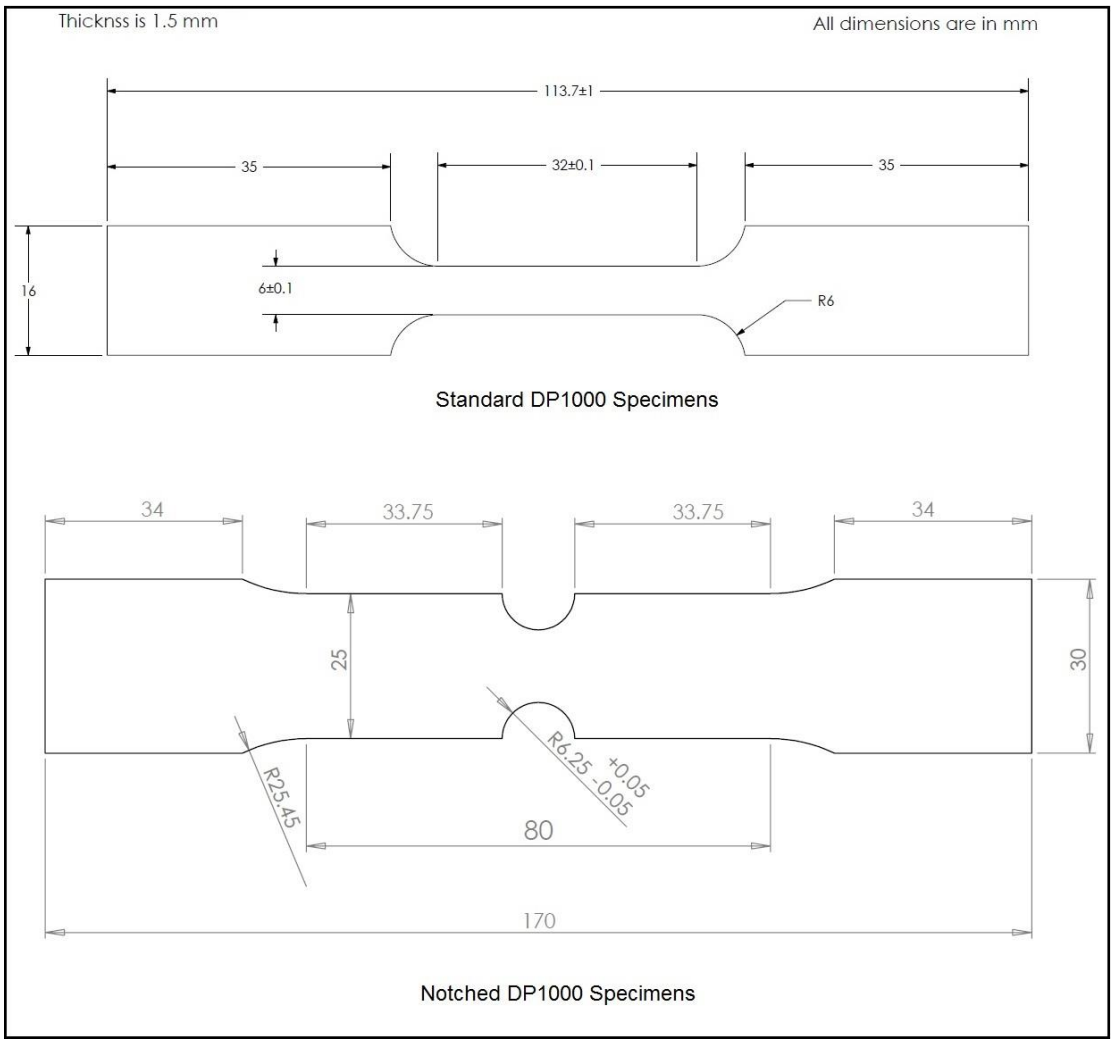

Figure 3-2: Specimens dimensions used for tensile experiments of DP1000 standard geometry (top) and notched DP1000 (bottom)

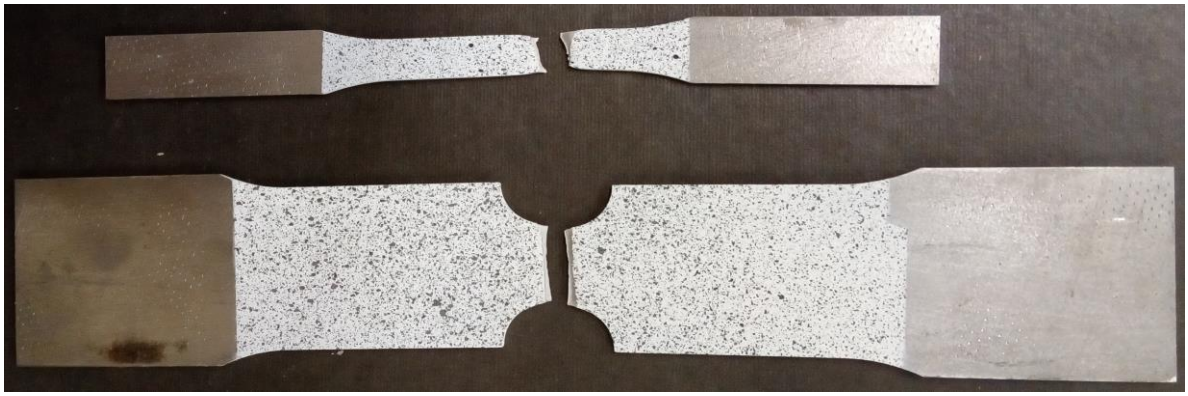

Figure 3-3: The standard specimen (top) and notch specimen (bottom) after failure with speckle pattern used for DIC analysis

3.2.2 In Situ Tensile Test

The main advantage of this type of experiments is the ability to track deformation of the specimen's microstructure at the surface of DP1000 instantaneously while applying the load. The in situ tensile test process includes running the test inside the SEM chamber. The specimen was fixed on a tensile stage which was then loaded inside the microscope chamber. The test is fully automatically controlled as the chamber needs to be under vacuum in order to be able to acquire SEM images. Once the microscope was ready to acquire images, the area of interest was chosen before starting to apply the load. Next, the load was applied until the desired deformation occurred. During this process, live images of the microstructure could be seen on the screen, which makes tracking the area of interest easier; however, SEM images could not be taken instantaneously. Acquiring SEM images required stopping or pausing the applied load, and adjusting the specimen location, so that the same area of interest can be followed from the undeformed image and in focus, and then waiting till the electron beam scanned the microstructure. The load was then re-applied and the steps followed again for the next deformation step, either until the specimen failed or the desired deformation was achieved.

In the current research, Deben Microtest tensile stage with 5 kN maximum load capacity was used. Special dog bone specimens with a small gauge section of 2 mm x 2 mm were designed for two main reasons. Firstly, the specimen will deform until specimen failure under the allowable load and displacement of the tensile stage. Secondly, the deformation needs to be localised in a small gauge area in order to track more easily the area of interest where development of damage leads to the final failure of the specimen. The dimensions and

specimen used are illustrated in Figure 3-4, as conducted by Ghadbeigi et al [25]. Two sets of specimens were manufactured in the rolling and transverse direction, in order to examine the rolling effect: this being, for instance, the possible microstructure banding along the rolling direction. The tests were displacement controlled, with a low speed at 0.1 mm/min. This was the minimum allowable speed with the tensile stage used. Running the test at low speed allows monitoring the deformation and pausing the test in case of any interesting event occur in the microstructure, such as a damage in martensite.

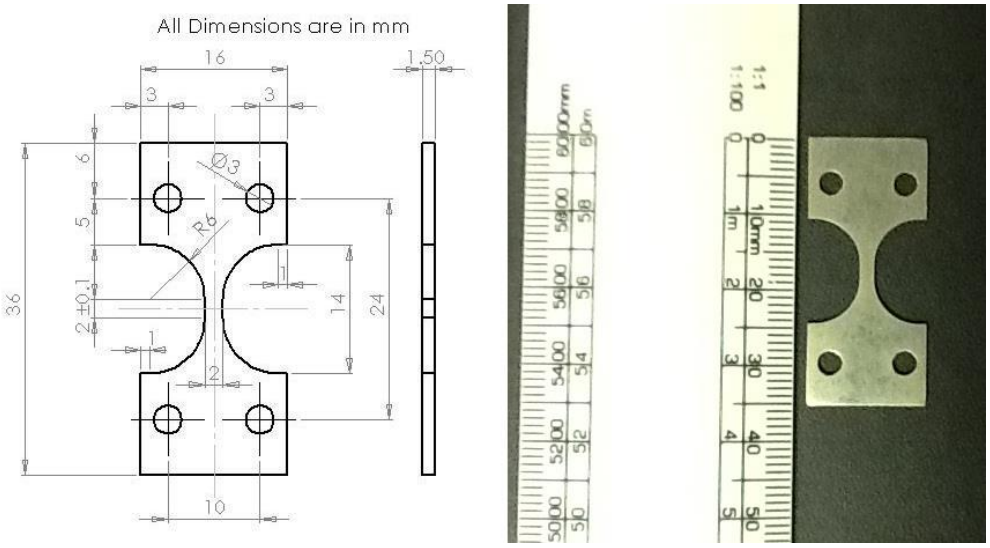

Figure 3-4: DP1000 specimens used for In-Situ tensile test

Camscan MK II SEM was utilised to acquire SEM images of DP1000 steels microstructure. The main advantages of this microscope are the large chamber, its capability to hold the weight of the tensile stage and good resolution. Due to the large chamber, it provides the ability to load the tensile stage inside its chamber. Before specimens were mounted on the tensile stage, DP 1000 specimens had to be polished and etched, following the steps mentioned earlier in this chapter. Figure 3-5 shows the tensile stage positionned inside the Camscan MK II SEM chamber. After this, the experiment was interrupted regularly after

controlled amounts of displacements (i.e. 0.05 mm) in order to capture SEM images of the deformed microstructure all the way to fracture. The recorded images were then exported for quantitative deformation analysis using the Digital Image Correlation (DIC) method, which is described in the following section.

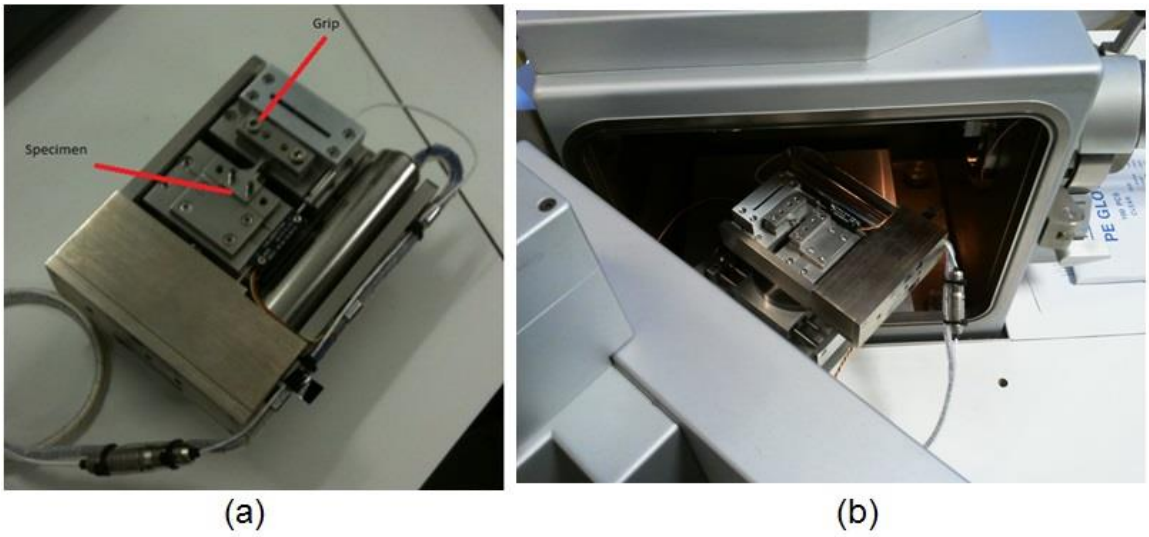

Figure 3-5: (a) Specimen and Deben tensile stage; (b) tensile stage introduced inside SEM microscope chamber

3.3 Digital Image Correlation (DIC)

After acquiring the images of the undeformed and deformed microstructure, quantitative deformation analysis using Digital Image Correlation (DIC) was implemented to calculate the displacement vectors and strain field in the microstructure of each deformed image, as compared to the reference image of the undeformed microstructure. LaVision 7.2 software [55] was used for the DIC measurements. In general, the technique starts with painting the surface of the specimen with background colour (usually white but it can be black) and creating a speckled pattern by spraying different spots of varying size, which have the opposite colour (i.e. if the background is white then the spots should be black). An example of a generated speckle pattern is given in Figure 3-6. Each spot in the speckled pattern is called a feature. Principally, the size and number of features in the speckle pattern depend on the sample size and the area of interest. If the area is big enough, spray paints can be used to generate the speckle; however, if the specimen is small, then an air brush can be used to generate a finer speckle pattern.

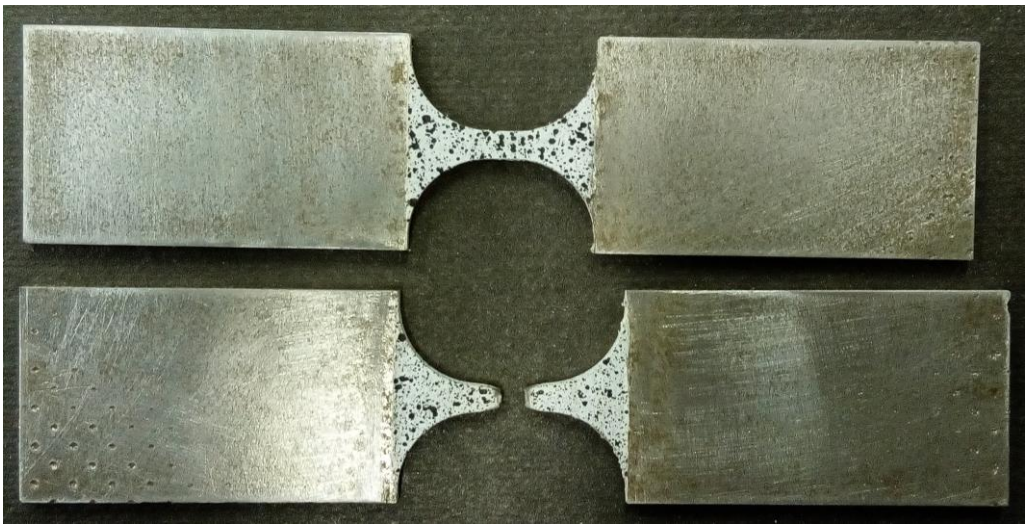

Figure 3-6: Speckle pattern generated using spray paints for region of interest: reduction area

For DIC measurements of the tensile tests, the samples were polished using silicon carbide grinding papers (grit size of 400) in order to remove any rust, dirt and smooth the surface. After that, white paint spray was used to produce thin layer of white background on the surface. The specimens were left to dry for about 15 minutes. Then, a speckle pattern was generated using matt black spray. Matt black was recommended to avoid light reflection when acquiring DIC images. Figure 3-3 and Figure 3-6 show the generated speckle pattern for the standard, notched and in-situ tensile specimens.

In the case of microstructure, the SEM image already has two distinct phases; one in dark (ferrite) and one in bright (martensite) which form the speckle pattern. Consequently, the SEM images were used directly without painting the surface to create the speckle pattern. This method had been used in this research while there are other methods to generate features in the microstructure, such as: i) a golden grid generated using an electron beam, and ii) coating the surface with SiO_2 particles which can be revealed using In-lens SE imaging, as utilized in [32, 42].

After that, the undeformed image (known as the reference image) is discretized into small subsets (which can be called interrogation windows) as shown in Figure 3-7. The size of the subset is given in pixels: for example, in LaVision 7.2 [55], the size ranges from 8, 16, 32 and duplication until 512 pixels. The shape can be square, circle or oval. In the DIC process, the subsets can be overlapped over each other with covered area such as; 0% (i.e. no overlap), 25%, 50% and 75%. Each subset has a unique pixel intensity array as a result of the random speckle pattern in the raw image. DIC is based on displacement calculations by tracking the subsets of the reference image in the deformed image using a correlation algorithm, as illustrated in Figure 3-7.

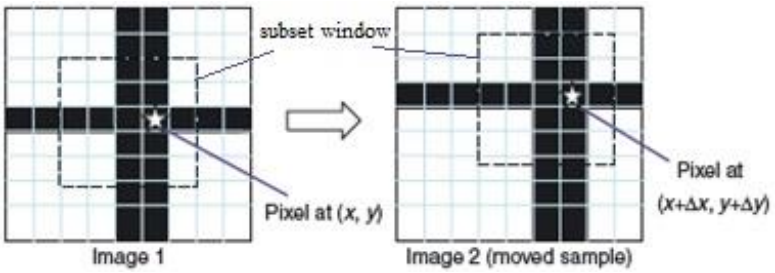

Figure 3-7: Image frame before (image 1) and after (image 2) deformation, adapted from Wang 2010 [56]

The correlation algorithm uses an intensity index of each subset to perform an optimisation process, in order to find the new location of the subset in the deformed image. Two correlation algorithms can be used in LaVision [55]. First, cross correlation uses the sum of intensity multiplication of two subsets through the following coefficient:

$$c(\Delta x, \Delta y) = \sum_{x=-n}^{n} \sum_{y=-n}^{n} I_1(x, y) I_2(x + \Delta x, y + \Delta y) \tag{18}$$

where n is half the length of the subset edges and thus the subset size is 2nx2n. I_1 stands for pixel intensity in the reference image at the location (x,y) while I_2 is pixel intensity in the deformed image at the location $(x + \Delta x, y + \Delta y)$ as shown in Figure 3-7. The maximum value of cross correlation coefficient indicates the optimal location of the subset in the deformed image. The second algorithm is normalized correlation, which practically provides better displacement results than cross correlation. The following expression is used to calculate the coefficient c':

$$c'(\Delta x, \Delta y) = \frac{\sum_{x=-n}^{n} \sum_{y=-n}^{n} I_1(x,y) I_2(x + \Delta x, y + \Delta y)}{\sqrt{\sum_{x=-n}^{n} \sum_{y=-n}^{n} I_1^2(x,y) I_2^2(x + \Delta x, y + \Delta y)}} \quad (19)$$

c' values should be less than one and the maximum value being calculated implies the optimal location of the subset in the deformed image [56].

Once the displacement vectors are calculated, the strain can be computed by subtracting the two neighbourhood vectors and dividing the result by the distance between their centre locations. The computed strain is similar to the calculation of engineering strain (i.e. $\Delta L/L_0$). As a result, any error on displacement vectors calculation will directly affect the computed strains. Additionally, different experimental and theoretical factors can affect the displacement vectors accuracy, such as the resolution of the image, vibration in the lab, unsteady lights, inaccurate interrogation size or overlap, and correlation algorithm. Displacement vectors are less sensitive to overlap, as compared to strain calculations. This is true as displacement vectors related to the subset size which is not affected by the overlap. However, strain calculations are related to the distance between two subsets. In this case,

increasing the overlap leads to decreasing the initial length (the denominator "L_0") which results in magnifying the error in the calculated numerator (ΔL). Table 3-2 shows the effect of changing the size of the subset window on displacement vectors and strain results. Reducing the subset size from 64 pixels to 32 pixels will amplify displacement vector errors to more than twice and increase the error for strain calculations to fourfold. On the other hand, a drawback of enlarging the subset size is reduction in the spatial resolution of the generated strain map [55]. Consequently, selecting a proper subset size is crucial in the DIC technique.

Table 3-2: Subset size effect on vectors and strain calculations, adapted from LaVision manual 2005 [55]

Subset size (pixel)	Vectors error (pixel)	Overlap	Strain error values
64X64	0.02 - 0.05	50%	0.3%
32X32	0.05 - 0.2	50%	1.25%

A technique called normalized autocorrelation can be used to estimate the feature size along a given line over a discrete intensity pattern [57]. The mathematical representation of the normalized autocorrelation technique is given by:

$$A = \frac{\int_{-\infty}^{\infty} I(x)I(x-u)dx}{\int_{-\infty}^{\infty}[I(x)]^2 dx} \tag{20}$$

where (x) and (x-u) are the positions of the intensity 'I'. 'u' is a variable displacement in pixel which assists the process of finding the feature size. From the previous expression, a

plot of ‘A’ against ‘u’ can be produced. At A = 0.5, the width of the autocorrelation function can provide the average feature size, along with the analysed line over the speckle pattern. After that, subset size can be estimated, which at least has to have one feature. Minimal over-sampling is accomplished if the subset size is chosen to have three features or less. As a result, the displacement vectors will likely sustain localized bias and probably rise in calculation errors. If the interrogation size has more than 6 features, it can be said that it is well oversampled. In this case, reduction in spatial resolution of the strain map can lead to a difficulty in obtaining local values. It is suggested that, for a reasonable amount of over-sampling, a proper subset size should contain from three to six features. Therefore, accurate calculations with adequate resolution of DIC method can be achieved [57, 58].

With LaVision 7.2 software [55], it is optional to use more than one iteration to calculate displacement vectors for the same deformed image. This is known as multi-pass analysis which can reduce the error and improve the accuracy. In addition, it is possible to use two subset sizes to analyse one deformed image. In this case, it is called multi-pass reduced analysis. The first set of passes utilizes a larger subset size as indices, whereas the second set of passes provides the final displacement vectors. Multi-pass reduced analysis can enhance the accuracy of the calculated results and the spatial resolution; however, the calculating time will increase, depending on the number of passes used and the subset size.

For tensile tests, the set up for DIC apparatus include LaVision camera (5 Mega-Pixels) mounted at 130 cm from the specimen and two sources of (led) light. The camera should be perpendicular to the surface of the sample and focused on the centre of the gauge section. The camera and load cell of the tensile machine should be connected to the PC in order to

allow LaVision 7.1 [55] to control image recording and data collection of the load at the same time so that the load-displacement curve can be generated. Image recording frequency varies with the specimen type depending on the gauge length of each type. The following recording frequencies of 0.5, 2 and one image/second (i.e. 2, 0.5 and one second per image) were used for in-situ, standard and notch specimens respectively. A reduced pass algorithm [55] with four iterations was used for DIC analysis. For the standard specimens, the interrogation window for the first two passes was 64 pixels x 64 pixels with 25% overlap. After this, the interrogation window size was reduced for the last two passes to 64 pixels x 64 pixels with 25% overlap. For the in-situ and notch specimens, the gauge section size is smaller than the area in standard tensile specimen. As a results, the subset size for the in-situ and notch specimens are smaller in size than the standard specimens. The interrogation window size for the first two passes was 32 pixels x 32 pixels with 25% overlap. After this, the interrogation window size was reduced for the last two passes to 16 pixels x 16 pixels with 25% overlap.

For microstructure analysis, the acquired SEM images of the undeformed (as shown in Figure 3-1) and deformed microstructure were imported to LaVision 7.2 software to measure microstructural deformation using DIC technique [55]. The image size was 193 µm x 131 µm, with a resolution of 2040 pixels x 1380 pixels. Microstructural phases were used directly as features for the correlation, without any filtration or image corrections. A reduced pass algorithm [55] with four iterations was used for DIC analysis. The interrogation window for the first two passes was 12.2 µm x 12.2 µm (i.e. 128 pixels x 128 pixels) with 50% overlap. After this, the interrogation window size was reduced for the last two passes to 6.1 µm x 6.1 µm (64 pixels x 64 pixels) with a 50% overlap. For damage analysis in the

microstructure constituents, refined subset sizes were used for a better spatial resolution of strain results. The subset sizes for the first two passes were 6.1 µm x 6.1 µm (64 pixels x 64 pixels) with 50% overlap that was reduced in the next two passes to 3.05 µm x 3.05 µm (32 pixels x 32 pixels) with 50% overlap. Illustration of the subset sizes and overlap used for the DP1000 microstructure is shown in Figure 3-8 for subset size 128 pixels in green, 64 pixels in blue and 32 pixels in red. The chosen sizes were based on analysis of the microstructure images, which will be discussed in Section 5.3 (Results).

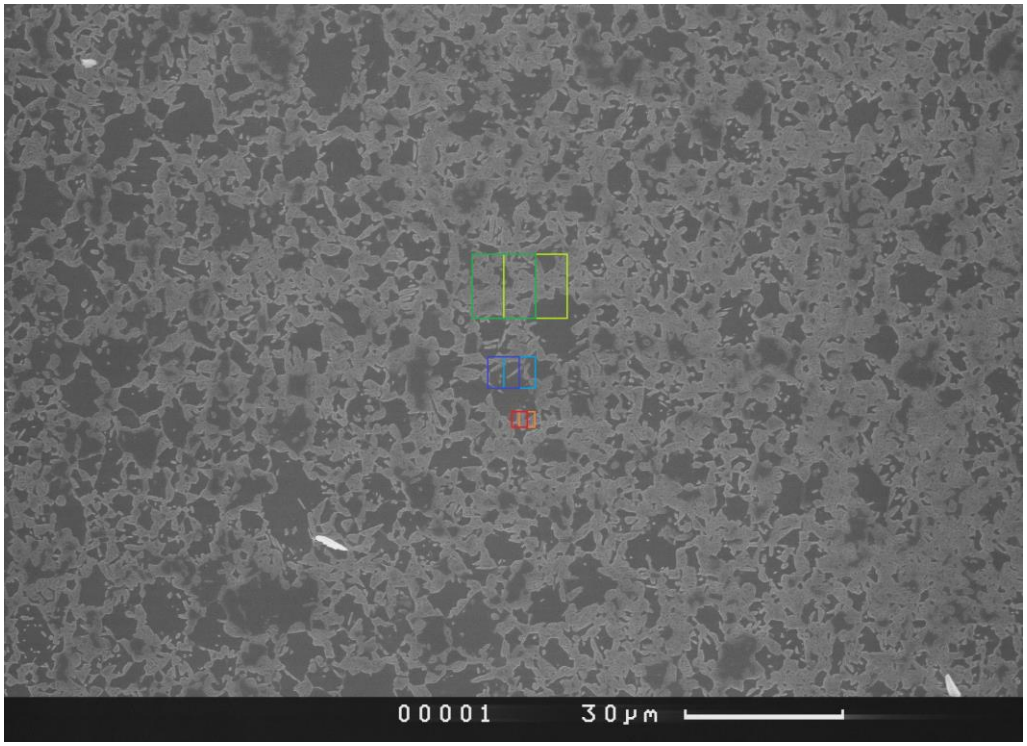

Figure 3-8: SEM image of undeformed microstructure of DP1000 steel with illustration of subset sizes used for DIC analysis, subset size 128 pixels in green, 64 pixels in blue and 32 pixels in red

The displacement vectors and in-plane strain fields of each successive loading step were determined in order to follow the development of the strain field from undeformed configuration at the beginning of the test, up to fracture. The displacement vectors were exported and used as boundary condition of the microstructure simulation and for validation.

The strain maps were also used and compared to microstructure simulation results. The strain measurements were used to analyse strain partitioning between DP1000 phases. The DIC results are shown in Section 5.3.

The provided material of DP1000 steels is a sheet metal which can exhibit anisotropy. Cold rolling and annealing to manufacture the material produce texture in the microstructure that leads to prefer deformation in certain slip planes and directions. In this case, the material is mechanically anisotropic. Strain ratio (r-value) is a method to examine material anisotropy. In a tensile test, the deformation along the width (contraction; ε_{xx}) should be equal to the deformation in the out of plane (thinning; ε_{zz}) for an isotropic material. The r-value can be calculated from the following relation:

$$r = \frac{\varepsilon_{xx}}{\varepsilon_{zz}} \tag{21}$$

For isotropic material, the r-value should be one. DIC measurements available here make it possible to calculate the r-value. However, DIC analysis along the surface does not provide strain values along the thickness (thinning; ε_{zz}). Conservation of volume implies that no change in volume during the deformation. In this case, the summation of all strains should be zero. Consequently, thinning (ε_{zz}) can be calculated from the known strain values as follow:

$$\varepsilon_{zz} = -(\varepsilon_{yy} + \varepsilon_{xx}) \tag{22}$$

ε_{yy} is the strain in the loading direction. Combining equation (21) and equation (22), the r-value can be re-written as follow:

$$r = \frac{\varepsilon_{xx}}{-(\varepsilon_{yy} + \varepsilon_{xx})} \tag{23}$$

The r-value usually calculated in the middle of the plastic deformation of the material after the yielding point and before the maximum tensile strength. Clearly, the strain ratio indicates the resistance of a sheet metal to thinning. In case r-value greater than unity, the material considered as plastic flow is preferred in the plane of the sheet metal and recommended for sheet metal forming [59, 60].

4. Simulation Procedure

Despite all the advantages of experimental measurements, stress distributions cannot be measured and need to be computed from a model. In this project, three main simulation approaches had been used. The first approach involved simulating deformation of the full specimen until the fracture point was reached, called ‘continuum damage modelling’. The second approach involved modelling the deformation behaviour of DP1000 microstructure, called ‘microstructure-based damage modelling’. The third method involved using representative volume elements to predict the behaviour of DP1000 steel, named ‘representative volume element (RVE)-based damage modelling’ that includes two dimensional (2D RVE) and three dimensional (3D RVE) models. The following sections will explain all three approaches in details. In this project, Abaqus version 6.10 was utilized to perform finite element analysis (FEA) [50].

4.1 Specimens simulation

Specimen simulations include modelling the DP1000 experiments carried out at a macro-scale. Figure 4-1 demonstrates the 3D full model which had been created with dimensions match the actual (a) dog-bone (in situ) specimen shown in Figure 3-4, (b) standard and (c) notched tensile specimens shown in Figure 3-2. Eight nodes solid (brick) elements were used for meshing, known as a linear hexahedron, type C3D8R in Abaqus.

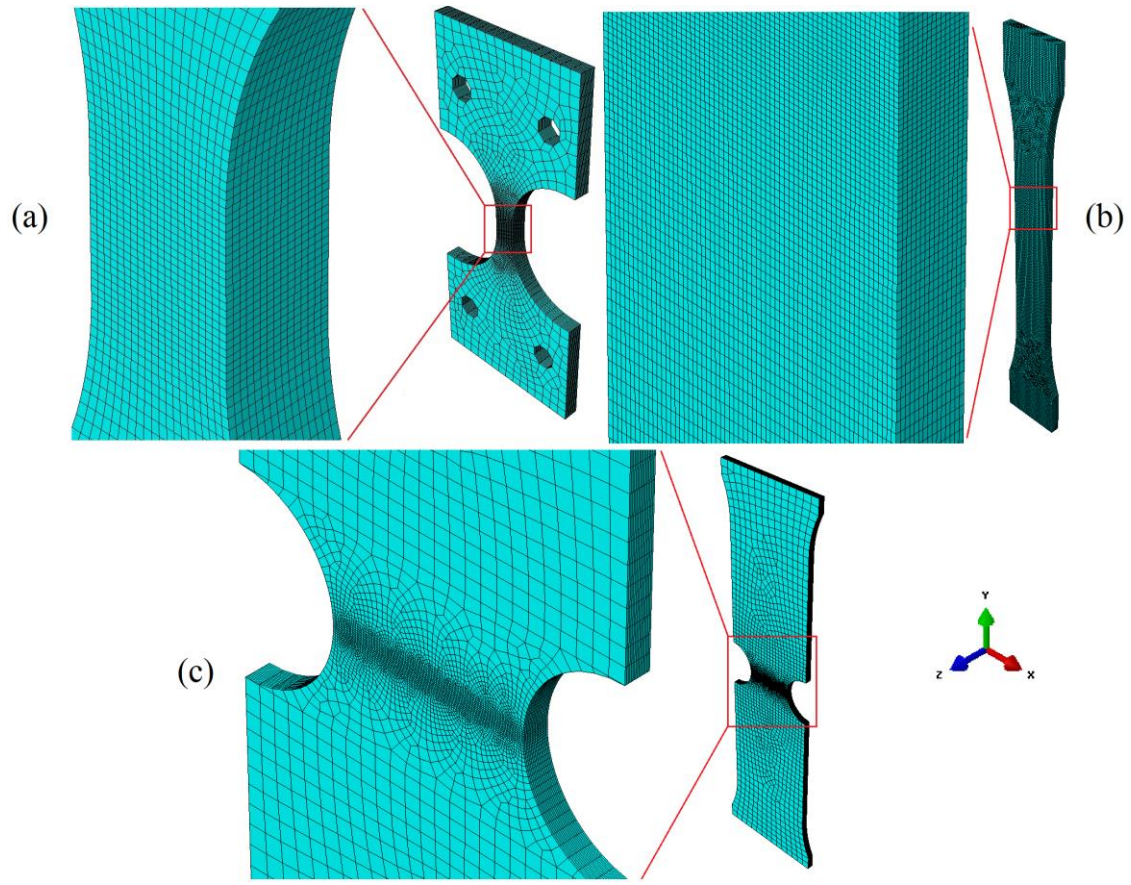

Figure 4-1: 3D mesh models for (a) in situ specimen, (b) standard specimen, and (c) notched specimen

The DP1000 stress/strain curve obtained from smooth standard geometry was used for material mechanical properties in the FE analysis, i.e. elastic modulus of 200 GPa and plastic behaviour shown with the blue line in Figure 5-1. The boundary conditions for in situ

specimen model were such that two bottom pin holes were fixed in all directions except rotation around the Z-axis (out of plane axis) to simulate the actual boundary conditions applied experimentally, while the two top pin holes were fixed from horizontal and out of plane (X and Z axis) displacements; and a longitudinal speed (0.1 mm/min) was applied in the Y direction to simulate the conditions used in the actual experiment. This is a slow speed and can be considered as quasi-static load. Consequently, Static analysis was used in Abaqus 6.10 [50]. In order to simulate the softening part of the material behaviour, the Gurson (GTN) model described in Section 2.5.3 was used. A strain-controlled method was used for void nucleation. The parameters for void nucleation f_N, ε_N, and S_N were chosen so that the softening effect started at an applied strain similar to the experimental observation, i.e. at the UTS point. The Gurson model parameters, q1 and q2, were adjusted in order to match as best as possible the experimental load-displacement curve. These parameters are listed in Table 6-1. The boundary conditions for standard and notched specimen models slightly differed from the in situ specimen model as the specimens were clamped instead of pins used in the in-situ specimen. The bottom surface had been fixed in all directions to represent the clamp holder of the tensile machine, while the top surface was constrained in the horizontal (X-direction) and out of plane direction (Z-direction). Displacement velocity same as the machine test speed (0.1 mm/min) at the top surface was applied in the vertical direction (Y-direction). Similar to the simulation of the in-situ model, this low speed considered as quasi-static load and thus static analysis was used. Gurson's parameters, q1 and q2, were calibrated to best match the load drop recorded in the experimental stress/strain curve of DP1000. The parameters for both standard and notch models are listed in Table 6-1.

4.2 Microstructure Simulation

The microstructure models were generated from the SEM image of the undeformed DP1000 microstructure. An area of interest was chosen for the simulation process, as shown with the red square in Figure 3-1. A MatLab [61] code developed by Chalon [62] was used to generate an input file of a meshed model from SEM image. The flowchart of the code is illustrated in Figure 4-2 and the configuration is shown in Figure 4-3. Firstly, the code analyses and divides the SEM image into square subset windows. The size of the subsets can be defined in pixels, according to the required precision and image size. The code then calculates the grey intensity level of each subset. The user has to define a threshold level at which the code will assign the subset to either ferrite, if the subset intensity level is bigger (darker) than the threshold number, or martensite, if the subset intensity level is smaller (brighter) than the threshold number. Then, the code generates an input file with a meshed model that has two sets of elements, ferrite and martensite.

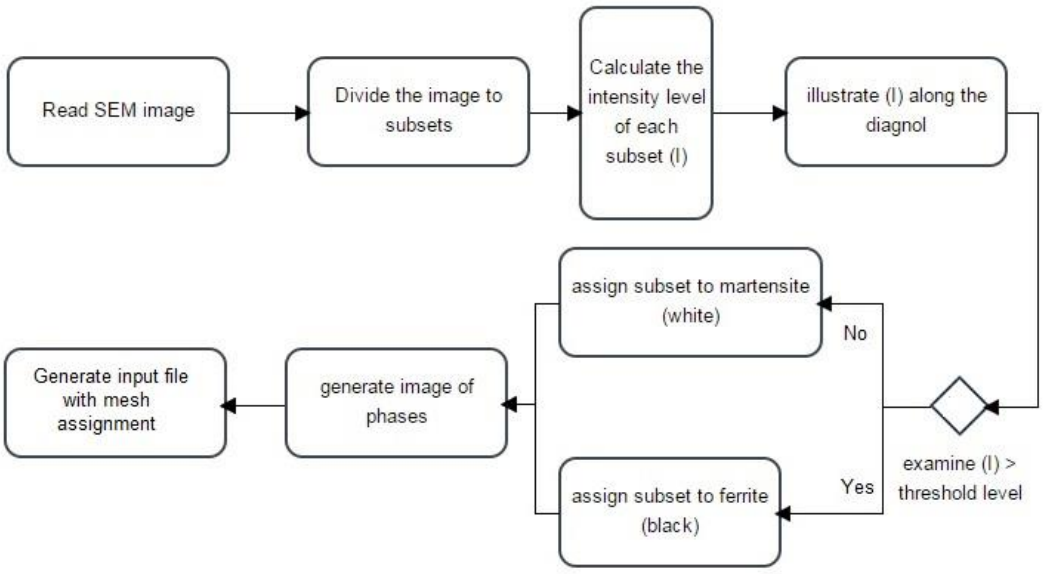

Figure 4-2: Flow chart of Chalon's code to generate mesh file from SEM images [62]

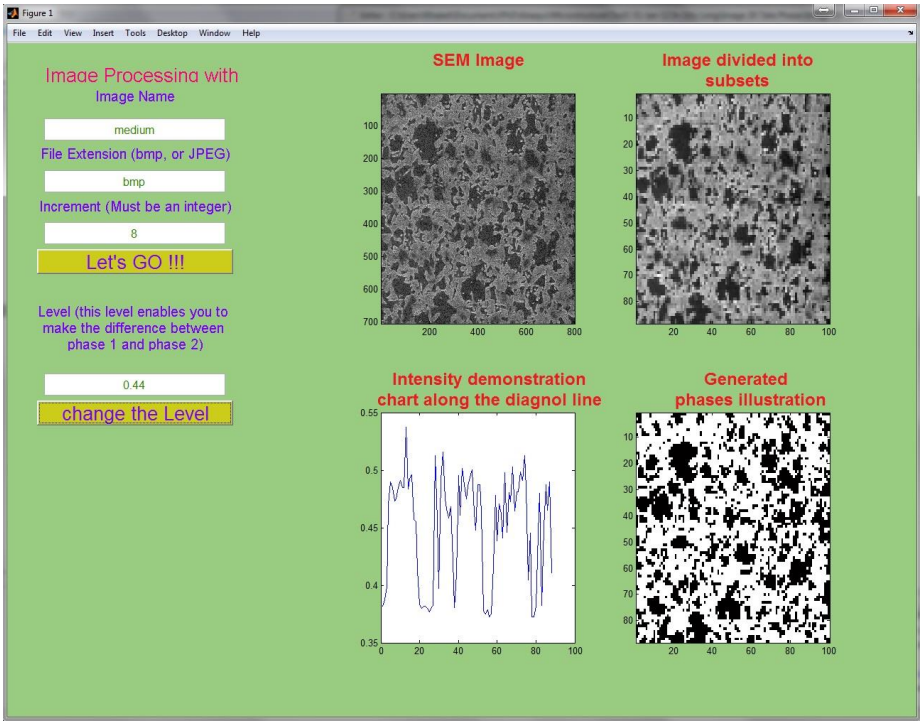

Figure 4-3: Configuration of Chalon's code [62] used to generate model of DP1000 microstructure from SEM image

The element type of the generated model was a linear 2D plane stress quadrilateral element (CPS4R). The increment value used in this research was 4 pixels (i.e. 8X8 elements in each

DIC subset of 64 pixels X 64 pixels with 50% overlap) and the intensity threshold value was set to 0.43. The generated input file then can be imported to Abaqus [50] to perform FE analysis. Figure 4-4 demonstrates the actual SEM image of the undeformed microstructure of DP1000 and the generated 2D model imported to Abaqus. 3D model cannot be built from the actual microstructure. A suggested method is by stacking the 2D model for every depth of cutting. However, this is a destructive method and the specimen cannot be used for tensile test. X-ray is a non-destructive method that can give information in 3D such as voids shown in Figure 2-8. However, the technique cannot be used to distinguish between the phases in DP-steels.

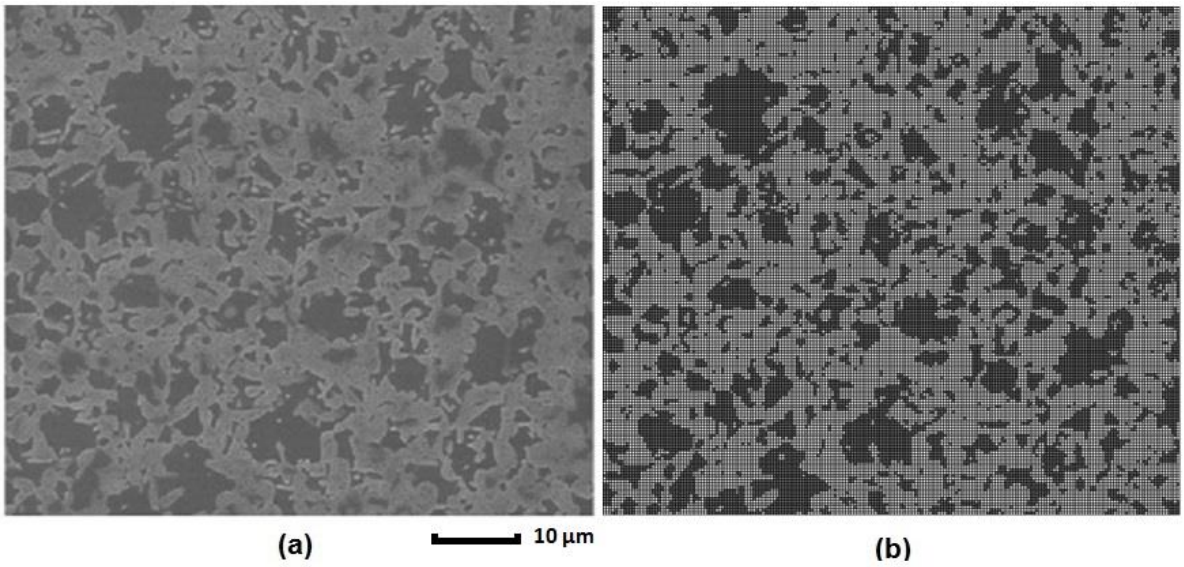

Figure 4-4: Grey (ferrite) and white (martensite) areas of (a) SEM image of undeformed microstructure and (b) model generated with square meshing element

Additionally, another MatLab [61] code was created in this work which updates the input file generated from Chalon's code in order to define the boundary conditions of the model. The procedure used includes four steps that are demonstrated in the flowchart shown in Figure 4-5.

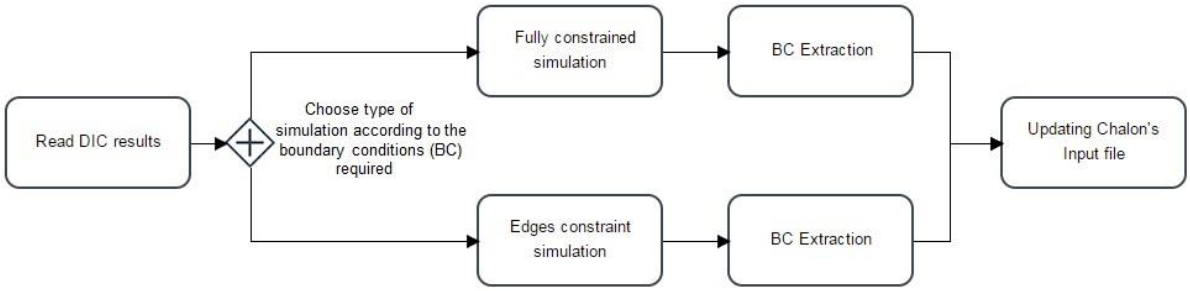

Figure 4-5: Flowchart of MatLab code for applying boundary conditions to microstructure model by updating Chalon's input file

Firstly, the DIC results of the SEM image at a certain state of applied displacement were exported in a text file, with displacement values along the X and Y directions with the corresponding coordinates. The results were given for the whole image, while the area of interest was part of the SEM image, as shown in Figure 3-1. Consequently, the code uses the coordinate's data to extract the displacement values of the area of interest in the SEM image, which can be used as boundary conditions for the analysed area. After this, the code gave an option of where to apply the DIC displacement results on the model nodes. Two sets of microstructural simulation were carried out depending on boundary conditions applied. The first set was fully constrained microstructural simulation where all nodes in the model were assigned X and Y displacements. As a result, the simulation is expected to represent the actual deformation of the analysed area. However, the number of elements in the model is greater than the number of subsets of the DIC results. It means that, between the two DIC data point results, there were a number of nodes in the FE model, and with the given values mentioned earlier; there were 7 nodes between two DIC data point results, as illustrated in Figure 4-6. The variation between two DIC grid points was assumed to be linear and thus the code uses a linear interpolation to calculate the values of displacement for the nodes between the DIC data points.

Figure 4-6: Illustration of number of nodes in microstructure model between DIC result points

The second set of microstructure simulations only applied boundary conditions on the edges of the simulated microstructure area, with all nodes along the edges subjected to displacement values extracted and interpolated from the DIC results. In this case, the rest of the nodes were left free to deform, according to the phases properties defined in the model. Figure 4-7 shows an example of the applied displacement values along the bottom edge of the model shown in Figure 4-4 (b) at an applied displacement of 0.22 mm. The code is available in Appendix I.

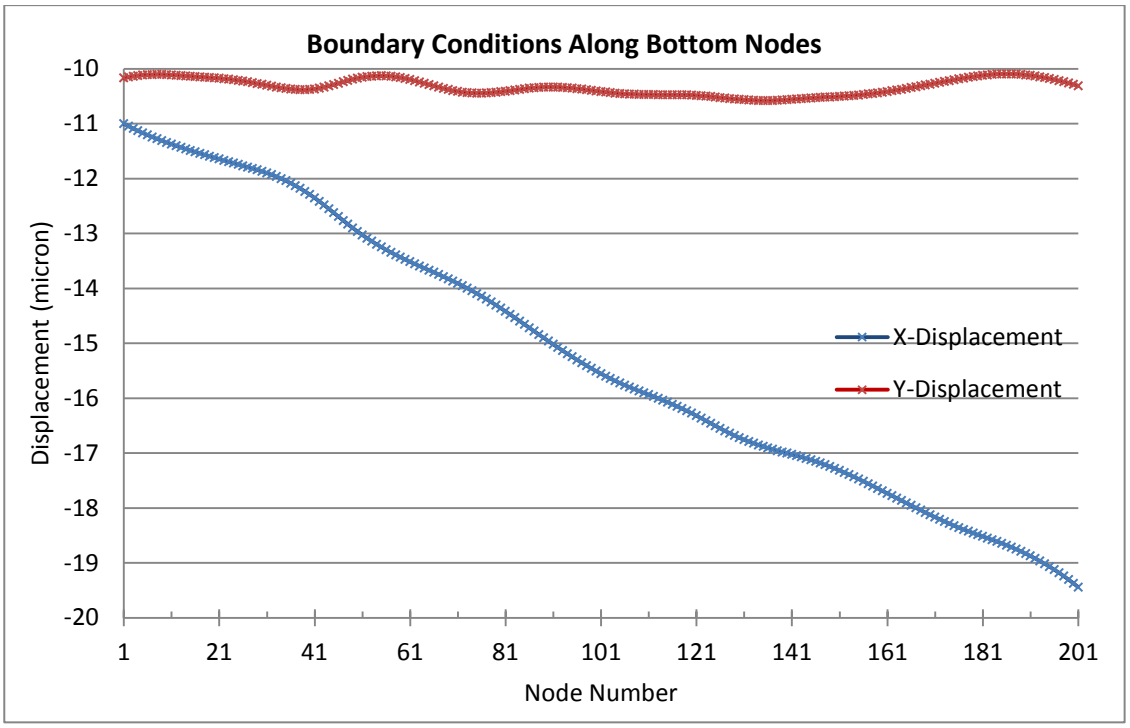

Figure 4-7: Displacement values assigned to bottom edge of model in Figure 4-4 at applied displacement of 0.22 mm

In microstructure simulation, stresses were calculated for each element in the model. In order to obtain stress value from the whole model, averaging the microstructure stress fields were conducted using the relation suggested by Smit et al [63] and Kouznetsova et al [64]:

$$\bar{\sigma} = \frac{1}{V}\int_V \sigma \, dV \tag{24}$$

$\bar{\sigma}$ is the average stress which represented the macroscopic response of the microstructure, V is the total microstructure volume of the model and σ is the microscopic stress computed at every Gauss point in the model [39, 63-65]. The von Misses stress computed in every element was used for microscopic stress in equation (21). The models were 2D with unit thickness and plane stress condition because the modelled microstructure was on the surface

of the specimen where the out of plane stress was zero. The models assume a perfect cohesive interface between martensite and ferrite in the microstructure.

In addition, the model shown in Figure 4-4 (b) was used to predict deformation and strain distribution using edge constraint microstructure simulation for an applied displacement of 0.22 mm near the UTS. For this particular applied displacement, no damage appeared in the SEM images of the deformed microstructure, as damage was not included in the FE simulations. Two techniques were used to validate the prediction of deformation by the microstructure model. The first technique for validation consists of overlaying the deformed model from the microstructure simulation, with the SEM image of the deformed microstructure acquired experimentally. For more quantitative comparison, a second technique was developed. A MatLab code was written to quantitatively compute the error between DIC and modelling results over the area of interest (boarded with the red box in Figure 3-1). Because the number of nodes in the FE model was higher than the number of DIC data points (i.e. 7 nodes in between two DIC data points), the DIC displacement results were linearly interpolated between two data points. Then, the code uses the interpolated displacement results from DIC and compares them with displacement values obtained from the microstructure simulation. The code therefore calculates the difference (or error) of displacement results of each node in the model with the corresponding DIC interpolated results at the exact same location in the microstructure. After this, the code plots the errors on a contour map, with the code which can be found in the Appendix II. Since the maximum DIC strain values were recorded in the loading direction, the comparison between modelling and DIC strain results were made for the strain component E_{yy} for the applied displacement

of 0.22 mm (i.e. the ultimate tensile strength point). The MatLab code for strain comparison is also available in Appendix III.

As far as damage is concerned, the first simulations focused on damage nucleation in martensite. Three areas of the microstructure, where the first damage sites in martensite islands were observed experimentally, were selected for the simulations. The aim of the simulations was to analyse stress distributions in the microstructure at the onset of damage formation in martensite in order to try establishing a nucleation criterion. Therefore images and DIC strain results corresponding to a deformed state of the microstructure just before the appearance of the first damage sites in martensite were selected. These particular deformation states of the microstructure were observed for applied displacement values around the UTS.

A fully constrained microstructure simulation method was used for the three areas, in order to ensure deformation of the model was similar to the actual state of the microstructure. After this, the stress and strain values were investigated at the location of damaged martensite, in order to suggest a criterion for damage nucleation in the martensite phase of DP1000 steels.

In order to simulate crack propagation in martensite, the nucleation criterion proposed for martensite cracking is employed and examined for applied displacement values beyond that leading to nucleation. Two damage initiation criteria available in Abaqus 6.10 [50] can be used; forming limit diagram (FLD) which is strain controlled, and forming limit stress diagram (FLSD) which is stress controlled. Depending on the suggested martensite cracking

criterion, one of them can be used to simulate crack propagation and further explanation of the method will be discussed later in the result section.

As far as damage propagation in the microstructure was concerned, the Gurson model was used for damage in the ferrite phase. A fully constrained microstructure simulation of the model shown in Figure 4-4 was utilised, so as to adjust Gurson (GTN) model parameters for deformation states beyond the UTS point from applied displacement values ranging from 0.22 to 0.61 mm. The stress results of the microstructure modelling were averaged using equation (24) and compared to the experimental true stress of each state. For better calibration of the Gurson parameters for the ferrite phase, the proposed damage criterion was used for the simulation of damage propagation in the martensite phase. This ensured that the stress loss due to martensite cracking is included in the averaged stress from the model and the comparison to true experimental stresses includes damage models in both phases. The adjusted Gurson damage parameters were then used for the ferrite phase in the representative volume element models described in the following section.

Damage is highly dependent on the stress triaxiality ratio which was calculated using the following equation:

$$\sigma_{triaxiality} = \eta = \frac{\sigma_m}{\sigma_{eq}} = -\frac{\sigma_{hydro}}{\sigma_{eq}} \tag{25}$$

$$\sigma_m = \frac{(\sigma_1 + \sigma_2 + \sigma_3)}{3} = -\sigma_{hydro} \tag{26}$$

$$\sigma_{eq} = \sqrt{\frac{(\sigma_1 - \sigma_2)^2 + (\sigma_2 - \sigma_3)^2 + (\sigma_3 - \sigma_1)^2}{2}} \quad (27)$$

where $\sigma_{triaxiality}$ or η are the stress triaxiality. σ_m and σ_{hydro} are the mean stress and the hydrostatic pressure respectively. The negative value of the mean stress gives the hydrostatic pressure. σ_{eq} is the equivalent Mises stress [66]. The triaxiality ratio of the ferrite elements in the microstructure model was examined for the deformation states used to calibrate the Gurson parameters as will be shown in Chapter 6.

4.3 Representative Volume Element (RVE) modelling

In order to check the accuracy of predicting the material behaviour using microstructure simulations, another 2D microstructure model was generated from another tested in situ specimen. Figure 4-9 shows the SEM image and the generated model used, which will be called 2D RVE. Additionally, two 3D RVE models were created using a MatLab code (available in Appendix IV) that generates randomly distributed martensite and ferrite phases but keeps the percentage of martensite volume fraction similar to that in the real DP1000 microstructure, at around 51%. The first 3D RVE model consisted of 20x20x20 elements while the second consisted of 30x30x30 elements along the X, Y and Z axes, as shown in Figure 4-10. The calibrated phase properties (shown in Figure 6-18 with red and blue lines) and GTN parameters for the ferrite phase (utilising the method in Section 4.2, the parameters are listed in Table 6-7) were used to describe the phase behaviour and damage to the microstructure constituents. The boundary conditions in the form of displacement values in all directions were extracted from the nodes of the element at the very centre of the model shown in Figure 4-1 (a) for the applied displacement values of 0.08, 0.18, 0.22, 0.4 and 0.61 mm. Two MatLab [61] codes (available in Appendix V and Appendix VI) were created in this work in order to apply the boundary conditions to the RVE models. The first one was used to extract displacement values from one face of the central element in Figure 4-1 (a). Then, the values were linearly interpolated between corners and applied to the edges of the 2D RVE as demonstrated in Figure 4-8. To represent the state of the central element, the 2D RVE are run under plane strain conditions and static analysis was used.

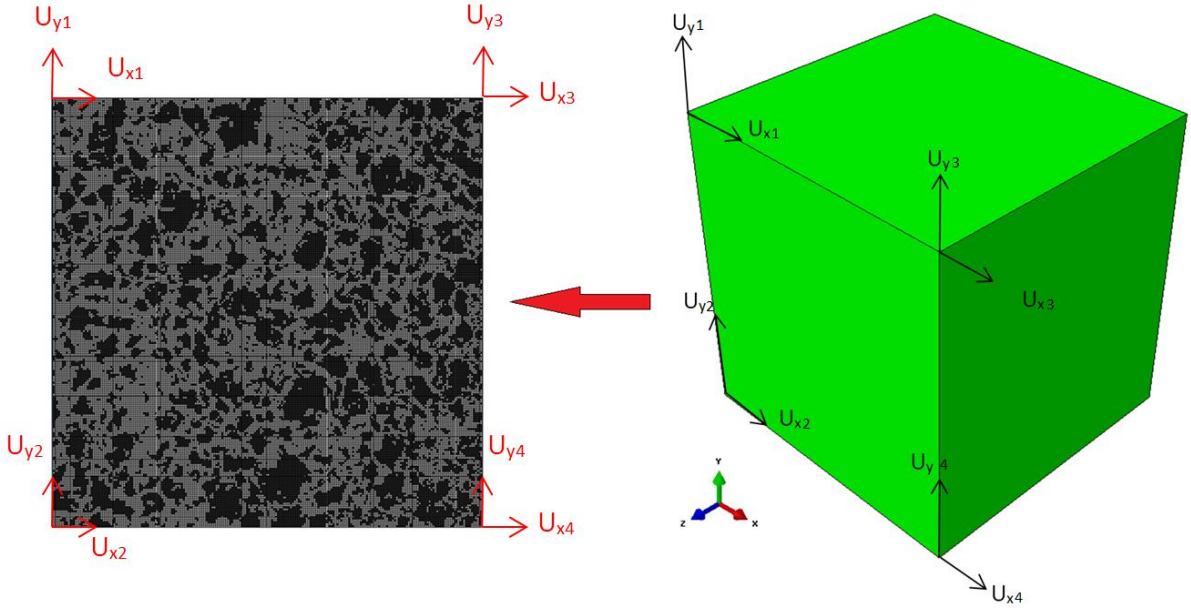

Figure 4-8: The boundary conditions extraction process from the central element of the full model and applying them to the 2D RVE

The second code uses the displacement values of all corners of the central element and interpolates them linearly to apply the deformation to the outer faces of the 3D RVE. Furthermore, static analysis is used to run the simulation as the load was quasi-static because of the low speed of the applied load (0.1 mm/min). After that, the models were imported into Abaqus and the stresses from 2D and 3D RVE models were averaged using equation (24), and the results were compared to the true experimental stresses. The true experimental stress is calculated from the engineering stress ($\sigma_{true} = \sigma_{engineering} \times (1 + \epsilon_{engineering})$. The later is calculated by dividing the load acquired experimentally from the load cell by the initial area of the specimen. This process was carried out to examine the models' ability to predict the macroscopic behaviour of the material.

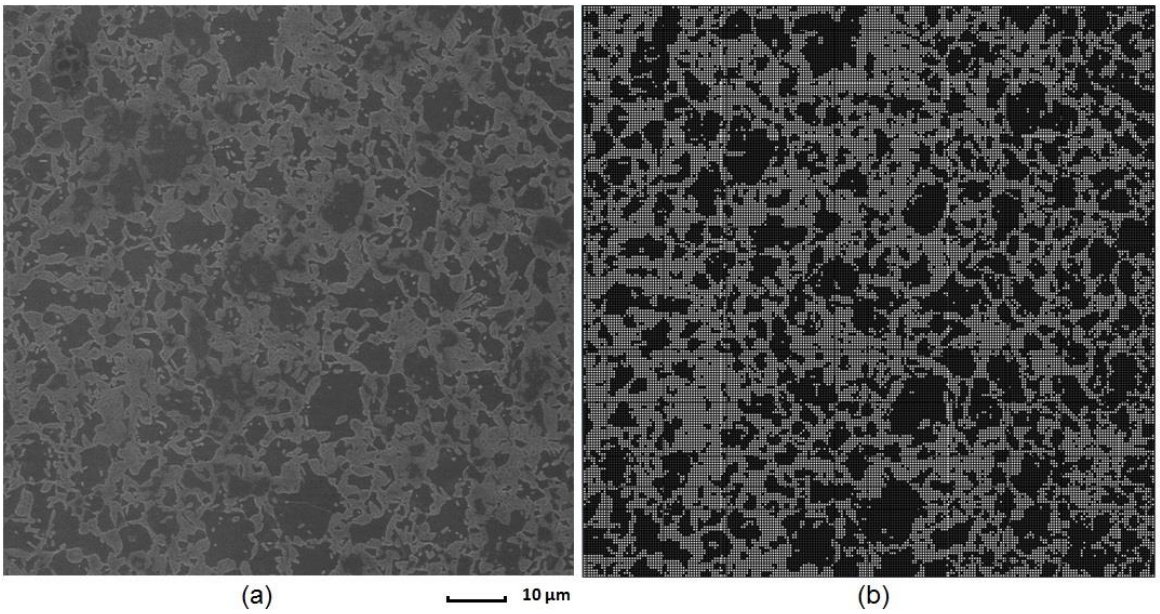

Figure 4-9: Dark (ferrite) and bright (martensite) of (a) SEM image of undeformed microstructure and (b) model generated with square meshing element used for 2D RVE

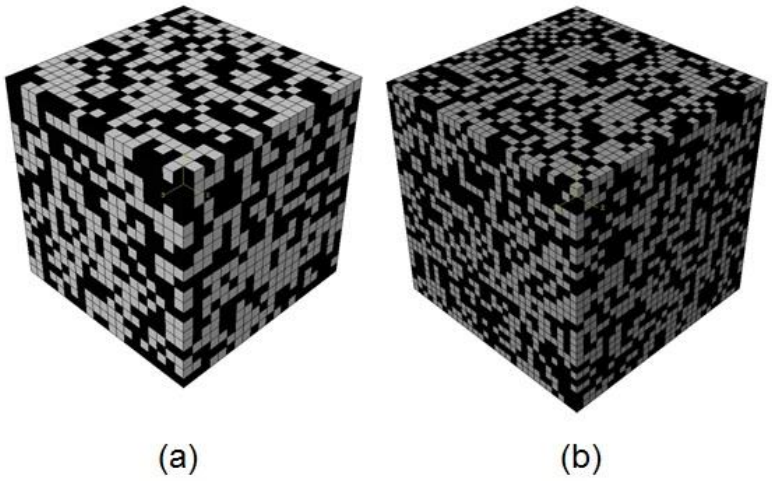

Figure 4-10: 3D RVE models generated with martensite volume fraction around 51% with (a) 20 elements and (b) 30 elements, along each edge.

Moreover, the 3D RVE was used to predict DP1000 stress/strain curves for different specimen geometries at three different states; before the UTS (i.e. the hardening part), at the UTS point and beyond the UTS but before fracture (i.e. the softening part). The boundary conditions were extracted from the nodes of the central elements of the standard and notched

models shown in Figure 4-1 (b) and (c), respectively. Equation (24) was used to average the stresses and the results were compared with the true experimental stresses in order to examine the ability of the random 3D RVE model to predict the macroscopic behaviour of the specimen.

5. Experimental Results

The aim of first set of experiments was to measure the stress/strain response of DP1000 steel using a standard geometry and results are reported in section 5.1. In situ tensile test run inside the microscope chamber gave the advantage of reporting deformation development in the microstructure during the tensile test and the damage mechanisms operating in DP1000. These results are discussed in Section 2 of this chapter. DIC subset size effect was examined and optimum size was suggested according to convergence study and technique called normalised autocorrelation. Both methods suggested a similar subset size for microstructure images of DP1000 acquired from the experimental results. After this, strain measurements were shown and analysed in relation to the area of interest.

5.1 Stress/Strain curves of DP1000

Figure 5-1 illustrates the stress strain curve of DP1000 steel obtained from the conventional tensile tests of the standard geometry shown in Figure 3-2. The green line represents the engineering stress strain curve calculated from the load displacement data. The true stress strain response is demonstrated by a blue line. This latter curve was defined as material properties for simulations of in situ specimen, standard geometry and notched specimen. From the curve, the yield strength was 720 MPa and the ultimate tensile strength (UTS) was around 1060 MPa while the modulus of elasticity and Poisson's ratio were 200 GPa and 0.3 respectively. The dashed blue line is the extrapolation of the true stress strain curve, with similar slope, for strain values beyond the experimental fracture strain value. This was done for modelling purposes as, otherwise, Abaqus 6.10 [50] would keep the maximum stress value, corresponding to the experimental fracture strain, constant for any computed strain values higher than the experimental fracture strain.

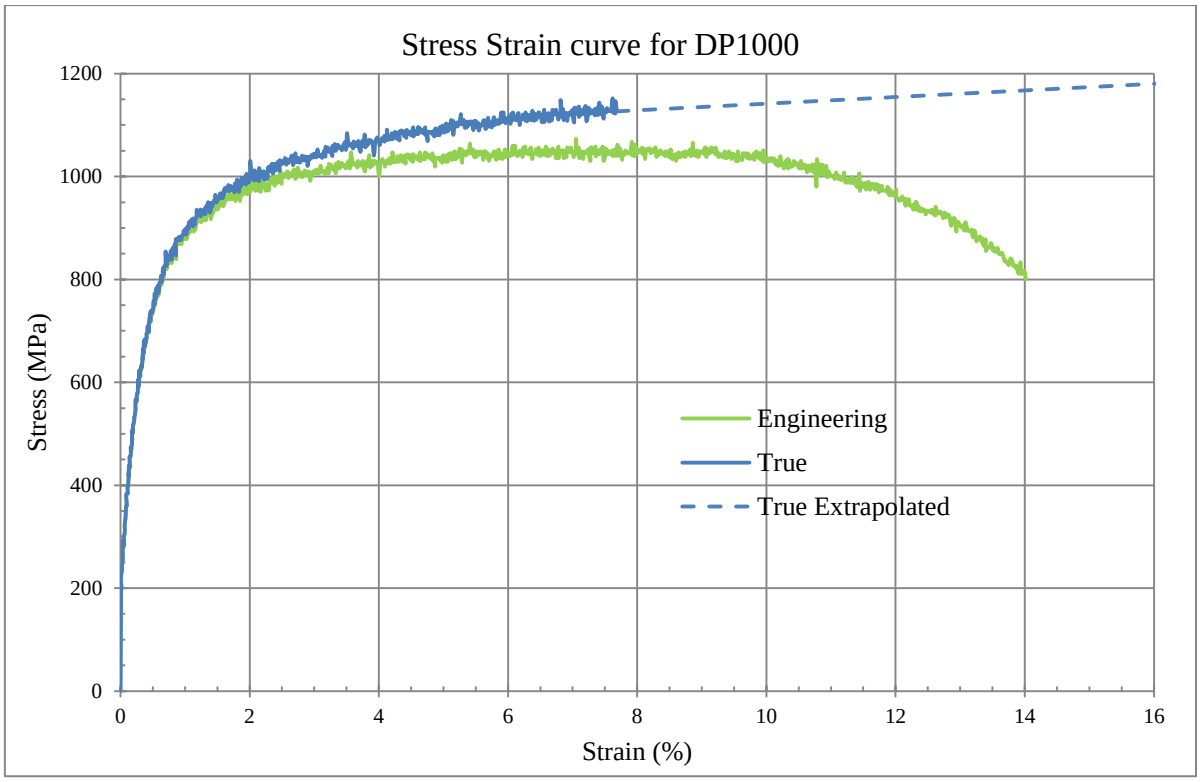

Figure 5-1: Engineering and true stress strain curves of standard geometry DP1000 steel

Figure 5-2 presents the calculated engineering tensile stress/strain curves for the DP1000 material tested inside the microscope chamber (i.e. in situ specimens shown in Figure 3-4). The curves correspond to two sets of specimens: one machined in the rolling direction, and one loaded in the transverse direction. As can be seen, the difference between the two directions was small, which suggests that the rolling effect on the stress/strain curve of DP1000 steels was not very significant.

As a result of the small gauge length of the in-situ tensile specimen, the uniform strain (i.e. the strain up to the ultimate tensile strength point) increased from 8% to 14% and the fracture strain increased from 14% to 48%, both strain values being greater than the values for DP1000 steel tested using standard geometries. This is an advantage which provided the

opportunity to observe the development of deformation and damage in the microstructure for such high strength steel grades that have reasonably limited elongation to fracture. The stress relaxations in the stress/strain curve shown in

Figure 5-2 are due to the regular interruption of the tensile test to capture SEM images of the deformed microstructure for damage observation and DIC analysis.

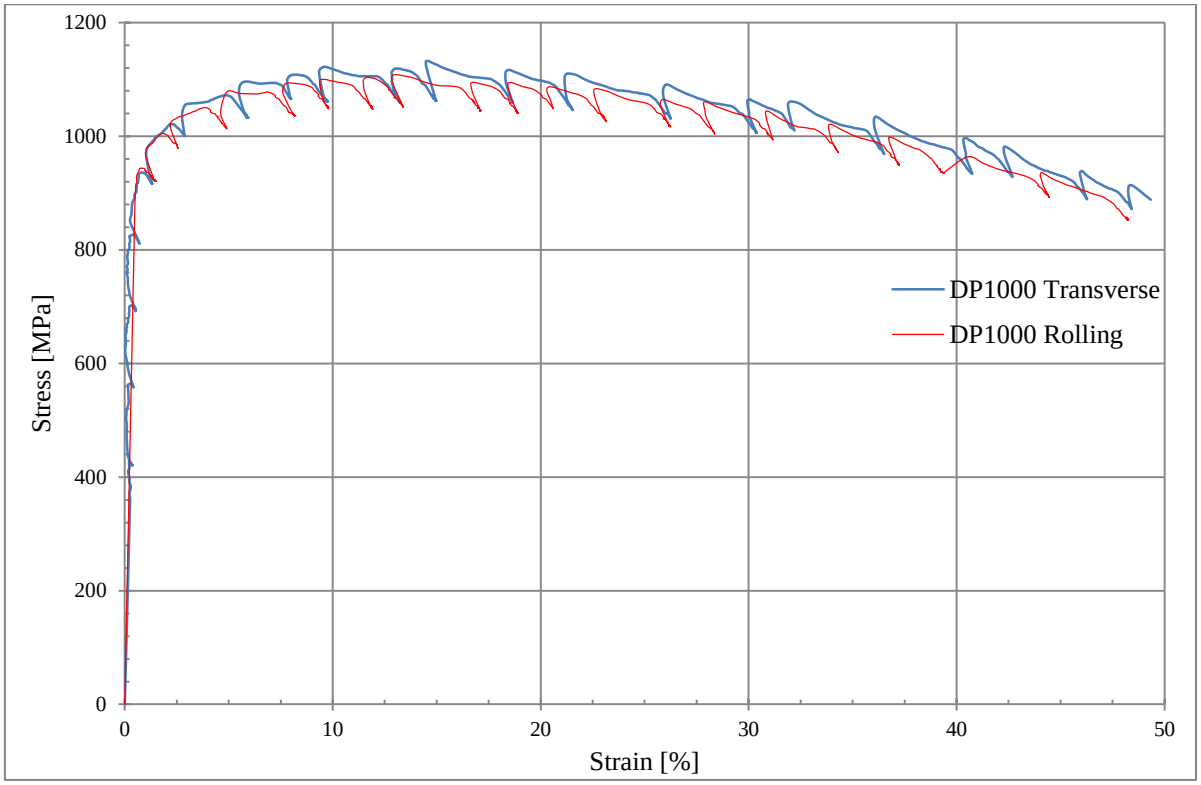

Figure 5-2: Stress/strain curves of DP1000 steels for in-situ tensile specimens in rolling direction (red) and transverse to rolling direction (blue)

5.2 Microstructural Observation

The SEM images acquired from in situ tensile tests of DP1000 have been investigated in order to study the initiation and development of damage in the material microstructure. DP-steels fail in a ductile manner, as can be seen from Figure 5-1, and this usually includes void initiation, propagation and coalescence. According to the observations of the specimen's surface of DP1000, void initiation can be invoked by two constituents in the microstructure: (i) non-metallic inclusions (NMI) or (ii) martensite islands. During the steel production and casting process, undesirable particles of NMI's are formed in the material. Figure 5-3 shows an example of NMI bounded by a characteristic cavity at the centre of the field of view. Generally, the cavity forms as a result of chemical dissolution during specimen preparation by mechanical polishing and etching media. The NMI shown in Figure 5-3 behaved in a brittle manner at an early stage of deformation. Elemental analysis using energy dispersive spectroscopy (EDS) in the SEM for 27 similar NMI's revealed that NMI's in the DP1000 consisted mainly of aluminium and oxygen, as shown in Figure 5-4.

At an applied displacement of 0.04 mm, at the beginning of the uniform deformation, the NMI had already failed. Thus, NMI was the first damaged feature observed in the microstructure. As the applied displacement increased, the cavity surrounding the NMI enlarged. However, apart from cavity enlargement, the crack did not develop into the ferrite or martensite around the NMI. According to the microscopic observations, it is suggested that NMI's in DP1000 steels do not contribute damage development in the microstructure. Consequently, the NMI was fairly innocuous.

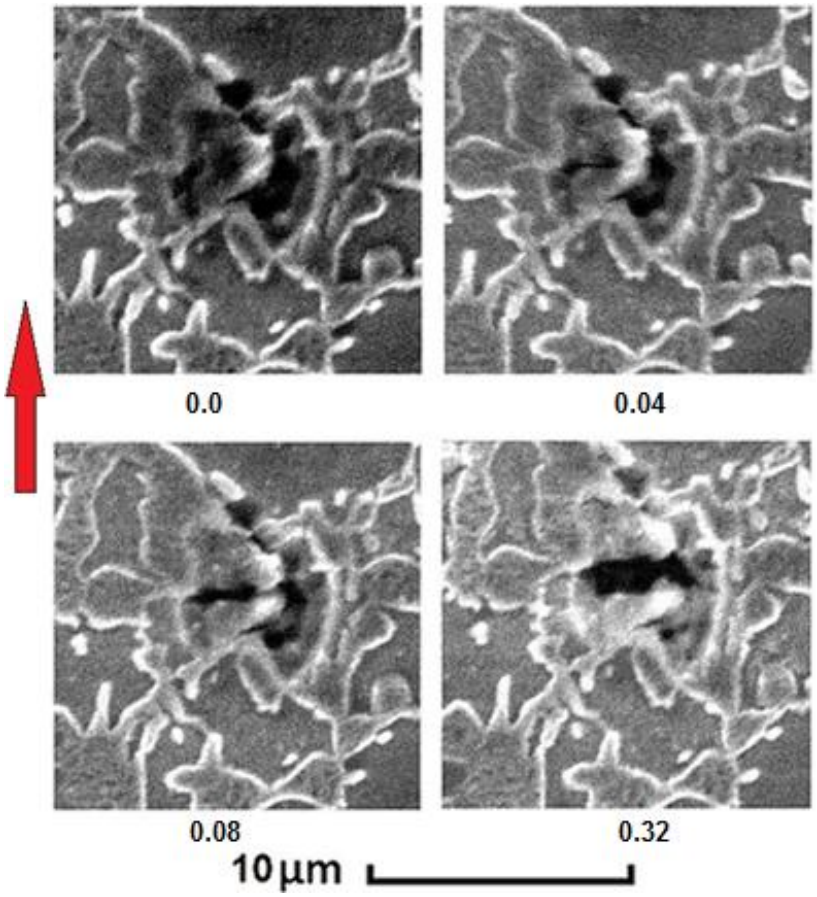

Figure 5-3: Void initiation and development due to NMI in the material with related applied displacement [mm] shown underneath SEM images (red arrow shows loading direction)

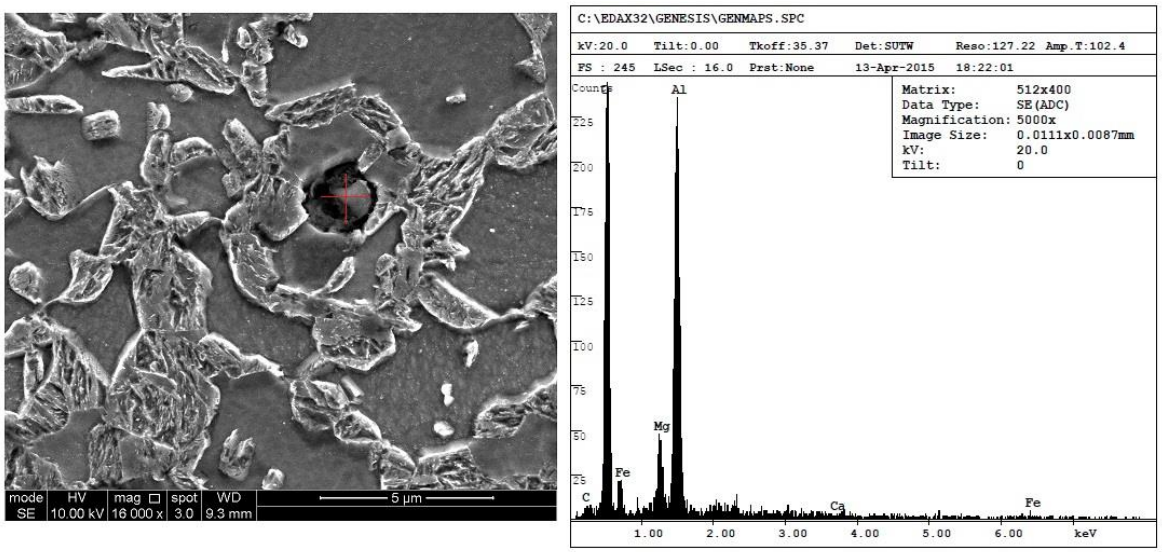

Figure 5-4: (a) SEM of NMI in DP1000 microstructure and (b) EDS analysis (measurements carried out by Dr H. Ghadbeigi)

Martensite is the hard phase in DP-steel microstructure that provides strength to the material, so observing damage at and near the martensite is important to understand its effect on the deformation and damage of DP-steels. Figure 5-5 demonstrates the development of a void initiated near martensite islands during progressive increase of the applied displacement. At an applied displacement of 0.63 mm, the microstructure experienced severe deformation, as indicated by the local elongation of the interface between ferrite and martensite, where the martensite phase nearly fractured. Then, a crack initiated in the martensite island at the location of a small notch-like feature which may have caused stress concentration. After this, the martensite fractured and divided into two segments as a result of the crack propagation. After the martensite phase failure, each broken segment was then flowing with the ferrite deformation as the applied displacement increased. At an applied displacement of 1.05 mm, a spherical void appeared in the ferrite phase near one of the separated martensite segments, as shown in Figure 5-5.

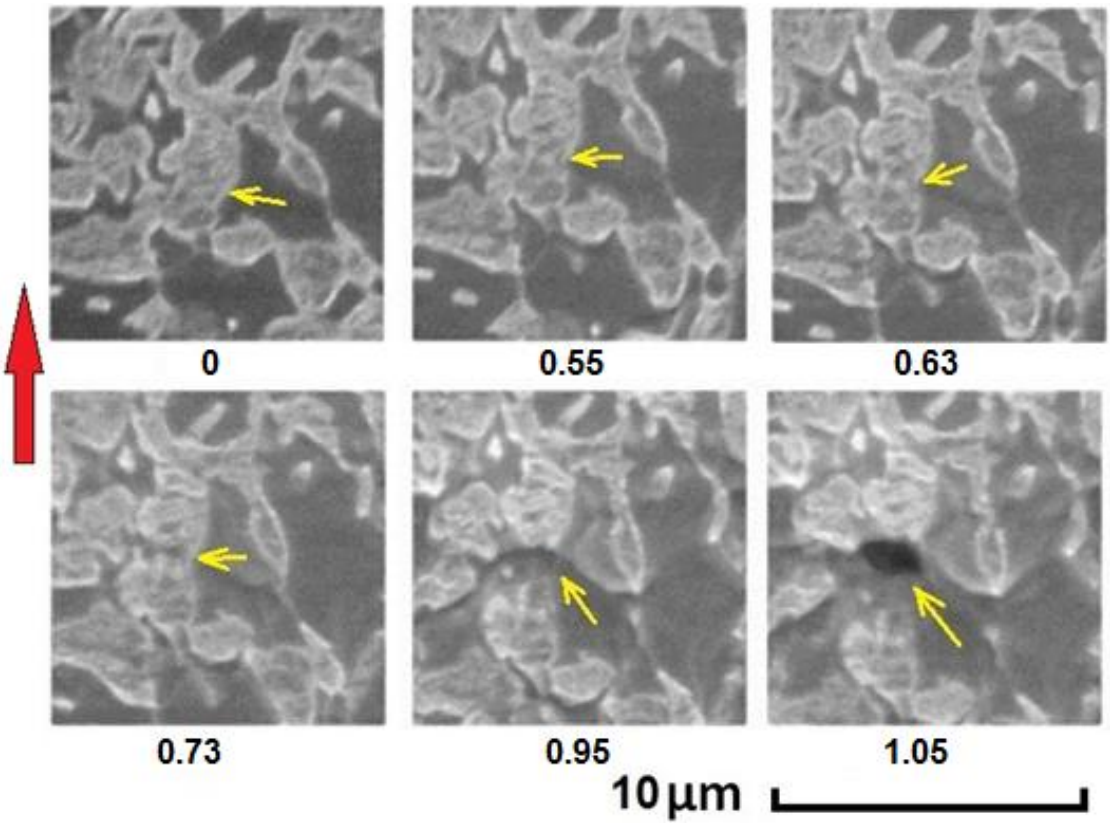

Figure 5-5: Spherical void nucleated near fractured martensite breaking in DP1000 steels as the applied displacement increased (indicated underneath SEM images in mm) (red arrow showing loading direction)

The development of damage in the martensite phase was observed in the microstructure of DP1000 steel. Three different areas were chosen as the damage was observed first and clearly in these deformed locations, as shown in Figure 5-6. At an applied displacement of 0.32 mm, after the UTS point, damage started at the interface between ferrite and martensite. Then, as the applied displacement increased, damage propagated into the martensite phase until it fractured and separation was observed at an applied displacement of 0.72 mm. The mechanism described here is representative of the damage in the martensite phase observed during the test at various locations in the DP1000 microstructure.

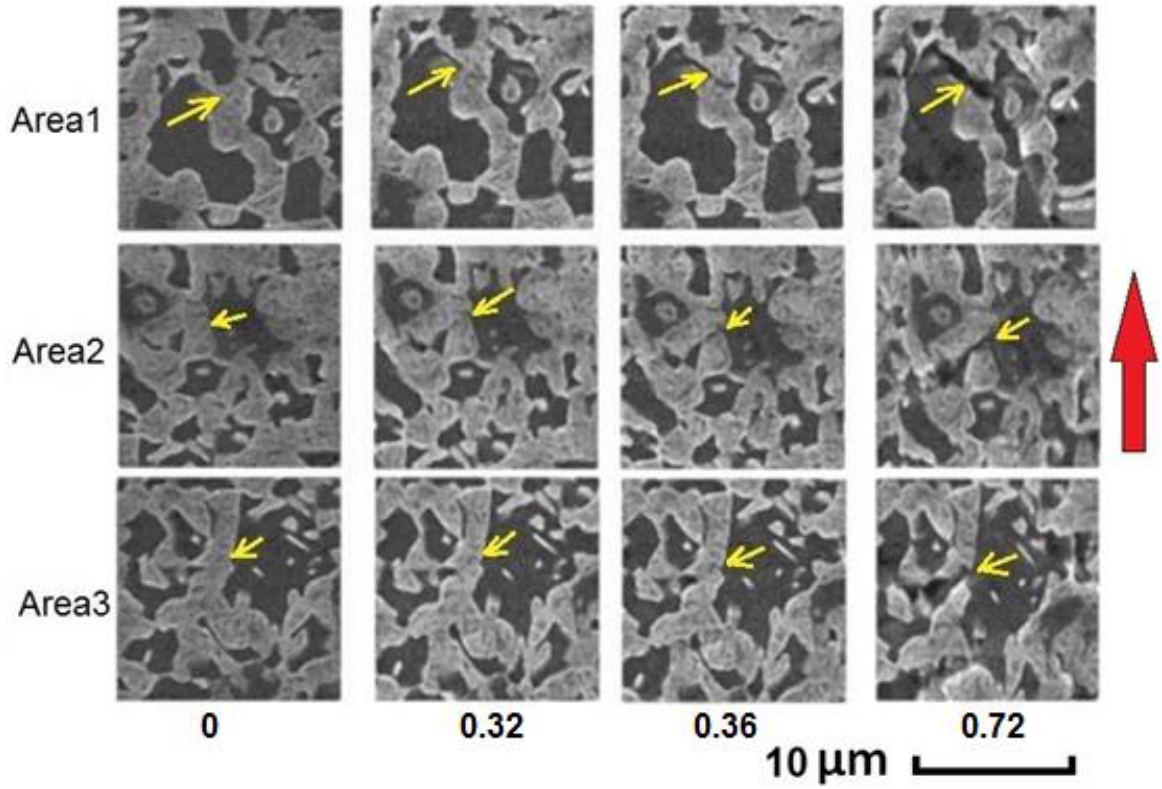

Figure 5-6: Damage development in martensite phase of three areas in DP1000 microstructure as the applied displacement increased (shown underneath each SEM image in mm) (red arrow showing loading direction)

5.3 DIC Results

Before running the DIC analysis, it is crucial to determine the most appropriate subset size. A normalized autocorrelation technique was used to analyse the SEM microstructure image shown in Figure 3-1. A MatLab code written by Haibo Lin [67] was utilised here in order to draw the autocorrelation function graph, and the results are shown in Figure 5-7. At a value of A = 0.5 calculated using equation (20), the normalized autocorrelation function width is around 11 pixels. This can provide an estimation of the average feature size in the microstructure. As described in Section 3.3, the subset size should have between three to six features for best DIC results. Consequently, a subset size from 33 to 66 pixels can achieve a suitable amount of over-sampling.

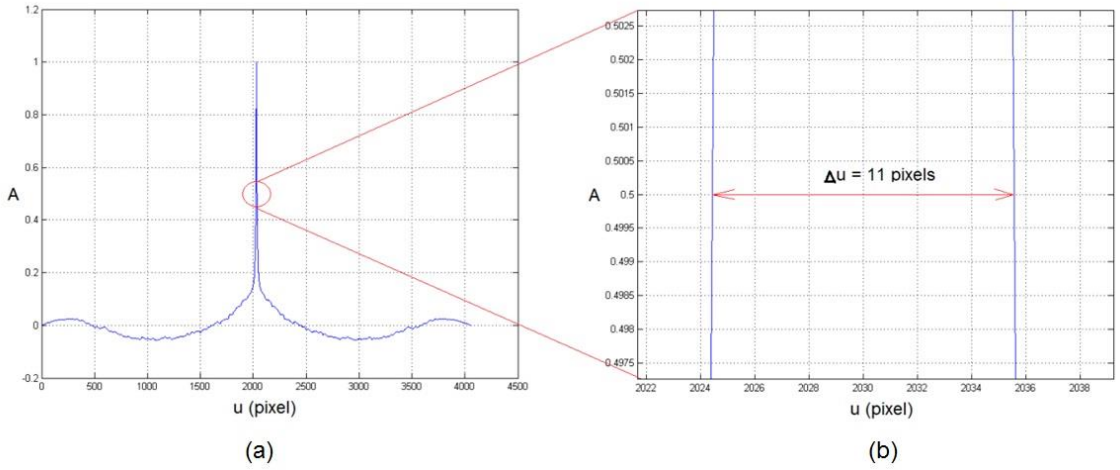

Figure 5-7: Normalized autocorrelation curve of undeformed SEM image shown in Figure 3-1, (a) is overall result, and (b) magnification around A=0.5

A convergence study over DIC results of the microstructure with different subset sizes was carried out for the same area of a specimen loaded in the transverse rolling direction. Only the DIC parameters were changing. This was done in order to ensure the validity of normalized autocorrelation estimation. Figure 5-8 shows an example of obtained DIC results

using 64 pixels subset size. Results include maximum displacement vectors showed with arrows and calculated strain in the Y-direction (loading direction, vertical in the figure), as illustrated in contour map.

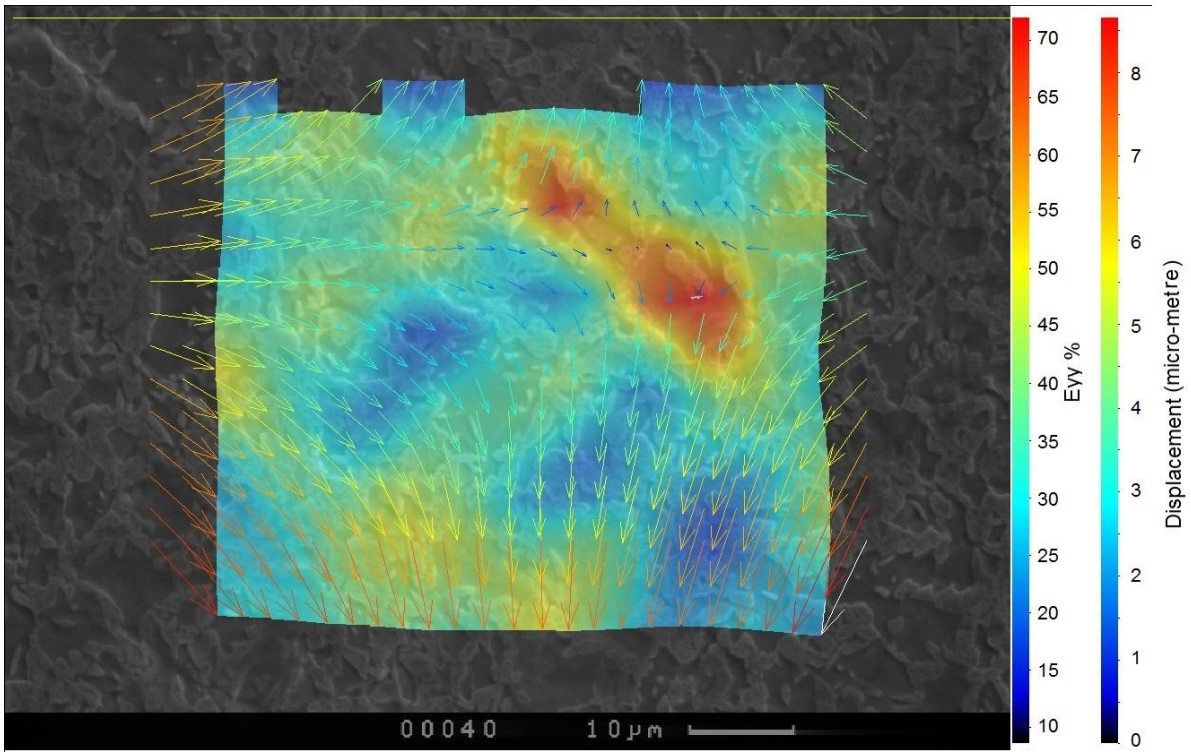

Figure 5-8: DIC results overlaid on DP1000 microstructure; ferrite in dark and martensite in bright, arrows refer to maximum displacement vectors; strain values in Y-direction (vertical in the figure) shown in background contour map

Figure 5-9 illustrates the convergence analysis of DIC results for maximum vector displacements. At the beginning, the DIC results with subset size of 128 pixels were calculated. Then the average percentage of differences in DIC results with subset sizes of 64, 32 and 16, as compared to 128 subset size results, were calculated and plotted versus subset size, as shown in Figure 5-9. As can be seen from Figure 5-9, the curve is levelled off after a subset size of around 40 pixels was reached, which is consistent with the range of subset sizes estimated by the normalized autocorrelation technique.

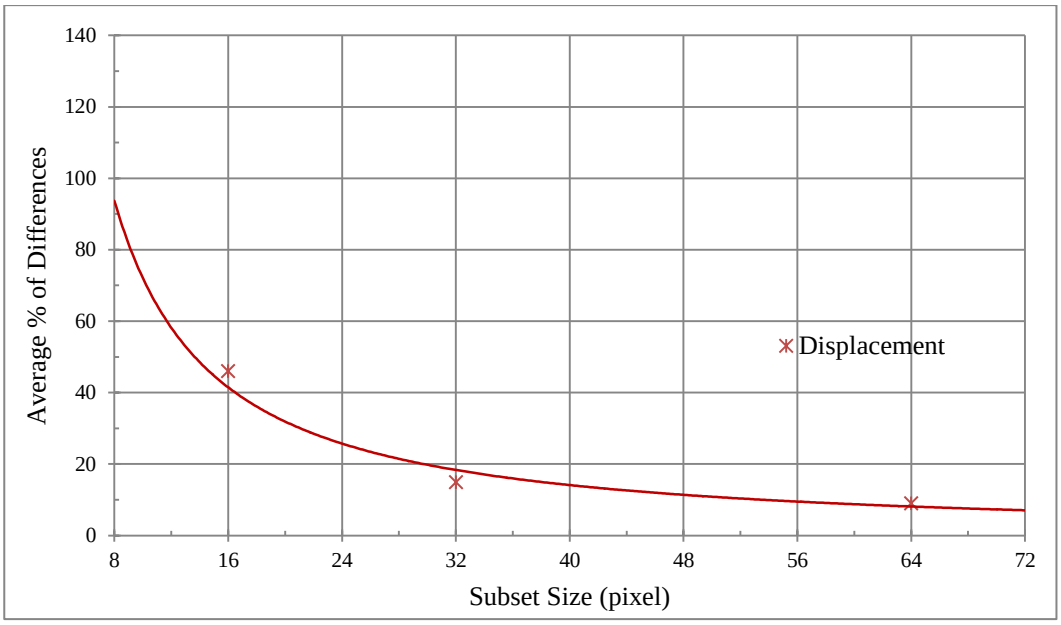

Figure 5-9: Subset size effect on DIC results of maximum displacement, both compared to DIC results with subset size of 128 pixels

As discussed in Section 3.3, there are two options in DIC analysis with LaVision 7.2, multi-pass analysis and multi-pass reduced analysis. Figure 5-10 illustrates the effect of using multi-pass with constant subset size (shown in red lines) and multi-pass with reduced analysis (shown in blue lines). The DIC results with subset sizes 32 and 16 pixels were compared to the DIC results obtained using 64 pixels interrogation window as a reference. In the multi-pass reduced analysis, the first iteration was with a 64 pixels subset size, then reduced to either 32 or 16 pixels. The percentage of difference was then calculated for both vector results and strain calculations, as plotted in Figure 5-10. As can be seen from the figure, a reduced pass analysis decreases the difference by more than a factor two for a subset size of 16 pixels for both vector and strain values. Additionally, the displacement vectors curves level off after a subset size of 32 pixels. Moreover, for both displacement vector and strain curves, the average % difference becomes negligible beyond a window size of 32 pixels. Therefore, multi-pass reduced analysis was chosen, especially since the

calculation time was not increased much, as the total number of deformed SEM images to analyse was relatively small (between 25 and 30).

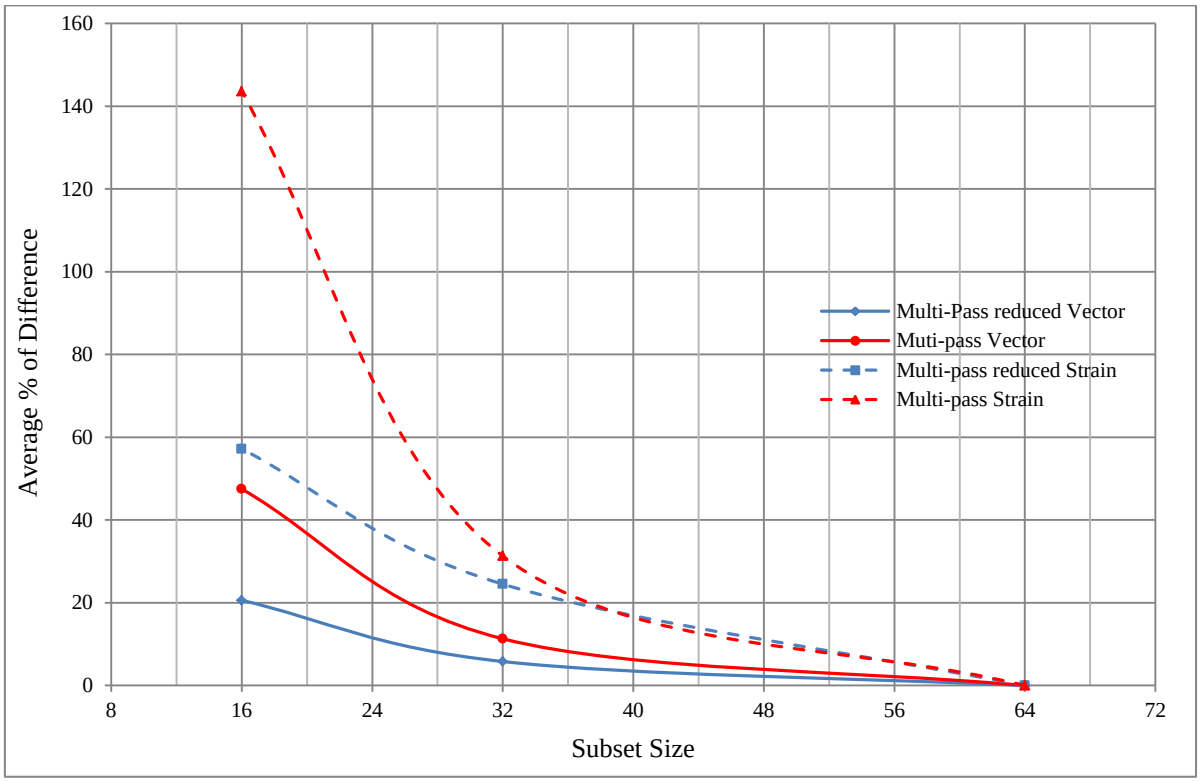

Figure 5-10: Effect of using multi-pass constant and reduced DIC analysis on accuracy of maximum displacement vectors and strain results in loading direction

Figure 5-11 shows the effect of overlap on vectors results (the red line) and strain measurements (the blue line). The result for multi-pass algorithm with subset size of 64 pixels and 0% overlap between the subsets was used as reference value. The overlap was then changed to 25%, 50%, 75% and 87%. Then, vector results and strain values were compared to the 0% overlap results. As can be seen from Figure 5-11, the red line remained flat, which indicates that the overlap had a negligible effect on vector calculations. However, strain values show a continuous gradual increase as the overlap increased. The average percentage of differences of strain calculations for the 25% overlap was 15%, whereas for

50% overlap it was 22%. As the difference between the two is small, 50% overlap will be used as it gives a better spatial resolution for strain maps.

From all the previous comparisons, it can be seen that normalized autocorrelation can provide good estimation of feature size and help select the appropriate subset size for DIC analysis of the DP1000 microstructure. In addition, multi-pass reduced analysis starting from a subset size of 128 pixels for first passes to 64 pixels for second passes with 50% overlap was used in this research for overall microstructure analysis, while multi-pass reduced analysis beginning with subset size of 64 pixels for first passes and reduced to 32 pixels for second passes with 50% overlap was utilised for local damage analysis, due to the need for increased spatial resolution. The selected subset size cannot be transferred directly to different SEM images. It is unique to the SEM images acquired in this research with 800X magnification and a resolution of 2000X1500 pixels.

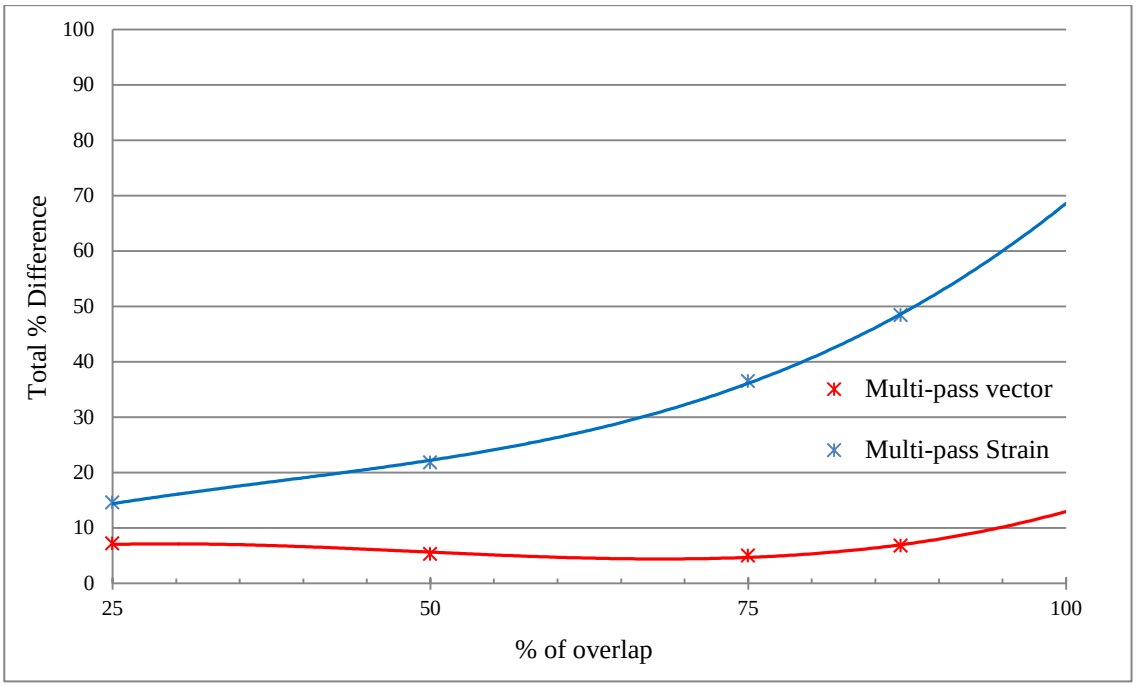

Figure 5-11: Overlap effect on maximum vector results and strain calculated in loading direction for DIC analysis of DP1000 microstructure

DIC was used to analyse the strain field over DP1000 deformed microstructure. Figure 5-12 shows the E_{yy} strain map overlaid on the SEM image of the deformed microstructure for an applied displacement of 0.32 mm. The y-axis (vertical in the figure) corresponds to the tensile direction shown with a white arrow in the figure. This was chosen since the longitudinal strain was large, as compared to other strain components, especially the out of plane strain, which can be neglected as the specimen was under uniaxial tensile load. Additionally, using actual measured results from DIC (such as E_{yy}) is better than using other calculated strain values such as the maximum principal strain as the later need some calculations which include the effect of out of plane strain that assumed to be small. The applied displacement value of 0.32 mm was chosen because it was the maximum applied displacement before damage was observed in the microstructure. DIC results become indeed unreliable after the appearance of any defect in the microstructure in the form of void or

crack, especially around the defected area. As can be seen from Figure 5-12, a maximum E_{yy} strain value around 20% was calculated within most of the large ferrite grain areas. However, the minimum strain values were found in the primarily martensite regions. Moreover, strain bands can be observed in the microstructure as highlighted by dashed lines orientated at 45^{o} with respect to the loading direction.

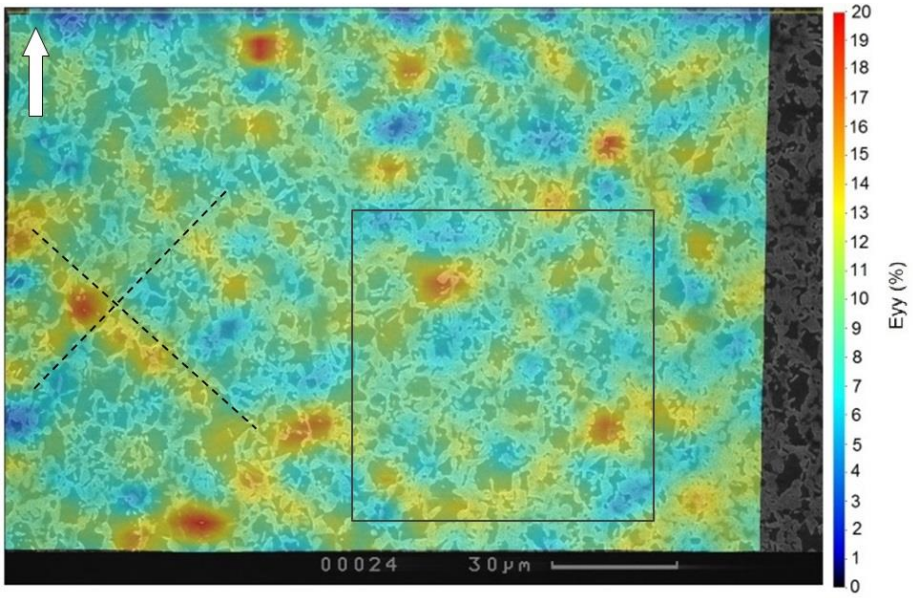

Figure 5-12: E_{yy} strain map (%) at applied displacement of 0.32 mm; dashed lines indicating examples of strain bands at 45^{o} with respect to tensile direction (vertical white arrow)

Frequency distributions of strain values along the tensile direction in the ferrite and martensite were analysed for the region bordered by the black square in Figure 5-12. In order to distinguish the strain values between ferrite and martensite, a microstructure FE simulation with fully constrained boundary conditions was used to ensure that the model deformed exactly in the same manner as the actual microstructure. It is then easier through microstructure modelling to separate strain values for each phase and plot distributions as shown in Figure 5-13. The results shown in Figure 5-13 indicate that the ferrite and martensite deformed similarly. The ferrite mean value of 9.2 % was marginally higher than

that of the martensite, at about 8.6 %. The ferrite had a standard deviation of 2.4 while this was 2.0 for the martensite, which is an indication of comparable strain heterogeneity for the constituents of DP1000 steels. Nonetheless, the differences were small and thus it can be claimed that a small strain partitioning exists in DP1000 steels. The mean values of the phases (i.e. 9%) match the local average strain of 9.5% measured from the displacement of the top and bottom edges of the analysed area.

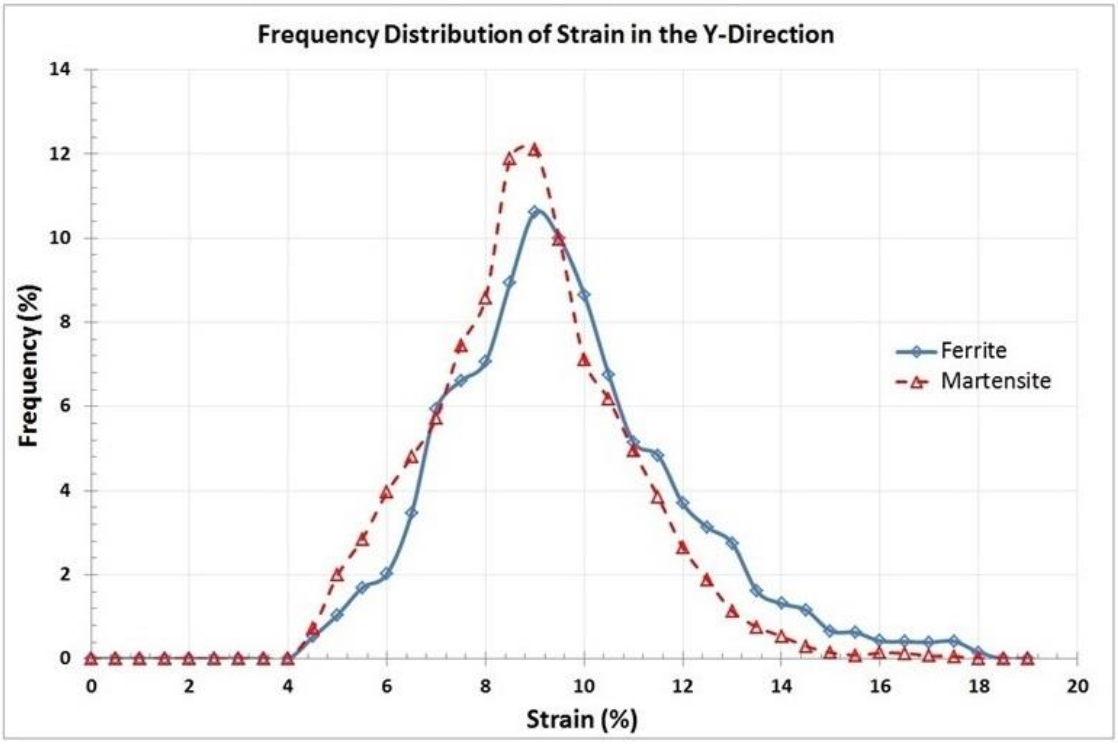

Figure 5-13: Frequency distribution of E_{yy} strain over analysed region of DP1000, outlined with black box in Figure 5-12

Available DIC analysis of both microstructure and standard tensile specimen make it possible to examine DP1000 steel anisotropy using equation (23) to calculate the r-value. Figure shows the location of the measured strain values.

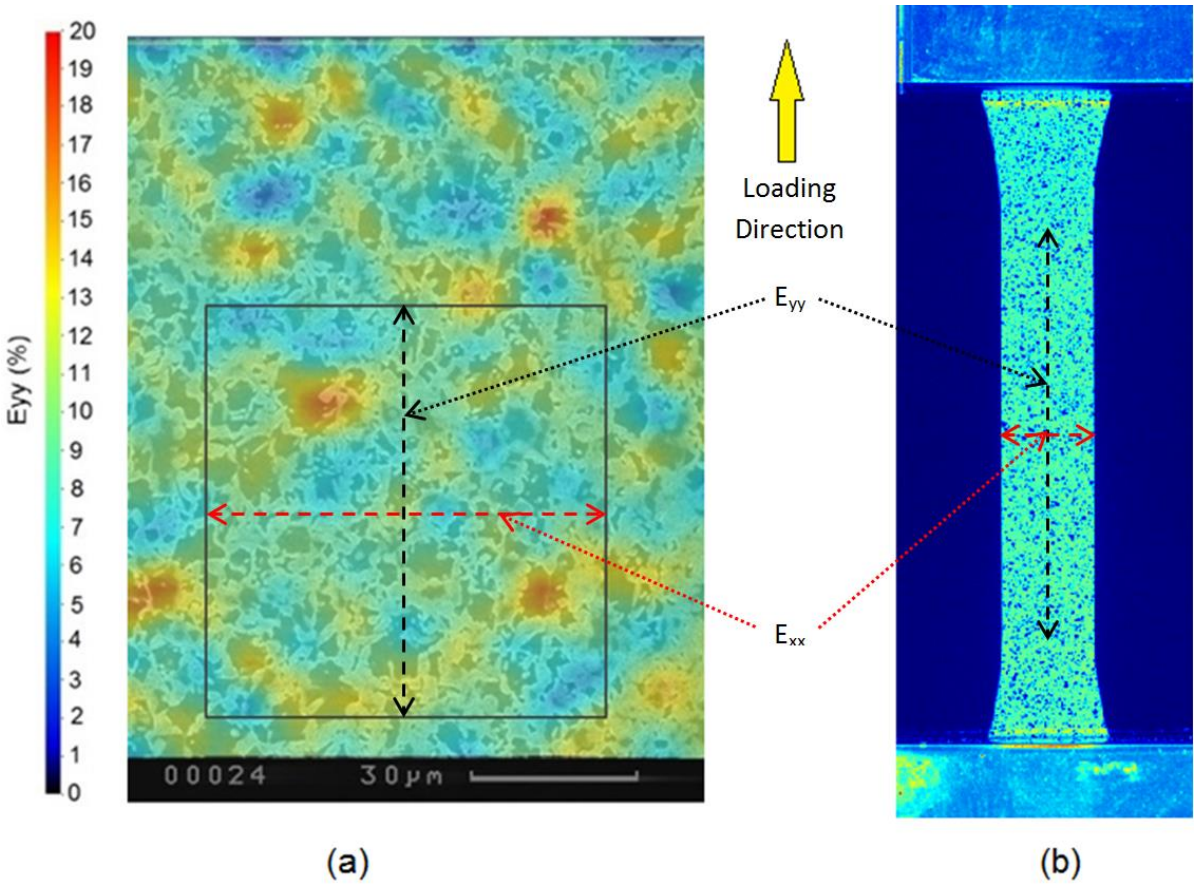

Figure 5-14: Location of measured strain values using DIC results in order to calculate the strain ratio (r-value); (a) microstructure results and (b) standard tensile specimen

Table lists the r-value calculated from the DIC results of the microstructure deformation and standard specimen test. The results show that the r-value greater than one with an average value of around 2.7. Consequently, DP1000 steel is an anisotropic material suitable for sheet metal forming due to the resistance to thinning indicated by the r-value greater than one.

Table 5-1: r-value of DP1000 steel calculated from DIC results obtained from microstructure deformation and tensile test of the standard specimen

	Microstructure analysis			**Standard specimen**		
	E_{yy}	E_{xx}	r-value	E_{yy}	E_{xx}	r-value
	0.047	-0.037	4.039	0.027	-0.021	3.618
	0.062	-0.043	2.347	0.052	-0.04	3.261
	0.080	-0.052	1.826	0.075	-0.045	1.464
Average			2.737			2.781

In summary, the stress/strain curve of DP1000 steel has been measured. The results showed that rolling direction has a weak effect on the stress/strain curve of the material investigated, also supported by the random distribution of the phases without any preferred direction for banding in the microstructure. Microstructural observations revealed three mechanisms of damage formation; inclusion failure, decohesion of the ferrite and martensite interface and martensite cracking. The strain fields along the loading direction were successfully measured through DIC using microstructural features for the correlation. A detailed analysis was carried out to control and optimise the DIC parameters (e.g. interrogation window size) used for the correlation carried out at the scale of the microstructure under large deformation, as this is a non-standard application of the DIC technique. The analysis was also carried out over large areas of the microstructure in order to produce statistically-meaningful results needed for RVE simulations. Results were also successful in generating damage in the areas analysed with DIC, therefore enabling a study of damage formation and development as a function of local strain distributions but also stress distributions through

the use of microstructure modelling to be presented in the next Chapter. Results showed strain bands at around 45^{o} to the loading direction. The analysis of strain distribution in the phases revealed no strain partitioning in the microstructure with similar strain distributions in both ferrite and martensite. Strain ratio measurement in the form of r-value showed anisotropy behaviour of DP1000 steel and recommended for sheet metal forming as a result of thinning resistance.

6. Modelling Results

In this chapter, the modelling results at macro-scale and micro-scale will be presented. The first section begins with results at macro-scale for simulating the deformation and damage of the tensile specimens up to fracture. Then, the microstructure simulation results are examined to predict the deformation and damage of DP1000 with the aid of the DIC results. The second section also includes the results of the martensite cracking investigation in terms of stress and strain values in order to propose a criterion for damage nucleation. Additionally, the effect of damage models for martensite and ferrite on the predicted stress of microstructure simulation is shown. Finally, RVE results to predict DP1000 stress/strain curves are examined and are illustrated at the end of this chapter.

6.1 Continuum Damage Modelling

In this section, the modelling results of DP1000 at macro-scale (i.e. scale of tensile specimens) are presented. As DP1000 steel is a ductile material, the tensile damage of this material includes voids nucleation, growth and coalescence. Gurson-Tvergaard-Needleman (GTN) model is a widely used damage model for porous materials and is implemented into Abaqus FE software. However, GTN has nine parameters to be calibrated in order to capture the material response. The effects of some of these parameters are well understood but the calibration of three of them (q_1, q_2 and q_3) has to be investigated. An analysis of the effect of parameters' values was carried out and is shown in the first sub-section of this section. The tested specimens were then simulated using the GTN damage model. Experimental load/displacement measurements of tensile tests were used for validation purpose.

6.1.1 Effect of Gurson's Parameters

As already described in Section 2.5.3, the Gurson-Tvergaard-Needleman (GTN) model is one of the most commonly used model to describe void growth in ductile materials (in this research, GTN was applied only on the ferrite phase because it is found that most of the voids were created in the ferrite phase). GTN model is chosen here because it has been incorporated into Abaqus. As the voids grow in size, the load required to deform the specimen after the ultimate tensile strength is decreased and this is shown in the form of softening of the load/displacement curve. Consequently, the load loss of the softening part in the load/displacement curve can be modelled using GTN. However, the model requires eight material parameters to be identified; f_0, ε_N, f_N, S_N, q_1, q_2, f_c and f_F (q_3 is calculated as q_1^2 as suggested in Abaqus manual [50]). These parameters were described in details in Section 2.5.3. The last two parameters (f_c and f_F) are related to the sudden drop in stress capacity corresponding to damage coalescence leading to the fracture of the specimen, but this part of the stress/strain curve was not the focus of this project. As a result, the simulation was terminated just before the beginning of coalescence part (i.e. the sudden loss of load) and these two parameters were therefore excluded from the analysis and were not defined in Abaqus. In order to understand the effect of each parameter on the load displacement curve, the model of the standard specimen shown in Figure 4-1 (b) was used. It is well-known that f_0 affects the load displacement curve from yielding to fracture. Increasing the value of f_0 will reduce the load values on the curve. ε_N controls the start of the void nucleation, whereas f_N controls the amount of void nucleation. It was found that S_N had a small or negligible effect on the load/displacement curve. The effect of the previous parameters is shown in the Appendix VII. However, q_1 and q_2 were inserted in the Gurson

model (by Tvergaard et al. [48] as explained in section 2.5.3) and their effect was not clear. As a result, their effect on load/displacement curves is shown in this section.

All Gurson model's parameters were, first, kept constant, except q_1 which varied with the values 1, 1.25, 1.35 and 1.5. The corresponding load/displacement curves are shown in Figure 6-1.

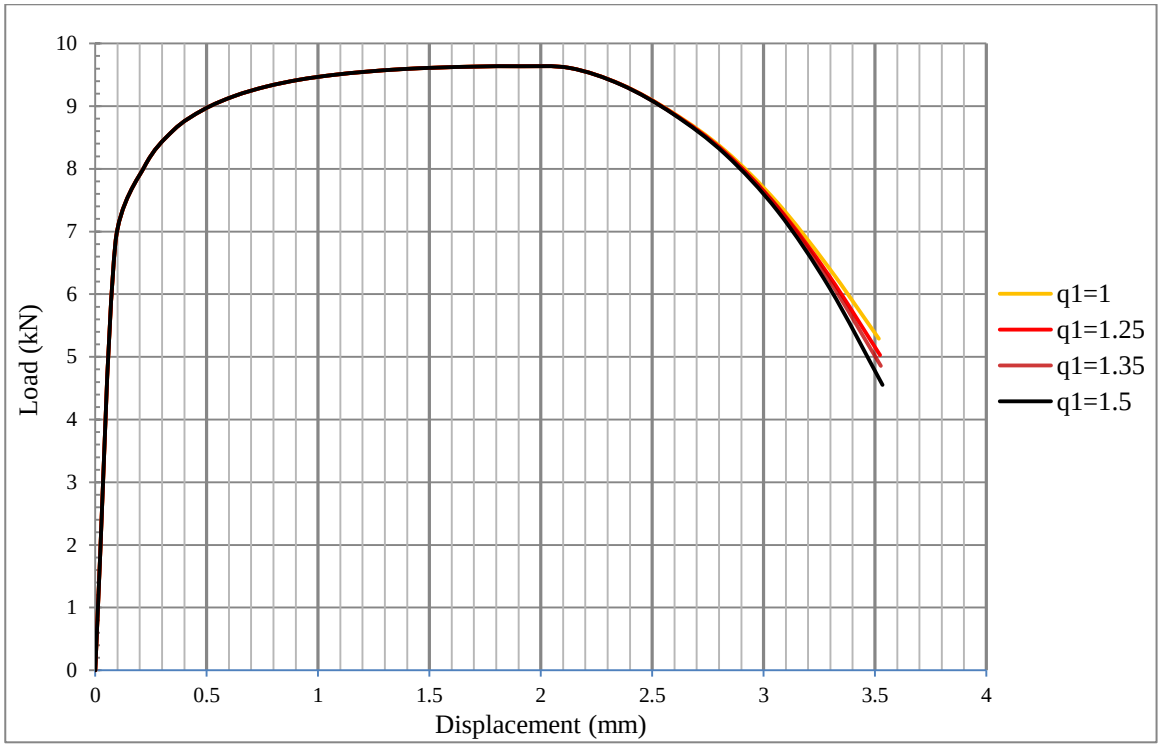

Figure 6-1: Effect of q_1 on load/displacement curve from standard model results with constant values of other Gurson model parameters

As can be seen, an effect started to be observed at the displacement value of 2.5mm and the softening was increased by increasing the value of q_1. After this, all parameters were kept constant except q_2 which had the values of 0.9, 1.0 and 1.1 and the effect of q_2 on the load/displacement curve is shown in Figure 6-2. The effect started to be observed at a displacement value of about 2.7 mm and the softening was increased by increasing the value of q_2. Consequently, it can be claimed that increasing the value of q_1 and q_2 leads to a

decrease in the stress capacity of the elements. Additionally, the softening effect of q_1 can be observed earlier than that of q_2 on the load/displacement curve.

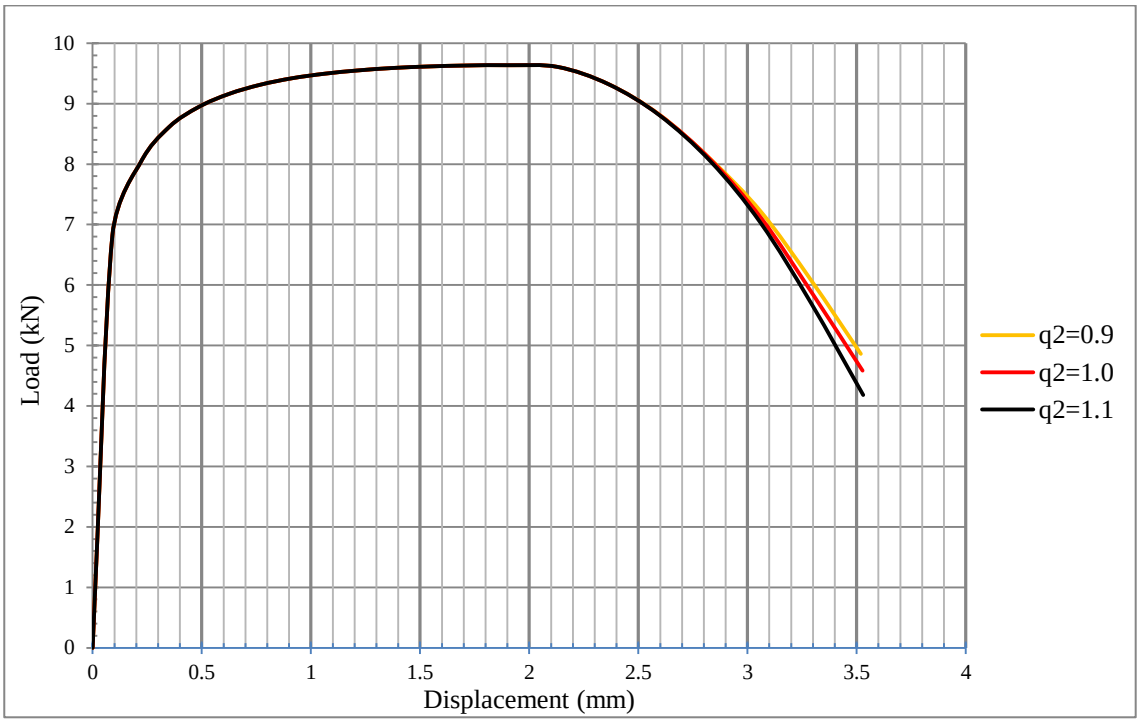

Figure 6-2: Effect of q_2 on load/displacement curve from standard model results with constant values of other Gurson model parameters

The dog-bone specimen model for the in-situ test shown in Figure 4-1 (a) was also used to check the results observed from the standard specimen model as far as the effect of q_1 and $q_2$are concerned. These are shown in Figure 6-3 and Figure 6-4 for q_1 and $q_{2,}$ respectively. Similar trend, as that reported for the standard geometry, for both Gurson parameters can be observed. Figure 6-5 shows the effect of q_3 on the load/displacement curve. The effect of q_3 can be observed near the failure of the specimen. It can be noted that increasing the value of q_3 will reduce the slope of the model response. This is opposite to the effect of q_1 and q_2 on the load/displacement curves. However, it is recommended in the literature that the q_3 value

is kept as q_1^2 [50] so that the calibration process is easier, due to adjusting two parameters rather than three.

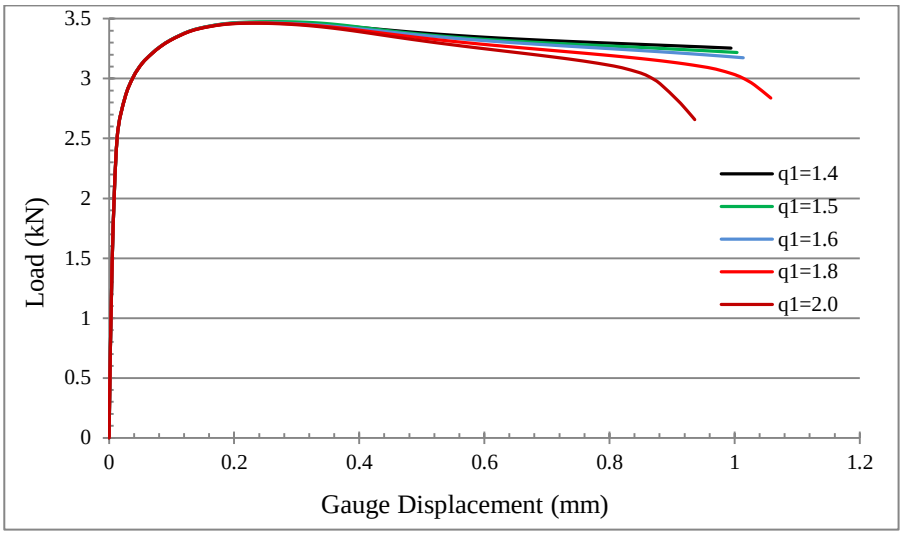

Figure 6-3: Effect of q_1 on load/displacement curve of dog-bone model with constant value of other Gurson model parameters

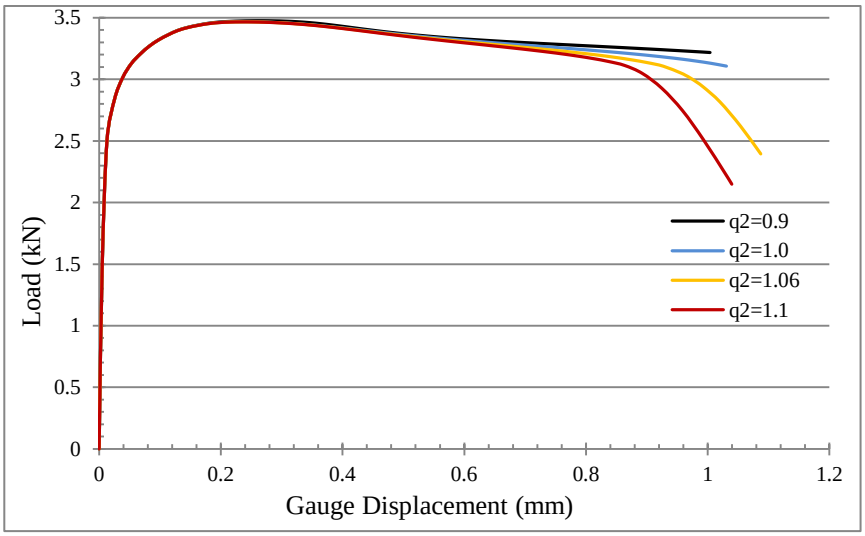

Figure 6-4: Effect of q_2 on load/displacement curve of dog-bone model with constant value of the other Gurson model parameters

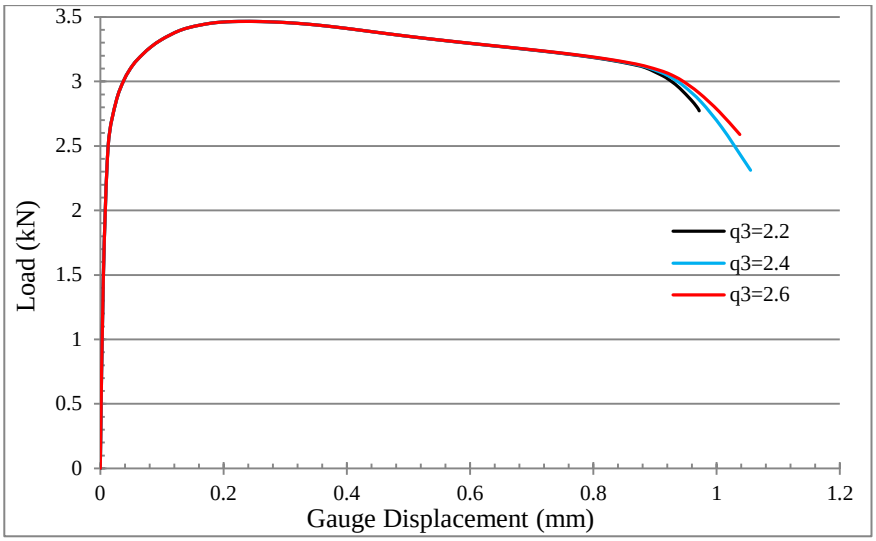

Figure 6-5: Effect of q_3 on load/displacement curve of dog bone model with constant value of other Gurson model parameters

6.1.2 Calibration of Gurson's Parameters

All models shown in Figure 4-1 were run and results of load and displacement of the gauge section were extracted and compared to the experimental measurements for validation. The GTN parameters were calibrated and tuned so that the error between experimental and modelling results was reduced. This section is divided into subsections for each specimen geometry; in situ specimen model, standard specimen model and notch specimen model.

6.1.2.1 In Situ Specimen Simulation Results

The load/displacement results obtained experimentally and from the model shown in Figure 4-1 (a) are plotted in Figure 6-6. As can be seen from the figure, the softening part of the experimental load/displacement curve was steady. Consequently, different values of q_1 of the Gurson model were calibrated with a constant q_2 value as the latter parameter affects the curve at a point beyond that for q_1. It was found that the best fit between modelling and experimental curves was obtained with parameter values of 1.1 for q_1 and 0.99 for q_2.

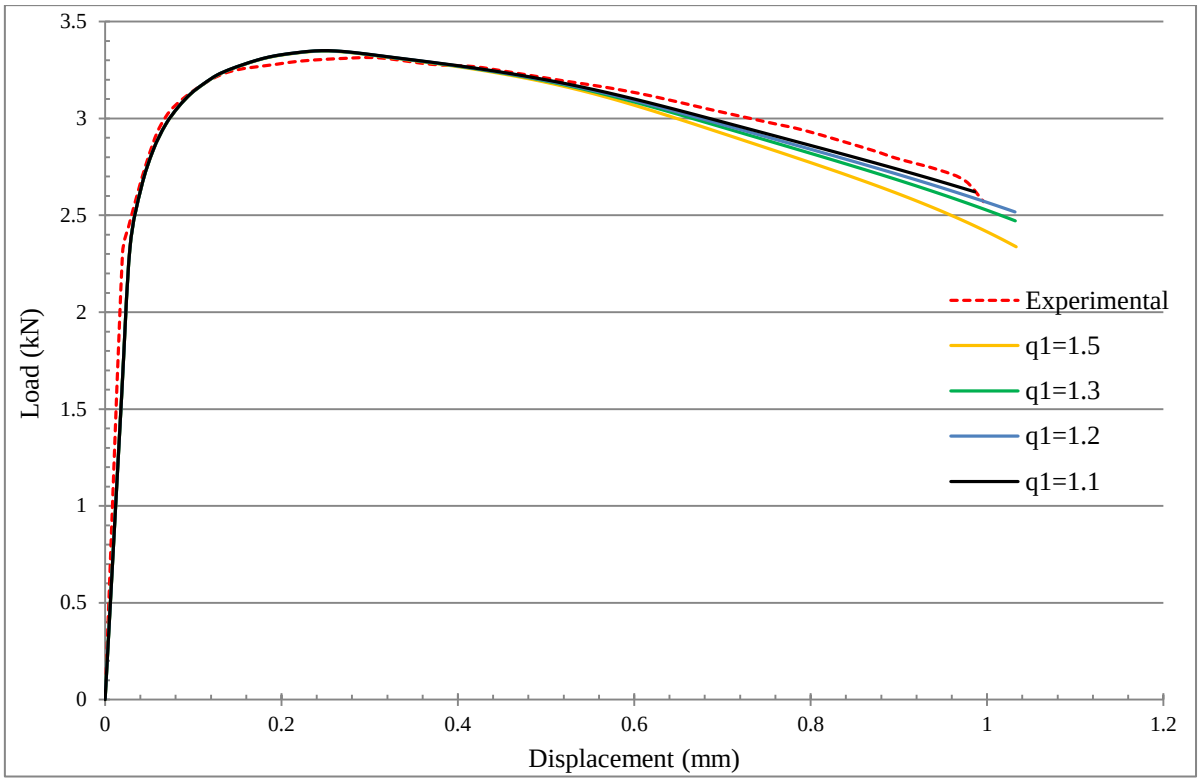

Figure 6-6: Experimental load/displacement curve of dog-bone specimen used for in situ test, and curves from the model to calibrate q_1 in the Gurson model

6.1.2.2 Standard Specimen Simulation Results

The parameters of the Gurson model used for dog-bone (in situ) specimen modelling were used as a starting point for the modelling of the standard geometry and comparison was made to the experimental load/displacement curve. As can be seen from Figure 6-7, the parameters needed to be re-calibrated for a better fit with experimental measurements. Both q_1 and q_2 were calibrated with the values of 1.3 and 0.95, respectively. No optimization method was used, only a trial and error method was applied, until the best fit curve was achieved.

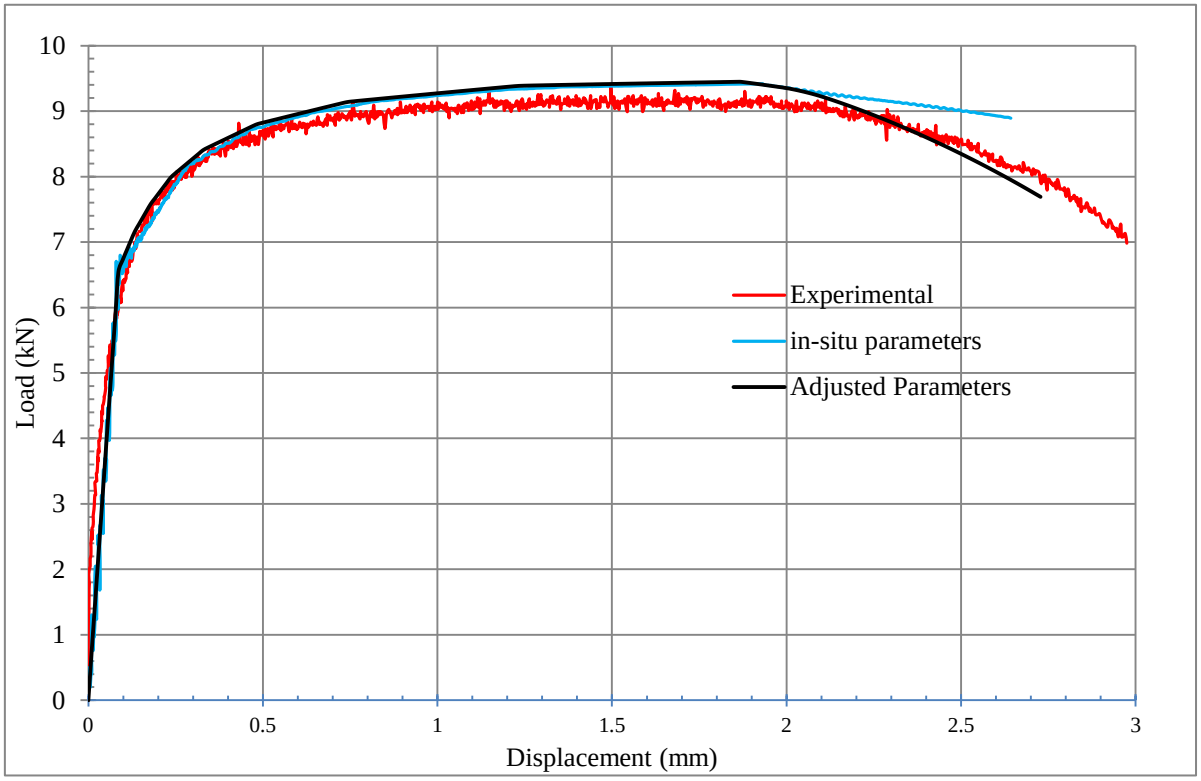

Figure 6-7: Experimental load/displacement curve of standard specimen and simulation results of the model using both in-situ parameters and newly calibrated parameters for the Gurson model

6.1.2.3 Notched Specimen Simulation Results

The notched specimen model shown in Figure 4-1 (c) was run with the GTN damage model. For notch specimens, the reduction in cross sectional area of the notch area should be used instead of elongation of the gauge section (used in smooth tensile specimens) [12]. Consequently, the load versus contraction of the notch width was used to calibrate GTN parameters. The effect of different parameters of the Gurson model on the load/reduction curve is presented in Figure 6-8, in comparison with the experimental measurements. As can

be seen, a q_1 value of 1.6 was chosen for the best fit; this value therefore differs from the values found for the standard and in-situ specimens.

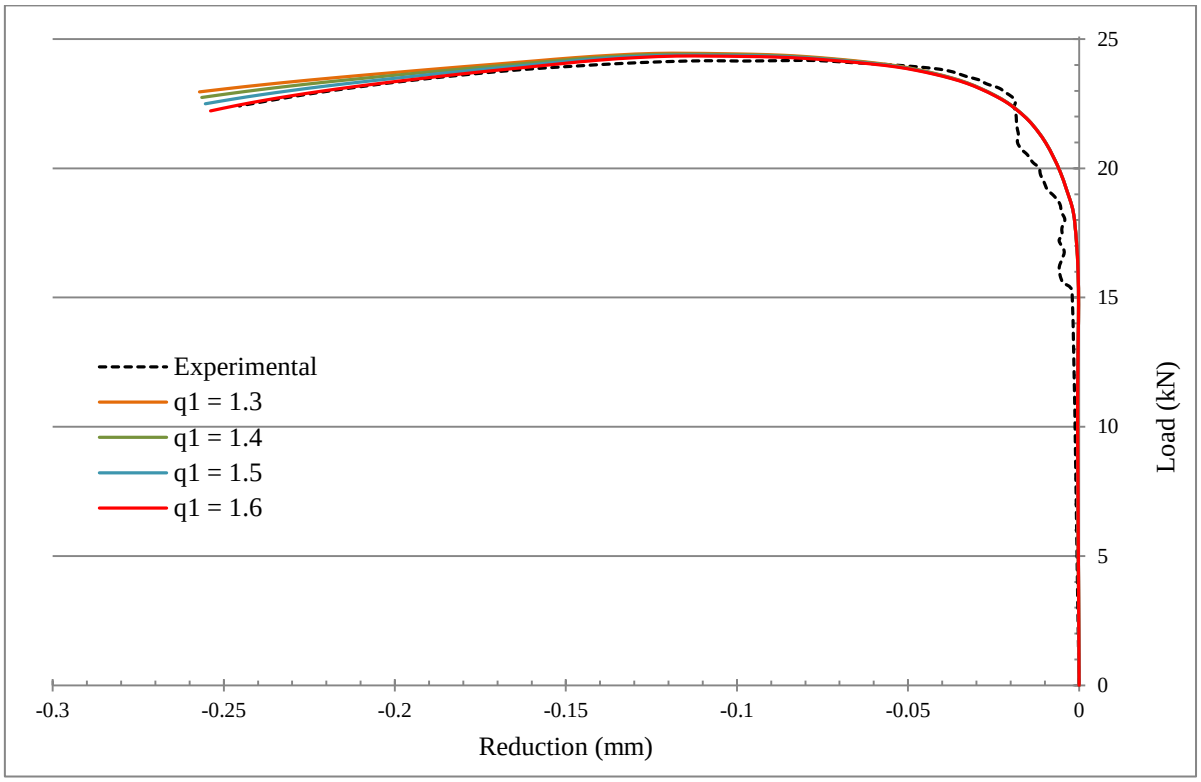

Figure 6-8: Experimental and modelling load/reduction curves of notched specimen

From the previous results, it was found that Gurson parameters used for the in situ specimen model needed to be adjusted for both standard and notched geometries. This is not a surprise as the Gurson model takes into account the effect of stress triaxiality. It is common practice that, to find the best fit parameters for the Gurson model, different specimen geometries (three or more) with different notch diameters (so that a variety of stress triaxiality is generated) have to be used for a particular material [68]. Table 6-1 summarises the parameters values used for in-situ, standard and notched simulations.

Table 6-1: Void nucleation and Gurson parameters used for modelling different specimen geometries

Specimen\Parameter	f_N	ε_N	S_N	q_1	q_2
In situ specimen	0.04	0.3	0.09	1.1	0.99
Standard specimen	0.04	0.1	0.09	1.3	0.95
Notched specimen	0.4	0.1	0.09	1.6	1.1

6.2 Microstructure-Based Damage Modelling

The modelling results of DP1000 at micro-scale (i.e. microstructure modelling) are presented in this section. Microstructure simulations were conducted to study deformation and damage at the scale of the microstructure. For instance, modelling can be used to calculate stress values and help investigate the conditions for damage formation in microstructures, which cannot be done with an experimental procedure only. Furthermore, microstructure-based modelling of deformation and damage was developed and compared to experimental results. Furthermore, the effect of damage models for the two phases on predicted overall stress is shown.

6.2.1 Mesh Refinement Study

A study of mesh dependency of results was carried out using microstructure simulation with the fully constraint model (i.e. displacement extracted from DIC results and applied to all nodes in the model to ensure similarity in deformation) and plane stress condition (to simulate the condition of the specimen surface). This is the most crucial microstructure modelling method in this research as it is utilised to calibrate the phases' flow curves and investigate damage in DP1000 microstructure. Area 3 shown in Figure 5-6 was used for the mesh dependency study. Three models were generated with element sizes ranging from 4 pixels, 2 pixels and one pixel as shown in Figure 6-9. An applied displacement of 0.32 mm was chosen as this state will be used for damage analysis in martensite in section 6.2.3.1.

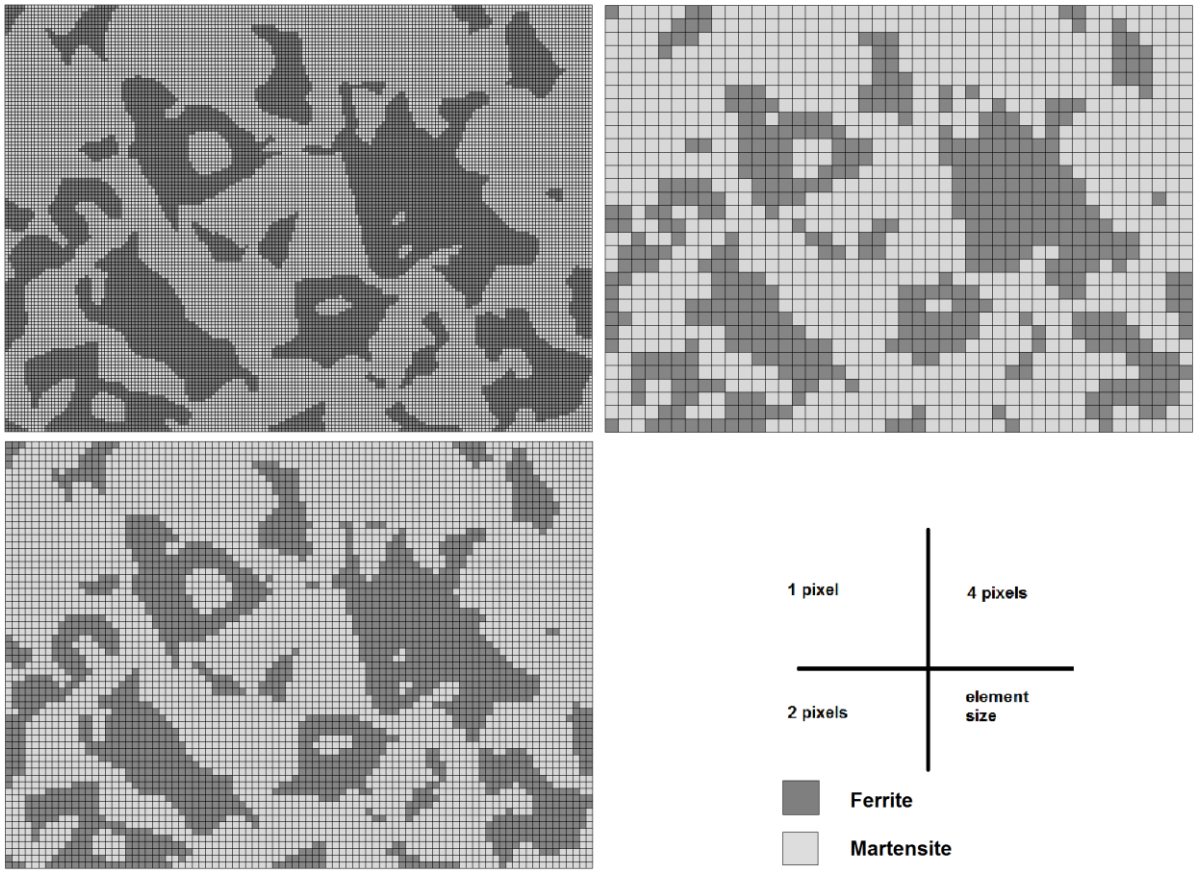

Figure 6-9: Three microstructure models with different element sizes generated for mesh dependency analysis of area 3 shown in Figure 5-6

Figure 6-10 shows the results of the maximum principal strain of the three models. As can be seen from the three model results, the distribution is not affected by the mesh size which is expected as the models are forced to deform according to the actual deformation of the microstructure. A negligible difference can be seen in strain values such as the maximum strain values of 0.161, 0.164 and 0.165 for models with element sizes of 4 pixels, 2 pixels and one pixel respectively.

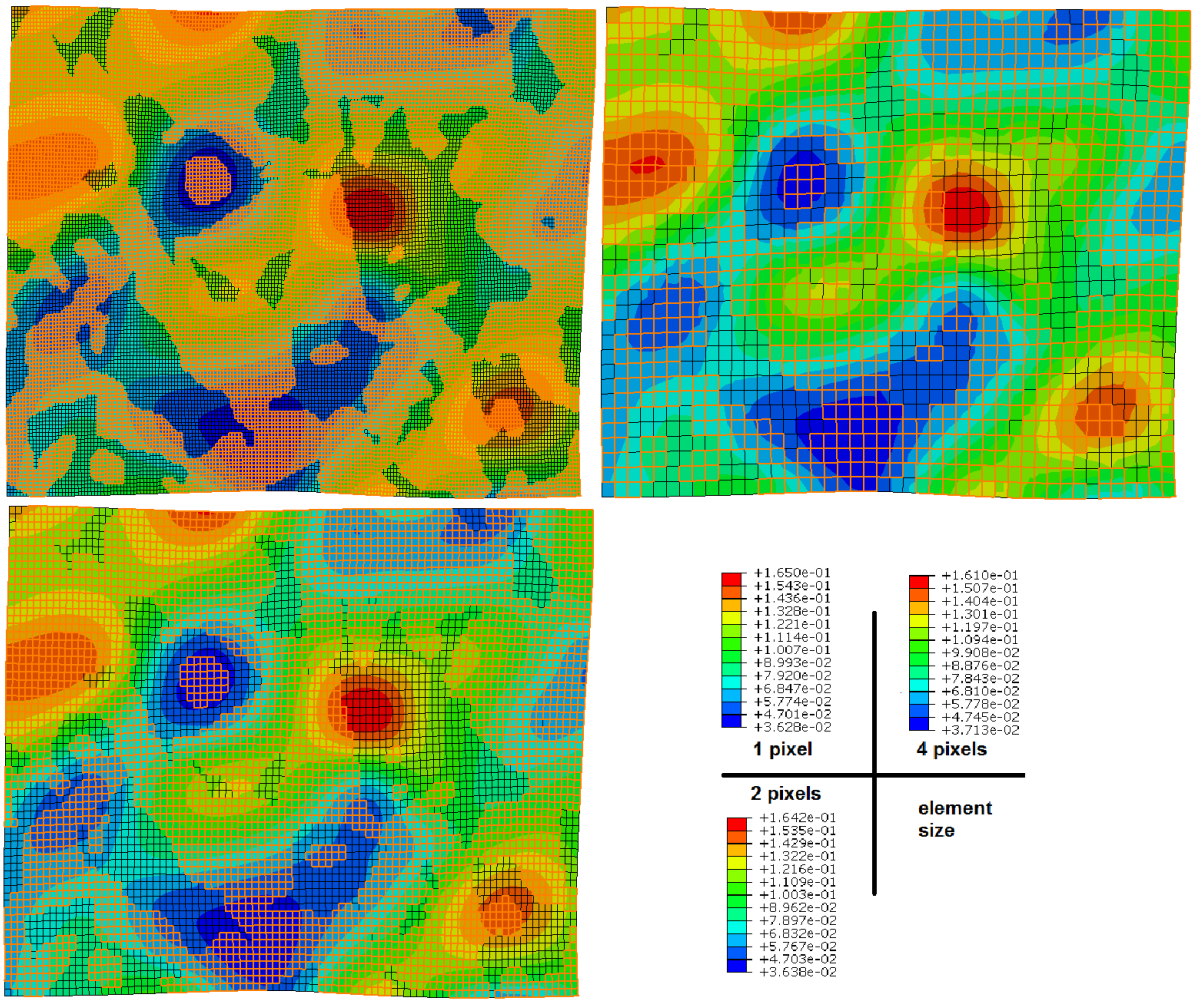

Figure 6-10: Maximum principal strain results of three microstructure models with different mesh element sizes

Figure 6-11 shows the maximum principal stress results in the martensite phase only, for the three microstructure models with different element sizes. Again, for fully constrained models, the stress results show a very small variance of 5 MPa (i.e. 0.3%) between model results with element sizes of 4 pixels and one pixel. This is negligible when compared to the maximum value of 1762 MPa obtained in stress results. As a result of the previous analysis of strain and stress results, values computed from the fully constrained model can be claimed as mesh independent.

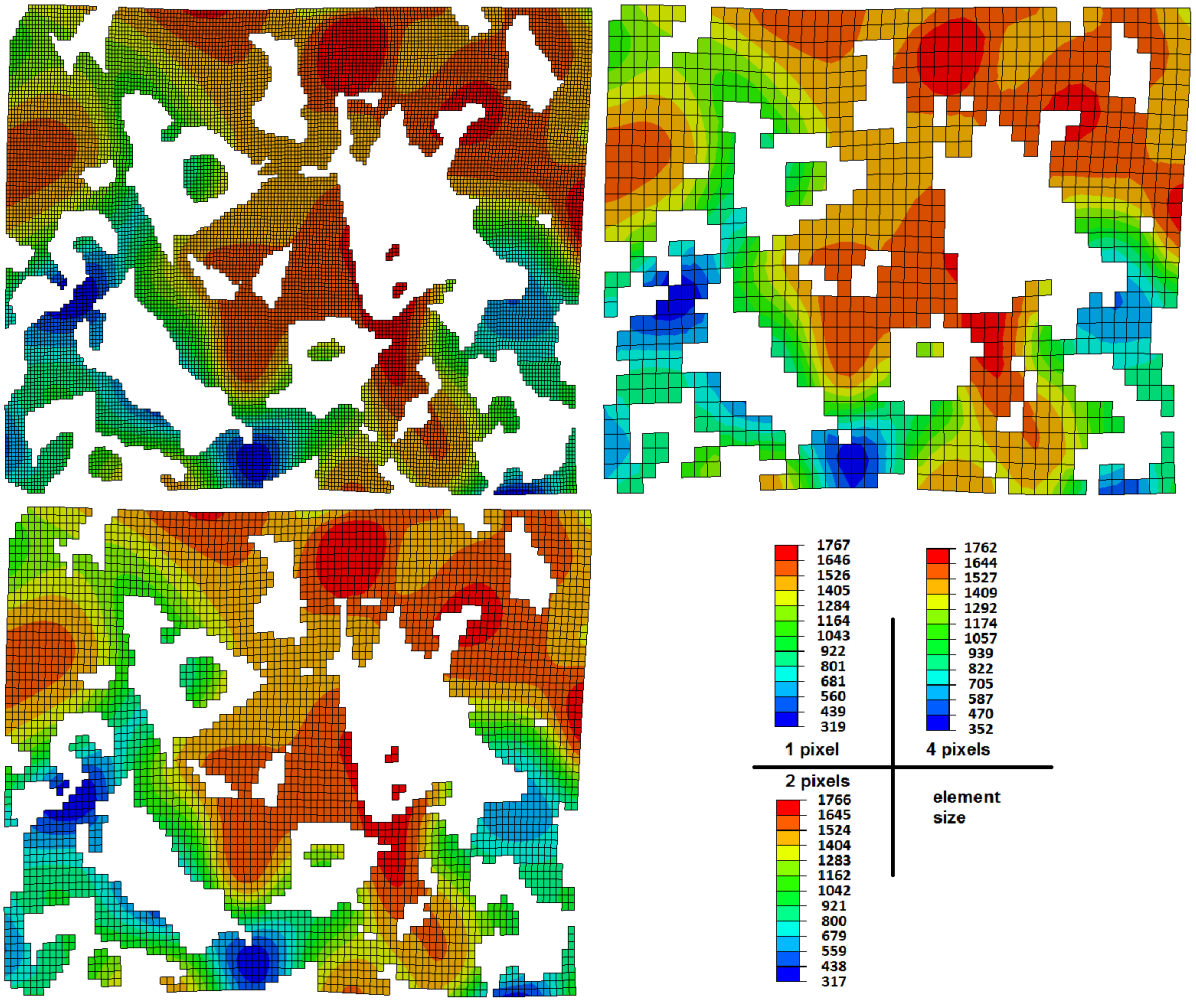

Figure 6-11: Maximum principal stress results in the martensite only for the three microstructure models with different mesh element sizes

A mesh convergence study was also carried out for the microstructure models with boundary conditions applied on the edges of the analysed area and plane strain conditions used to represent the mechanical conditions at the centre of the specimen. This state will be used to predict the behaviour of DP1000 steel using 2D microstructure model. Figure 6-12 shows the maximum principal strain results of the three models.

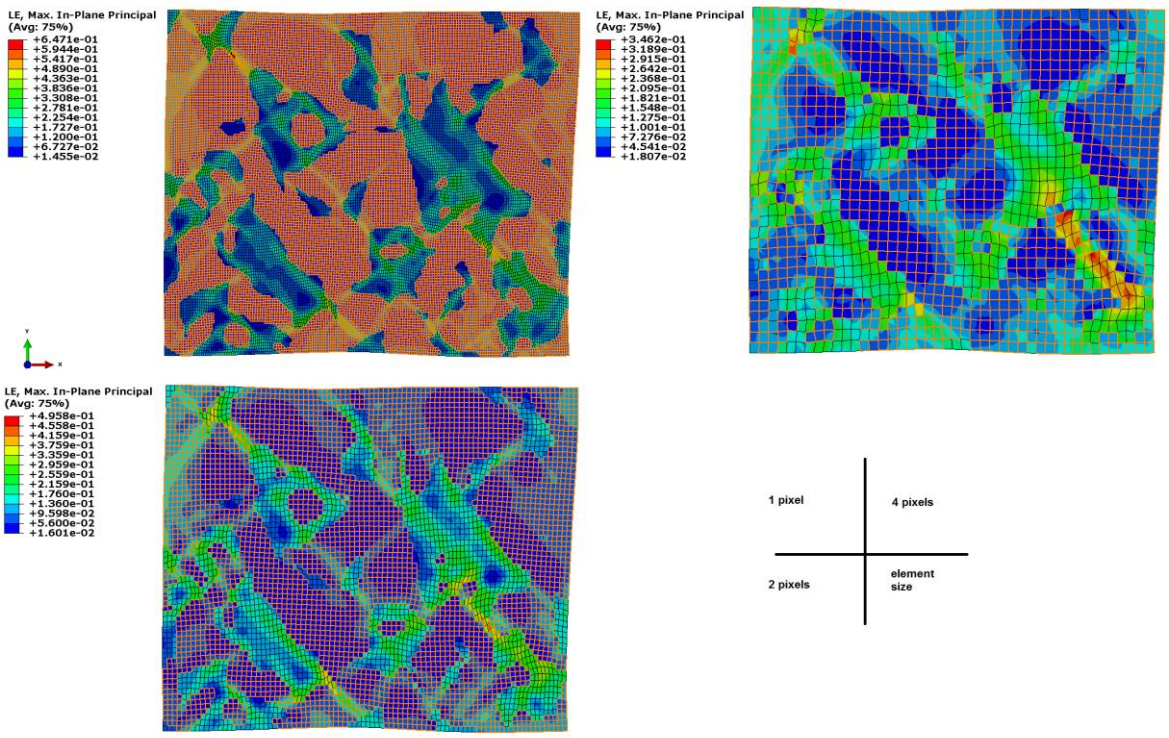

Figure 6-12: Maximum principal strain results of three microstructure models with different mesh element sizes

As can be seen from the figure, the distribution is quite similar especially for models with 2 pixels and one pixel element sizes. However, the maximum value recorded varies from 0.65 for the one pixel model to 0.35 for the 4 pixels model. For more precise comparison, the maximum strain values were compared along a line starting from the martensite phase, going through the interface between the phases, and ending in the ferrite phase as shown in Figure 6-13.

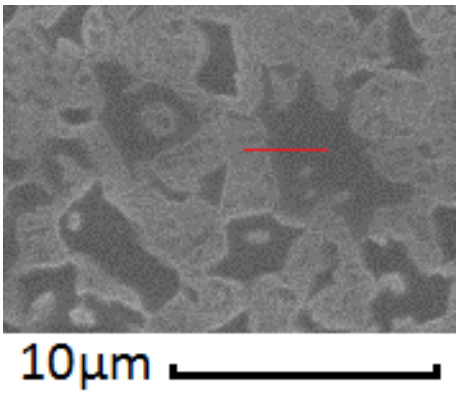

Figure 6-13: SEM image of the modelled microstructure for mesh refinement analysis, maximum principal strain values were extracted along the red line for the three models and plotted in Figure 6-14

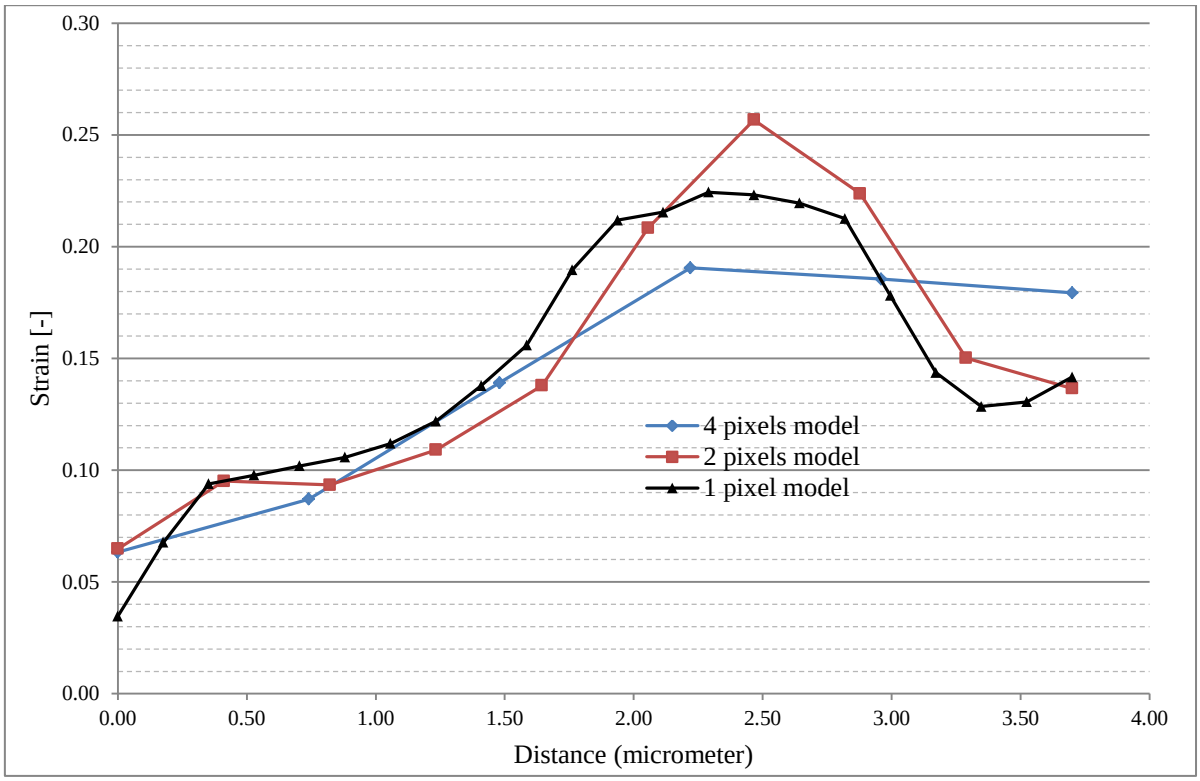

Figure 6-14: Maximum principal strain values extracted along the red line shown in Figure 6-13 for the microstructure models with different mesh element sizes

Results of strain distribution along the red line for the three models are shown in Figure 6-14. Both one pixel and two pixels element sizes show a better resolution of the local strain values. It is worth noting that the distribution is smoother as the element size is

reduced. However, the overall trend for the three models is similar. In addition, the computing time for one pixel element size model is four times the period required to run a model with element size of 4 pixels. Consequently, the models with mesh element size of 4 pixels will be used plastic deformation in the microstructure (section 6.2.2) while the models with one pixel element size will be utilised for damage analysis (section 6.2.3).

6.2.2 Plastic Deformation

At the beginning of this sub-section, phase properties are adjusted and then used for microstructure modelling. This is an important step, as the measured phase properties using fully martensitic and ferritic strips may differ from the actual properties of the phases in the microstructure of DP1000 steel. Real deformation vectors in the form of displacement values calculated from DIC measurements were used as boundary conditions for the microstructure simulation and the results were used to adjust phase properties by minimising the error between averaged stress from the simulation with the corresponding experimental true stress up to the UTS before damage is expected to start. Moreover, microstructure simulations were carried out to analyse and model deformation observed during the in situ test. Corrected phase properties were used in these simulations.

6.2.2.1 Phase Flow curves

To start the simulations, equation (1) was used to produce stress strain curves of the phases and the flow curves are shown in Figure 6-15.

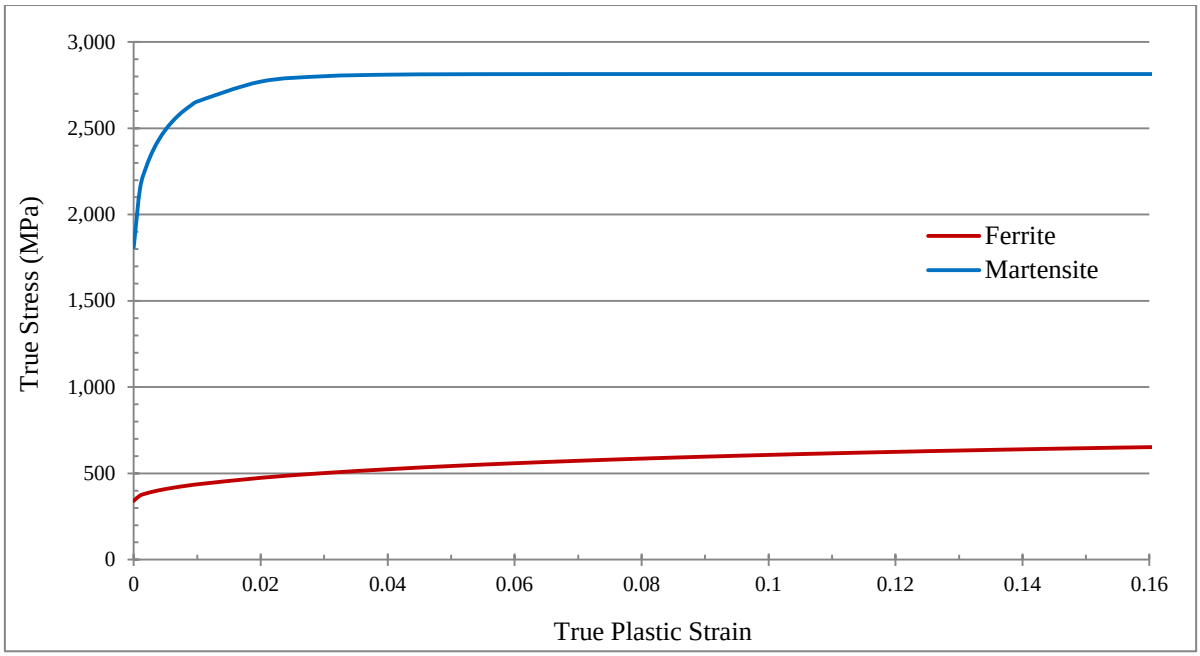

Figure 6-15: Stress/strain curves for ferrite and martensite generated using empirical model

As can be seen from Figure 6-15, the martensite can be said to be overestimated as compared to reported curves in the literature [10, 22] such as the curve shown in Figure 2-6. In the current research, another method was used to estimate the phase mechanical properties. The flow curves were measured from pure strips of fully martensite samples with high-carbon and fully ferrite samples with low-carbon, which were fabricated, and supplied by Tata Steel, to have a chemical composition and microstructure as close as possible to that of the individual constituents in the two-phase DP1000 steel. A modulus of elasticity was determined as 198 GPa for ferrite, while 182 GPa was measured for martensite, with a 0.3 Poisson's ratio for both phases. The tested strips gave flow curves that are shown in

Figure 6-16. As mentioned before, it is likely that the measured stress/strain response of pure phase specimens differ from that of the actual ferrite and martensite within the DP1000 material. Consequently, the curves should be calibrated before they can be used for accurate modelling.

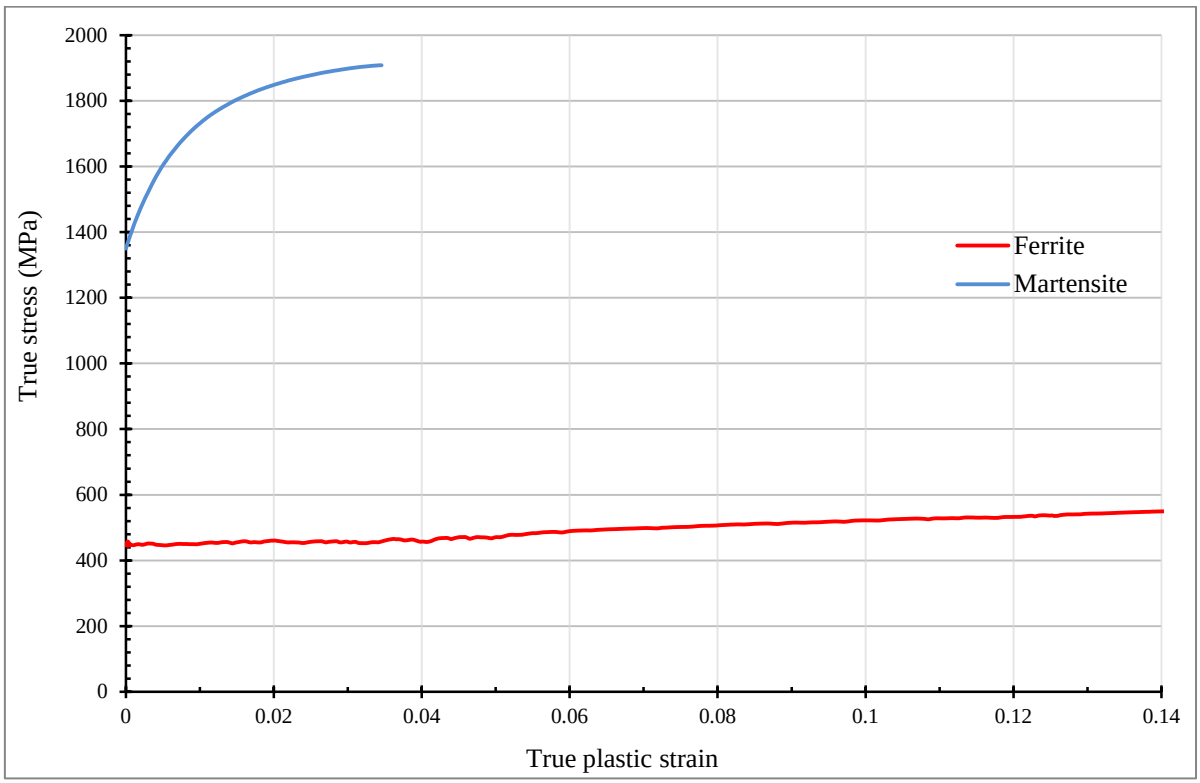

Figure 6-16: Flow curve response of fully ferrite and fully martensite specimens.

Microstructure simulation was used to calibrate phase properties by minimising the error between the averaged stress from the simulation and experimental true stress of the in situ test specimen. The model shown in Figure 4-4 (b) was fully constrained to adjust the phase properties to ensure that the model deforms in a similar way to the actual deformation of the DP1000 microstructure. Four deformed images were simulated for applied displacement values corresponding to stress values between the yield strength and the ultimate tensile strength as highlighted with blue circles in Figure 6-17.

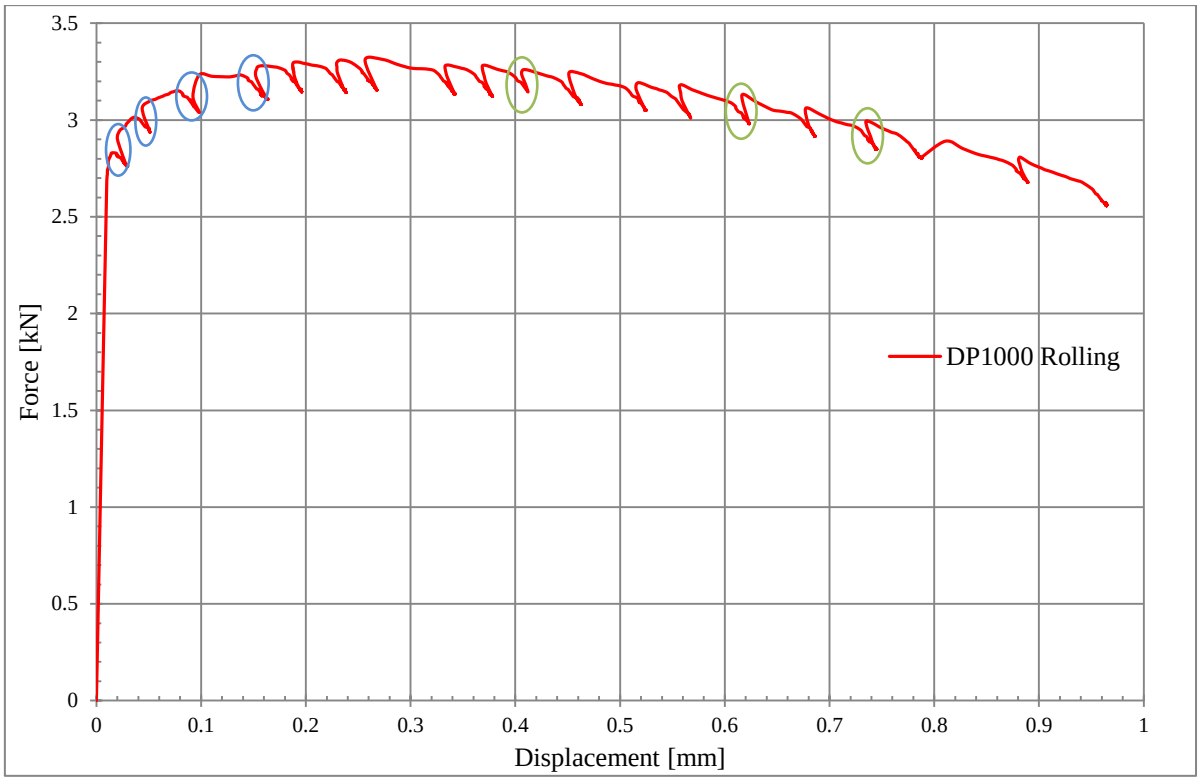

Figure 6-17: The four deformed states used to adjust phases' properties; highlighted with blue circles, and the three states used to examine crack propagation in martensite; highlighted with green circles on the load/displacement curve of DP1000 steels for the in-situ tensile specimen

The selected deformed images were chosen because no damage in the microstructure was observed, and therefore DIC results were considered reliable and not affected by damage sites in the microstructure. Equation (24) was used to average the stress values of the microstructure simulation in order to compare modelling results with experimental measurements of the true stress. The phase properties were adjusted with a trial and error method until acceptable errors were achieved between the experimental true stresses of the in situ specimen and the fully constraint microstructure averaged stress values. Table 6-2 illustrates the comparison between experimental true stresses and modelling averaged stress results with the percentage of error. As can be seen from the table, a maximum error value of less than 3% is recorded, which is relatively small and considered acceptable.

Table 6-2: Experimental true stresses of dog bone specimen (in situ specimen) compared to simulated average stress values of microstructure model during uniform elongation

applied displacement (mm)	0.04	0.08	0.15	0.18
True Stress (MPa)	1012	1076	1135	1153
Model Average Stress (MPa)	980	1045	1104	1132
Error (%)	3.2	2.9	2.7	1.9

Figure 6-18 shows the original mechanical properties of the DP1000 phases measured using pure martensitic and ferritic strips compared to the adjusted curves. The true stress and true plastic strain flow curves for the strips were first introduced in Abaqus to simulate the plastic deformation of the microstructure, along with the measured values of the modulus of elasticity and Poisson's ratio for the pure strips. As can be seen, small adjustment has been made to the ferrite response, while the majority of the adjustment was for martensite. The martensite phase response was also extrapolated artificially as the strips fractured at an applied plastic strain of around 3.8%. This was done to prevent Abaqus use a constant stress value for any element deformed beyond the measured plastic strain value at fracture.

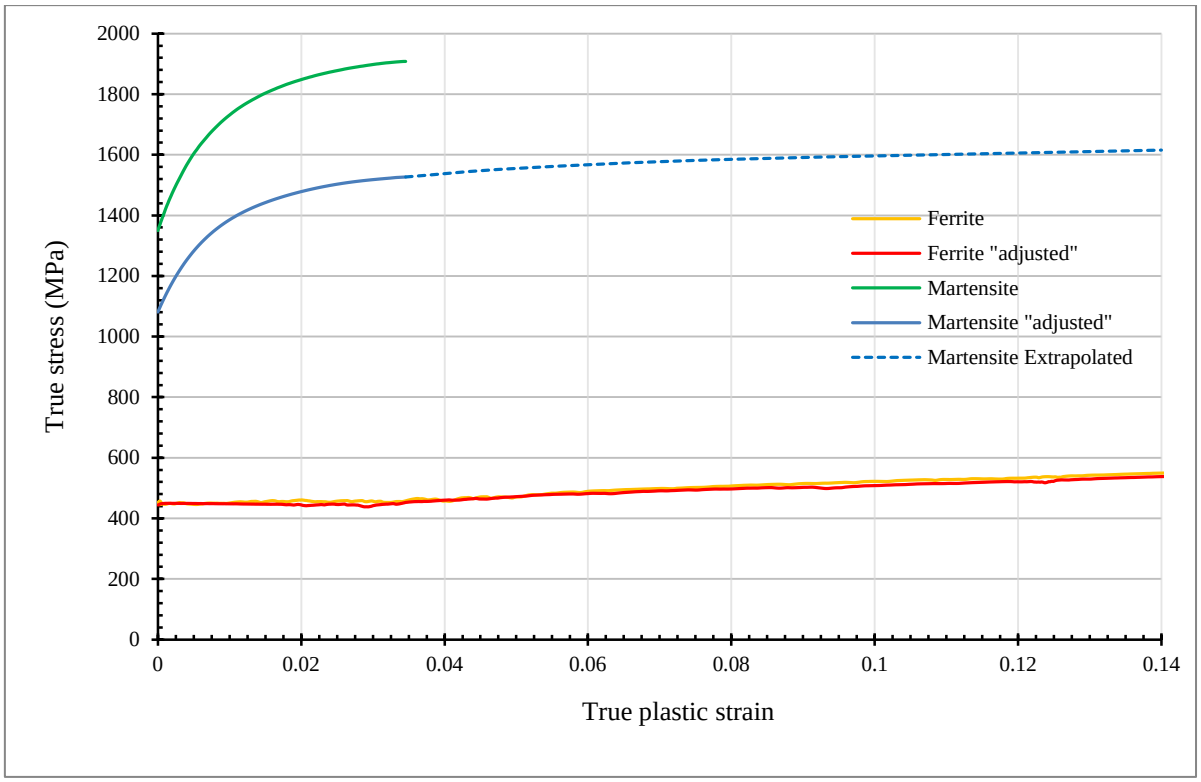

Figure 6-18: Mechanical response of fully martensite and ferrite strips plotted with adjusted phase properties used for microstructure modelling

Table 6-3 compares the error using the phase mechanical properties obtained directly from the strips and the adjusted mechanical properties of the DP1000 constituents. The pure martensitic and ferritic strips overestimated the actual mechanical response of the phases. This can be seen in Table 6-3 as the averaged stress values from the constraint microstructure model are bigger than the experimental true stress values. As can be seen from Figure 6-18, the adjusted curves of the phases were lower in comparison, resulting in a reduction of the error values below 3.2% for the four images reported in Table 6-3.

Table 6-3: Comparison between experimental true stresses and predicted stresses, with percentage of error, before and after adjusting mechanical properties of DP1000 phases

applied displacement (mm)	0.04	0.08	0.15	0.18
Experimental True Stress (MPa)	1012	1076	1135	1153
Before adjusting phase properties				
Model Average Stress (MPa) **[% of error]**	1104 [-9.1]	1104 [-2.6]	1119.5 [1.4]	1310 [-13.7]
Adjusted phase properties				
Model Average Stress (MPa) **[% of error]**	980 [3.2]	1045 [2.9]	1104 [2.7]	1132 [1.9]

6.2.2.2 Analysis and validation of Microstructure Simulation Results

The model shown in Figure 4-4 was run with boundary conditions applied only to the edges. These were extracted from the DIC vector measurements at an applied displacement of 0.22 mm at the UTS point. Overlaying the deformed model on the SEM image of the deformed microstructure was the first technique of validation, as described in Section 4.2. A good qualitative agreement was obtained, as illustrated in Figure 6-19. Small discrepancies can be observed in some areas and may relate to either the accuracy of the mesh in representing the real geometry of the phases in the undeformed SEM image or errors in the response of the model. For better comparison, the second validation technique described in Section 4.2 was utilised. The second technique gave quantitative analysis and was therefore preferred over the visualisation method. The percentage of errors between the DIC displacement vector measurements and the modelling results was calculated over the analysed area using the code described in section 4.2.

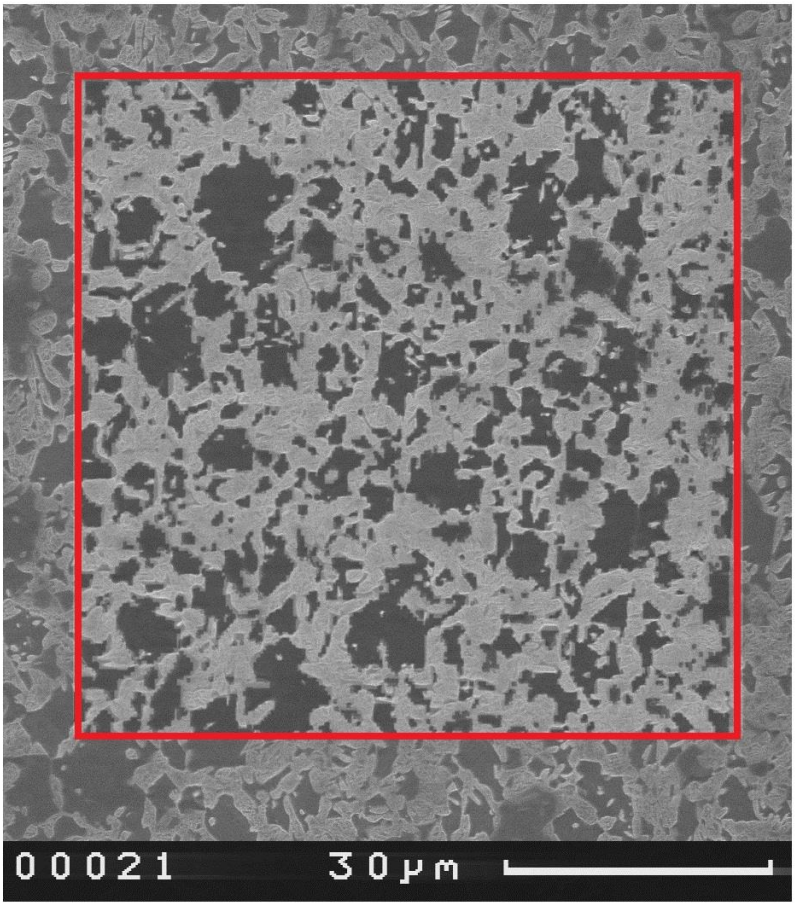

Figure 6-19: SEM image of deformed microstructure overlaid on the modelling result (highlighted by red box) at applied displacement of 0.22 mm

Figure 6-20 shows the comparison between the DIC interpolated displacement vector results and the displacements calculated at the nodes in the model. The plot was generated by a MatLab code written for this purpose. As can be seen from the figure, a maximum error of 6% was recorded locally. The error map was overlaid on top of the SEM image of the microstructure, as shown at the bottom of Figure 6-20. An investigation of the areas of error in relation to the microstructure did not show any preferable locations. However, it can be noticed that some of the errors were located near the interface of ferrite and martensite in regions of large ferrite grains.

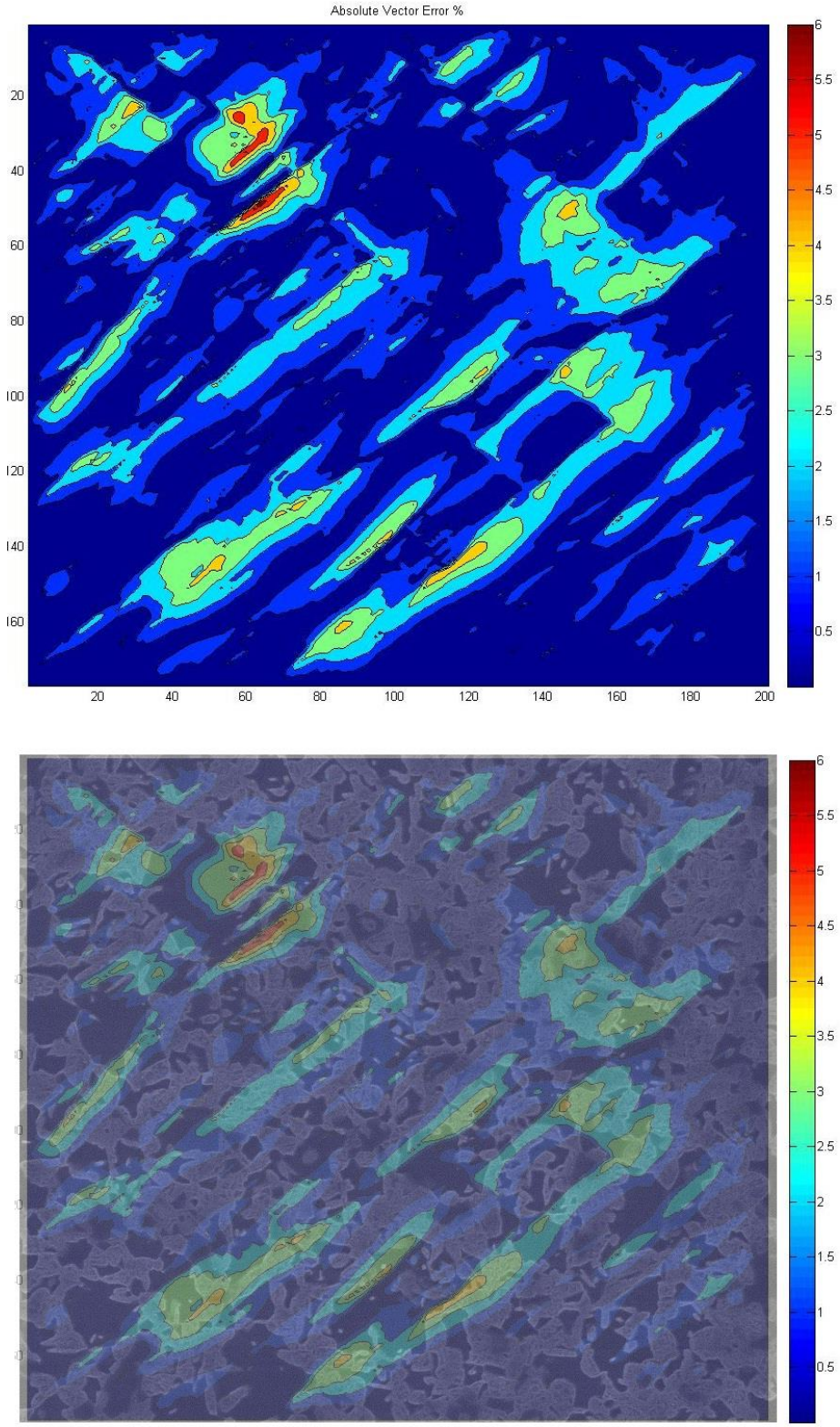

Figure 6-20: Comparison between DIC interpolated displacement vector results and modelling results at nodes (top) and overlaid on SEM image of the microstructure (bottom)

It is most important to compare the strain map of the microstructure modelling to the DIC results. Figure 6-21 (a) shows the DIC map of the strain in the loading direction (i.e. ε_{yy}, which is vertical in the figure) for an applied displacement of 0.22 mm. The strain map is overlaid on the microstructure with a dark ferrite phase and bright martensite phase. The strain map in the y-direction (i.e. loading direction; vertical in the figure) of the microstructure modelling was also overlaid on the microstructure, and is shown in Figure 6-21 (b). The predicted modelling map is comparable in complexity to the DIC strain map. On the other hand, it can be noticed that there are a number of differences between the two maps and, for quantitative comparison, the percentage of differences between the DIC and modelling strain maps were plotted in Figure 6-21 (c). A maximum value of 5% of difference was recorded between the two maps. The percentage of differences was overlaid on the SEM image of the microstructure in order to investigate the cause or preferable location of the discrepancies. However, there was no particular correlation between the areas of maximum difference and their locations in the microstructure.

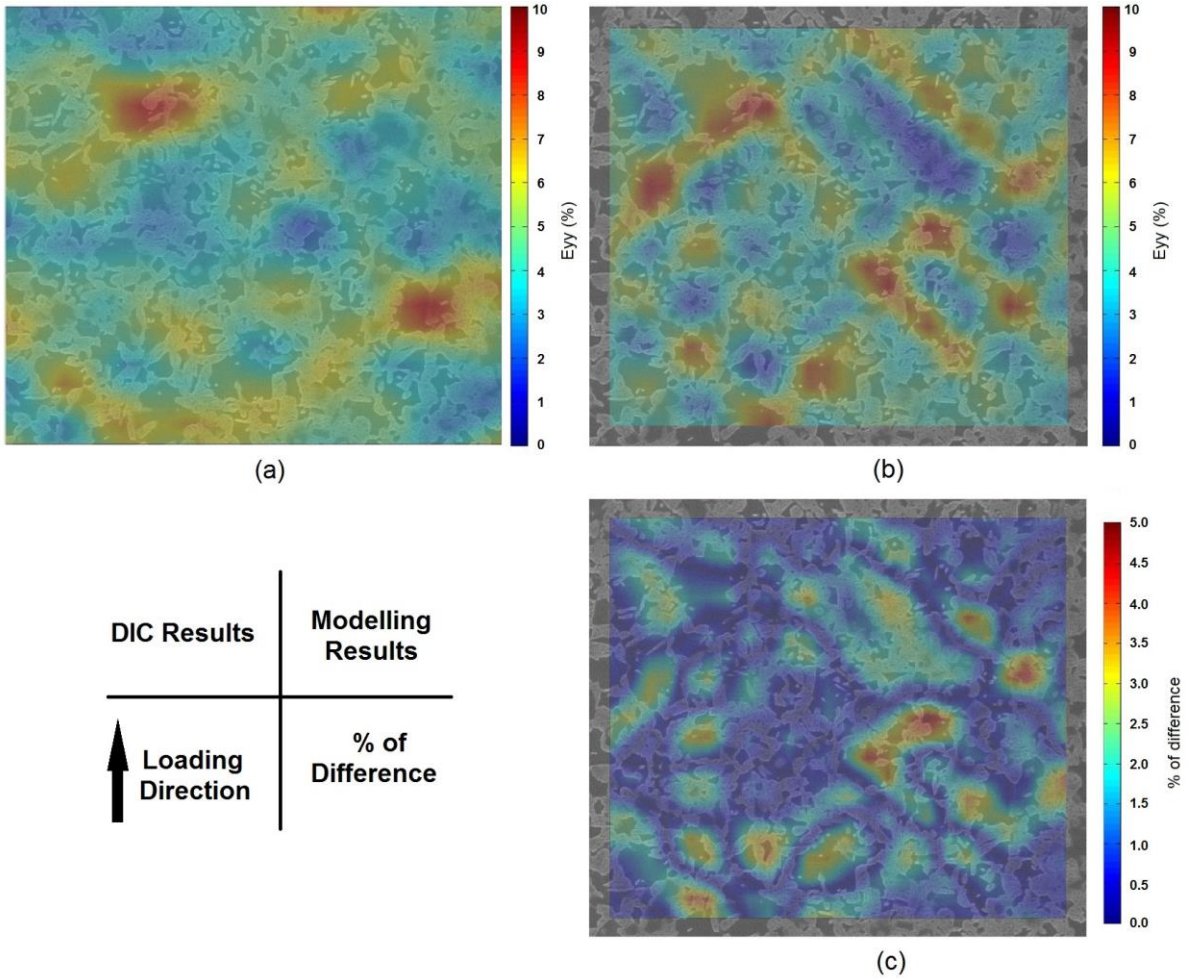

Figure 6-21: Maps of strain in loading direction overlaid on SEM microstructure of DP1000 steel for: (a) DIC results, (b) microstructure simulation results, and (c) percentage of difference between DIC and modelling strain results; loading direction is vertical, shown with black arrow and results obtained at applied displacement of 0.22 mm

Figure 6-22 illustrates the frequency distribution of the DIC and modelling strain results that were shown in Figure 6-21. As can be seen, the distributions of modelling results were comparable to those of the DIC calculations. The DIC median of the strain in the Y-direction was 4.5% and the standard deviation was 1.19. Likewise, the median strain of the microstructure simulation was 4.3% while a standard deviation was 1.58. The comparison, which also includes maximum and minimum strain values, is summarized in Table 6-4. The percentage of error is about 4% between the DIC median value and modelling median value

for the strain results in the loading direction. A local average strain of 4.56% was calculated experimentally for the analysed microstructure area and the value matches the median value of local DIC strain distributions (4.5%).

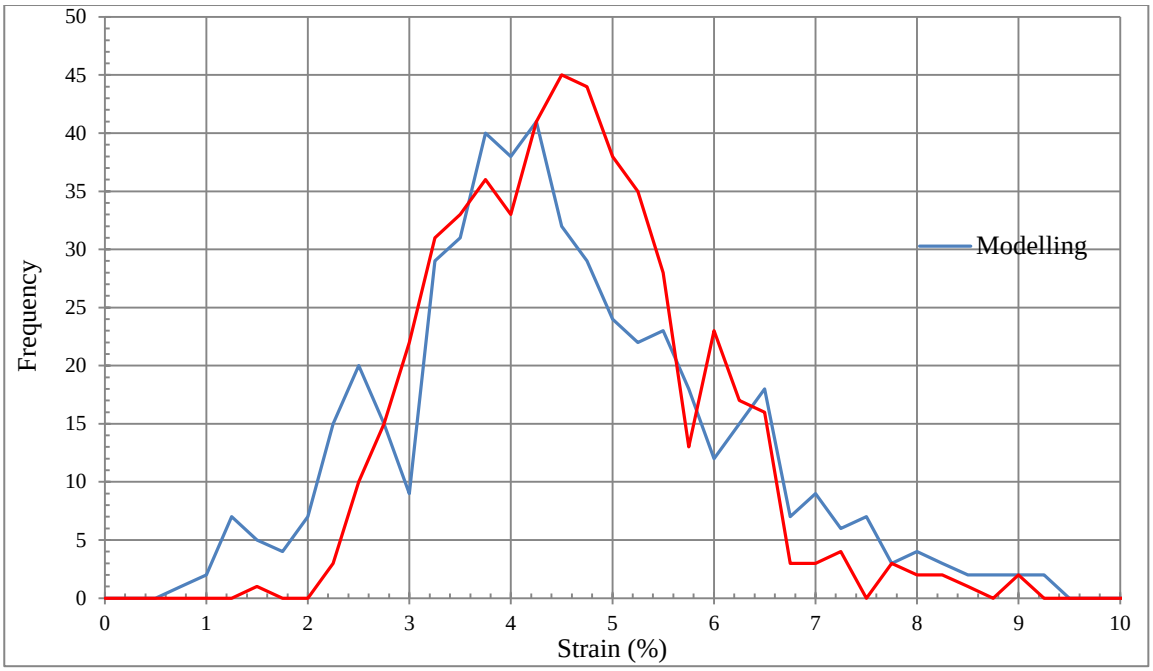

Figure 6-22: Frequency distribution of DIC results (red) and microstructure simulation results (blue) for strain in loading direction at applied displacement of 0.22 mm

Table 6-4: Comparison between DIC and modelling main values of strain distribution, as shown in Figure 6-22

	DIC results	Modelling Results
Median (%)	4.5	4.3
Standard Deviation	1.19	1.58
Maximum strain (%)	9.1	9.3
Minimum strain (%)	1.6	0.8

Microstructure simulation was used in order to investigate the stress distribution in the microstructure in relation to the results shown in Figure 5-12 in Section 5.3, which showed the strain results and distribution in the phases of DP1000 steel for an applied displacement of 0.32 mm, for which no damage appeared on the surface. The simulation results of the model are shown in Figure 6-23 (a) and analysed to give the frequency distribution of stress values in DP1000 constituents in Figure 6-23 (b). For an applied displacement of 0.32 mm, the von Mises stress distributions in martensite were very different from those in ferrite, in contrast to strain results. The stress distributions shown in Figure 6-23 (b) suggest that stress values in ferrite are about one third smaller than those in martensite. The mean stress value for ferrite is about 505 MPa, as opposed to about 1535 MPa for martensite. A standard deviation of 14 was calculated for the ferrite stress distribution, which was larger than the standard deviation of 4 for the martensite distribution. This clearly indicates that stress distribution in the softer phase of DP1000 steel is distinctly more heterogeneous.

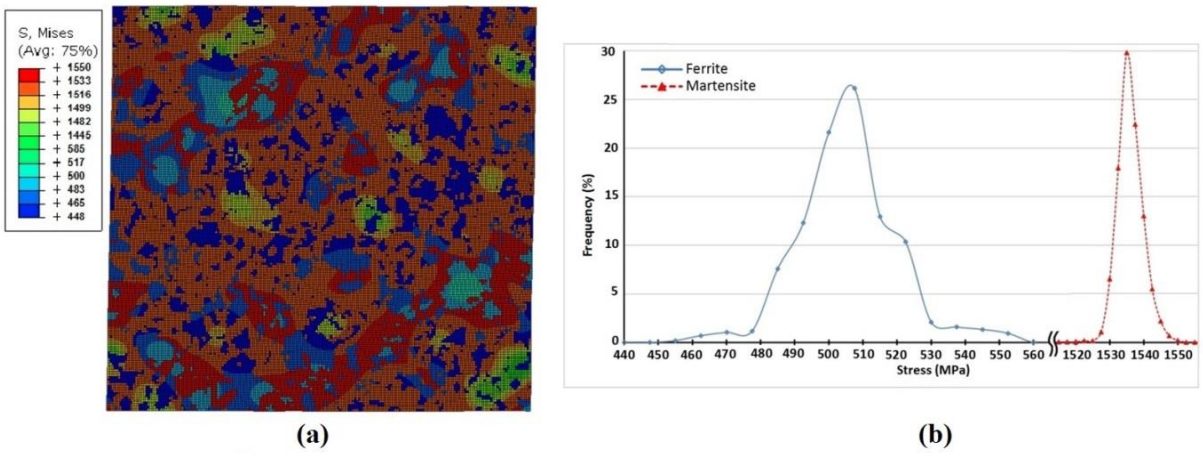

Figure 6-23: (a) Microstructure modelling results of Von Mises stress and (b) distribution in phases for DP1000 at applied displacement of 0.32 mm

6.2.3 Damage Analysis

Microstructure simulation was used to investigate the martensite crack initiation locations, as observed in section 5.2. After this, a criterion is suggested following the unique technique developed in this research that combines DIC results and microstructure simulation. Moreover, combining DIC results and microstructure simulation helped the process of predicting microstructure deformation and adjusting the Gurson parameters of the ferrite phase which will be used in the RVE modelling to be presented in Section 4. Then, the effect of the damage models for both phases on stress predictions was investigated.

6.2.3.1 Damage Development in Martensite

Microstructure simulation was utilised for damage analysis of the martensite cracking that was clearly observed in three areas, as shown in Figure 5-6. Figure 6-24 shows the generated finite element meshes of the three areas and the actual SEM images, with the location of the damage highlighted by yellow lines.

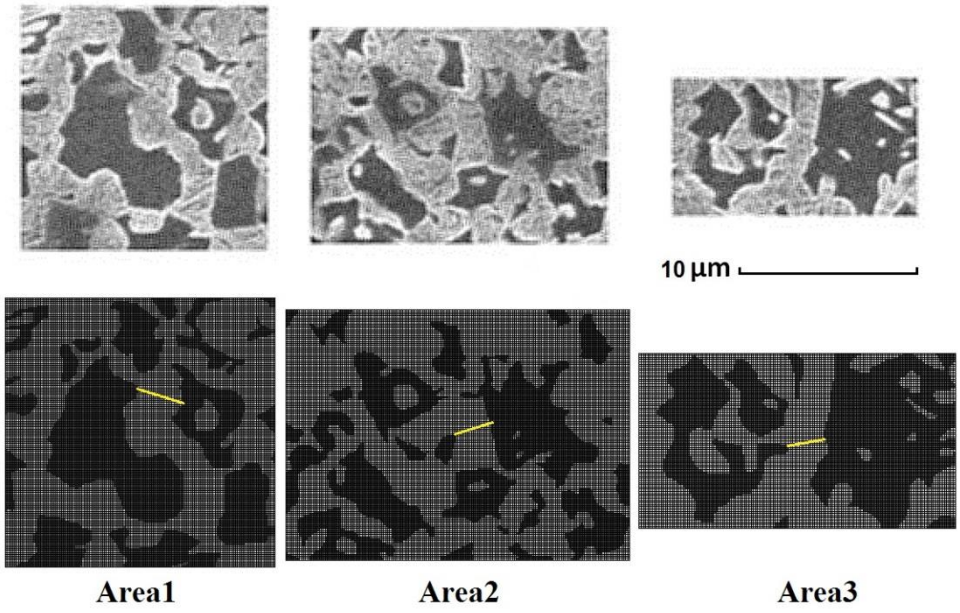

Figure 6-24: Three microstructure models (bottom) produced from SEM images (top) to investigate the deformation state of martensite islands before onset of damage, highlighted with yellow lines.

The martensite islands in these three areas were the regions where first damage sites were observed in the DP1000 microstructure at an applied displacement of 0.36 mm. Consequently, an applied displacement of 0.32 mm was chosen in the simulations, in order to investigate the stress and strain distributions in the microstructure just before damage appeared in martensite and possibly suggest a criterion for damage nucleation in the martensite phase of DP1000 steels. The aim of the modelling was indeed to investigate the local strain and stress state that might have initiated cracking in the martensite phase.

Experimentally, it was observed that initiation began at the interface between ferrite and martensite. Consequently, it is expected that the local state of strain or/and stress at or near the interface were responsible for initiating cracks in the martensite. Figure 6-25 shows the simulation results in the martensite only for the strain component along the tensile direction (vertical in the figure) ε_{22} (Figure 6-25 (a)) and for the maximum principal stress distribution (Figure 6-25 (b) and Figure 6-25 (c)).

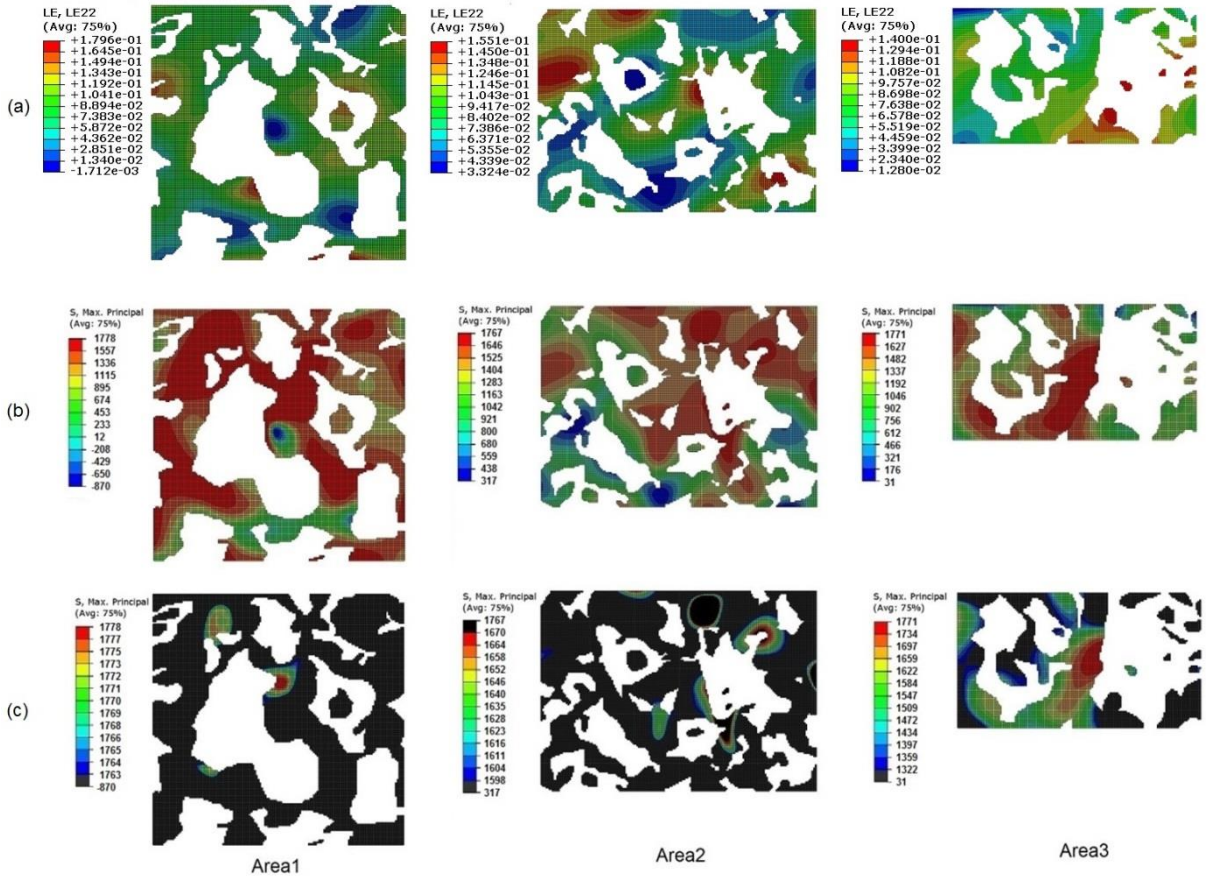

Figure 6-25: Microstructure modelling results of three areas of interest shown in Figure 6-24 for: (a) ε_{22} strain results (axis-2 along the loading direction, vertical in the images) and (b) maximum principal stress results; Stress levels were adjusted in (c) to clearly show the location of maximum principal stress values

At the location of martensite cracking highlighted with yellow lines in Figure 6-24 for the three areas, Figure 6-25 (a) shows that ε_{22} values range from 8.6 % in area 3 to 14 % in area

2. Therefore, it can be concluded that there is no particular correlation between martensite crack initiation sites and local strain values. All other strain values (i.e. strain in the X-direction, maximum principal, minimum principal, and shear strain) have been checked, and no correlation could be found either. Stress results were also checked following the same process as for strain values. Unlike strain results, as can be noticed from the maximum principal stress results shown in Figure 6-25 (c), especially for area 1 and area 3, the highest value is located where a crack appeared during the in situ tensile test. According to the FE results for area 2, there may be more than one site where a possible crack could have happened. Although a crack appeared at one of the sites, the third dimension effect that was not taken into account in the modelling might be accountable for the selected location of crack initiation. The maximum principal stress values situated close to the crack locations in the martensite near the interface with ferrite were all remarkably comparable. The values for area 1, 2 and 3 were 1771 MPa, 1670 MPa and 1722 MPa, respectively. As a result, a critical maximum principal stress value of 1700 MPa is proposed for damage initiation in the martensite phase of the DP1000 steel.

As discussed earlier in section 4.2, forming limit stress diagram (FLSD) criterion can be utilised in Abaqus to simulate crack propagation as the initiation study showed that damage in martensite is stress controlled. With FLSD criterion, one can set a critical maximum principal stress value that will be examined against the maximum principal stress state of the element for every load step. Then, the condition ‘ω’ will be calculated as follows:

$$\omega = \frac{\sigma_{element}^{maximum\ principal}}{\sigma_{critical}^{maximum\ principal}} \quad (28)$$

Once the condition 'ω' reaches a value of unity, the initiation is met and sudden drop of the element load is set.

As for the simulation of damage development in the martensite phase, the proposed damage nucleation criterion and FLSD procedure were utilised to initiate damage in the martensite phase. A maximum principal stress value of 1700 MPa was set as critical maximum principal stress in the FLSD criterion. Once a martensite element reached the critical value, the load capacity of this element is then reduced to zero. The element is not removed from the mesh but has no load-bearing capacity. The three states highlighted with green circles in Figure 6-17 after the UTS were examined using a fully constrained simulation method for the model shown in Figure 4-4. The results are illustrated in Figure 6-26, alongside the SEM images of the deformed microstructure for applied displacement values of 0.4, 0.61 and 0.72 mm. The martensite cracking is highlighted with red circles in the SEM images and with white lines in the microstructure models. As can be seen from the figure, the blue elements correspond to the elements in which the damage criterion has been met at the initiation stage or after some extent of crack propagation, and thus their stress values are reduced to zero.

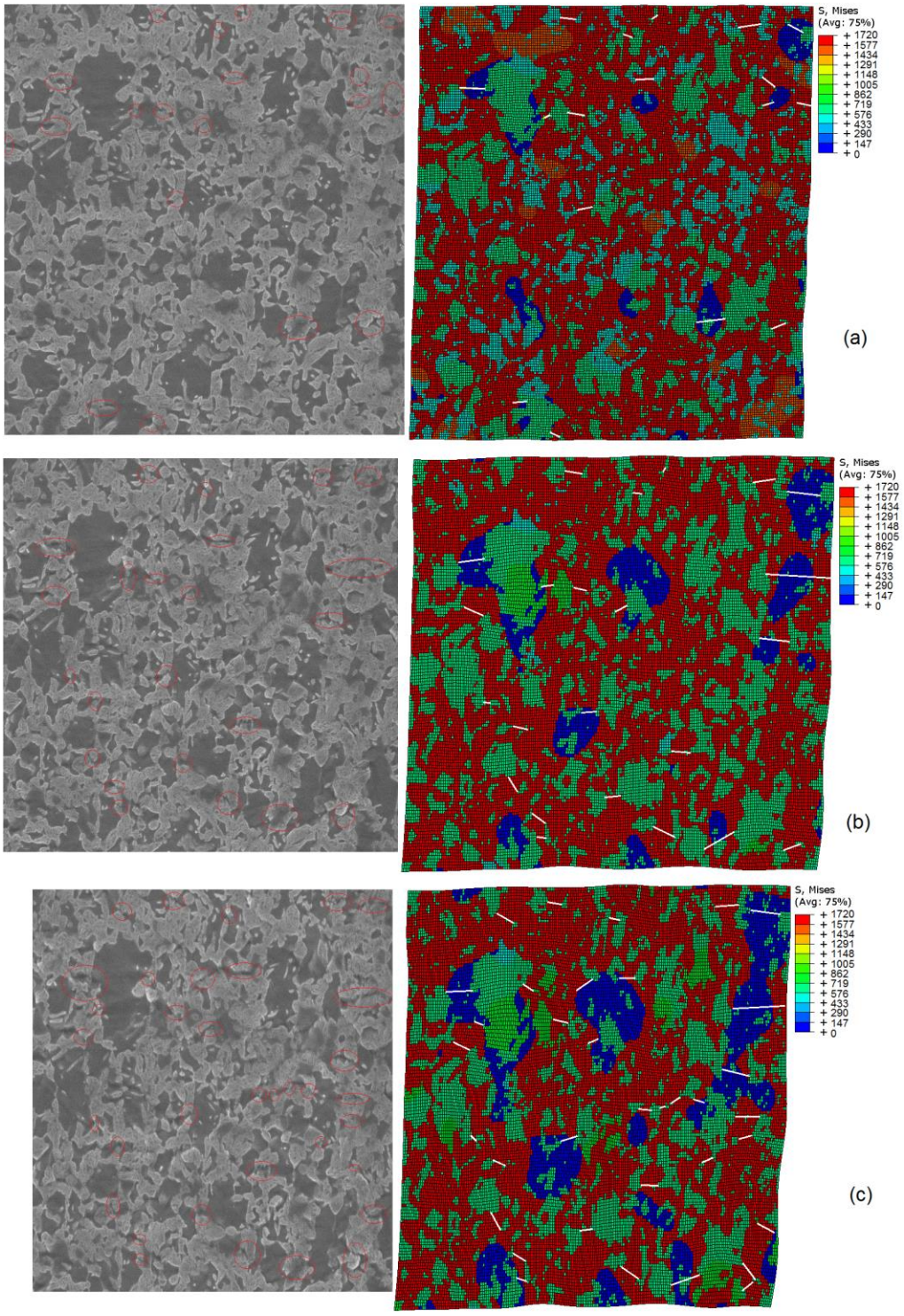

Figure 6-26: SEM images of DP1000 microstructure with broken martensite particles highlighted with red circles (left) and sites of martensite with zero stress shown in blue in the modelling results (right) for applied displacement values of: (a) 0.4, (b) 0.61 and (c) 0.72 mm. White lines are location of broken martensite particles in the SEM images

The results shown in Figure 6-26, which clearly show large discrepancies between modelling prediction and experimental measurements, are summarised in Table 6-5, which compares the number of cracked martensite islands and the total number of sites with zero stress in the modelling results, along with the number of sites captured correctly. As can be noticed from the table, around one third of cracked martensite islands were captured by the simulation for all three states of deformation. The number of sites in the model is therefore lower than the number of cracked martensite particles observed experimentally, with the model predicting a large number of failed elements leading to a fractured area much bigger than the actual observed crack area. Possible reasons for this discrepancy between the model and actual microstructure include the method to simulate crack in the martensite phase using FLSD that suddenly drop the load capacity of the element, and a lack of physical basis for crack propagation simulations in terms of local toughness, an effect of the element size which should be much more refined around a crack tip as well as the two-dimensionality of the model.

Table 6-5: Comparison between cracked martensite particles in microstructure based on SEM images and sites of martensite elements with zero stress in models, as shown in Figure 6-26

applied displacement (mm)	0.4	0.61	0.72
Number of cracked martensite islands in the microstructure	17	23	35
Number of areas in the model which predict correctly the sites of cracked martensite in the microstructure	5	7	12
Total number of zero stress areas in the model	14	16	25

Summary: this section has clearly shown the new knowledge gained in understanding damage nucleation in DP1000 by combining in a unique manner DIC measurements of the deformation of the microstructure and microstructure simulations. By applying measured displacements as boundary conditions over the entire simulation area in the model a nucleation criterion for damage initiation in martensite has been established for the first time. Results from the extension of the model to crack propagation have however shown the limitations of the current model in predicting the correct martensite fractured area in comparison with experimental results and further investigation would therefore be needed.

6.2.3.2 DP Microstructure Simulation

The microstructure model shown in Figure 4-4 was also utilised to calibrate the Gurson model parameters to be used to predict damage in the ferrite phase for the RVE models. However, the Gurson model parameters had to be tuned to reduce the error between the stress values calculated from the microstructure simulations and the experimental true stresses. Table 6-6 summarises the comparison between experimental true stresses and averaged modelling stress values for four different models used to simulate four damage states beyond the UTS point. The table also shows the percentage of error, in which a negative sign is an indication of stress prediction being overestimated, as compared to experimental true stress.

Table 6-6: Comparison between experimental true stresses at different applied displacement and predicted averaged stress results from microstructure simulation with different damage models introduced to model

applied displacement (mm)	**0.22**	**0.4**	**0.61**	**0.72**
Experimental true stress (MPa)	1160	1295	1344	1348
Averaged modelling Stress (MPa) No damage models [error]	1215 [-4.7%]	1315 [-1.5%]	1384 [-3.0%]	1405 [-4.3%]
Averaged modelling Stress (MPa) Martensite damage model only [error]	1214 [-4.7%]	1313 [-1.4%]	1381 [-2.7%]	1353 [-0.4%]
Averaged modelling Stress (MPa) Ferrite damage model only [error]	1187 [-2.3%]	1286 [0.7%]	1354 [-0.7%]	1368 [-1.5%]
Averaged modelling Stress (MPa) Damage models for both phases [error]	1187 [-2.3%]	1271 [1.9%]	1323 [1.6%]	1313 [2.6%]

At the beginning, no damage models were used for the DP1000 constituents. The results are listed in the third row and show a gradual increase in estimated stress values as the applied displacement increased. The percentage of error in predicting true stress increased from -0.4% to -4.3%. Next, the critical maximum principal stress value of 1700MPa was used to initiate damage in the martensite. Any martensite element reaching the critical value had its load-bearing capacity reduced to zero. The results of the microstructure model were shown in Figure 6-26 and a comparison between averaged stress and experimental true stress is listed in the fourth row of Table 6-6. The error results were reduced slightly but they still showed that the predicted stresses were overestimated. Consequently, a damage model in the ferrite was required in order to obtain a better stress prediction using microstructure simulation. The Gurson model was introduced to the ferrite phase and the parameters were adjusted to best fit the experimental true stress value. The sixth row in Table 6-6 shows the comparison between averaged modelling stress results and experimental true stresses. A reasonable prediction was achieved, with a maximum error of 2.6%. Table 6-7 reports the adjusted Gurson's parameters for this last simulation (the values of GTN parameters for the in situ specimen of the full model reported in Table 6-1 were initially used). These parameter values were subsequently used for the RVE simulation.

Table 6-7: Adjusted Gurson's parameters using microstructure simulation

Gurson Parameters	f_N	ε_N	S_N	q_1	q_2
Adjusted value	0.04	0.11	0.5	1.1	0.9

In order to check the effect of the Gurson model in the ferrite phase on the prediction of experimental true stress, microstructure simulations were also run with no damage model introduced to the martensite phase and only GTN was used for the ferrite phase. The results are shown in the fifth row in Table 6-6. Compared to the stress prediction obtained with no damage models, the use of the Gurson model resulted in a steady reduction of the predicted stresses. However, the stress prediction for the states near the fracture point was still overestimated.

Figure 6-27 shows the stress triaxiality ratio distributions in the ferrite phase in the microstructure model shown in Figure 4-4 (b) for the three deformation stages at applied displacement values of 0.22, 0.4, and 0.61 mm. The stress triaxiality was calculated using equation (25). These states were used to adjust the Gurson parameters of the ferrite phase in the microstructure model. As can be seen, the triaxiality ratio values range from -0.4 to 0.5. Negative triaxiality stress relates to uniaxial compression while zero triaxiality represents shear condition. Positive ratios can lead to two different states: around 0.3, the element is under uniaxial tension which is similar to the situation in smooth specimens; whereas a 0.6 value leads to biaxial tension, as in the case of notched specimens [66]. Therefore the 2D microstructure modelling for the three deformation states investigated covers a wide range of different stress triaxiality situations: compression, shear, and tension, all in one model.

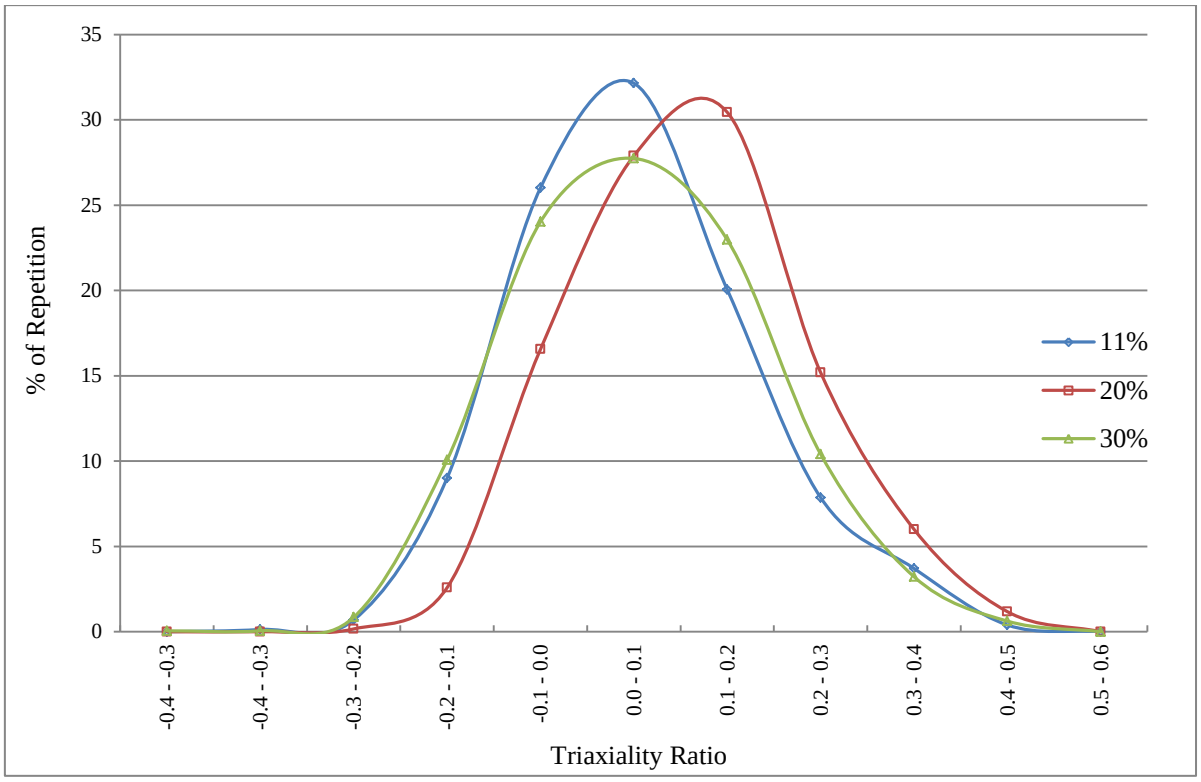

Figure 6-27: Stress triaxiality ratio distribution from microstructure simulation used to adjust Gurson parameters at three applied displacement of 0.22, 0.4 and 0.61 mm

6.3 RVE-Based Damage Modelling

Two dimensional (2D) and three dimensional (3D) Representative Volume Element (RVE) models were used to predict the stress/strain curves of DP1000 steels. The boundary conditions extracted from the central element with maximum deformation in the specimen model (section 6.1.2) were applied to the RVE model. For the 2D RVE the boundary conditions were applied to the edges, whereas for 3D RVE the boundary conditions were applied to the outer surfaces. The RVE average stresses were compared to the true experimental stresses. The first section shows the results for the RVE models for the in situ tensile specimen. The second section focuses on the comparison between RVE average stress values and experimental stresses for the standard geometry specimen and notched bar. Finally, the results of 3D RVE prediction in terms of stress/strain curves are shown.

6.3.1 RVE Results for In Situ Tensile Test Specimen

Representative volume element (RVE) models, shown in Figure 4-9 and Figure 4-10, were used to predict the stress values at different deformation states for the in situ tested specimen. The deformation states are highlighted in Figure 6-28 (a) with blue ovals at applied displacement values of 0.08, 0.18, 0.22, 0.4 and 0.61 mm. The boundary conditions in the form of displacement vectors were extracted from the element at the mid-central region of the in situ specimen model, as shown in Figure 6-28 (b) (Note that the full model was cut in half in order to show the element in the mid-central region).

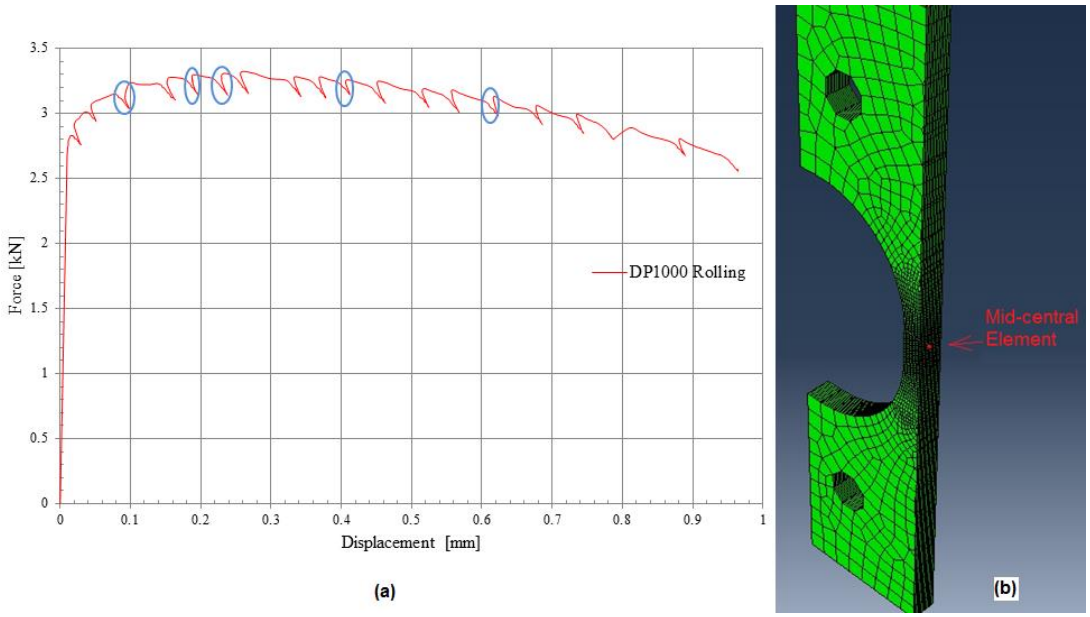

Figure 6-28: (a) Load/displacement curve of in situ test and selected deformation states in blue ovals to conduct RVE stress prediction, and (b) element at mid-central region of in situ specimen model chosen to extract boundary conditions used for RVE models

From now on, the 3D RVE model with 20 elements along each edge will be named 3D RVE 20, whereas the 3D RVE model with 30 elements along the edges will be called 3D RVE 30. Equation (24) described in Section 4.2 was used to average the stresses from the model results. As the element was in the mid-central region of the model, plane strain condition

was used for the 2D RVE. The average stress results of the 2D RVE are shown in the third row of Table 6-8. The averaged stress values from 2D RVE are compared with the corresponding true experimental stresses in order to examine the prediction of the macro-response of the material using the micro-model. The percentage of error is calculated and listed in Table 6-8 in the square brackets. As can be seen, the maximum percentage of error was 12% in the hardening part of the curve. As the deformation increased, the predicted stresses improved and were close in value to the experimental true stresses.

Table 6-8: Comparison between experimental true stresses of in situ tensile test and RVE models; 2D RVE, 3D RVE 20 and 3D RVE 30, with percentage of errors

applied displacement (mm)	**0.08**	**0.18**	**0.22**	**0.4**	**0.61**
Experimental true stress (MPa)	1087	1153	1160	1295	1344
2D RVE average stress (MPa) [error]	958 [12%]	1084 [6%]	1115 [4%]	1253 [3%]	1370 [-2%]
3D RVE 20 average stress (MPa) [error]	978 [10%]	1056 [8.4%]	1081 [6.8%]	1224 [5.5%]	1234 [6%]
3D RVE 30 average stress (MPa) [error]	976 [10%]	1057 [8.4%]	1083 [6.6%]	1223 [5.6%]	-

To compare the prediction of experimental true stress, the 3D RVE 20 model was used for the same deformation states as for the 2D RVE. The results of the 3D RVE 20 simulations are listed in the fourth row of Table 6-8, in terms of the average stress results from the model and the percentage of error between the predicted stresses using 3D micro-model and the experimental true stresses at the macro-scale. Equation (24) described in Section 4.2 was also used here to average the stresses from the 3D models. It can be seen from the table that the maximum error in 3D RVE 20 prediction was 10%. In addition, the differences tended to be small between the predicted averaged stresses from 3D RVE 20 and the experimental true

stresses. The maximum percentage of error was smaller with 3D RVE 20 than with the 2D RVE. In order to check the mesh refinement effect on 3D RVE prediction, the number of elements along the edges was increased from 20 to 30 elements. The results of 3D RVE 30 are shown in the fifth row of Table 6-8. As can be noticed, the results were similar, with less than 0.2% difference. Consequently, the 3D RVE 20 was chosen to predict stresses for the standard and notched specimens.

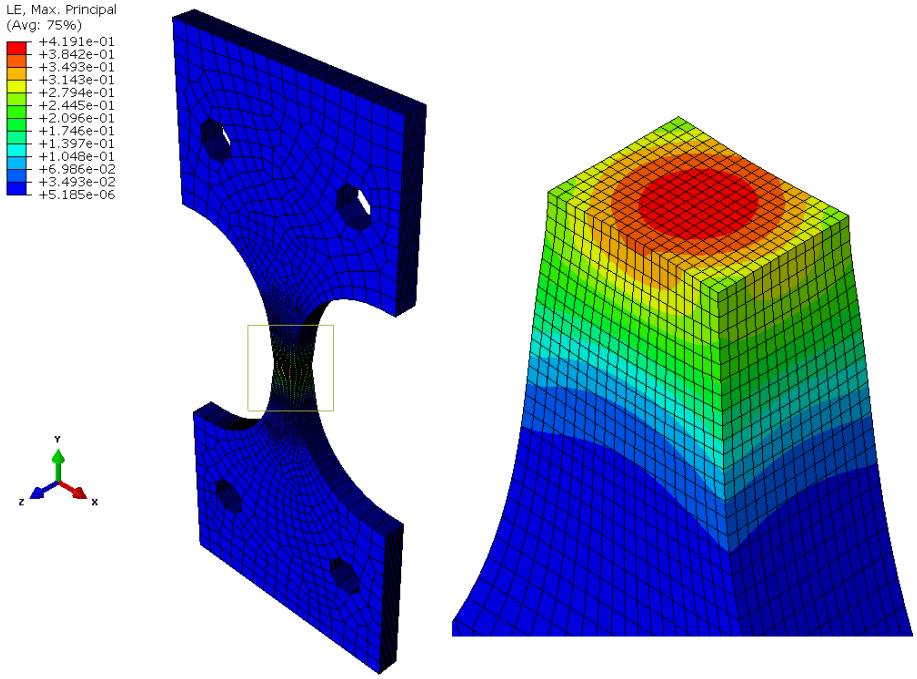

Figure 6-29: Strain results in the necking region of in situ tensile model during the softening part of the load/displacement curve

Figure 6-29 shows the strain distribution in the necking region of the in situ tensile specimen model for an applied displacement of 0.61 mm. As can be noticed, the strain at the edges was around 0.27, whereas at the centre of the necking region the strain was 0.419. A factor of 1.5 was therefore calculated for the difference between strain values at the edges and in the central region of the necking region. As a result of an almost square cross-section of the in situ specimen, the distributions were relatively uniform across the section with localised

strain were gradually reducing towards the edges in a similar way in all directions. This result will be used in the following subsection to compare the strain distribution after the UTS and their effect on RVE stress prediction.

6.3.2 RVE Results for Standard and Notched Specimens

Similar procedures were followed to predict the stress response of standard and notched specimens (at macro-scale) with 3D RVE 20 (micro-scale simulations) that utilised the Gurson model with parameters calibrated using microstructure simulations. The boundary conditions (BC) in the form of displacement values were extracted from the mid-central element of the standard and notched specimen at the macro-scale models and applied to the micro-scale models. The procedure of extracting the BC is explained in section 4.3. The elements used to extract the BC are shown in Figure 6-30 for standard and notched specimen models.

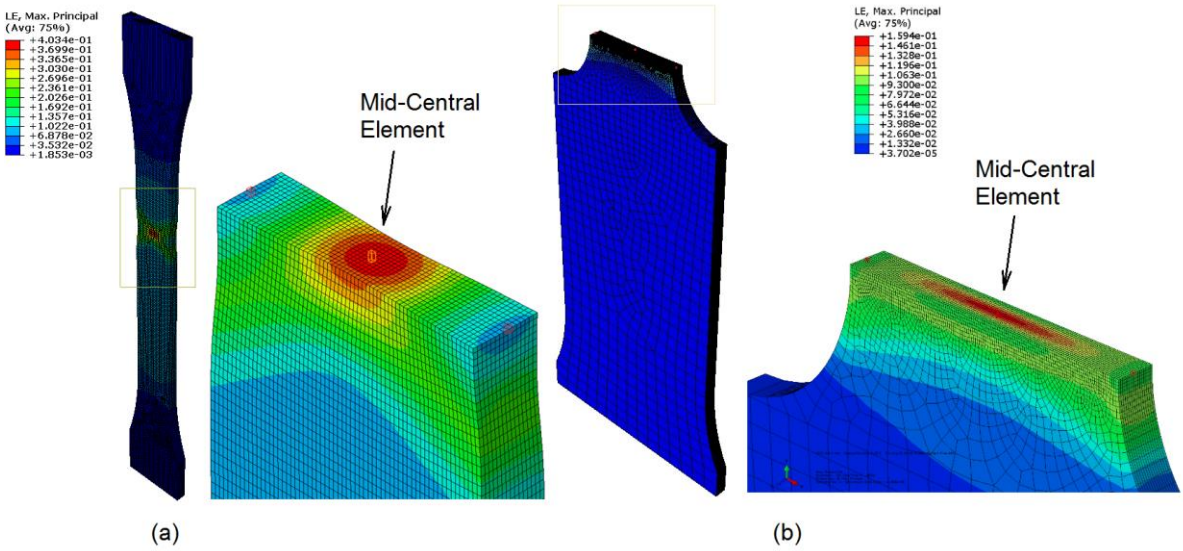

Figure 6-30: Mid-central element used to extract boundary conditions for 3D RVE models of (a) standard geometry model, and (b) notched specimen model

For standard geometry specimen, the three deformation states selected for stress prediction using 3D RVE 20 were as follows: in the hardening region, at the UTS, and in the softening region of the load displacement curve, as shown in Figure 6-31 (a) with blue ovals. These states were chosen as they are representative of the transition between pure plastic

deformation and then damage in the tensile tests for a ductile material and to check the ability of the 3D RVE 20 model to predict the overall stress/strain curves. The comparison between experimental true stresses at macro-scale and the predicted average stress values from 3D RVE 20 at the scale of microstructure are listed with the percentage of error in the third row of Table 6-9. The mesh refinement was also checked for this specimen geometry, using the 3D RVE 30 model for the deformation states corresponding to the hardening phase and at the UTS. The results for 3D RVE 30 are listed in the fourth row with the percentage of error in Table 6-9. The percentage of error, during the hardening part of the curve, was less than 10% and, at the UTS, less than 9% for both 3D RVE 20 and 3D RVE 30 models. A similar trend is therefore observed for this geometry; in comparison with the results of the in situ test model prediction as far as mesh refinement is concerned. There was no significant difference between the two models in terms of stress prediction; and consequently 3D RVE 20 was only chosen for the simulation of the softening phase, as the computing cost was much lower i.e. 3D RVE 20 models were five times faster than 3D RVE 30 models.

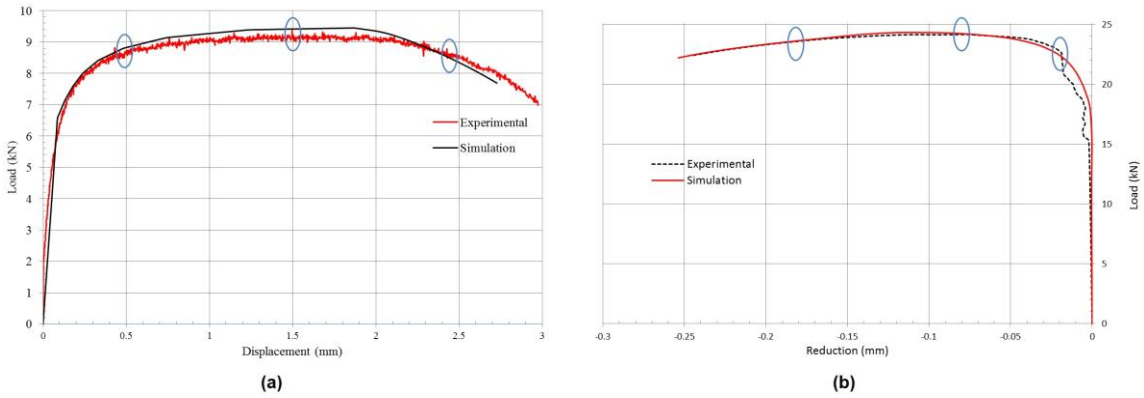

Figure 6-31: Experimental and modelling load/displacement and load/reduction curves of (a) standard geometry, and (b) notched bar; blue ovals are locations where boundary conditions were extracted for three deformation states: in the hardening region, at the UTS, and in the softening region

Table 6-9: Comparison between experimental true stresses and predicted averaged stresses of 3D RVE for the standard geometry for three states of deformation

Standard specimen deformation state (mm)	Hardening (0.5)	UTS (1.5)	Softening (2.4)
Experimental true stress (MPa)	1017	1120.1	1150.3
3D RVE 20 average stress (MPa) [error]	921 [9.4 %]	1024 [8.6 %]	1238 [-7.6 %]
3D RVE 30 average stress (MPa) [error]	919 [9.6 %]	1023 [8.7 %]	-

The averaged stress prediction of 3D RVE 20 for the softening state overestimated the experimental true stress with a percentage of error of around 8 %, as shown in the third row of Table 6-9. The softening or load capacity loss region in the load/displacement curve commonly includes localisation of deformation and necking in uniaxial tension tests. This results in an irregular distribution of the deformation with strain gradients within the localised area [69]. The elements in the necking region were examined for the three deformation states corresponding the hardening, UTS and softening regions of the stress/strain curves. Figure 6-32 shows the distribution of maximum principal strain values in the necking region for the standard specimen geometry. As can be seen from the Figure 6-32 (a) and (b), the distribution was almost uniform during the hardening phase and at the UTS. However, Figure 6-32 (c) shows a variation in strain levels within the necking region. At the edges the strain was about 0.09, while it was around 0.4 at the mid-central region. A factor of 4.4 was calculated for the difference between the strain for the element at the edge and the strain for the mid-central element.

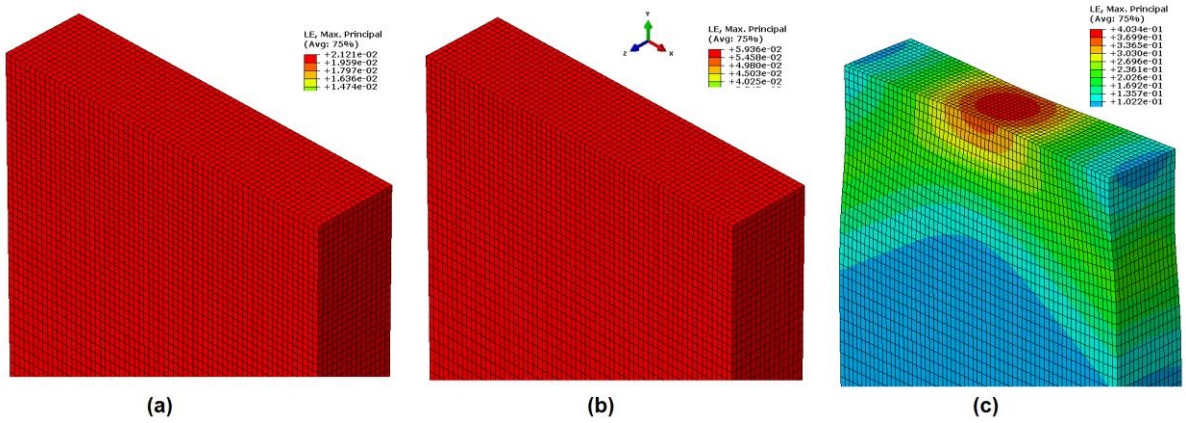

Figure 6-32: Strain distributions in the central region of the standard specimen model for three states; (a) in the hardening region, (b) at UTS, and (c) in softening region

The true experimental stress is a result of the overall response of all elements in the necking region. In case the strain distribution of deformation is uniform along the cross-sectional area, the predicted stress of the micro-scale gives a similar results wherever the BC is extracted; near the edges or in the mid-central area. However, when the strain varies along the cross section of the material, caution must be taken due to the non-uniform strain distribution along the necking region. In this case, using micro-model in certain location only to predict the macro response of the material can be misleading. Consequently, the stress prediction for the softening region was adapted by including the variation of strain along the cross-section within the necking region. The boundary conditions were extracted from three elements; two at the edges and one mid-central element, as highlighted in Figure 6-30 (a). Then the boundary conditions were applied to three 3D RVE 20 models and the stresses were averaged using equation (24). The results for the two methods of boundary conditions are shown in Table 6-10.

Table 6-10: Comparison between experimental true stress of standard geometry in softening region and 3D RVE 20 models with boundary conditions extracted from mid-central element only and with boundary conditions extracted from mid-central and edge elements

Experimental true stress (MPa)	1150.3
3D RVE 20 average stress (MPa) [error] of the mid-central element only	1238 [- 7.6 %]
3D RVE 20 average stress (MPa) [error] of the two edges and mid-central elements	1123 [2.4 %]

From the comparison between the two methods of predicting the experimental stress at macro-scale in the softening region, the prediction obtained by averaging the stress results from three 3D RVE 20 models (as micro-scale simulation) of the edges and mid-central elements is better than that obtained using the mid-central element only. The percentage of error reduced from -7.6 % to 2.4 %. Going back to the in situ test, the prediction of 3D RVE 20 in the softening part used only the mid-central element for boundary conditions. The situation for in situ specimen model was different. Figure 6-29 shows the distribution of strain at the necking region of the in situ tensile specimen model during the softening part. A factor of 1.5 was calculated for the difference between strains at the edges, as compared to the central strain of the necking region. Consequently, the factor was smaller for the in situ specimen model, as compared to the standard geometry model, and the strain distribution was also different. This is a result of geometry variation between the two specimens. In the standard geometry, the localization was concentrated in the centre of the necking region, which is related to the ratio between the width and thickness of the specimen, which was larger than for the in situ geometry.

Figure 6-31 (b) demonstrates the experimental and modelling results of the load/contraction curves for the notched bar geometry. The three states chosen to extract boundary conditions for the 3D RVE 20 model are highlighted with blue ovals. These include the hardening region for a width contraction of the notch area of - 0.018 mm, the UTS with a contraction value of - 0.08 mm, and the softening region with a contraction value of - 0.18 mm. The contraction values were measured at the notched region between the left and right edges of the reduction area. The stresses from 3D RVE 20 models were averaged using equation (24). Table 6-11 compares the experimental true stresses at macro-scale and 3D RVE 20 modelling (as micro-scale simulation) averaged stress results of the notched specimen during the hardening, at the UTS and during the softening region. For the boundary conditions extracted from mid-central element only, the results and percentage of error are listed in the third row of Table 6-11. Additionally, boundary conditions were extracted from three elements at the necking region: the mid-central element and two elements at the edges. In this case, the results are shown in the fourth row of Table 6-11. For notch specimens, heterogeneity in strain distribution emerges at an early stage during the hardening process of the load/contraction curve. Consequently, using only the mid-central element to predict experimental true stress led to unrealistic stress predictions and bigger error values, even before the softening part of the load/contraction curve.

Table 6-11: Comparison between experimental true stresses and predicted averaged stresses of 3D RVE for notched geometry at three states of deformation

Notched specimen deformation state (mm)	0.018 Hardening	0.08 UTS	0.18 Softening
Experimental true stress (MPa)	1099	1209	1395
3D RVE 20 average stress (MPa) [error] of the mid-central element only	822 [25%]	989 [18%]	1180 [16%]
3D RVE 20 average stress (MPa) [error] of the two edges and mid-central elements	902 [18%]	1017 [16%]	1109 [21%]

The comparison in Table 6-11 shows a maximum percentage of error of about 25% for mid-central element modelling results, whereas for three elements modelling, the maximum recorded percentage of error was reduced to 21%. Figure 6-33 shows the distribution of strain along the smallest width of the reduction region of the notched bar specimen.

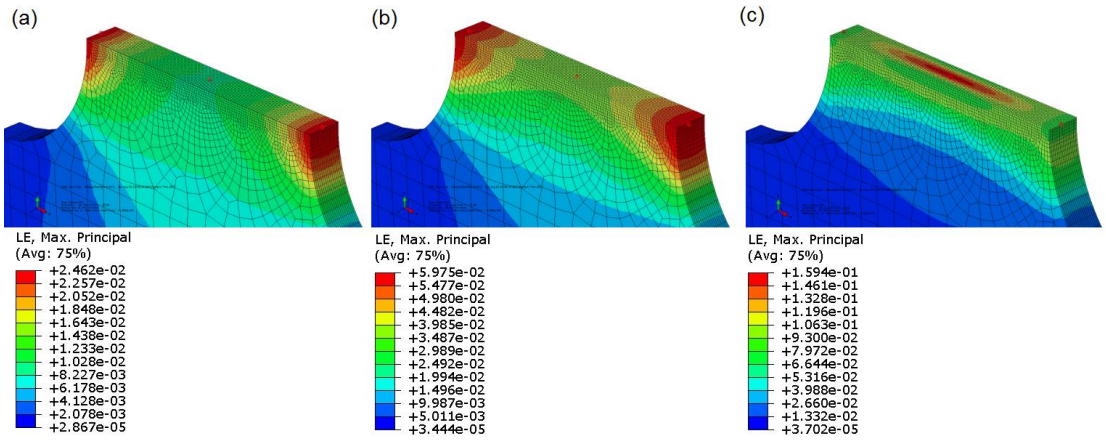

Figure 6-33: Strain distribution at smallest width of reduction region of notched specimen model for three states; (a) in the hardening region, (b) at UTS, and (c) in the softening region.

The results suggest that considering the variation in strain distribution at macro-scale is crucial when using micro-scale modelling to predict the stress values at macro-scale. In case of non-uniform distribution of the deformation along the necking region of the specimen, the

boundary conditions should be extracted from different locations in order to achieve acceptable prediction of the material response using micro-scale modelling.

6.3.3 Prediction of DP1000 Behaviour Using 3D RVE

From Figure 6-32 (c) and Figure 6-33, the local strain values differ from the experimental true strain of the specimen and consequently; the local stresses diverge from true experimental stress of the test. For example, Figure 6-34 shows the maximum principal strain (0.4) and von Mises stress (1370 MPa) values computed from the mid-central element of the standard specimen model in the softening region compared to the calculated maximum principal strain (0.09) and von Mises stress (1145 MPa) of the element at the edge of the model.

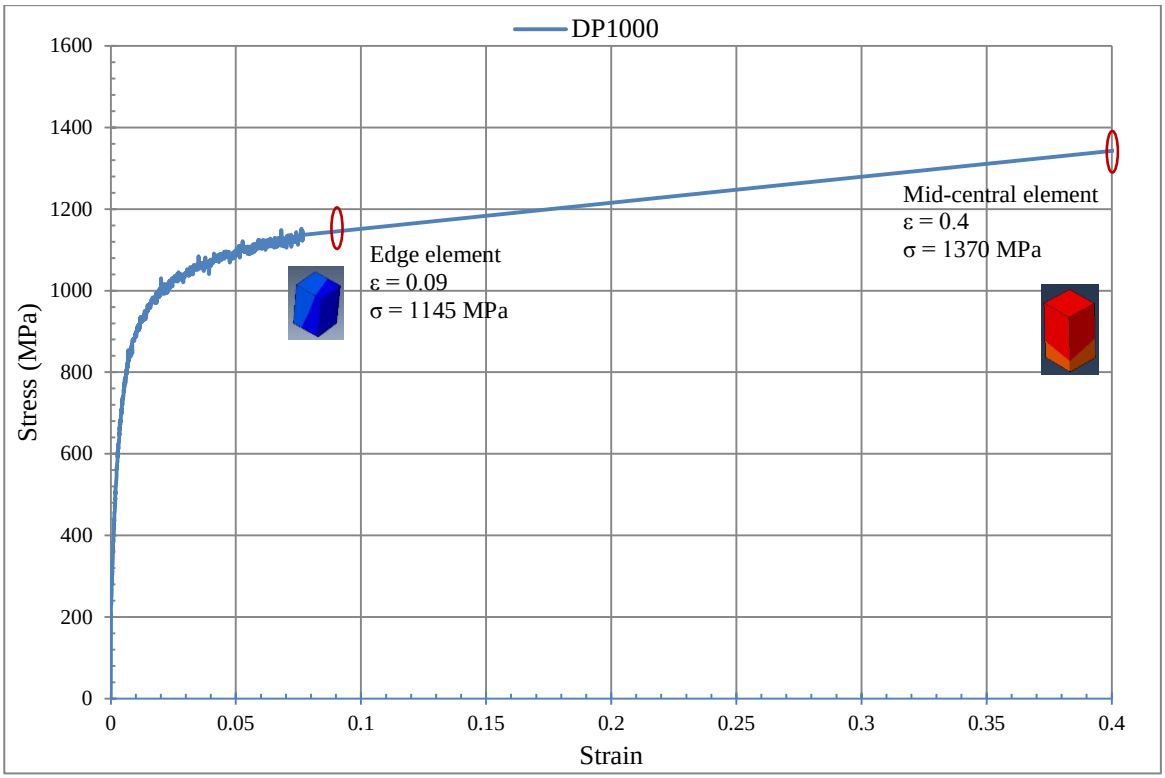

Figure 6-34: Comparison between specimen calculated true strain and stress and values for mid-central element in softening part

Therefore for better comparison, the average stress values of the 3D RVE 20 model was examined against the true stress values computed from the specimen model in the element

used to extract the boundary conditions, in order to examine the ability to predict the behaviour of DP1000 steel at macro-scale level shown in Figure 6-34 using micro-scale modelling of the 3D RVE. The average stresses of the 3D RVE model were therefore compared to the true stress of DP1000 steel for the corresponding strain in the true stress/strain curve. Table 6-12 shows the comparison between 3D RVE 20 average stress values and DP1000 steel true stress for different strain states. The strains were measured from different elements (i.e. mid-central and edge elements) of all specimen models at macro-scale level (i.e. in situ, standard, and notched models). The maximum principal strain values were used and they are arranged in the table starting from the smallest value of 0.011 to the largest value of 0.4.

Table 6-12: Comparison between DP1000 true stress and stress prediction using 3D RVE 20 model for different deformation states for model elements of standard, in-situ and notched specimens

True Strain	DP1000 true stress (MPa)	3D RVE 20 average stress (MPa)	Error (%)	Source of true strain
0.011	935	822	12	Notched mid-central element (hardening)
0.021	1017	921	9.4	Standard mid-central element (hardening)
0.025	1045	941	10	Notched edge element (hardening)
0.038	1080	989	8.5	Notched mid-central element (UTS)
0.05	1087	978	10	In-situ mid-central element (hardening)
0.06	1120	1031	8	Notched edge element (UTS)
0.06	1120	1024	8.6	Standard mid-central element (UTS)
0.09	1145	1073	6	Notched edge element (softening)
0.09	1145	1056	8	In-situ mid-central element (hardening)
0.09	1145	1065	6.9	Standard edge element (softening)
0.11	1160	1081	7	In-situ mid-central element (UTS)
0.16	1195	1180	2	Notched mid-central element (softening)
0.2	1225	1224	0.1	In-situ mid-central element (softening)
0.3	1300	1234	5	In-situ mid-central element (softening)
0.4	1370	1238	9.6	Standard mid-central element (softening)

The stress values in Table 6-12 were extracted from the corresponding strain using Figure 6-34. As can be seen from Table 6-12, a maximum error of 12 % with an average of 7 % were calculated between the average stresses of 3D RVE 20 in micro-scale modelling and the true stresses of DP1000 steel at macro-scale level. This is relatively small, given all the simplifications made in the model, demonstrating a reasonable prediction of the behaviour of the material by the 3D RVE model.

In this section, it has been shown that the 3D RVE model developed in this work can predict reasonably well the behaviour of DP1000 steel. The novel procedure used to calibrate the Gurson parameters for the ferrite phase from a single microstructure simulation can be used effectively for the investigated material without the need to run several tests with different geometries. Figure 6-20 indeed showed that the stress triaxiality computed within the microstructure covered a wide range of values usually generated by using specimens with different notch geometries and the transferability of the adjusted parameters of the Gurson model for ferrite was checked from in situ test specimens to standard and notched specimens. This result has therefore practical implications for DP1000 steel as cost and time related to design, manufacturing and testing of different specimen geometries to generate a variety of stress triaxiality can be avoided.

7. Discussion

7.1 Local Deformation and Damage in DP1000 steel

In this study, the effect of using a small gauge length on post-necking elongation were noticed, as the uniform elongation increased twofold (i.e. from 8% for standard geometry to around 15% for the in situ specimen) and the fracture strain increased threefold (i.e. from 14% for standard geometry to 48% for the in situ specimen), as shown in Figure 5-1 and

Figure 5-2. The deformation in small size specimens was less localised [12], as shown in Figure 6-29 and Figure 6-32. Relatively, the reducing the gauge length of the specimens leads to increasing the total deformation to fracture [12]. Studying the effect of rolling,

Figure 5-2 showed that the rolling direction did not affect the stress/strain response of DP1000 steel. A microstructural observation shown in Figure 3-1 supported the fact that there was no preferred direction or banding for the martensite particles in the microstructure in this particular material. It was clearly visible that the phases were uniformly distributed. However, strain ratio calculated using the r-value showed that the DP1000 steel is anisotropic material. The r-value was greater than one (2.7 in average) which makes the material is recommended for sheet metal forming as a result of thinning resistance. The anisotropy behaviour is caused by the presence of the texture in the microstructure for both phases; the ferrite and martensite. This is in line with the literature reporting texture in DP980/1000 [10, 70].

For DIC measurements, the normalized autocorrelation method gave a good estimation of the subset size for microstructure analysis. The suggested subset size correlated well with

the subset size analysed through a convergence study, shown in Figure 5-9 and Figure 5-10. The strain distribution in the microstructure did not show strain partitioning between phases in DP1000 steel, as shown in Figure 5-13, and this might be due to the high martensite volume fraction (over 50%). This is consistent with the results of Ghadbeigi et al [25] for DP1000 steel; however, the analysed area here is bigger. The lack of strain partition is likely to be related to the microstructure, as Kang et al [17] suggested that strain heterogeneity develops in the microstructure of DP steel when the phase size ratio between ferrite and martensite is more than three. A possible explanation can also be found in Tasan et al [32], Saeidi et al [18] and Kim et al [27], who found that well-distributed martensite islands led to better load transition between the phases in DP-steels, which increased plasticity deformation in martensite and thus reduced the strain partitioning, as discussed in the literature review (Sections 2.3 and 2.4).

The material used in this research shows normally distributed martensite particles, as can be seen in Figure 3-1. The strain bands at 45^{o} to the loading direction is in agreement with Ghadbeigi et al [25] for DP1000 steel. DP1000 steel has high martensite volume fraction (i.e. more than 50%) and Sodjit et al [21] found that such DP-steels exhibit long continuous localization bands. In the current strain measurements at micro-scale, before the UTS point, the local applied strain of 4.56% (calculated from the edges of the analysed area bordered with black box in Figure 5-12) was similar to the mean strain of the DIC results of 4.5% (maximum value of strain in the loading direction was 9.5%) as shown in Figure 6-22. In addition, when the specimen deformed beyond the UTS point, the mean strain value of the phases along the loading direction (i.e. 9% with a maximum value of 20%) was similar to the local applied strain (9.5%), as shown in Figure 5-12 and Figure 5-13. This is consistent

with Ghadbeigi et al [25] who measured local strain values in the phases along the loading direction using DIC for DP600 steel. Results showed local average strain values match the mean strain value in the phases as shown in Figure 2-10. They reported that local strain values within the phases were much higher than the local average strain as also observed in this work.

As far as damage is concerned, one interesting observation was the void shown in Figure 5-5, which is rarely observed at the surface. Maire et al. [3] and Landron et al. [5] used X-ray tomography to measure the porosity fractions in DP-steel after necking. Their results showed that the maximum volume fraction of void was measured at the centre of the necking region and decreased until it reached nearly zero near the surface. This can be an explanation that voids at the surface is rarely observed using tensile tests.

The importance of the experimental procedure used in this research arises as one can claim from the last image in Figure 5-5 (at an applied displacement of 1.05 mm) that the void had initiated at the interface between ferrite and martensite. The in-situ test carried out in this work therefore enables following the history of damage development and void formation in relation to the microstructure. As can be seen from the deformation steps in this work, the martensite breakage occurred before the initiation of the void. The void may have initiated at the subsurface and grown to the surface through the weak region around the broken martensite particle. One can hardly tell that the two broken martensite particles were one part by only observing the last image for the damaged area. The martensite cracking mechanism shown in Figure 5-6 is representative of the damage mechanism in the martensite phase, as observed at different locations in the DP1000 microstructure during the

test. From the observation of the DP1000 microstructure, it can be concluded that there are three damage mechanisms. Non-metallic inclusion (NMI) failure at early stages of deformation but this mechanism did not seem to have a significant contribution to damage development in the material. Martensite cracking was then observed at different locations beyond the UTS point. However, these failed martensite particles did not lead to large void extension or crack propagation at the surface of the specimen. However damage generated by broken martensite phase may affect subsequent void propagation in the ferrite phase.

7.2 Microstructural Modelling

Adjusting phase mechanical properties was an essential step before investigating damage initiation in the martensite. The calibration of phase properties of DP1000 steel using microstructure simulation resulted in relatively small errors between the average stress of microstructure modelling and experimental true stress with a maximum error of 3.2%, as shown in Table 6-2. A possible source of this error can be the discrepancy between the model and the actual DP1000 steel, in terms of microstructure phase properties or/and a 3D effect, as the model did not take into account the effect of the geometry of the under-surface microstructure and was run under plane stress conditions. The martensite mechanical properties were adjusted more than those for ferrite, as can be seen in Figure 6-18. This was necessary as, before the calibration process, the stress prediction was overestimated and needed a large reduction, as listed in Table 6-3.

In addition, the average stress values of the calibrated phases ($\frac{\sigma_{ferrite} + \sigma_{martensite}}{2}$) for yield strength, at strains of 0.02, and 0.08 (i.e. UTS) were comparable to the experimental true stress of DP1000, as shown in Figure 5-1. These were 770, 960 and 1045 MPa for average phase stresses compared to 720, 980 and 1060 MPa for DP1000 true stresses. The extrapolation of martensite phase properties was also necessary for microstructure and RVE modelling purposes as much larger strain values than the tensile strain value to fracture have been measured in martensite using DIC.

A comparison between DIC displacement measurements and 2D microstructure simulation results recorded a small error with a local maximum value of 6%, as shown in Figure 6-20. Investigating locations of maximum errors and microstructure morphology did not show a

preferable location for error. The strain results of DIC and microstructure simulation showed a maximum difference of 5%, as shown in Figure 6-21. However, the strain distribution within the analysed area showed a similarity between the DIC measurements and the modelling results, as demonstrated in Figure 6-22. In addition, the mean values and standard deviation values were similar, as listed in Table 6-4. Unlike strain distributions, the von Mises stress distributions in the phases were different, as expected and as shown in Figure 6-23 (b). This is related to the variation in mechanical properties of each constituent of DP1000 steel.

The DIC measurements and microstructure simulation results of the damaged area shown in Figure 6-24 were combined in a novel approach to investigate damage in the martensite phase of DP1000 steel. Full-field strain measurements were applied as boundary conditions in the microstructure simulations to compute the distribution of local stress values. These simulations proved necessary to investigate damage formation in martensite as strain values did not show any correlation with the damage location sites observed in the three analysed areas of the microstructure. This included, for example, maximum principal strain, shear strain and strain along the tensile direction, as can be seen in Figure 6-25 (a). The stress components were investigated in the same way. Interestingly, from the maximum principal stress results shown in Figure 6-25 (b) and (c), it is suggested that maximum principal stress at the interface between ferrite and martensite correlates reasonably well with damage locations. A critical maximum principal stress value of about 1700 MPa is proposed to initiate a crack in the martensite. Such finding could not be compared to results from the literature as no equivalent study combining experimental strain measurements in the microstructure of DP steels with microstructure modelling could be found. However this

finding could be utilised in future physically-based models for the development of damage in DP-steels. However, caution must be applied, as the real nucleation stress value can be greatly dependent on several factors, such as chemical composition, the martensite volume fraction and distribution of constituents, in addition to the crystallographic orientation of grains. However, the combined experimental/numerical procedure developed in this work at the scale of microstructures can be implemented to investigate damage sites in the ferrite and/or in different materials.

The uncertainties in the 2D microstructure simulation results are likely to be related to four main simplifications in the model, which caused the differences between the DIC measurements and microstructure modelling results. These uncertainties therefore also influence interpretation of proposed stress value for damage initiation. Firstly, even though the code generated a reasonable mesh for the two phases with a geometry similar to that of the real microstructure, in small areas the contrast in SEM images were insufficient for the code to clearly distinguish between ferrite and martensite. This may relate to the fact that the etching process did not corrode sufficiently the ferrite in these small areas surrounded by martensite particles. This is hard to control, as leaving the sample in the etching media for a longer time may result in burning the large ferrite areas. Secondly, there is a possibility of variation in actual phase properties and the properties defined by the model. Ghassemi-Armaki et al [28] found that the ferrite phase's mechanical behaviour varies within the grains of the same phase. They reported that near the interface with martensite the ferrite was harder and stronger than in the interior of the grain. Thirdly, the 3D effect was not included in the 2D model, as the lack of information about the microstructure under the surface meant that it was not possible to include this in the model. A 3D model similar to the

actual microstructure can be built with stacking method as discussed in section 4.2 but it is a destructive method. Using 2D model found to be underestimating the experimental stress as reported in [35-37]. Such limitation is common and this is why 2D microstructures are used in most similar studies found in the literature (e.g. [34, 42]). Finally, apart from the sub-surface morphology effect, the sensitivity of the calculated stresses to crystal orientation of the grains was not included in the model and could be another source of uncertainty. Even though the DP1000 steel showed isotropic behaviour at the macro-scale, as shown in

Figure 5-2, texture and its effect on stress calculations were reported in the literature for DP-steels, such as in the investigation by Choi et al [10] for DP980, who studied stress distributions calculated using two models; one using crystal plasticity FEM (CPFEM); the other using an isotropic elasto-plastic model. CPFEM results showed 14 % and 8 % increase in maximum von Mises stress values in martensite and ferrite, respectively. Therefore, the isotropic assumption made in this research is likely to lead to inaccurate stress calculations.

Despite these uncertainties, the small discrepancies between DIC measurements and microstructure simulation, as well as the proposed critical value of maximum principal stress that matches the location of crack initiation in the martensite seems reasonable from the results achieved, and importantly it is physically based. Therefore, the results obtained here are of particular value for the 2D microstructure modelling of DP-steels. Additionally, the criterion were utilised for deformation states beyond the UTS point, as shown in Figure 6-26, in order to simulate crack development in martensite. Results shown in Figure 6-26 and Table 6-5 revealed that the number of damage sites in the SEM images was higher than that predicted by the model. Only one third of broken martensite particles were

also captured by the simulation. A possible explanation of this discrepancy, in addition to the simplifications mentioned earlier, is that the DIC results for the high applied displacement values (i.e. 0.61 and 0.72 mm) may not be accurate, due to the change in brightness of the SEM images, as a result of the high deformation of the phases. The change in brightness is too small and spread over all the microstructure which makes it hard to resolve the issue. A more likely reason is the lack of physical basis for the modelling of crack propagation in the martensite phase.

It is interesting to note that the stress prediction of microstructure modelling overestimated experimental true stress values for deformation states after the UTS, as listed in Table 6-6 (third row), even though the phase properties were adjusted. Consequently, the importance of defining a damage model to phases emerged. The critical maximum principal stress value described earlier was used to initiate damage in the martensite with a total loss of the load bearing capacity for the martensite elements as soon as the crack initiation criterion is met, in order to simulate damage propagation. As for the ferrite phase, a Gurson (GTN) model was used to simulate damage development. Table 6-6 showed that the effect of damage in ferrite on reducing predicted stress was more than for the effect caused by martensite cracking and thus only a Gurson model for the ferrite phase was used for the RVE modelling. This is in line with Lian et al.'s results [11] who claimed that most of voids were initiated in the ferrite phase. Furthermore, Ghadbeigi et al. [24] investigated damage development in the microstructure of DP600. Results showed that crack propagation takes place essentially in the ferrite phase.

7.3 Stress/Strain Curve Prediction for DP1000

Results of 3D RVE shown in Table 6-8 and Table 6-9 reveal that the average stress prediction using 20 elements or 30 elements along the edges were similar. This is in agreement with Uthaisangsuk et al. [36], who found that mesh refinement in 3D RVE had small discrepancies when predicting DP-steel mechanical behaviour. However the calculation time was reduced by a factor of five using 3D RVE 20. Predicting experimental true stress using 3D RVE 20 gave a smaller error than using 2D RVE with actual representation of the microstructure morphology. Uncertainty was caused by the plane strain condition used in the 2D RVE model. This is in agreement with similar studies in the literature that showed 2D RVE with plane strain conditions underestimated the stress prediction for DP-steels [35-37]. Iung et al. [35] reported two causes for the error using 2D plain strain conditions: the assumption of no out-of-plane deformation as mechanical restriction; and the cylindrical extension of the 2D mesh as geometrical restriction. These differ from the actual deformation and phase distribution of DP-steels.

3D RVE were used to predict DP1000 steel behaviour for different geometries. Results for in situ specimen showed acceptable predicted stress values with a maximum error of 11%. For the standard geometry specimen, 3D RVE 20 showed an error of 7.6 % for the softening phase. This was explained by the non-uniform strain distribution in the necking region during softening, as shown in Figure 6-32. When the applied boundary conditions for 3D RVE 20 were extracted from the three elements within the necking region (i.e. two at the edges and mid-central elements), the error reduced from 7.6 % to 2.4 %, as listed in Table 6-10. An explanation for this is that the measured load of the standard specimen is the

result of the overall deformation and damage acting on all elements across the area of maximum width reduction in the necking region. Consequently, to predict the behaviour of the material under large deformation (i.e. after the UTS and during the softening part), the boundary conditions should be extracted from the elements within the necking region that represent the deformation state of the material. This was not the case for the in situ specimen, as the cross sectional area was small (2 mm x 1.5 mm) and the variance in strain distribution recorded a factor of 1.5 between the strain values near the edges, as compared to the mid-central element, as shown in Figure 6-29. The standard geometry recorded a factor of 4.4 between strains near edges and at the centre of the necking region.

For the notched bar, the 3D RVE 20 predicted the overall stress/strain curve of DP1000 steel with a maximum error of 21%, as listed in Table 6-11. It is worth noting that the strain distribution in the necking region was not uniform from the beginning of the test, during the hardening phase, as shown in Figure 6-33. The average stresses of 3D RVE 20 model at different deformation states were compared to the true stress values of the DP1000 curve for the corresponding deformation states using the true stress/strain curve. A maximum error of 12 % was recorded with an overall average error of 7 %, as shown in Table 6-12. Microstructure simulations and RVE modelling have been used in the literature, as discussed in Section 2.4 to investigate damage in DP steels and/or to predict the material behaviour. However, the novel modelling approach reported in this study raises the possibility of conducting microstructure simulation to adjust the Gurson's parameters with a single test given the range of stress triaxiality values recorded at the scale of the microstructure as shown in Figure 6-27 and use them in RVE models to predict the overall stress/strain curve without the need for several specimens with different notch geometries. This is likely due to

the wide range of stress triaxiality computed in the ferrite phase in the microstructure, as shown in Figure 6-27, for the deformation states where the Gurson's parameters were adjusted. This is in line with a study by Zhang et al [68] who showed that a single specimen approach to determining nucleation parameters for the GTN model can give two possible solutions for the fit of the experimental load/displacement curves using the model. They found that two alternative parameter values can give the same prediction for smooth specimens (i.e. low triaxiality) but a different prediction in the case of a notched specimen (high stress triaxiality). So they argued that a multi-specimen approach cover a wide range of stress triaxiality which can solve the uncertainty in the GTN parameters.

The new physically-based damage model developed in this work, which made use of state-of-the-art full-field strain measurements at the scale of the microstructure, therefore offers new perspectives for the simulation of damage and the prediction of stress/strain curves for AHSS given the results obtained in this study for the investigated DP1000 steel, with a simpler calibration procedure of damage models relevant for a range of stress triaxiality values based on microstructural modelling.

8. Conclusion and Recommendations

The aim of this investigation was to analyse damage formation in DP1000 steel from tensile tests carried out inside the chamber of a SEM with local full-field strain measurements at the scale of the microstructure combined with microstructural modelling in order to predict the overall stress/strain curve of the material. Strain measurements carried out on a large representative area of the microstructure have shown strain localisation in the form of bands of deformation running at 45^{o} with respect to the loading direction and mainly localised in the ferrite phase during the hardening part of the tensile stress/strain curve. Damage formation is then observed through martensite cracking which has been analysed in detail in this study. Results showed that no correlation could be found between damage sites and local strain values. A novel modelling approach was then developed to accurately predict stress distributions in the microstructure. First, the local phase' stress/strain curves were adjusted through comparison of the average stress, computed from a finite element model of the microstructure with boundary conditions in displacements corresponding to measured DIC values, with the overall experimental true stress/strain curve. In a second stage a model of very local areas around observed damage sites in the experiments were simulated for a deformation state prior to the appearance of damage. In this model full-field displacements measured by DIC were applied as boundary conditions over the whole simulated area. Results showed that damage locations observed in the experiment correlated with reasonable agreement with the locations of maximum values of maximum principal stress. A new criterion for damage initiation in martensite with a critical stress value of 1700MPa was therefore generated. Similar work could not be found in the literature to compare with this value. This criterion was subsequently used in simulations of crack propagation in

martensite but discrepancies between model prediction of the damage shape and density and experimental observations clearly showed the limitations of the current model and especially the lack of implemented physics as far as crack propagation in martensite is concerned. However it is believed from this work and from the literature review that martensite cracking has a relatively small influence on the final failure of DP steels with elongation to fracture controlled by damage in the ferrite phase. A Gurson model implemented in the microstructural model for the ferrite phase was calibrated against the overall experimental load/displacement curve in order to describe damage development in the material. One very interesting outcome of this model was the wide range of stress triaxiality values generated by the plane stress model. The calibrated Gurson parameters from the microstructure model were then used in two types of RVE model (one microstructure-based two-dimensional model and one statistical three-dimensional model) to predict the overall load/displacement curves of one standard geometry and one notched tensile specimens for validation purposes. Results showed that the Gurson parameters calibrated using the microstructural model can predict reasonably the experimental true stress of the two types of specimen geometry using the 3D RVE model after correction from strain gradients between the edges and the central part of the specimens through the cross-section area of minimum width in the necking region and by validating RVE prediction against the true stress/strain curve.

The new physically-based damage modelling approach developed in this work, which used state-of-the-art full-field strain measurements at the scale of the microstructure as full-field boundary conditions for the microstructure simulation has led to the successful determination of a criterion for martensite cracking and accurate prediction of the overall stress/strain curve for DP1000. No similar work could be found in the literature and

therefore these results and the combined experimental/modelling approach developed at the scale of the microstructure offer new perspectives for the prediction of the behaviour of AHSS which is of tremendous importance to the steel industry.

Future Work

Further experimental investigations are recommended to assess damage nucleation in the ferrite phase. A bending test inside the microscope chamber may help capture the initiation of voids in the ferrite phase, as the maximum deformation and stress will be on the top surface. Another possible suggestion is to reduce the tensile sample thickness from 1.5 mm (as-received sheet) to less than 0.5 mm, so that the distribution of deformation along the out of plane section is reduced, which may help produce deformation on the surface similar to the amount of deformation experienced by the material in the centre of the specimen. Developing experimentally based void nucleation is not an easy task but is possible with the newly developed experimental/numerical procedure combining, in-situ mechanical testing, full-field strain measurements in the microstructure and microstructural modelling informed by DIC measurements. Crack propagation would be the following next step after developing criteria for initiation in both phases. A bending test would also be useful for that purpose as crack propagation is likely to take place on the top surface where stresses are maximal.

9. References:

1. C.C. Tasan, M.D., 1 D. Yan, M. Bechtold, F. Roters, L. Schemmann, C. Zheng, N. Peranio, D. Ponge, M. Koyama, K. Tsuzaki, and D. Raabe, *An Overview of Dual-Phase Steels: Advances in Microstructure-Oriented Processing and Micromechanically Guided Design.* Annual Review of Materials Research, 2015. **45**: p. 391-431.
2. Steinbrunner, D.L., D.K. Matlock, and G. Krauss, *Void Formation during Tensile Testing of Dual Phase Steels.* Metallurgical Transactions a-Physical Metallurgy and Materials Science, 1988. **19**(3): p. 579-589.
3. Maire, E., et al., *Initiation and growth of damage in a dual-phase steel observed by X-ray microtomography.* Acta Materialia, 2008. **56**(18): p. 4954-4964.
4. Avramovic-Cingara, G., et al., *Void Nucleation and Growth in Dual-Phase Steel 600 during Uniaxial Tensile Testing.* Metallurgical and Materials Transactions a-Physical Metallurgy and Materials Science, 2009. **40A**(13): p. 3117-3127.
5. Landron, C., et al., *Characterization and modeling of void nucleation by interface decohesion in dual phase steels.* Scripta Materialia, 2010. **63**(10): p. 973-976.
6. Landron, C., et al., *Validation of void growth models using X-ray microtomography characterization of damage in dual phase steels.* Acta Materialia, 2011. **59**(20): p. 7564-7573.
7. Lian, J.H., et al., *A method to quantitatively upscale the damage initiation of dual-phase steels under various stress states from microscale to macroscale.* Computational Materials Science, 2014. **94**: p. 245-257.
8. Zhao, Z.Z., et al., *Microstructure, mechanical properties and fracture behavior of ultra-high strength dual-phase steel.* Materials Science and Engineering a-Structural Materials Properties Microstructure and Processing, 2014. **618**: p. 182-188.
9. Saeidi, N., et al., *Damage mechanism and modeling of void nucleation process in a ferrite-martensite dual phase steel.* Engineering Fracture Mechanics, 2014. **127**: p. 97-103.
10. Choi, S.H., et al., *The effect of crystallographic orientation on the micromechanical deformation and failure behaviors of DP980 steel during uniaxial tension.* International Journal of Plasticity, 2013. **45**: p. 85-102.
11. Lian, J.H., N. Vajragupta, and S. Munstermann, *Micromechanical modelling of damage and failure in dual phase steels.* Current State-of-the-Art on Material Forming: Numerical and Experimental Approaches at Different Length-Scales, Pts 1-3, 2013. **554-557**: p. 2369-2374.
12. *Ductility*. 1968, Metal Park, Ohio: American Society for Metals.
13. Callister, W.D.j. and D.G. Rethwisch, *Materials Science and Engineering: An Introduction*. 2011: John Wiley & Sons Canada.
14. Dowling, N.E., *Mechanical Behavior of Materials: Engineering Methods for Deformation, Fracture, and Fatigue*. Second ed. 1999: Prentice Hall. 830.
15. Rashid, M.S., *Dual Phase Steels.* Annual Review of Materials Science, 1981. **11**: p. 245-266.
16. Pierman, A.P., et al., *The influence of microstructure and composition on the plastic behaviour of dual-phase steels.* Acta Materialia, 2014. **73**: p. 298-311.

17. Kang, J.D., et al., *Digital image correlation studies for microscopic strain distribution and damage in dual phase steels.* Scripta Materialia, 2007. **56**(11): p. 999-1002.
18. Saeidi, N., F. Ashrafizadeh, and B. Niroumand, *Development of a new ultrafine grained dual phase steel and examination of the effect of grain size on tensile deformation behavior.* Materials Science and Engineering a-Structural Materials Properties Microstructure and Processing, 2014. **599**: p. 145-149.
19. Ramazani, A., et al., *Modelling the effect of microstructural banding on the flow curve behaviour of dual-phase (DP) steels.* Computational Materials Science, 2012. **52**(1): p. 46-54.
20. Park, K., et al., *Effect of the martensite distribution on the strain hardening and ductile fracture behaviors in dual-phase steel.* Materials Science and Engineering a-Structural Materials Properties Microstructure and Processing, 2014. **604**: p. 135-141.
21. Sodjit, S. and V. Uthaisangsuk, *Microstructure based prediction of strain hardening behavior of dual phase steels.* Materials & Design, 2012. **41**: p. 370-379.
22. Uthaisangsuk, V., U. Prahl, and W. Bleck, *Failure modeling of multiphase steels using representative volume elements based on real microstructures.* Mesomechanics 2009, 2009. **1**(1): p. 171-176.
23. Kadkhodapour, J., et al., *A micro mechanical study on failure initiation of dual phase steels under tension using single crystal plasticity model.* International Journal of Plasticity, 2011. **27**(7): p. 1103-1125.
24. Ghadbeigi, H., C. Pinna, and S. Celotto, *Failure mechanisms in DP600 steel: Initiation, evolution and fracture.* Materials Science and Engineering a-Structural Materials Properties Microstructure and Processing, 2013. **588**: p. 420-431.
25. Ghadbeigi, H., et al., *Local plastic strain evolution in a high strength dual-phase steel.* Materials Science and Engineering a-Structural Materials Properties Microstructure and Processing, 2010. **527**(18-19): p. 5026-5032.
26. Poruks, P., I. Yakubtsov, and J.D. Boyd, *Martensite-ferrite interface strength in a low-carbon bainitic steel.* Scripta Materialia, 2006. **54**(1): p. 41-45.
27. Kim, J.H., et al., *Hole-expansion formability of dual-phase steels using representative volume element approach with boundary-smoothing technique.* Materials Science and Engineering a-Structural Materials Properties Microstructure and Processing, 2010. **527**(27-28): p. 7353-7363.
28. Ghassemi-Armaki, H., et al., *Deformation response of ferrite and martensite in a dual-phase steel.* Acta Materialia, 2014. **62**: p. 197-211.
29. Kadkhodapour, J., et al., *Simulation of shear failure in dual phase steels using localization criteria and experimental observation.* Computational Materials Science, 2014. **94**: p. 106-113.
30. Han, Q.H., et al., *Quantitative measurement of strain partitioning and slip systems in a dual-phase steel.* Scripta Materialia, 2013. **69**(1): p. 13-16.
31. Paul, S.K. and A. Kumar, *Micromechanics based modeling to predict flow behavior and plastic strain localization of dual phase steels.* Computational Materials Science, 2012. **63**: p. 66-74.

32. Tasan, C.C., et al., *Strain localization and damage in dual phase steels investigated by coupled in-situ deformation experiments and crystal plasticity simulations.* International Journal of Plasticity, 2014. **63**: p. 198-210.
33. Ramazani, A., Z. Ebrahimi, and U. Prahl, *Study the effect of martensite banding on the failure initiation in dual-phase steel.* Computational Materials Science, 2014. **87**: p. 241-247.
34. Sun, X., et al., *Predicting failure modes and ductility of dual phase steels using plastic strain localization.* International Journal of Plasticity, 2009. **25**(10): p. 1888-1909.
35. Iung, T. and M. Grange, *Mechanical-Behavior of 2-Phase Materials Investigated by the Finite-Element Method - Necessity of 3-Dimensional Modeling.* Materials Science and Engineering a-Structural Materials Properties Microstructure and Processing, 1995. **201**(1-2): p. L8-L11.
36. Uthaisangsuk, V., U. Prahl, and W. Bleck, *Modelling of damage and failure in multiphase high strength DP and TRIP steels.* Engineering Fracture Mechanics, 2011. **78**(3): p. 469-486.
37. Ramazani, A., et al., *Correlation between 2D and 3D flow curve modelling of DP steels using a microstructure-based RVE approach.* Materials Science and Engineering a-Structural Materials Properties Microstructure and Processing, 2013. **560**: p. 129-139.
38. Sun, X., et al., *On key factors influencing ductile fractures of dual phase (DP) steels.* Materials Science and Engineering a-Structural Materials Properties Microstructure and Processing, 2009. **526**(1-2): p. 140-149.
39. Asgari, S.A., et al., *Modeling of Advanced High Strength Steels with the realistic microstructure-strength relationships.* Computational Materials Science, 2009. **45**(4): p. 860-866.
40. Hosseini-Toudeshky, H., et al., *Microstructural deformation pattern and mechanical behavior analyses of DP600 dual phase steel.* Materials Science and Engineering a-Structural Materials Properties Microstructure and Processing, 2014. **600**: p. 108-121.
41. Vajragupta, N., et al., *The modeling scheme to evaluate the influence of microstructure features on microcrack formation of DP-steel: The artificial microstructure model and its application to predict the strain hardening behavior.* Computational Materials Science, 2014. **94**: p. 198-213.
42. Tasan, C.C., et al., *Integrated experimental-simulation analysis of stress and strain partitioning in multiphase alloys.* Acta Materialia, 2014. **81**: p. 386-400.
43. Sirinakorn, T., S. Wongwises, and V. Uthaisangsuk, *A study of local deformation and damage of dual phase steel.* Materials & Design, 2014. **64**: p. 729-742.
44. Kadkhodapour, J., A. Butz, and S.Z. Rad, *Mechanisms of void formation during tensile testing in a commercial, dual-phase steel.* Acta Materialia, 2011. **59**(7): p. 2575-2588.
45. Ramazani, A., et al., *Characterization and modelling of failure initiation in DP steel.* Computational Materials Science, 2013. **75**: p. 35-44.
46. Rice, J.R. and D.M. Tracey, *On Ductile Enlargement of Voids in Triaxial Stress Fields.* Journal of the Mechanics and Physics of Solids, 1969. **17**(3): p. 201-+.

47. Rousselier, G., *Finite deformation constitutive relations including ductile fracture damage, three dimensional constitutive relations and ductile fracture.* 1981: p. 331-355.
48. Tvergaard, V., A. Needleman, and K.K. Lo, *FLOW LOCALIZATION IN THE PLANE STRAIN TENSILE TEST.* Mech. Phys. Solids, 1981. **29**(2): p. 115-142.
49. Berdin, C., *Local approach to fracture*. 2004, Paris: Presses de l'Ecole des Mines.
50. Simulia, *Abaqus 6.10*. 2010.
51. Needleman, A. and V. Tvergaard, *AN ANALYSIS OF DUCTILE RUPTURE IN NOTCHED BARS.* Mech. Phys. Solids, 1984. **32**(6): p. 461-490.
52. Rousselier, G., *Ductile Fracture Models and Their Potential in Local Approach of Fracture.* Nuclear Engineering and Design, 1987. **105**(1): p. 97-111.
53. Ghadbeigi, H., et al., *Strain evolution measurement at the microscale of a Dual Phase steel using Digital Image Correlation.* Advances in Experimental Mechanics Vii, 2010. **24-25**: p. 201-206.
54. *Annual book of ASTM standards. Section 3, Vol.03.01, Metals test methods and analytical procedures*. 2000, West Conshohocken: American Society for Testing and Materials.
55. LaVision, *Davis Strain master Software*. 2001.
56. Wang, Y.H., et al., *Whole Field Sheet-Metal Tensile Test Using Digital Image Correlation.* Experimental Techniques, 2010. **34**(2): p. 54-59.
57. Sutton, M.A., J.-J. Orteu, and H.W. Schreier, *Image correlation for shape, motion and deformation measurements basic concepts, theory and applications*. 2009, New York: Springer.
58. Bornert, M., et al., *Assessment of Digital Image Correlation Measurement Errors: Methodology and Results.* Experimental Mechanics, 2009. **49**(3): p. 353-370.
59. Pearce, R., *Sheet Metal Forming*. 1991: Springer Science & Business Media.
60. Semiatin, S.L. and J.J. Jonas, *Formability and Workability of Metals: Plastic Instability and Flow Localization*. 1984: American Society for Metals.
61. The MathWorks, I., *MATLAB.* 2010.
62. Chalon, I., *Modelling of the microstructural deformation of duplex stainless steel during plane strain compression, Internal Report*, in *Department of Mechanical Engineering*. 2004, The University of Sheffield.
63. Smit, R.J.M., W.A.M. Brekelmans, and H.E.H. Meijer, *Prediction of the mechanical behavior of nonlinear heterogeneous systems by multi-level finite element modeling.* Computer Methods in Applied Mechanics and Engineering, 1998. **155**(1-2): p. 181-192.
64. Kouznetsova, V., M.G.D. Geers, and W.A.M. Brekelmans, *Multi-scale constitutive modelling of heterogeneous materials with a gradient-enhanced computational homogenization scheme.* International Journal for Numerical Methods in Engineering, 2002. **54**(8): p. 1235-1260.
65. Nemat-Nasser, S. and M. Hori, *Micromechanics: overall properties of heterogeneous materials*. 2nd rev. ed. 1999, Amsterdam: Elsevier.
66. Li, Z.H., J.P. Shi, and A.M. Tang, *Investigation on fracture mechanisms of metals under various stress states.* Acta Mechanica, 2014. **225**(7): p. 1867-1881.
67. Lin, H., *SPECKLE MECHANISM IN HOLOGRAPHIC OPTICAL COHERENCE IMAGING*, in *The Faculty of the Graduate School*. 2009, University of Missouri.

68. Zhang, Z.L., C. Thaulow, and J. Odegard, *A complete Gurson model approach for ductile fracture.* Engineering Fracture Mechanics, 2000. **67**(2): p. 155-168.
69. Cabezas, E.E. and D.J. Celentano, *Experimental and numerical analysis of the tensile test using sheet specimens.* Finite Elements in Analysis and Design, 2004. **40**(5-6): p. 555-575.
70. Alharbi, K., et al., *Damage in dual phase steel DP1000 investigated using digital image correlation and microstructure simulation.* Modelling and Simulation in Materials Science and Engineering, 2015. **23**(8): p. 085005.

10. Appendices

Appendix I MatLab code to apply boundary conditions on microstructure model:

MatLab Code to apply boundary condition on all nodes of the model:

```
% This code written by Khaled Alharbi
% The code help generate ABAQUS input file with material properties and
% boundary conditions.
% Please add to the folder the following:
%   1. DIC results from Lavision as DIC.DAT
%   2. Image of area of interest in bmb ot jpg extension format

%-----------------------------------------------

%IMPORTING DIC RESULTS
%NOTE:
%DATA SOURCE: LAVISION
%FILE NAME: DIC.DAT
%DATA ARRANGED:Y-POSITION THEN X-POSITION
%DATA TYPE: X-POSITION Y-POSITION X-DISP Y-DISP
%OTHER: Import function used to import data from lavision results
% please make sure lavision results file named and extension is as DIC.DAT
% and make sure that the data are arranged according to y position first
% from top to bottom and then arranged according to x position from left
to
% right
importDIC('DIC.DAT');
dicall=data;
%-----------------------------------------------

%EXTRACT AREA OF INTEREST DATA
% User should specify area of interest according to x/y-positions
XDic1=input( 'Please enter the DIC X Start Left ' );
XDic2=input( 'Please enter the DIC X end Right ' );
YDic1=input( 'Please enter the DIC Y start Top ' );
YDic2=input( 'Please enter the DIC Y end Bottom ' );

%to find the number of data along x and y axis from lavision file
xlength=0;
ylength=0;
yvalue=dicall(1,2);
xvalue=dicall(1,1);
for i=1:length(dicall);
    if dicall(i,2)== yvalue;
        xlength=xlength+1;
    end
end
for i=1:length(dicall);
    if dicall(i,1)== xvalue;
```

```
        ylength=ylength+1;
    end
end


%construct dic matrix with cells of interest and vector magnitude
% this dic matrix has arranged in similar way of lavision data
%meaning that first according to y position then according to y position
%first column x position
%2nd column   y position
%3rd          x disp
%4th          y disp
%5th          magnitude disp
m=0;
n=0;
a=0;
b=1;
w=0;    %No of vectors along x axis for SELECTED AREA OF INTEREST
h=0;    %No of vectors along y axis for SELECTED AREA OF INTEREST
for i=1:ylength; % move as cluster for every y value
    if ((dicall(b,2)<= YDic1) && (dicall(b,2)>= YDic2));
        h=h+1;
        m=i*xlength; % to set the start of the cells to check and the end
for that y value
        n=m-xlength+1;
        w=0;
        for j=n:m;
            if ((dicall(j,1)<= XDic2) && (dicall(j,1)>= XDic1))
                w=w+1;
                a=a+1; % to creat new cell number for dic matrix
                dic(a,5)= sqrt(dicall(j,3)^2+dicall(j,4)^2); %calculate
the magnitude
                dic(a,4)= dicall(j,4);
                dic(a,3)= dicall(j,3);
                dic(a,2)=dicall(j,2);
                dic(a,1)=dicall(j,1);
            end
        end
    end
    b=b+xlength; %this one will be used to set the index for next y value
checking
end

%-------------------------------------------------
%The following lines call code written by:

% I.CHALON,
%french visiting student,
%in second year at ENSMN (Nancy, France),
%at IMMPETUS, 07/2004

%to generate abaqus zazamesh.inp input file with two phases

gen=input('Do you want to generate the input file from an image? (Y/N)
[Y]: ','s');
```

```
if isempty(gen);,gen='Y';,end;
if gen=='y' || gen=='Y';
    disp('')
    disp('')
    disp('')
    disp('Please use I.Chalon window and when you finish close the window
and')
    disp('write "return" (as lower case lette) at the command line.')
    pixel3;
    keyboard
else
    disp('')
    disp('')
    disp('')
    disp('Please make sure you copy and paste the generated mesh input
file')
    disp('in the current folder with name of "zaza_mesh.inp" before
proceeding.')
    disp('To continue write "return" (as lower case lette) at the command
line.')
end;

% ==============
% Reset YDic and XDic to exact value for accurate Factor calculation
YDic1=max(dic(:,2));
YDic2=min(dic(:,2));
XDic2=max(dic(:,1));
XDic1=min(dic(:,1));

% ==============



%-------------------------------------------------
% Update the generated input file from I.Chalon CODE
fid=fopen('zaza_mesh.inp','a');
%Define section assignment and Assembly
fprintf(fid,'\r\n');
fprintf(fid,'** Section: Section-1-PHASE1\r\n');
fprintf(fid,'*Solid Section, elset=PHASE1, material=Martensite\r\n');
fprintf(fid,'1.,\r\n');
fprintf(fid,'** Section: Section-2-PHASE2\r\n');
fprintf(fid,'*Solid Section, elset=PHASE2, material=Ferrite\r\n');
fprintf(fid,'1.,\r\n');
fprintf(fid,'*End Part\r\n');
fprintf(fid,'** \r\n');
fprintf(fid,'** \r\n');

fprintf(fid,'** ASSEMBLY\r\n');
fprintf(fid,'**\r\n');
fprintf(fid,'*Assembly, name=Assembly\r\n');
fprintf(fid,'**\r\n');
fprintf(fid,'*Instance, name=PART-1-1, part=PART-1\r\n');
fprintf(fid,'*End Instance\r\n');
fprintf(fid,'**\r\n');
```

```
fprintf(fid,'*End Assembly\r\n');
fprintf(fid,'*Amplitude, name=Amp-1\r\n');
fprintf(fid,'0.,0.,300.,1.\r\n');
fprintf(fid,'**\r\n');

%-----------------------------------------------
%Define Phases Mechanical Properties
%Phases Material properties in mm
% Ferrite
FeD=7.60292e-06;  %kg/mm3
FeE=198000;  %MPa Modulus
FeSs=[444.095988    444.423576  446.506089  447.44946   448.09632
448.34174   448.692069  449.046936  449.46005   449.618676  449.618676
449.648 449.648 449.648 449.648 449.648 449.648 449.648 449.648 449.648
449.648 449.648 449.648 449.648 449.648 449.648 449.648 449.648 449.648
449.648 449.648 449.648 449.648 449.648 449.648 449.648 449.648 449.648
449.648 449.648 449.648 449.648 449.648 449.648 449.648 449.648 449.648
449.648 449.648 449.648 449.648 449.648 449.648 449.648 449.648 449.648
449.648 449.648 449.648 449.648 449.648 449.648 449.648 449.648 449.648
449.648 449.648 449.648 449.648 449.648 449.648 449.648 449.648 449.648
449.648 449.648 449.648 449.648 449.648 449.648 449.648 449.648 449.648
449.648 449.648 449.648 449.648 449.648 449.648 449.648 449.648 449.648
449.648 449.648 449.648 449.648 449.648 449.648 449.648 449.648 449.648
449.648 449.648 449.648 449.648 449.648 449.648 449.648 449.648 449.648
449.648 449.648 449.648 449.648 449.648 449.648 449.648 449.648 449.648
449.648 449.648 449.648 450.51837   451.535452  452.548519  452.9386
453.935664  454.22654   454.612707  454.90375   455.186115  455.348064
455.526522  455.526522  455.526522  455.526522  455.741994  455.92492
455.92492   456.070269  456.25327   456.54492   456.936516  457.32822
458.016428  458.299725  458.59188   458.884111  459.2808    459.6732
459.856872  460.22873   460.521392  460.81413   460.81413   460.81413
460.81413   460.81413   460.81413   460.81413   460.81413   460.81413
461.215674  462.316725  462.605661  462.899088  463.498056  463.791688
464.085396  464.37475   465.06297   465.56232   465.56232   465.56232
465.56232   465.56232   465.56232   465.56232   465.56232   465.56232
465.56232   465.56232   466.059022  466.480888  466.902898  466.913104
467.76513   468.626424  469.72274   469.85654   470.20556   470.67351
471.031749  471.614493  472.092006  473.07904   473.7954    475.045085
476.093184  476.617644  477.597614  478.14545   478.49067   479.26916
479.5268    479.79348   480.161847  480.478156  480.478156  480.478156
481.167 482.072916  482.655159  482.655159  482.655159  482.655159
482.655159  482.751097  484.190148  485.197604  486.897858  487.916642
488.399667  489.08857   489.08857   490.091679  490.889448  490.93872
490.93872   491.359902  491.839996  492.531545  493.699997  493.960544
493.960544  493.960544  494.431184  495.237608  496.400232  496.77886
496.77886   496.77886   496.77886   497.075954  497.672032  498.846922
499.543808  499.687055  499.843944  499.887036  500.689398  501.55848
501.55848   501.55848   501.55848   501.55848   501.55848   501.55848
501.717564  502.417344  502.463048  502.943584  502.943584  502.943584
502.943584  502.943584  502.943584  502.943584  502.943584  503.169196
505.134933  505.51512   506.439648  507.369442  507.626034  507.882626
```

```
508.41872   509.01753   509.621276  510.003104  510.598256  510.980436
511.499445  512.202337  512.682723  513.386399  513.88116   514.299028
514.56606   514.70746   514.70746   514.70746   514.943814  515.322549
515.322549  515.673875  516.4972    517.091814  517.695976  518.183424
518.93387   519.417276  519.896292  520.272025  520.63864   520.89252
521.263917  521.455824  521.455824  521.455824  521.455824  521.455824
521.455824  521.455824  521.662593  521.662593  521.662593  521.662593
521.662593  521.662593  521.662593  521.662593  521.662593  521.662593
521.662593  521.662593  521.662593  521.662593  521.662593  521.662593
521.662593  521.662593  521.662593  521.662593  521.662593  521.662593
521.662593  521.662593  522.022008  522.022008  522.022008  522.915498
524.117044  525.100644  525.870873  526.652516  527.00512   527.00512
527.00512   527.00512   527.00512   527.197464  527.93575   528.197967
528.574337  529.06032   529.45089   529.565644  529.565644  529.8948
530.51904   531.038482  531.457675  531.75793   532.253439  532.56784
532.873029  533.19225   533.39685   533.711552  534.23568   534.564558
534.888874  534.983328  535.307734  535.63223   536.30012   536.629548
536.737878  537.072058  537.410991  537.96904   538.072569  538.4164
538.63542   538.974735  539.318808  539.542584  539.99946   540.343777
540.567601  540.796088  541.024575  541.257725  541.826208  542.170965
542.404215  542.64213   542.88471   543.234384  543.355875  543.948282
544.190914  544.3122    544.666846  544.91881   545.03994   545.520435
545.763015  546.122638  546.248175  546.500085  546.742665  546.755402
547.254343  547.501482  547.757947  548.009749  548.012414  548.525124
548.776818  548.91538   549.053832  549.2961    549.43439   549.449904
549.96672   550.104625  550.128843  550.384758  550.403991  550.669098
550.829832  550.966908  551.222493 1572.73];
                %Mpa Plastic Stress
FeSn=[0 5.97961E-05 0.000229199 0.000318871 0.000418498 0.000518114
0.000627681 0.000747194 0.000996135 0.00112556  0.001264922 0.001414216
0.001553538 0.001702789 0.001852018 0.002160355 0.002319459 0.002498421
0.002667411 0.002846311 0.00319408  0.003362953 0.003551659 0.00374033
0.003909111 0.004097714 0.004286282 0.004653391 0.004841854 0.005030282
0.005218674 0.005397118 0.005744001 0.005932259 0.006120481 0.006308668
0.006477015 0.006665135 0.00685322  0.007219388 0.007397475 0.007575531
0.007763444 0.007951322 0.008307204 0.008485098 0.00868272  0.008850669
0.009038343 0.009225981 0.009403712 0.009778817 0.009966316 0.010143915
0.010331346 0.010518743 0.010706104 0.011070864 0.011267976 0.011445344
0.01162268  0.011809835 0.011996954 0.012184038 0.01254826  0.012735241
0.012932026 0.013118935 0.013295975 0.013482816 0.013669623 0.014023477
0.014210182 0.014396853 0.014593311 0.01477009  0.014956656 0.015329684
0.01549652  0.015682951 0.015849728 0.016045901 0.016232229 0.016604782
0.016781206 0.016967397 0.017153554 0.017339676 0.01751597  0.017897835
0.018083818 0.018269767 0.018445898 0.018621997 0.018807846 0.018983882
0.019345636 0.019521577 0.019707259 0.019892906 0.020088287 0.020283631
0.02066444  0.020840149 0.021025586 0.021220746 0.021406113 0.021591445
0.021766992 0.02212774  0.022303193 0.022478614 0.022663748 0.022829365
0.023199468 0.023364997 0.023549966 0.023715437 0.023890611 0.024075483
0.024250594 0.024629896 0.024824354 0.025009054 0.02519372  0.025368635
0.025553234 0.025902909 0.0260777   0.026271876 0.026456309 0.026631004
0.026815371 0.027184002 0.027358569 0.027542802 0.027727001 0.027920857
0.02829877  0.028492516 0.028686224 0.028879895 0.029054167 0.029238087
0.029421974 0.029770298 0.029944415 0.03010883  0.030292557 0.030447248
0.030630912 0.030978816 0.031162383 0.031345916 0.031529415 0.031703226
0.03188666  0.03207006  0.032417463 0.032600766 0.032764746 0.032957629
0.033140833 0.033324003 0.033680607 0.033863679 0.034046717 0.03421046
```

```
0.034393434 0.034566748 0.034740031 0.035105754 0.035288565 0.035452104
0.035634852 0.035798334 0.036154057 0.036317455 0.036490436 0.036663386
0.036845913 0.037018802 0.037191661 0.037556488 0.037738851 0.037911586
0.038093885 0.038266559 0.038439202 0.038803574 0.03896654  0.039148646
0.03933072  0.03951276  0.039685189 0.039857588 0.04021187  0.04039375
0.040575597 0.040757411 0.040948758 0.041120939 0.041293091 0.041665984
0.041838042 0.04201007  0.042191624 0.042354038 0.042697887 0.042869768
0.043051165 0.04321344  0.043394775 0.043576077 0.043747806 0.044100713
0.044272353 0.044453496 0.044634606 0.044825213 0.045006256 0.045358719
0.045539665 0.045720579 0.045891941 0.046082308 0.046272639 0.04669124
0.046919494 0.047147696 0.047394856 0.047641955 0.047907994 0.048449353
0.048734161 0.049028378 0.049350968 0.04966397  0.050005316 0.050346545
0.051094945 0.051492601 0.051899561 0.052325272 0.052760256 0.053705221
0.05418681  0.054687039 0.05520588  0.055743304 0.056299281 0.056845533
0.057946549 0.058491903 0.059055749 0.059600499 0.060154336 0.060698487
0.061785902 0.062347895 0.062900213 0.06346158  0.063994586 0.064536652
0.065069087 0.066142434 0.06669266  0.067242585 0.06777358  0.068322911
0.069383475 0.069913335 0.070452203 0.070981498 0.071529069 0.072067068
0.072595509 0.073651553 0.074179158 0.074724981 0.075261264 0.07578802
0.076323732 0.0773574   0.077901493 0.078445289 0.078970371 0.079504382
0.080028908 0.080571549 0.081619208 0.082142627 0.08264742  0.083179472
0.083702074 0.084215243 0.0852957   0.085817198 0.086347566 0.08688679
0.08740746  0.08791873  0.088466231 0.089542107 0.090061396 0.090589519
0.091108264 0.091644928 0.092735559 0.093271351 0.093806855 0.094351142
0.094886069 0.09540259  0.095936955 0.096986738 0.097520257 0.098035421
0.09855935  0.099064952 0.099570299 0.100625289 0.101147864 0.101679168
0.10221019  0.102722944 0.103253412 0.104268608 0.104771333 0.105273805
0.105776025 0.106304876 0.107334885 0.107853966 0.108345949 0.108855567
0.109373859 0.109891883 0.110409638 0.11143543  0.111961298 0.112469077
0.112967697 0.113483863 0.11399087  0.115004113 0.115501471 0.115989707
0.116495445 0.116983196 0.117470709 0.117966842 0.118984915 0.119462609
0.119887035 0.120275934 0.120620513 0.12092965  0.121229863 0.121768254
0.121997644 0.122200522 0.122350449 0.122482719 0.122606155 0.122826539
0.122941119 0.123038062 0.123117371 0.123214296 0.123311212 0.123487399
0.123584288 0.123672361 0.123751621 0.123839679 0.12392773  0.124086201
0.12413902  0.124200637 0.124288656 0.124403069 0.12449987  0.124631856
0.124842997 0.12493096  0.125036504 0.125159625 0.125300317 0.125467362
0.125871673 0.126108909 0.126372439 0.126618338 0.126864176 0.127101177
0.127338122 0.127873236 0.128153837 0.128434359 0.12870604  0.129012687
0.129660719 0.129975826 0.130282084 0.130596995 0.130929294 0.131287703
0.131637246 0.132353428 0.132728782 0.133086547 0.133470347 0.133854
0.134228791 0.134995369 0.135395846 0.135787462 0.136178924 0.136570234
0.13696139  0.137777979 0.138177344 0.138593902 0.139001614 0.139417829
0.140241077 0.140648118 0.141072304 0.141479007 0.141894192 0.142317849
0.142732687 0.143579112 0.144002057 0.144416196 0.144838787 0.145261199
0.145692047 0.146527365 0.146949064 0.147379187 0.147817721 0.148264656
0.148694213 0.149132171 0.150007512 0.15045347  0.150890658 0.151327656
0.151790151 0.152226755 0.153107945 0.153552522 0.153996902 0.154441085
0.154902142 0.155345923 0.155798035 0.156710168 0.157161664 0.157629982
0.158089572 0.158523436 0.15945858  0.15991733  0.16038436  0.160851172
0.161292321 0.161758709 0.162216406 0.16315657  0.16362209  0.164095851
0.164560934 0.165025801 0.165507344 0.16644442  0.166908413 0.167372189
2];
    %Plastic Strain
% Martensite
MnD=7.60292e-06;
```

```
MnE=182000;
MnSs=[1079.844948   1088.563488 1093.020698 1097.720938 1102.491834
1107.446938 1112.472756 1117.76393  1128.915245 1134.694702 1140.648315
1146.695486 1152.755584 1158.967548 1171.685126 1178.248882 1185.080662
1191.83376  1198.762763 1206.02984  1213.149636 1227.559367 1234.849366
1242.409749 1250.228763 1258.157094 1273.550987 1280.679329 1287.661441
1294.428989 1301.161611 1307.679542 1313.97001  1326.060058 1332.021852
1337.918473 1343.41144  1348.920493 1354.093613 1364.379756 1369.248464
1373.956769 1378.4095   1382.891612 1387.294576 1391.699892 1399.94624
1403.786936 1407.657226 1411.352454 1415.06352  1422.01508  1425.30924
1428.455459 1431.781058 1434.930734 1438.096147 1441.099448 1446.633197
1449.299107 1452.00888  1454.52768  1457.115686 1459.501346 1464.301671
1466.801896 1468.946052 1471.173581 1473.320005 1475.191946 1477.175823
1481.146602 1482.886246 1484.777218 1486.561843 1488.469097 1490.226682
1491.820006 1494.911805 1496.439173 1498.035434 1499.413332 1500.845552
1502.2392   1504.955688 1506.516883 1507.815608 1509.017402 1511.271029
1512.420336 1513.526335 1514.427293 1515.534029 1516.587232 1517.543042
1519.538768 1520.245757 1521.119416 1521.895391 1522.715392 1523.241626
1523.851253 1525.05606  1525.597    1526.025192 1526.453328 1526.532538
1898.02];
MnSn=[0 0.000148644 0.000237819 0.000326987 0.00040624  0.000505298
0.000594442 0.000703385 0.000921235 0.001030142 0.001148936 0.001277614
0.001416171 0.001544815 0.001841621 0.001989991 0.002158118 0.002326216
0.002504171 0.002691978 0.002889632 0.003284823 0.003482359 0.003699605
0.003926674 0.004173431 0.004676625 0.004923196 0.005179566 0.005455583
0.005701963 0.005967984 0.006243784 0.006785312 0.007051045 0.007326546
0.007601972 0.007887154 0.008162424 0.008722563 0.009007426 0.009292207
0.009567091 0.009861527 0.010155875 0.010450137 0.011038401 0.011332404
0.011645911 0.011949527 0.012262841 0.012898958 0.013202194 0.013515116
0.013837714 0.014150437 0.01447283  0.014795119 0.015449145 0.015761364
0.016102743 0.016424507 0.016736422 0.017077468 0.017720267 0.018080443
0.018421031 0.018761503 0.019101859 0.01942266  0.019762791 0.020442706
0.020782491 0.021112456 0.021481113 0.021820545 0.022169554 0.022518442
0.02320617  0.023564376 0.023912778 0.024280404 0.024628556 0.025005584
0.025710922 0.026087543 0.02645437  0.026811415 0.027534763 0.027910697
0.028257588 0.028633251 0.028979892 0.02934566  0.029701674 0.030413322
0.030768956 0.031124464 0.031470242 0.0318447   0.032190229 0.032535639
0.033216515 0.033571153 0.033906507 0.034241748 0.034567303 2];

%Poissons Ratio for both are the same and will be written direct to the
input
%file

% Transformation from mm scale to element width scale

% Specify Abaqus no. of elements along the width and hight in case user
had
% not used the current script and folder to generate the input file
if gen=='n' || gen=='N';
   L2=input('Please specify number of elements along the X-Axis: ');
   L1=input('Please Specify number of elements along the Y-Axis: ');
   save ('L1.mat','L1');
   save ('L2.mat','L2');
end
load L1.mat
load L2.mat
```

```
%L1=L1(1,1).L1(1,1);
%L2=L2(1,1).L2(1,1)

% Factor to convert from mm to Abaqus element size
factor=((YDic1-YDic2)./L1 + (XDic2-XDic1)./L2)./2; % the unit is
"mm/Element"
MnD=MnD.*factor^4;
MnE=MnE.*factor^2;
MnSs=MnSs.*factor^2;
FeD=FeD.*factor^4;
FeE=FeE.*factor^2;
FeSs=FeSs.*factor^2;

% The following lines will update the generated inpute file with Phases
% Properties
fprintf(fid,'**\r\n');
fprintf(fid,'** MATERIALS\r\n');
fprintf(fid,'**\r\n');
fprintf(fid,'*Material, name=Ferrite\r\n');
fprintf(fid,'*Density\r\n');
fprintf(fid,'%6.8e,\r\n',FeD);
fprintf(fid,'*Elastic\r\n');
fprintf(fid,'%6.8f,\t%6.2f\r\n',FeE, 0.33);
fprintf(fid,'*Plastic\r\n');
for i=1:length(FeSs);
    fprintf(fid,'%6.5e,\t%6.8f\r\n',FeSs(i),FeSn(i));
end
fprintf(fid,'*Material, name=Martensite\r\n');
fprintf(fid,'*Density\r\n');
fprintf(fid,'%6.8e,\r\n',MnD);
fprintf(fid,'*Elastic\r\n');
fprintf(fid,'%6.8f,\t%6.2f\r\n',MnE, 0.33);
fprintf(fid,'*Plastic\r\n');
for i=1:length(MnSs);
    fprintf(fid,'%6.5e,\t%6.8f\r\n',MnSs(i),MnSn(i));
end
fprintf(fid,'** ----------------------------------------------------------
------\r\n');


%-----------------------------------------------
%Define Step and Amplitude
fprintf(fid,'** \r\n');
fprintf(fid,'** STEP: Step-1\r\n');
fprintf(fid,'**\r\n');
fprintf(fid,'*Step, name=Step-1, nlgeom=YES, inc=10000\r\n');
fprintf(fid,'*Static\r\n');
fprintf(fid,'1., 300., 0.003, 300.\r\n');
fprintf(fid,'**\r\n');


%-----------------------------------------------
% Define Boundary Conditions
% Here the difference between DIC Vector location and Abaqus node location
% is small enough
```

```
fprintf(fid,'** BOUNDARY CONDITIONS\r\n');
fprintf(fid,'**\r\n');

if L2+1>=w && L1+1>=h
    xstep=w./(L2+1);
    ystep=h./(L1+1);
    %no. of nodes per one DIC subset = 1/xstep
    xn=[XDic1:xstep:XDic2];
    yn=[YDic2:ystep:YDic1];

    % To set the dic Matric (which is DIC results for area of interest) as
    % square matrix of the vector magnitude ONLY with left, top, right,
bottom edges and scatter inside the
    % edges.
    %------------
    % That is meant the arrangment for the matrices from now on are
    % according to position in the matrix not according to the coordinates
    % of the vectors. YOU MAY NEED TO ADAPT THIS FOR MORE PRECISE
    % COMPARISON (and you don't meed xn and yn).
    %-------------
    n=0;
    for i=1:h;
        for j=1:w;
            n=n+1;
            xadpdic(i,j)=dic(n,3);
            yadpdic(i,j)=dic(n,4);
        end
    end

    % Creating Edges matrix of DIC results for interpolation
    for i=1:w;
        xtopadpdic(i)=xadpdic(1,i);
        ytopadpdic(i)=yadpdic(1,i);
        xbottomadpdic(i)=xadpdic(h,i);
        ybottomadpdic(i)=yadpdic(h,i);
    end
    for i=1:h;
        xleftadpdic(i)=xadpdic(i,1);
        yleftadpdic(i)=yadpdic(i,1);
        xrightadpdic(i)=xadpdic(i,w);
        yrightadpdic(i)=yadpdic(i,w);
    end


    % Creating matrix to set cordinates for the adpdic matrix
    xdic=[1:w];
    ydic=[1:h];


    % It should be done like this
    % xabaqus=[1:w./(L2+5):w];
    % yabaqus=[1:h./(L1+10):h];
    % But when the number of steps is high the accurrcy decrease and you
    % may end up with less no of nodes
    xnode=L2+1;
```

```
    ynode=L1+1;
    for i=0:L2;
        xabaqus(i+1)=1*(L2-i)/L2+w*i/L2;
    end
    for i=0:L1;
        yabaqus(i+1)=1*(L1-i)/L1+h*i/L1;
    end

    %==============
    %BC for all nodes of the meshed model
    %For square interpolation
    % DIC
    n=0;
    for i=1:h;
        for j=1:w;
            sqxdic(i,j)=xdic(j);
            sqydic(i,j)=ydic(i);
        end
    end
    %Abaqus
    for i=0:L1;
        for j=0:L2;
            sqxabaqus(i+1,j+1)=xabaqus(j+1);
            sqyabaqus(i+1,j+1)=yabaqus(i+1);
        end
    end

    % Interpolation

xadpabq=interp2(sqxdic,sqydic,xadpdic,sqxabaqus,sqyabaqus,'spline')./facto
r;

yadpabq=interp2(sqxdic,sqydic,yadpdic,sqxabaqus,sqyabaqus,'spline')./facto
r;


    %========================
    % For X boundary condition
    fprintf(fid,'** Name: x Type: Displacement/Rotation Using
Analytical\r\n');
    fprintf(fid,'Field: x\r\n');
    fprintf(fid,'*Boundary, amplitude=Amp-1\r\n');
    n=0;
    for j=1:xnode;
        for i=1:ynode;
            n=n+1;
            fprintf(fid,'PART-1-1.%u, 1, 1, %6.5f\r\n',n,xadpabq(i,j));
        end
    end
    % For Y boundary condition
    fprintf(fid,'** Name: y Type: Displacement/Rotation Using
Analytical\r\n');
    fprintf(fid,'Field: y\r\n');
    fprintf(fid,'*Boundary, amplitude=Amp-1\r\n');
    n=0;
    for j=1:xnode;
```

```
        for i=1:ynode;
            n=n+1;
            fprintf(fid,'PART-1-1.%u, 2, 2, %6.5f\r\n',n,yadpabq(i,j));
        end
    end
    %=========================


    fprintf(fid,'**\r\n');
    fprintf(fid,'** OUTPUT REQUESTS\r\n');
    fprintf(fid,'**\r\n');
    fprintf(fid,'*Restart, write, frequency=0\r\n');
    fprintf(fid,'**\r\n');
    fprintf(fid,'** FIELD OUTPUT: F-Output-1\r\n');
    fprintf(fid,'**\r\n');
    fprintf(fid,'*Output, field\r\n');
    fprintf(fid,'*Node Output\r\n');
    fprintf(fid,'CF, COORD, RF, U\r\n');
    fprintf(fid,'*Element Output, directions=YES\r\n');
    fprintf(fid,'LE, PE, PEEQ, PEMAG, S, EVOL, IVOL\r\n');
    fprintf(fid,'*Contact Output\r\n');
    fprintf(fid,'CDISP, CSTRESS\r\n');
    fprintf(fid,'**\r\n');
    fprintf(fid,'** HISTORY OUTPUT: H-Output-1\r\n');
    fprintf(fid,'**\r\n');
    fprintf(fid,'*Output, history, variable=PRESELECT\r\n');
    fprintf(fid,'*End Step\r\n');
else
    disp('No. of nodes in Abaqus less than no. vectors in DIC');
    disp('There might be something wrong or you might need to recode this
coding');
    disp('Sorry!!!');
end
fclose('all');
```

MatLab Code to apply boundary condition on edges only:

```
% This code written by Khaled Alharbi
% The code help generate ABAQUS input file with material properties and
% boundary conditions.
% Please add to the folder the following:
%   1. DIC results from Lavision as DIC.DAT
%   2. Image of area of interest in bmb ot jpg extension format

%-----------------------------------------------

%IMPORTING DIC RESULTS
%NOTE:
%DATA SOURCE: LAVISION
%FILE NAME: DIC.DAT
%DATA ARRANGED:Y-POSITION THEN X-POSITION
%DATA TYPE: X-POSITION Y-POSITION X-DISP Y-DISP
%OTHER: Import function used to import data from lavision results
% please make sure lavision results file named and extension is as DIC.DAT
% and make sure that the data are arranged according to y position first
% from top to bottom and then arranged according to x position from left
to
% right
importDIC('DIC.DAT');
dicall=data;
%-----------------------------------------------

%EXTRACT AREA OF INTEREST DATA
% User should specify area of interest according to x/y-positions
XDic1=input( 'Please enter the DIC X Start Left ' );
XDic2=input( 'Please enter the DIC X end Right ' );
YDic1=input( 'Please enter the DIC Y start Top ' );
YDic2=input( 'Please enter the DIC Y end Bottom ' );

%to find the number of data along x and y axis from lavision file
xlength=0;
ylength=0;
yvalue=dicall(1,2);
xvalue=dicall(1,1);
for i=1:length(dicall);
    if dicall(i,2)== yvalue;
        xlength=xlength+1;
    end
end
for i=1:length(dicall);
    if dicall(i,1)== xvalue;
        ylength=ylength+1;
    end
end


%construct dic matrix with cells of interest and vector magnitude
% this dic matrix has arranged in similar way of lavision data
%meaning that first according to y position then according to y position
```

```
%first column x position
%2nd column   y position
%3rd          x disp
%4th          y disp
%5th          magnitude disp
m=0;
n=0;
a=0;
b=1;
w=0;    %No of vectors along x axis for SELECTED AREA OF INTEREST
h=0;    %No of vectors along y axis for SELECTED AREA OF INTEREST
for i=1:ylength; % move as cluster for every y value
    if ((dicall(b,2)<= YDic1) && (dicall(b,2)>= YDic2));
        h=h+1;
        m=i*xlength; % to set the start of the cells to check and the end
for that y value
        n=m-xlength+1;
        w=0;
        for j=n:m;
            if ((dicall(j,1)<= XDic2) && (dicall(j,1)>= XDic1))
                w=w+1;
                a=a+1; % to creat new cell number for dic matrix
                dic(a,5)= sqrt(dicall(j,3)^2+dicall(j,4)^2); %calculate
the magnitude
                dic(a,4)= dicall(j,4);
                dic(a,3)= dicall(j,3);
                dic(a,2)=dicall(j,2);
                dic(a,1)=dicall(j,1);
            end
        end
    end
    b=b+xlength; %this one will be used to set the index for next y value
checking
end

%-------------------------------------------------
%The following lines call code written by:

% I.CHALON,
%french visiting student,
%in second year at ENSMN (Nancy, France),
%at IMMPETUS, 07/2004

%to generate abaqus zazamesh.inp input file with two phases

gen=input('Do you want to generate the input file from an image? (Y/N)
[Y]: ','s');
if isempty(gen);,gen='Y';,end;
if gen=='y' || gen=='Y';
    disp('')
    disp('')
    disp('')
    disp('Please use I.Chalon window and when you finish close the window
and')
    disp('write "return" (as lower case lette) at the command line.')
    pixel3;
```

```
    keyboard
else
    disp('')
    disp('')
    disp('')
    disp('Please make sure you copy and paste the generated mesh input
file')
    disp('in the current folder with name of "zaza_mesh.inp" before
proceeding.')
    disp('To continue write "return" (as lower case lette) at the command
line.')
end;

% ==============
% Reset YDic and XDic to exact value for accurate Factor calculation
YDic1=max(dic(:,2));
YDic2=min(dic(:,2));
XDic2=max(dic(:,1));
XDic1=min(dic(:,1));

% ==============


%-------------------------------------------------
% Update the generated input file from I.Chalon CODE
fid=fopen('zaza_mesh.inp','a');
%Define section assignment and Assembly
fprintf(fid,'\r\n');
fprintf(fid,'** Section: Section-1-PHASE1\r\n');
fprintf(fid,'*Solid Section, elset=PHASE1, material=Martensite\r\n');
fprintf(fid,'1.,\r\n');
fprintf(fid,'** Section: Section-2-PHASE2\r\n');
fprintf(fid,'*Solid Section, elset=PHASE2, material=Ferrite\r\n');
fprintf(fid,'1.,\r\n');
fprintf(fid,'*End Part\r\n');
fprintf(fid,'** \r\n');
fprintf(fid,'** \r\n');

fprintf(fid,'** ASSEMBLY\r\n');
fprintf(fid,'**\r\n');
fprintf(fid,'*Assembly, name=Assembly\r\n');
fprintf(fid,'**\r\n');
fprintf(fid,'*Instance, name=PART-1-1, part=PART-1\r\n');
fprintf(fid,'*End Instance\r\n');
fprintf(fid,'**\r\n');
fprintf(fid,'*End Assembly\r\n');
fprintf(fid,'*Amplitude, name=Amp-1\r\n');
fprintf(fid,'0.,0.,300.,1.\r\n');
fprintf(fid,'**\r\n');

%-------------------------------------------------
%Define Phases Mechanical Properties
%Phases Material properties in mm
% Ferrite
% Ferrite
```

```
FeD=7.60292e-06;  %kg/mm3
FeE=198000;  %MPa Modulus
FeSs=[444.095988    444.423576  446.506089  447.44946   448.09632
448.34174   448.692069  449.046936  449.46005   449.618676  449.618676
449.648 449.648 449.648 449.648 449.648 449.648 449.648 449.648 449.648
449.648 449.648 449.648 449.648 449.648 449.648 449.648 449.648 449.648
449.648 449.648 449.648 449.648 449.648 449.648 449.648 449.648 449.648
449.648 449.648 449.648 449.648 449.648 449.648 449.648 449.648 449.648
449.648 449.648 449.648 449.648 449.648 449.648 449.648 449.648 449.648
449.648 449.648 449.648 449.648 449.648 449.648 449.648 449.648 449.648
449.648 449.648 449.648 449.648 449.648 449.648 449.648 449.648 449.648
449.648 449.648 449.648 449.648 449.648 449.648 449.648 449.648 449.648
449.648 449.648 449.648 449.648 449.648 449.648 449.648 449.648 449.648
449.648 449.648 449.648 449.648 449.648 449.648 449.648 449.648 449.648
449.648 449.648 449.648 449.648 449.648 449.648 449.648 449.648 449.648
449.648 449.648 449.648 449.648 449.648 449.648 449.648 449.648 449.648
449.648 449.648 449.648 450.51837   451.535452  452.548519  452.9386
453.935664  454.22654   454.612707  454.90375   455.186115  455.348064
455.526522  455.526522  455.526522  455.526522  455.741994  455.92492
455.92492   456.070269  456.25327   456.54492   456.936516  457.32822
458.016428  458.299725  458.59188   458.884111  459.2808    459.6732
459.856872  460.22873   460.521392  460.81413   460.81413   460.81413
460.81413   460.81413   460.81413   460.81413   460.81413   460.81413
461.215674  462.316725  462.605661  462.899088  463.498056  463.791688
464.085396  464.37475   465.06297   465.56232   465.56232   465.56232
465.56232   465.56232   465.56232   465.56232   465.56232   465.56232
465.56232   465.56232   466.059022  466.480888  466.902898  466.913104
467.76513   468.626424  469.72274   469.85654   470.20556   470.67351
471.031749  471.614493  472.092006  473.07904   473.7954    475.045085
476.093184  476.617644  477.597614  478.14545   478.49067   479.26916
479.5268    479.79348   480.161847  480.478156  480.478156  480.478156
481.167 482.072916  482.655159  482.655159  482.655159  482.655159
482.655159  482.751097  484.190148  485.197604  486.897858  487.916642
488.399667  489.08857   489.08857   490.091679  490.889448  490.93872
490.93872   491.359902  491.839996  492.531545  493.699997  493.960544
493.960544  493.960544  494.431184  495.237608  496.400232  496.77886
496.77886   496.77886   496.77886   497.075954  497.672032  498.846922
499.543808  499.687055  499.843944  499.887036  500.689398  501.55848
501.55848   501.55848   501.55848   501.55848   501.55848   501.55848
501.717564  502.417344  502.463048  502.943584  502.943584  502.943584
502.943584  502.943584  502.943584  502.943584  502.943584  503.169196
505.134933  505.51512   506.439648  507.369442  507.626034  507.882626
508.41872   509.01753   509.621276  510.003104  510.598256  510.980436
511.499445  512.202337  512.682723  513.386399  513.88116   514.299028
514.56606   514.70746   514.70746   514.70746   514.943814  515.322549
515.322549  515.673875  516.4972    517.091814  517.695976  518.183424
518.93387   519.417276  519.896292  520.272025  520.63864   520.89252
521.263917  521.455824  521.455824  521.455824  521.455824  521.455824
521.455824  521.455824  521.662593  521.662593  521.662593  521.662593
521.662593  521.662593  521.662593  521.662593  521.662593  521.662593
521.662593  521.662593  521.662593  521.662593  521.662593  521.662593
```

```
521.662593  521.662593  521.662593  521.662593  521.662593  521.662593
521.662593  521.662593  522.022008  522.022008  522.022008  522.915498
524.117044  525.100644  525.870873  526.652516  527.00512   527.00512
527.00512   527.00512   527.00512   527.197464  527.93575   528.197967
528.574337  529.06032   529.45089   529.565644  529.565644  529.8948
530.51904   531.038482  531.457675  531.75793   532.253439  532.56784
532.873029  533.19225   533.39685   533.711552  534.23568   534.564558
534.888874  534.983328  535.307734  535.63223   536.30012   536.629548
536.737878  537.072058  537.410991  537.96904   538.072569  538.4164
538.63542   538.974735  539.318808  539.542584  539.99946   540.343777
540.567601  540.796088  541.024575  541.257725  541.826208  542.170965
542.404215  542.64213   542.88471   543.234384  543.355875  543.948282
544.190914  544.3122    544.666846  544.91881   545.03994   545.520435
545.763015  546.122638  546.248175  546.500085  546.742665  546.755402
547.254343  547.501482  547.757947  548.009749  548.012414  548.525124
548.776818  548.91538   549.053832  549.2961    549.43439   549.449904
549.96672   550.104625  550.128843  550.384758  550.403991  550.669098
550.829832  550.966908  551.222493 1572.73];
                %Mpa Plastic Stress
FeSn=[0 5.97961E-05 0.000229199 0.000318871 0.000418498 0.000518114
0.000627681 0.000747194 0.000996135 0.00112556  0.001264922 0.001414216
0.001553538 0.001702789 0.001852018 0.002160355 0.002319459 0.002498421
0.002667411 0.002846311 0.00319408  0.003362953 0.003551659 0.00374033
0.003909111 0.004097714 0.004286282 0.004653391 0.004841854 0.005030282
0.005218674 0.005397118 0.005744001 0.005932259 0.006120481 0.006308668
0.006477015 0.006665135 0.00685322  0.007219388 0.007397475 0.007575531
0.007763444 0.007951322 0.008307204 0.008485098 0.00868272  0.008850669
0.009038343 0.009225981 0.009403712 0.009778817 0.009966316 0.010143915
0.010331346 0.010518743 0.010706104 0.011070864 0.011267976 0.011445344
0.01162268  0.011809835 0.011996954 0.012184038 0.01254826  0.012735241
0.012932026 0.013118935 0.013295975 0.013482816 0.013669623 0.014023477
0.014210182 0.014396853 0.014593311 0.01477009  0.014956656 0.015329684
0.01549652  0.015682951 0.015849728 0.016045901 0.016232229 0.016604782
0.016781206 0.016967397 0.017153554 0.017339676 0.01751597  0.017897835
0.018083818 0.018269767 0.018445898 0.018621997 0.018807846 0.018983882
0.019345636 0.019521577 0.019707259 0.019892906 0.020088287 0.020283631
0.02066444  0.020840149 0.021025586 0.021220746 0.021406113 0.021591445
0.021766992 0.02212774  0.022303193 0.022478614 0.022663748 0.022829365
0.023199468 0.023364997 0.023549966 0.023715437 0.023890611 0.024075483
0.024250594 0.024629896 0.024824354 0.025009054 0.02519372  0.025368635
0.025553234 0.025902909 0.0260777   0.026271876 0.026456309 0.026631004
0.026815371 0.027184002 0.027358569 0.027542802 0.027727001 0.027920857
0.02829877  0.028492516 0.028686224 0.028879895 0.029054167 0.029238087
0.029421974 0.029770298 0.029944415 0.03010883  0.030292557 0.030447248
0.030630912 0.030978816 0.031162383 0.031345916 0.031529415 0.031703226
0.03188666  0.03207006  0.032417463 0.032600766 0.032764746 0.032957629
0.033140833 0.033324003 0.033680607 0.033863679 0.034046717 0.03421046
0.034393434 0.034566748 0.034740031 0.035105754 0.035288565 0.035452104
0.035634852 0.035798334 0.036154057 0.036317455 0.036490436 0.036663386
0.036845913 0.037018802 0.037191661 0.037556488 0.037738851 0.037911586
0.038093885 0.038266559 0.038439202 0.038803574 0.03896654  0.039148646
0.03933072  0.03951276  0.039685189 0.039857588 0.04021187  0.04039375
0.040575597 0.040757411 0.040948758 0.041120939 0.041293091 0.041665984
0.041838042 0.04201007  0.042191624 0.042354038 0.042697887 0.042869768
0.043051165 0.04321344  0.043394775 0.043576077 0.043747806 0.044100713
0.044272353 0.044453496 0.044634606 0.044825213 0.045006256 0.045358719
```

```
0.045539665 0.045720579 0.045891941 0.046082308 0.046272639 0.04669124
0.046919494 0.047147696 0.047394856 0.047641955 0.047907994 0.048449353
0.048734161 0.049028378 0.049350968 0.04966397  0.050005316 0.050346545
0.051094945 0.051492601 0.051899561 0.052325272 0.052760256 0.053705221
0.05418681  0.054687039 0.05520588  0.055743304 0.056299281 0.056845533
0.057946549 0.058491903 0.059055749 0.059600499 0.060154336 0.060698487
0.061785902 0.062347895 0.062900213 0.06346158  0.063994586 0.064536652
0.065069087 0.066142434 0.06669266  0.067242585 0.06777358  0.068322911
0.069383475 0.069913335 0.070452203 0.070981498 0.071529069 0.072067068
0.072595509 0.073651553 0.074179158 0.074724981 0.075261264 0.07578802
0.076323732 0.0773574   0.077901493 0.078445289 0.078970371 0.079504382
0.080028908 0.080571549 0.081619208 0.082142627 0.08264742  0.083179472
0.083702074 0.084215243 0.0852957   0.085817198 0.086347566 0.08688679
0.08740746  0.08791873  0.088466231 0.089542107 0.090061396 0.090589519
0.091108264 0.091644928 0.092735559 0.093271351 0.093806855 0.094351142
0.094886069 0.09540259  0.095936955 0.096986738 0.097520257 0.098035421
0.09855935  0.099064952 0.099570299 0.100625289 0.101147864 0.101679168
0.10221019  0.102722944 0.103253412 0.104268608 0.104771333 0.105273805
0.105776025 0.106304876 0.107334885 0.107853966 0.108345949 0.108855567
0.109373859 0.109891883 0.110409638 0.11143543  0.111961298 0.112469077
0.112967697 0.113483863 0.11399087  0.115004113 0.115501471 0.115989707
0.116495445 0.116983196 0.117470709 0.117966842 0.118984915 0.119462609
0.119887035 0.120275934 0.120620513 0.12092965  0.121229863 0.121768254
0.121997644 0.122200522 0.122350449 0.122482719 0.122606155 0.122826539
0.122941119 0.123038062 0.123117371 0.123214296 0.123311212 0.123487399
0.123584288 0.123672361 0.123751621 0.123839679 0.12392773  0.124086201
0.12413902  0.124200637 0.124288656 0.124403069 0.12449987  0.124631856
0.124842997 0.12493096  0.125036504 0.125159625 0.125300317 0.125467362
0.125871673 0.126108909 0.126372439 0.126618338 0.126864176 0.127101177
0.127338122 0.127873236 0.128153837 0.128434359 0.12870604  0.129012687
0.129660719 0.129975826 0.130282084 0.130596995 0.130929294 0.131287703
0.131637246 0.132353428 0.132728782 0.133086547 0.133470347 0.133854
0.134228791 0.134995369 0.135395846 0.135787462 0.136178924 0.136570234
0.13696139  0.137777979 0.138177344 0.138593902 0.139001614 0.139417829
0.140241077 0.140648118 0.141072304 0.141479007 0.141894192 0.142317849
0.142732687 0.143579112 0.144002057 0.144416196 0.144838787 0.145261199
0.145692047 0.146527365 0.146949064 0.147379187 0.147817721 0.148264656
0.148694213 0.149132171 0.150007512 0.15045347  0.150890658 0.151327656
0.151790151 0.152226755 0.153107945 0.153552522 0.153996902 0.154441085
0.154902142 0.155345923 0.155798035 0.156710168 0.157161664 0.157629982
0.158089572 0.158523436 0.15945858  0.15991733  0.16038436  0.160851172
0.161292321 0.161758709 0.162216406 0.16315657  0.16362209  0.164095851
0.164560934 0.165025801 0.165507344 0.16644442  0.166908413 0.167372189
2];
    %Plastic Strain
% Martensite
MnD=7.60292e-06;
MnE=182000;
MnSs=[1079.844948   1088.563488 1093.020698 1097.720938 1102.491834
1107.446938 1112.472756 1117.76393  1128.915245 1134.694702 1140.648315
1146.695486 1152.755584 1158.967548 1171.685126 1178.248882 1185.080662
1191.83376  1198.762763 1206.02984  1213.149636 1227.559367 1234.849366
1242.409749 1250.228763 1258.157094 1273.550987 1280.679329 1287.661441
1294.428989 1301.161611 1307.679542 1313.97001  1326.060058 1332.021852
1337.918473 1343.41144  1348.920493 1354.093613 1364.379756 1369.248464
1373.956769 1378.4095   1382.891612 1387.294576 1391.699892 1399.94624
```

```
1403.786936 1407.657226 1411.352454 1415.06352  1422.01508  1425.30924
1428.455459 1431.781058 1434.930734 1438.096147 1441.099448 1446.633197
1449.299107 1452.00888  1454.52768  1457.115686 1459.501346 1464.301671
1466.801896 1468.946052 1471.173581 1473.320005 1475.191946 1477.175823
1481.146602 1482.886246 1484.777218 1486.561843 1488.469097 1490.226682
1491.820006 1494.911805 1496.439173 1498.035434 1499.413332 1500.845552
1502.2392   1504.955688 1506.516883 1507.815608 1509.017402 1511.271029
1512.420336 1513.526335 1514.427293 1515.534029 1516.587232 1517.543042
1519.538768 1520.245757 1521.119416 1521.895391 1522.715392 1523.241626
1523.851253 1525.05606  1525.597    1526.025192 1526.453328 1526.532538
1898.02];
MnSn=[0 0.000148644 0.000237819 0.000326987 0.00040624  0.000505298
0.000594442 0.000703385 0.000921235 0.001030142 0.001148936 0.001277614
0.001416171 0.001544815 0.001841621 0.001989991 0.002158118 0.002326216
0.002504171 0.002691978 0.002889632 0.003284823 0.003482359 0.003699605
0.003926674 0.004173431 0.004676625 0.004923196 0.005179566 0.005455583
0.005701963 0.005967984 0.006243784 0.006785312 0.007051045 0.007326546
0.007601972 0.007887154 0.008162424 0.008722563 0.009007426 0.009292207
0.009567091 0.009861527 0.010155875 0.010450137 0.011038401 0.011332404
0.011645911 0.011949527 0.012262841 0.012898958 0.013202194 0.013515116
0.013837714 0.014150437 0.01447283  0.014795119 0.015449145 0.015761364
0.016102743 0.016424507 0.016736422 0.017077468 0.017720267 0.018080443
0.018421031 0.018761503 0.019101859 0.01942266  0.019762791 0.020442706
0.020782491 0.021112456 0.021481113 0.021820545 0.022169554 0.022518442
0.02320617  0.023564376 0.023912778 0.024280404 0.024628556 0.025005584
0.025710922 0.026087543 0.02645437  0.026811415 0.027534763 0.027910697
0.028257588 0.028633251 0.028979892 0.02934566  0.029701674 0.030413322
0.030768956 0.031124464 0.031470242 0.0318447   0.032190229 0.032535639
0.033216515 0.033571153 0.033906507 0.034241748 0.034567303 2];

%Poissons Ratio for both are the same and will be written direct to the
input
%file

% Transformation from mm scale to element width scale

% Specify Abaqus no. of elements along the width and hight in case user
had
% not used the current script and folder to generate the input file
if gen=='n' || gen=='N';
   L2=input('Please specify number of elements along the X-Axis: ');
   L1=input('Please Specify number of elements along the Y-Axis: ');
   save ('L1.mat','L1');
   save ('L2.mat','L2');
end
load L1.mat
load L2.mat
%L1=L1(1,1).L1(1,1);
%L2=L2(1,1).L2(1,1)

% Factor to convert from mm to Abaqus element size
factor=((YDic1-YDic2)./L1 + (XDic2-XDic1)./L2)./2; % the unit is
"mm/Element"
MnD=MnD.*factor^4;
MnE=MnE.*factor^2;
MnSs=MnSs.*factor^2;
```

```
FeD=FeD.*factor^4;
FeE=FeE.*factor^2;
FeSs=FeSs.*factor^2;

% The following lines will update the generated inpute file with Phases
% Properties
fprintf(fid,'**\r\n');
fprintf(fid,'** MATERIALS\r\n');
fprintf(fid,'**\r\n');
fprintf(fid,'*Material, name=Ferrite\r\n');
fprintf(fid,'*Density\r\n');
fprintf(fid,'%6.8e,\r\n',FeD);
fprintf(fid,'*Elastic\r\n');
fprintf(fid,'%6.8f,\t%6.2f\r\n',FeE, 0.33);
fprintf(fid,'*Plastic\r\n');
for i=1:length(FeSs);
    fprintf(fid,'%6.5e,\t%6.8f\r\n',FeSs(i),FeSn(i));
end
fprintf(fid,'*Material, name=Martensite\r\n');
fprintf(fid,'*Density\r\n');
fprintf(fid,'%6.8e,\r\n',MnD);
fprintf(fid,'*Elastic\r\n');
fprintf(fid,'%6.8f,\t%6.2f\r\n',MnE, 0.33);
fprintf(fid,'*Plastic\r\n');
for i=1:length(MnSs);
    fprintf(fid,'%6.5e,\t%6.8f\r\n',MnSs(i),MnSn(i));
end
fprintf(fid,'** ------------------------------------------------------------
------\r\n');


%-------------------------------------------------
%Define Step and Amplitude
fprintf(fid,'** \r\n');
fprintf(fid,'** STEP: Step-1\r\n');
fprintf(fid,'**\r\n');
fprintf(fid,'*Step, name=Step-1, nlgeom=YES, inc=10000\r\n');
fprintf(fid,'*Static\r\n');
fprintf(fid,'1., 300., 0.003, 300.\r\n');
fprintf(fid,'**\r\n');


%-------------------------------------------------
% Define Boundary Conditions
% Here the difference between DIC Vector location and Abaqus node location
% is small enough
fprintf(fid,'** BOUNDARY CONDITIONS\r\n');
fprintf(fid,'**\r\n');

if L2+1>=w && L1+1>=h
    xstep=w./(L2+1);
    ystep=h./(L1+1);
    %no. of nodes per one DIC subset = 1/xstep
    xn=[XDic1:xstep:XDic2];
    yn=[YDic2:ystep:YDic1];
```

```
    % To set the dic Matric (which is DIC results for area of interest) as
    % square matrix of the vector magnitude ONLY with left, top, right,
bottom edges and scatter inside the
    % edges.
    %------------
    % That is meant the arrangment for the matrices from now on are
    % according to position in the matrix not according to the coordinates
    % of the vectors. YOU MAY NEED TO ADAPT THIS FOR MORE PRECISE
    % COMPARISON (and you don't meed xn and yn).
    %-------------
    n=0;
    for i=1:h;
        for j=1:w;
            n=n+1;
            xadpdic(i,j)=dic(n,3);
            yadpdic(i,j)=dic(n,4);
        end
    end

    % Creating Edges matrix of DIC results for interpolation
    for i=1:w;
        xtopadpdic(i)=xadpdic(1,i);
        ytopadpdic(i)=yadpdic(1,i);
        xbottomadpdic(i)=xadpdic(h,i);
        ybottomadpdic(i)=yadpdic(h,i);
    end
    for i=1:h;
        xleftadpdic(i)=xadpdic(i,1);
        yleftadpdic(i)=yadpdic(i,1);
        xrightadpdic(i)=xadpdic(i,w);
        yrightadpdic(i)=yadpdic(i,w);
    end


    % Creating matrix to set cordinates for the adpdic matrix
    xdic=[1:w];
    ydic=[1:h];


    % It should be done like this
    % xabaqus=[1:w./(L2+5):w];
    % yabaqus=[1:h./(L1+10):h];
    % But when the number of steps is high the accurrcy decrease and you
    % may end up with less no of nodes
    xnode=L2+1;
    ynode=L1+1;
    for i=0:L2;
        xabaqus(i+1)=1*(L2-i)/L2+w*i/L2;
    end
    for i=0:L1;
        yabaqus(i+1)=1*(L1-i)/L1+h*i/L1;
    end

    % The interpolation
```

```
    xtopabaqus=interp1(xdic,xtopadpdic,xabaqus,'spline')./factor;
    ytopabaqus=interp1(xdic,ytopadpdic,xabaqus,'spline')./factor;
    xbottomabaqus=interp1(xdic,xbottomadpdic,xabaqus,'spline')./factor;
    ybottomabaqus=interp1(xdic,ybottomadpdic,xabaqus,'spline')./factor;
    xleftabaqus=interp1(ydic,xleftadpdic,yabaqus,'spline')./factor;
    yleftabaqus=interp1(ydic,yleftadpdic,yabaqus,'spline')./factor;
    xrightabaqus=interp1(ydic,xrightadpdic,yabaqus,'spline')./factor;
    yrightabaqus=interp1(ydic,yrightadpdic,yabaqus,'spline')./factor;

    % For bottom X boundary condition
    fprintf(fid,'** Name: bottom x Type: Displacement/Rotation Using
Analytical\r\n');
    fprintf(fid,'Field: bottom x\r\n');
    fprintf(fid,'*Boundary, amplitude=Amp-1\r\n');
    n=0;
    for i=ynode:ynode:xnode*ynode;
        n=n+1;
        fprintf(fid,'PART-1-1.%u, 1, 1, %6.5f\r\n',i,xbottomabaqus(n));
    end
    % For bottom Y boundary condition
    fprintf(fid,'** Name: bottom y Type: Displacement/Rotation Using
Analytical\r\n');
    fprintf(fid,'Field: bottom y\r\n');
    fprintf(fid,'*Boundary, amplitude=Amp-1\r\n');
    n=0;
    for i=ynode:ynode:xnode*ynode;
        n=n+1;
        fprintf(fid,'PART-1-1.%u, 2, 2, %6.5f\r\n',i,ybottomabaqus(n));
    end

    % For top X boundary condition
    fprintf(fid,'** Name: top x Type: Displacement/Rotation Using
Analytical\r\n');
    fprintf(fid,'Field: top x\r\n');
    fprintf(fid,'*Boundary, amplitude=Amp-1\r\n');
    n=0;
    for i=1:ynode:xnode*ynode-ynode+1;
        n=n+1;
        fprintf(fid,'PART-1-1.%u, 1, 1, %6.5f\r\n',i,xtopabaqus(n));
    end
    % For top Y boundary condition
    fprintf(fid,'** Name: top y Type: Displacement/Rotation Using
Analytical\r\n');
    fprintf(fid,'Field: top y\r\n');
    fprintf(fid,'*Boundary, amplitude=Amp-1\r\n');
    n=0;
    for i=1:ynode:xnode*ynode-ynode+1;
        n=n+1;
        fprintf(fid,'PART-1-1.%u, 2, 2, %6.5f\r\n',i,ytopabaqus(n));
    end

    % For right X boundary condition
    fprintf(fid,'** Name: right x Type: Displacement/Rotation Using
Analytical\r\n');
    fprintf(fid,'Field: right x\r\n');
    fprintf(fid,'*Boundary, amplitude=Amp-1\r\n');
```

```
    n=1;
    for i=(xnode-1)*ynode+2:xnode*ynode-1;
        n=n+1;
        fprintf(fid,'PART-1-1.%u, 1, 1, %6.5f\r\n',i,xrightabaqus(n));
    end
    % For right Y boundary condition
    fprintf(fid,'** Name: right y Type: Displacement/Rotation Using
Analytical\r\n');
    fprintf(fid,'Field: right y\r\n');
    fprintf(fid,'*Boundary, amplitude=Amp-1\r\n');
    n=1;
    for i=(xnode-1)*ynode+2:xnode*ynode-1;
        n=n+1;
        fprintf(fid,'PART-1-1.%u, 2, 2, %6.5f\r\n',i,yrightabaqus(n));
    end

    % For left X boundary condition
    fprintf(fid,'** Name: left x Type: Displacement/Rotation Using
Analytical\r\n');
    fprintf(fid,'Field: left x\r\n');
    fprintf(fid,'*Boundary, amplitude=Amp-1\r\n');
    n=1;
    for i=2:ynode-1;
        n=n+1;
        fprintf(fid,'PART-1-1.%u, 1, 1, %6.5f\r\n',i,xleftabaqus(n));
    end
    % For left Y boundary condition
    fprintf(fid,'** Name: left y Type: Displacement/Rotation Using
Analytical\r\n');
    fprintf(fid,'Field: left y\r\n');
    fprintf(fid,'*Boundary, amplitude=Amp-1\r\n');
    n=1;
    for i=2:ynode-1;
        n=n+1;
        fprintf(fid,'PART-1-1.%u, 2, 2, %6.5f\r\n',i,yleftabaqus(n));
    end

    fprintf(fid,'**\r\n');
    fprintf(fid,'** OUTPUT REQUESTS\r\n');
    fprintf(fid,'**\r\n');
    fprintf(fid,'*Restart, write, frequency=0\r\n');
    fprintf(fid,'**\r\n');
    fprintf(fid,'** FIELD OUTPUT: F-Output-1\r\n');
    fprintf(fid,'**\r\n');
    fprintf(fid,'*Output, field\r\n');
    fprintf(fid,'*Node Output\r\n');
    fprintf(fid,'CF, COORD, RF, U\r\n');
    fprintf(fid,'*Element Output, directions=YES\r\n');
    fprintf(fid,'LE, PE, PEEQ, PEMAG, S, EVOL, IVOL\r\n');
    fprintf(fid,'*Contact Output\r\n');
    fprintf(fid,'CDISP, CSTRESS\r\n');
    fprintf(fid,'**\r\n');
    fprintf(fid,'** HISTORY OUTPUT: H-Output-1\r\n');
    fprintf(fid,'**\r\n');
    fprintf(fid,'*Output, history, variable=PRESELECT\r\n');
    fprintf(fid,'*End Step\r\n');
```

```
else
    disp('No. of nodes in Abaqus less than no. vectors in DIC');
    disp('There might be something wrong or you might need to recode this
coding');
    disp('Sorry!!!');
end
fclose('all');
```

Appendix II MatLab Code to calculate error in displacement results of the microstructure modelling

```
data=zeros;
keyboard;
% Import Abaqus Results
importfileAbaqus('abaqus.rpt');
abaqus=data;

% Change abaqus imported results to square matrix
n=1;
for i=1:xnode;
    for j=1:ynode;
        abaqusv(j,i)=data(n,4);
        abaqusx(j,i)=data(n,5);
        abaqusy(j,i)=data(n,6);
        n=n+1;
    end

end

% Creat square matrix of DIC Results
n=0;
for i=1:h;
    for j=1:w;
        n=n+1;
        adpdic(i,j)=dic(n,5);
    end
end
% ----------------------------
% For interpolation Purposes: Creating square matrices of the positions of
% DIC vectors (x/ydicsq are for actual DIC Results and x/ynodesq are for
% interpolated DIC results with number of vectors matches no of results
from Abaqus
for i=1:h;
    xdicsq(i,:)=xdic;
end
for i=1:w;
    ydicsq(:,i)=ydic';
end
for i=1:ynode;
    xnodesq(i,:)=xabaqus;
end
for i=1:xnode;
    ynodesq(:,i)=yabaqus';
end

% Generating interpolated DIC results with number of vectors matches no
% of results from Abaqus
dictoabaqus=interp2(xdicsq,ydicsq,adpdic,xnodesq,ynodesq,'spline');
xdictoabaqus=interp2(xdicsq,ydicsq,xadpdic,xnodesq,ynodesq,'spline');
%++++++
```

```
ydictoabaqus=interp2(xdicsq,ydicsq,yadpdic,xnodesq,ynodesq,'spline');
%++++++

% Here Figure of the actual DIC Results topped with interpolated one.
figure(1);
mesh(xdicsq,ydicsq,adpdic), hold,
mesh(xnodesq,ynodesq,dictoabaqus+mean(mean(adpdic)));
hold off;


dictoabaqusm=dictoabaqus*1000;   %Change DIC vector results from mm to
micron
xdictoabaqusm=xdictoabaqus*1000; %Change DIC X      results from mm to
micron +++++++++
ydictoabaqusm=ydictoabaqus*1000; %Change DIC Y      results from mm to
micron +++++++++
abaqusvm=abaqusv*factor*1000;    %Change abaqus vector results to mm by
factor and from mm to micron by *1000
abaqusxm=abaqusx*factor*1000;    %Change abaqus X      results to mm by
factor and from mm to micron by *1000 ++++
abaqusym=abaqusy*factor*1000;    %Change abaqus Y      results to mm by
factor and from mm to micron by *1000 ++++

dif=dictoabaqusm-abaqusvm;
absdif=abs(dictoabaqusm-abaqusvm);
abserror=absdif./abs(dictoabaqusm)*100;
error=dif./dictoabaqusm*100;
%****************
xdif=xdictoabaqusm-abaqusxm;
xabsdif=abs(xdictoabaqusm-abaqusxm);
xabserror=xabsdif./abs(xdictoabaqusm)*100;
xerror=xdif./xdictoabaqusm*100;

ydif=ydictoabaqusm-abaqusym;
yabsdif=abs(ydictoabaqusm-abaqusym);
yabserror=yabsdif./abs(ydictoabaqusm)*100;
yerror=ydif./ydictoabaqusm*100;
%****************
AverageError=mean(mean(abserror));
MaxDif=max(max(dif));
MinDif=min(min(dif));
MaxAbaqus=max(max(abaqusvm));
MaxDic=max(max(dictoabaqusm));
MinAbaqus=min(min(abaqusvm));
MinDic=min(min(dictoabaqusm));
%=================
xAverageError=mean(mean(xabserror));
xMaxDif=max(max(xdif));
xMinDif=min(min(xdif));
xMaxAbaqus=max(max(abaqusxm));
xMaxDic=max(max(xdictoabaqusm));
xMinAbaqus=min(min(abaqusxm));
xMinDic=min(min(xdictoabaqusm));

yAverageError=mean(mean(yabserror));
```

```
yMaxDif=max(max(ydif));
yMinDif=min(min(ydif));
yMaxAbaqus=max(max(abaqusym));
yMaxDic=max(max(ydictoabaqusm));
yMinAbaqus=min(min(abaqusym));
yMinDic=min(min(ydictoabaqusm));
%=================
fid=fopen('Summary.txt','w');
fprintf(fid,'\r\n');
fprintf(fid,'SUMMARY\r\n');
fprintf(fid,'\r\n');
fprintf(fid,'\r\n');
fprintf(fid,'\r\n');
fprintf(fid,'Overall Error:\r\n');
fprintf(fid,'==============\r\n');
fprintf(fid,'Overall Averaged (Absolute) Vector Error:
%6.2f%%\r\n',AverageError);
fprintf(fid,'Overall Averaged (Absolute) X-Disp Error:
%6.2f%%\r\n',xAverageError); %+++++
fprintf(fid,'Overall Averaged (Absolute) Y-Disp Error:
%6.2f%%\r\n',yAverageError); %+++++
fprintf(fid,'\r\n');
fprintf(fid,'\r\n');
fprintf(fid,'Vector Error:\r\n');
fprintf(fid,'==============\r\n');
fprintf(fid,'Maximum Absolute Vector Error:
%6.5f\r\n',max(max(abserror)));
fprintf(fid,'Maximum Vector Error          : %6.5f\r\n',max(max(error)));
fprintf(fid,'Minimum Vector Error          : %6.5f\r\n',min(min(error)));
fprintf(fid,'\r\n');
%//////////////
fprintf(fid,'\r\n');
fprintf(fid,'X-Disp Error:\r\n');
fprintf(fid,'==============\r\n');
fprintf(fid,'Maximum Absolute X-Disp Error:
%6.5f\r\n',max(max(xabserror)));
fprintf(fid,'Maximum X-Disp Error          : %6.5f\r\n',max(max(xerror)));
fprintf(fid,'Minimum X-Disp Error          : %6.5f\r\n',min(min(xerror)));
fprintf(fid,'\r\n');
fprintf(fid,'\r\n');
fprintf(fid,'Y-Disp Error:\r\n');
fprintf(fid,'==============\r\n');
fprintf(fid,'Maximum Absolute Y-Disp Error:
%6.5f\r\n',max(max(yabserror)));
fprintf(fid,'Maximum Y-Disp Error          : %6.5f\r\n',max(max(yerror)));
fprintf(fid,'Minimum Y-Disp Error          : %6.5f\r\n',min(min(yerror)));
fprintf(fid,'\r\n');
fprintf(fid,'\r\n');
%//////////////
fprintf(fid,'Maximum Results:\r\n');
fprintf(fid,'================\r\n');
fprintf(fid,'Maximum Abaqus Vector Results: %6.5f micron\r\n',MaxAbaqus);
fprintf(fid,'Maximum Vector DIC Results    : %6.5f micron\r\n',MaxDic);
fprintf(fid,'\r\n');
fprintf(fid,'Maximum X-Disp Abaqus Results: %6.5f micron\r\n',xMaxAbaqus);
%+++++
```

```
fprintf(fid,'Maximum X-Disp DIC Results   : %6.5f micron\r\n',xMaxDic);
%+++++
fprintf(fid,'\r\n');
fprintf(fid,'Maximum Y-Disp Abaqus Results: %6.5f micron\r\n',yMaxAbaqus);
%+++++
fprintf(fid,'Maximum Y-Disp DIC Results   : %6.5f micron\r\n',yMaxDic);
%+++++
fprintf(fid,'\r\n');
fprintf(fid,'\r\n');
fprintf(fid,'Minimum Results:\r\n');
fprintf(fid,'================\r\n');
fprintf(fid,'Minimum Abaqus Vector Results: %6.5f micron\r\n',MinAbaqus);
fprintf(fid,'Minimum Vector DIC Results   : %6.5f micron\r\n',MinDic);
fprintf(fid,'\r\n');
fprintf(fid,'Minimum Abaqus X-Disp Results: %6.5f micron\r\n',xMinAbaqus);
%+++++
fprintf(fid,'Minimum X-Disp DIC Results   : %6.5f micron\r\n',xMinDic);
%+++++
fprintf(fid,'\r\n');
fprintf(fid,'Minimum Abaqus Y-Disp Results: %6.5f micron\r\n',yMinAbaqus);
%+++++
fprintf(fid,'Minimum Y-Disp DIC Results   : %6.5f micron\r\n',yMinDic);
%+++++
fprintf(fid,'\r\n');
fprintf(fid,'\r\n');
fprintf(fid,'Differences:\r\n');
fprintf(fid,'============\r\n');
fprintf(fid,'Maximum Absolute Vector Difference Results: %6.5f
micron\r\n',max(max(absdif)));
fprintf(fid,'Maximum Vector Difference Results         : %6.5f
micron\r\n',MaxDif);
fprintf(fid,'Minimum Vector Difference Results         : %6.5f
micron\r\n',MinDif);
fprintf(fid,'\r\n');
fprintf(fid,'Maximum Absolute X-Disp Difference Results: %6.5f
micron\r\n',max(max(xabsdif)));
fprintf(fid,'Maximum X-Disp Difference Results         : %6.5f
micron\r\n',xMaxDif);
fprintf(fid,'Minimum X-Disp Difference Results         : %6.5f
micron\r\n',xMinDif);
fprintf(fid,'\r\n');
fprintf(fid,'Maximum Absolute Y-Disp Difference Results: %6.5f
micron\r\n',max(max(yabsdif)));
fprintf(fid,'Maximum Y-Disp Difference Results         : %6.5f
micron\r\n',yMaxDif);
fprintf(fid,'Minimum Y-Disp Difference Results         : %6.5f
micron\r\n',yMinDif);
fclose('all');

% Ask user to set the maximum error of showing absolute error contour plot
usererror=input('Please Specify the maximum absolute error of contour
plot: ');

%Figures

% Here Figure of the actual DIC Results topped with interpolated one.
```

```
figure(1);
mesh(xdicsq,ydicsq,adpdic), hold,
mesh(xnodesq,ynodesq,dictoabaqus+mean(mean(adpdic)));
hold off;

figure(2)
hold on;
subplot(2,2,1);
surf(dictoabaqusm);
title('Interpolated DIC "Micron"')
colorbar;
subplot(2,2,2);
surf(abaqusvm);
title('ABAQUS "Micron"');
colorbar;
subplot(2,2,3);
surf(dif);
title('DIFFERENCE');
colorbar;
subplot(2,2,4);
mesh(error);
title('%Error');
colorbar;
hold off;

figure(3);
surf(dif);
colorbar;
title('DIFFERENCE');
figure(4);
surfc(error);
colorbar;
title('%Error');
figure(5);
hold on;
contourf(error,10);
colorbar;
clabel(contourf(error,10));
title('%Error');
hold off;

figure(6);
surfc(abserror);
colorbar;
title('%AbsError');
figure(7);
hold on
contourf(abserror,10);
colorbar;
clabel(contourf(abserror,10));
title('%AbsError');
hold off

figure(8)
subplot(1,2,1)
surf(error)
```

```
title('Error')
subplot(1,2,2)
surf(abserror)
title('AbsError')

for i=1:ynode;
    for j=1:xnode;
        if abserror(i,j)>=usererror;
            abserrorplot(i,j)=usererror;
        else
            abserrorplot(i,j)=abserror(i,j);
        end
    end
end
figure
hold on;
contourf(abserrorplot);
colorbar;
title('Absolute Vector Error %')
hold off;

for i=1:ynode;
    for j=1:xnode;
        if xabserror(i,j)>=usererror;
            xabserrorplot(i,j)=usererror;
        else
            xabserrorplot(i,j)=xabserror(i,j);
        end
    end
end
figure
hold on;
contourf(xabserrorplot);
colorbar;
title('Absolute X-Disp Error %')
hold off;

for i=1:ynode;
    for j=1:xnode;
        if yabserror(i,j)>=usererror;
            yabserrorplot(i,j)=usererror;
        else
            yabserrorplot(i,j)=yabserror(i,j);
        end
    end
end
figure
hold on;
contourf(yabserrorplot);
colorbar;
title('Absolute Y-Disp Error %')
hold off;
```

Appendix III MatLab Code to compare DIC strain results and microstructure simulation strain results

```
importfiledic('dic.DAT');
dicall=data;
importfileabq('abq.rpt');
abqvec=data;
%EXTRACT AREA OF INTEREST DATA
% User should specify area of interest according to x/y-positions
XDic1=input( 'Please enter the DIC X Start Left ' );
XDic2=input( 'Please enter the DIC X end Right ' );
YDic1=input( 'Please enter the DIC Y start Top ' );
YDic2=input( 'Please enter the DIC Y end Bottom ' );

%to find the number of data along x and y axis from lavision file
xlength=0;
ylength=0;
yvalue=dicall(1,2);
xvalue=dicall(1,1);
for i=1:length(dicall);
    if dicall(i,2)== yvalue;
        xlength=xlength+1;
    end
end
for i=1:length(dicall);
    if dicall(i,1)== xvalue;
        ylength=ylength+1;
    end
end

%construct dic matrix with cells of interest and vector magnitude
% this dic matrix has arranged in similar way of lavision data
%meaning that first according to y position then according to y position
%first column x position
%2nd column   y position
%3rd          x disp
%4th          y disp
%5th          magnitude disp
m=0;
n=0;
a=0;
b=1;
w=0;    %No of vectors along x axis for SELECTED AREA OF INTEREST
h=0;    %No of vectors along y axis for SELECTED AREA OF INTEREST
for i=1:ylength; % move as cluster for every y value
    if ((dicall(b,2)<= YDic1) && (dicall(b,2)>= YDic2));
        h=h+1;
        m=i*xlength; % to set the start of the cells to check and the end
for that y value
        n=m-xlength+1;
        w=0;
        for j=n:m;
            if ((dicall(j,1)<= XDic2) && (dicall(j,1)>= XDic1))
```

```
                w=w+1;
                a=a+1; % to creat new cell number for dic matrix
%                dic(a,5)= sqrt(dicall(j,3)^2+dicall(j,4)^2); %calculate
the magnitude
%                dic(a,4)= dicall(j,4);
                 dic(a,3)=dicall(j,3)*100;
                 dic(a,2)=dicall(j,2);
                 dic(a,1)=dicall(j,1);
            end
        end
    end
    b=b+xlength; %this one will be used to set the index for next y value
checking
end

% arrange DIC in square matrix for victor and strain
%x128=0;
%y128=0;
xdic=0;
ydic=0;
for i=1:length(dic);
    if dic(i,2)==dic(1,2);
        xdic=xdic+1;
    end
    if dic(i,1)==dic(1,1);
        ydic=ydic+1;
    end
end
a=0;
for y=1:ydic;
    for x=1:xdic;
        a=a+1;
        sqdic(y,x)=dic(a,3);
    end
end


% DIC for bell Shape, Removing the edges
a=0;
for y=2:ydic-1;
    for x=2:xdic-1;
        a=a+1;
        belldic(a)=sqdic(y,x);
    end
end
belldic=belldic';

% arrange Abaqus YY Vectors in square
xabq=input('number of elements at x-axis = ');
yabq=input('number of elements at y-axis = ');


a=0;
for x=1:xabq+1;
    for y=1:yabq+1;
```

```
        a=a+1;
        sqabqvec(y,x)=abqvec(a,2);
    end
end



% Averaging the vectors of the top row and bottom row then calculate the
strain:
a=0;
m=0;
for x=1:8:xabq-15;
% xabq-16 ===> xabq+1-17 nodes
    m=m+1;
    n=0;
    sqabqavgvec=0;
    for y=1:8:yabq-15;
        n=n+1;
        sqabqavg(n,m)=0;
        sqabqavgvec(n,m)=0;
        for a=x:x+16;
            sqabqavgvec(n,a)=sqabqvec(y,a)-sqabqvec(y+16,a);
        end
        for a=x:x+16;
            sqabqavg(n,m)=sqabqavg(n,m)+sqabqavgvec(n,a);
        end
        sqabqavg(n,m)=sqabqavg(n,m)/17;
    end
end
sqabqavg=sqabqavg*100/16;


% Arrange Average Abaqus Strain in row (for bell shape plot)
a=0;
for x=1:m;
    for y=1:n;
        a=a+1;
        abqavg(a)=sqabqavg(y,x);
    end
end
abqavg=abqavg';

% Comparison

t=0;
avgdiff=0;
avgerror=0;
for y=1:n;
    for x=1:m;
        t=t+1;
        diff(y,x)=abs(sqdic(y+1,x+1)-sqabqavg(y,x));
        error(y,x)=abs((sqdic(y+1,x+1)-sqabqavg(y,x))/sqdic(y+1,x+1))*100;
        avgdiff=avgdiff+diff(y,x);
        avgerror=avgerror+error(y,x);
```

```
    end
end
avgdiff=avgdiff/t;
avgerror=avgerror/t;
a=0;
for y=1:n;
    for x=1:m;
        a=a+1;
        errorhistograpgh(a)=error(y,x);
    end
end

% For Error Histograph

%==========
% ---------------------------
% For interpolation Purposes: Creating square matrices of the positions of
% DIC vectors (x/ydicsq are for actual DIC Results and x/ynodesq are for
% interpolated DIC results with number of vectors matches no of results
from Abaqus
xorid=[1:xdic];
yorid=[1:ydic]';
xintd=[1:.1:xdic];
yintd=[1:.1:ydic]';
xori=[1:m];
yori=[1:n]';
xint=[1:.1:m];
yint=[1:.1:n]';


% Generating interpolated DIC results with number of vectors matches no
% of results from Abaqus
sqdicint=interp2(xorid,yorid,sqdic,xintd,yintd,'linear');
sqabqavgint=interp2(xori,yori,sqabqavg,xint,yint,'linear');

% Comparison interpolated results

tint=0;
avgdiffint=0;
avgerrorint=0;
[nint,mint]=size(sqabqavgint);
for yint=1:nint;
    for xint=1:mint;
        tint=tint+1;
        diffint(yint,xint)=abs(sqdicint(yint+10,xint+10)-
sqabqavgint(yint,xint));
        errorint(yint,xint)=abs((sqdicint(yint+10,xint+10)-
sqabqavgint(yint,xint))/sqdicint(yint+10,xint+10))*100;
        avgdiffint=avgdiffint+diffint(yint,xint);
        avgerrorint=avgerrorint+errorint(yint,xint);
    end
end
avgdiffint=avgdiffint/tint;
avgerrorint=avgerrorint/tint;
%==========
```

```
histo=[0:.25:11];
[dichist,ss]=hist(belldic,histo);
[abqhist,ss]=hist(abqavg,histo);

errorhisto=[0:1:200];
errorhist=hist(errorhistograpgh,errorhisto);

figure (1);
pcolor(sqdic);
caxis([0 10]);
%shading interp;
colorbar;
title('DIC');
figure (2);
pcolor(sqabqavg);
caxis([0 10]);
%shading interp;
colorbar;
title('Abaqus Averaged');
figure (3);
pcolor(error);
%caxis([0 100]);
%shading interp;
colorbar;
title('%Error');
figure (4);
hist(dic(:,3),histo);
title('DIC');
figure (5);
hist(abqavg,histo);
title('Abaqus');

figure (6);
pcolor(sqdicint);
caxis([0 10]);
shading interp;
colorbar;
title('DIC Interpolated');
figure (7);
pcolor(sqabqavgint);
caxis([0 10]);
shading interp;
colorbar;
title('Abaqus Averaged Interpolated');
figure (8);
pcolor(errorint);
%caxis([0 100]);
shading interp;
colorbar;
title('% Error Interpolated');
figure (9);
pcolor(diffint);
%caxis([0 100]);
shading interp;
colorbar;
```

```
title('Difference Interpolated');
figure(10);
hist(errorhistograpgh,errorhisto);
caxis([0 200]);
title('Error Histograph');


%=============
% Not Working, it increase the % of error
%----------------------------------------
% Comparison: Average strain error Excluding strain less than .02
(selected error : selerror)
%m=0;
%selerror=0;
%for y=1:ydic-3;
%    for x=1:xdic-2;
%        if (sqdic(y,x)>=0.1 && sqabqavg(y,x)>=0.1)
%            m=m+1;
%            selerror=selerror+abs(sqdic(y,x)-
sqabqavg(y,x)/sqdic(y,x))*100;
%        end
%    end
%end
%selerror=selerror/m;
%=================
fid=fopen('Approx Summary.txt','w');
fprintf(fid,'SUMMARY\r\n');
fprintf(fid,'\r\n');
fprintf(fid,'\r\n');
fprintf(fid,'max Diff              \t %8.3f\r\n',max(max(diff)));
fprintf(fid,'min Diff              \t %8.3f\r\n',min(min(diff)));
fprintf(fid,'max Error             \t %8.3f%%\r\n',max(max(error)));
fprintf(fid,'min Error             \t %8.3f%%\r\n',min(min(error)));
fprintf(fid,'Average diff          \t %8.3f\r\n',avgdiff);
fprintf(fid,'Average Error         \t %8.3f%%\r\n',avgerror);
%fprintf(fid,'Average Excluded Error\t %8.3f%%\t Exclude strain Less than
0.1\r\n',selerror);
%fprintf(fid,'Number of total Strain values\t %6.1f\t Number of Strain
values at Excluded Error\t %6.1f\t\r\n',n,m);
%=================
```

Appendix IV MatLab Code to generate 3D RVE models with random distribution of ferrite and martensite for DP1000 steel

```
% Code to Create Random mesh of Mn and Fe By Khaled Alharbi
fid=fopen('RVE.inp','w');
% Heading
fprintf(fid,'*Heading\r\n');
fprintf(fid,'** Job name: Job-1 Model name: Model-1\r\n');
fprintf(fid,'** Generated by: Abaqus/CAE 6.10-2\r\n');
fprintf(fid,'*Preprint, echo=NO, model=NO, history=NO, contact=NO\r\n');
fprintf(fid,'**\r\n');
fprintf(fid,'** PARTS\r\n');
fprintf(fid,'**\r\n');
fprintf(fid,'*Part, name=Part-1\r\n');
fprintf(fid,'*Node\r\n');
%---------------------------------
% Choose number of Element
N=input('Choose No. of Element along RVE edge (8, 10, 15, 20, 30): ');
%---------------------------------
% Import Data (Nodes and Elements from Original files 8, 10, 15 and 20)
and Create Nodes and Element
if N==8;
    % Importing Data
    importNode('8.INP');
    Heading=textdata;
    Node=data;
    importElement8('8.INP');
    Element=data;
elseif N==10;
    importNode('10.INP');
    Heading=textdata;
    Node=data;
    importElement10('10.INP');
    Element=data;
elseif N==15;
    importNode('15.INP');
    Heading=textdata;
    Node=data;
    importElement15('15.INP');
    Element=data;
elseif N==20;
    importNode('20.INP');
    Heading=textdata;
    Node=data;
    importElement20('20.INP');
    Element=data;
else
    importNode('30.INP');
    Heading=textdata;
    Node=data;
    importElement30('30.INP');
    Element=data;
end
```

```
% Write Node to the .inp file
for i=1:(N+1)*(N+1)*(N+1);

fprintf(fid,'%7u,%13.10f,%13.10f,%13.10f\r\n',i,Node(i,2),Node(i,3),Node(i
,4));
end
% Write Element to the .inp file and assign to Ferrite (0) or Martensite
(1)
Element(:,10)=randint(N*N*N,1,[0,1]);
fprintf(fid,'*Element, type=C3D8R, ELSET=Ferrite\r\n');
for i=1:N*N*N;
    if Element(i,10)==0

fprintf(fid,'%4u,%5u,%5u,%5u,%5u,%5u,%5u,%5u,%5u\r\n',Element(i,1),Element
(i,2),Element(i,3),Element(i,4),Element(i,5),Element(i,6),Element(i,7),Ele
ment(i,8),Element(i,9));
    end
end
fprintf(fid,'*Element, type=C3D8R, ELSET=Martensite\r\n');
for i=1:N*N*N;
    if Element(i,10)==1

fprintf(fid,'%4u,%5u,%5u,%5u,%5u,%5u,%5u,%5u,%5u\r\n',Element(i,1),Element
(i,2),Element(i,3),Element(i,4),Element(i,5),Element(i,6),Element(i,7),Ele
ment(i,8),Element(i,9));
    end
end

% Define Sections, Assembly, Amplitude, Material
fprintf(fid,'** Section: Section-Fe\r\n');
fprintf(fid,'*Solid Section, elset=Ferrite, material=Fe\r\n');
fprintf(fid,',\r\n');
fprintf(fid,'** Section: Section-2-Mn\r\n');
fprintf(fid,'*Solid Section, elset=Martensite, material=Mn\r\n');
fprintf(fid,',\r\n');
fprintf(fid,'*End Part\r\n');
fprintf(fid,'**\r\n');
fprintf(fid,'**\r\n');
fprintf(fid,'** ASSEMBLY\r\n');
fprintf(fid,'**\r\n');
fprintf(fid,'*Assembly, name=Assembly\r\n');
fprintf(fid,'**\r\n');
fprintf(fid,'*Instance, name=PART-1-1, part=PART-1\r\n');
fprintf(fid,'*End Instance\r\n');
fprintf(fid,'**\r\n');
fprintf(fid,'*End Assembly\r\n');
fprintf(fid,'*Amplitude, name=Amp-1\r\n');
fprintf(fid,'0.,0.,300.,1.\r\n');
fprintf(fid,'**\r\n');
fprintf(fid,'**\r\n');
% Ferrite
FeSs=[444.095988    444.423576  446.506089  447.44946   448.09632
448.34174   448.692069  449.046936  449.46005   449.618676  449.618676
449.648 449.648 449.648 449.648 449.648 449.648 449.648 449.648 449.648
449.648 449.648 449.648 449.648 449.648 449.648 449.648 449.648 449.648
449.648 449.648 449.648 449.648 449.648 449.648 449.648 449.648 449.648
```

```
449.648 449.648 449.648 449.648 449.648 449.648 449.648 449.648 449.648
449.648 449.648 449.648 449.648 449.648 449.648 449.648 449.648 449.648
449.648 449.648 449.648 449.648 449.648 449.648 449.648 449.648 449.648
449.648 449.648 449.648 449.648 449.648 449.648 449.648 449.648 449.648
449.648 449.648 449.648 449.648 449.648 449.648 449.648 449.648 449.648
449.648 449.648 449.648 449.648 449.648 449.648 449.648 449.648 449.648
449.648 449.648 449.648 449.648 449.648 449.648 449.648 449.648 449.648
449.648 449.648 449.648 449.648 449.648 449.648 449.648 449.648 449.648
449.648 449.648 449.648 449.648 449.648 449.648 449.648 449.648 449.648
449.648 449.648 449.648 449.648 449.648 449.648 449.648 449.648 449.648
449.648 449.648 449.648 449.648 449.648 449.648 449.648 449.648 449.648
449.648 449.648 449.648 449.648 449.648 449.648 449.648 449.648 449.648
449.648 449.648 449.648 449.648 449.648 449.648 449.648 449.648 449.648
449.648 449.648 449.648 450.51837   451.535452  452.548519  452.9386
453.935664  454.22654   454.612707  454.90375   455.186115  455.348064
455.526522  455.526522  455.526522  455.526522  455.741994  455.92492
455.92492   456.070269  456.25327   456.54492   456.936516  457.32822
458.016428  458.299725  458.59188   458.884111  459.2808    459.6732
459.856872  460.22873   460.521392  460.81413   460.81413   460.81413
460.81413   460.81413   460.81413   460.81413   460.81413   460.81413
461.215674  462.316725  462.605661  462.899088  463.498056  463.791688
464.085396  464.37475   465.06297   465.56232   465.56232   465.56232
465.56232   465.56232   465.56232   465.56232   465.56232   465.56232
465.56232   465.56232   466.059022  466.480888  466.902898  466.913104
467.76513   468.626424  469.72274   469.85654   470.20556   470.67351
471.031749  471.614493  472.092006  473.07904   473.7954    475.045085
476.093184  476.617644  477.597614  478.14545   478.49067   479.26916
479.5268    479.79348   480.161847  480.478156  480.478156  480.478156
481.167 482.072916  482.655159  482.655159  482.655159  482.655159
482.655159  482.751097  484.190148  485.197604  486.897858  487.916642
488.399667  489.08857   489.08857   490.091679  490.889448  490.93872
490.93872   491.359902  491.839996  492.531545  493.699997  493.960544
493.960544  493.960544  494.431184  495.237608  496.400232  496.77886
496.77886   496.77886   496.77886   497.075954  497.672032  498.846922
499.543808  499.687055  499.843944  499.887036  500.689398  501.55848
501.55848   501.55848   501.55848   501.55848   501.55848   501.55848
501.717564  502.417344  502.463048  502.943584  502.943584  502.943584
502.943584  502.943584  502.943584  502.943584  502.943584  503.169196
505.134933  505.51512   506.439648  507.369442  507.626034  507.882626
508.41872   509.5265475 510.6405186 511.5331133 512.640649  513.5353382
514.5684417 515.7877534 516.7841848 518.0068766 519.0199716 519.9563173
520.7408527 521.398657  521.9133644 522.4280719 523.182915  524.0830323
524.5983549 525.4716786 526.827144  527.9507421 529.0852875 530.1016428
531.3882829 532.4027079 533.4135956 534.3193697 535.2165219 535.9984031
536.9018345 537.6209545 538.1424104 538.6638662 539.185322  539.7067778
540.2282337 540.7496895 541.4857715 542.0074341 542.5290967 543.0507593
543.5724219 544.0940845 544.6157471 545.1374097 545.6590723 546.1807349
546.7023975 547.2240601 547.7457227 548.2673852 548.7890478 549.3107104
549.832373  550.3540356 550.8756982 551.3973608 551.9190234 552.440686
552.9623486 553.4840112 554.3873725 554.9093945 555.4314165 556.9050054
558.7087689 560.2823871 561.6300924 562.9915396 563.8954784 564.4224835
564.9494886 565.4764938 566.0034989 566.7372738 568.058867  568.8692105
569.8031353 570.8560853 571.8069612 572.4604612 572.9900268 573.8760684
575.0826394 576.176753  577.1630351 578.0208699 579.0917416 579.9663778
580.8316016 581.7127448 582.4693602 583.3467263 584.4538339 585.348191
```

```
586.2382059 586.8767108 587.7678919 588.6598208 589.930132  590.8291323
591.4851416 592.39048   593.3017341 594.4557892 595.1082613 596.0269548
596.8080454 597.7229811 598.6438769 599.4318108 600.4793995 601.4026238
602.1923075 602.9876381 603.7834257 604.5848788 605.7617005 606.6893098
607.4927208 608.3018277 609.1166446 610.0522132 610.7320035 611.9418173
612.7589692 613.4398494 614.3842023 615.2133365 615.8951322 616.983612
617.803733  618.7569489 619.4454305 620.2775965 621.0996674 621.6608921
622.7754423 623.604188  624.4440596 625.2791236 625.8301768 626.9642167
627.8006798 628.5081101 629.2156915 630.0426267 630.7506797 631.3179397
632.461728  632.6203188 632.6481695 632.9424717 632.9645897 633.2694627
633.4543068 633.6119442 633.905867  1808.6395];
%Mpa Plastic Stress
FeSn=[0 5.97961E-05 0.000229199 0.000318871 0.000418498 0.000518114
0.000627681 0.000747194 0.000996135 0.00112556  0.001264922 0.001414216
0.001553538 0.001702789 0.001852018 0.002160355 0.002319459 0.002498421
0.002667411 0.002846311 0.00319408  0.003362953 0.003551659 0.00374033
0.003909111 0.004097714 0.004286282 0.004653391 0.004841854 0.005030282
0.005218674 0.005397118 0.005744001 0.005932259 0.006120481 0.006308668
0.006477015 0.006665135 0.00685322  0.007219388 0.007397475 0.007575531
0.007763444 0.007951322 0.008307204 0.008485098 0.00868272  0.008850669
0.009038343 0.009225981 0.009403712 0.009778817 0.009966316 0.010143915
0.010331346 0.010518743 0.010706104 0.011070864 0.011267976 0.011445344
0.01162268  0.011809835 0.011996954 0.012184038 0.01254826  0.012735241
0.012932026 0.013118935 0.013295975 0.013482816 0.013669623 0.014023477
0.014210182 0.014396853 0.014593311 0.01477009  0.014956656 0.015329684
0.01549652  0.015682951 0.015849728 0.016045901 0.016232229 0.016604782
0.016781206 0.016967397 0.017153554 0.017339676 0.01751597  0.017897835
0.018083818 0.018269767 0.018445898 0.018621997 0.018807846 0.018983882
0.019345636 0.019521577 0.019707259 0.019892906 0.020088287 0.020283631
0.02066444  0.020840149 0.021025586 0.021220746 0.021406113 0.021591445
0.021766992 0.02212774  0.022303193 0.022478614 0.022663748 0.022829365
0.023199468 0.023364997 0.023549966 0.023715437 0.023890611 0.024075483
0.024250594 0.024629896 0.024824354 0.025009054 0.02519372  0.025368635
0.025553234 0.025902909 0.0260777   0.026271876 0.026456309 0.026631004
0.026815371 0.027184002 0.027358569 0.027542802 0.027727001 0.027920857
0.02829877  0.028492516 0.028686224 0.028879895 0.029054167 0.029238087
0.029421974 0.029770298 0.029944415 0.03010883  0.030292557 0.030447248
0.030630912 0.030978816 0.031162383 0.031345916 0.031529415 0.031703226
0.03188666  0.03207006  0.032417463 0.032600766 0.032764746 0.032957629
0.033140833 0.033324003 0.033680607 0.033863679 0.034046717 0.03421046
0.034393434 0.034566748 0.034740031 0.035105754 0.035288565 0.035452104
0.035634852 0.035798334 0.036154057 0.036317455 0.036490436 0.036663386
0.036845913 0.037018802 0.037191661 0.037556488 0.037738851 0.037911586
0.038093885 0.038266559 0.038439202 0.038803574 0.03896654  0.039148646
0.03933072  0.03951276  0.039685189 0.039857588 0.04021187  0.04039375
0.040575597 0.040757411 0.040948758 0.041120939 0.041293091 0.041665984
0.041838042 0.04201007  0.042191624 0.042354038 0.042697887 0.042869768
0.043051165 0.04321344  0.043394775 0.043576077 0.043747806 0.044100713
0.044272353 0.044453496 0.044634606 0.044825213 0.045006256 0.045358719
0.045539665 0.045720579 0.045891941 0.046082308 0.046272639 0.04669124
0.046919494 0.047147696 0.047394856 0.047641955 0.047907994 0.048449353
0.048734161 0.049028378 0.049350968 0.04966397  0.050005316 0.050346545
0.051094945 0.051492601 0.051899561 0.052325272 0.052760256 0.053705221
0.05418681  0.054687039 0.05520588  0.055743304 0.056299281 0.056845533
0.057946549 0.058491903 0.059055749 0.059600499 0.060154336 0.060698487
0.061785902 0.062347895 0.062900213 0.06346158  0.063994586 0.064536652
```

```
0.065069087 0.066142434 0.06669266  0.067242585 0.06777358  0.068322911
0.069383475 0.069913335 0.070452203 0.070981498 0.071529069 0.072067068
0.072595509 0.073651553 0.074179158 0.074724981 0.075261264 0.07578802
0.076323732 0.0773574   0.077901493 0.078445289 0.078970371 0.079504382
0.080028908 0.080571549 0.081619208 0.082142627 0.08264742  0.083179472
0.083702074 0.084215243 0.0852957   0.085817198 0.086347566 0.08688679
0.08740746  0.08791873  0.088466231 0.089542107 0.090061396 0.090589519
0.091108264 0.091644928 0.092735559 0.093271351 0.093806855 0.094351142
0.094886069 0.09540259  0.095936955 0.096986738 0.097520257 0.098035421
0.09855935  0.099064952 0.099570299 0.100625289 0.101147864 0.101679168
0.10221019  0.102722944 0.103253412 0.104268608 0.104771333 0.105273805
0.105776025 0.106304876 0.107334885 0.107853966 0.108345949 0.108855567
0.109373859 0.109891883 0.110409638 0.11143543  0.111961298 0.112469077
0.112967697 0.113483863 0.11399087  0.115004113 0.115501471 0.115989707
0.116495445 0.116983196 0.117470709 0.117966842 0.118984915 0.119462609
0.119887035 0.120275934 0.120620513 0.12092965  0.121229863 0.121768254
0.121997644 0.122200522 0.122350449 0.122482719 0.122606155 0.122826539
0.122941119 0.123038062 0.123117371 0.123214296 0.123311212 0.123487399
0.123584288 0.123672361 0.123751621 0.123839679 0.12392773  0.124086201
0.12413902  0.124200637 0.124288656 0.124403069 0.12449987  0.124631856
0.124842997 0.12493096  0.125036504 0.125159625 0.125300317 0.125467362
0.125871673 0.126108909 0.126372439 0.126618338 0.126864176 0.127101177
0.127338122 0.127873236 0.128153837 0.128434359 0.12870604  0.129012687
0.129660719 0.129975826 0.130282084 0.130596995 0.130929294 0.131287703
0.131637246 0.132353428 0.132728782 0.133086547 0.133470347 0.133854
0.134228791 0.134995369 0.135395846 0.135787462 0.136178924 0.136570234
0.13696139  0.137777979 0.138177344 0.138593902 0.139001614 0.139417829
0.140241077 0.140648118 0.141072304 0.141479007 0.141894192 0.142317849
0.142732687 0.143579112 0.144002057 0.144416196 0.144838787 0.145261199
0.145692047 0.146527365 0.146949064 0.147379187 0.147817721 0.148264656
0.148694213 0.149132171 0.150007512 0.15045347  0.150890658 0.151327656
0.151790151 0.152226755 0.153107945 0.153552522 0.153996902 0.154441085
0.154902142 0.155345923 0.155798035 0.156710168 0.157161664 0.157629982
0.158089572 0.158523436 0.15945858  0.15991733  0.16038436  0.160851172
0.161292321 0.161758709 0.162216406 0.16315657  0.16362209  0.164095851
0.164560934 0.165025801 0.165507344 0.16644442  0.166908413 0.167372189
2];
%Plastic Strain
% Martensite
MnSs=[1059.387427   1071.700468 1079.481665 1086.574633 1092.237742
1098.441087 1104.75436  1111.796259 1125.46307  1131.860501 1137.748872
1144.010298 1150.622562 1156.675679 1169.96735  1176.421353 1183.569525
1190.560752 1197.78889  1205.229426 1212.796925 1227.280661 1234.268118
1241.736794 1249.312029 1257.282104 1272.676573 1279.881451 1287.123449
1294.644471 1301.136125 1307.906831 1314.677828 1327.216913 1333.085732
1338.958669 1344.625781 1350.285031 1355.627063 1365.81215  1370.794566
1375.608125 1380.245282 1385.035598 1389.669546 1394.432961 1402.98593
1407.347068 1411.828288 1416.062418 1420.292827 1427.943147 1432.016349
1436.095798 1440.177285 1444.070322 1447.969248 1451.782418 1458.383873
1461.879495 1465.545739 1468.983158 1472.281773 1475.741671 1481.310016
1484.719523 1487.931402 1491.08617  1494.185576 1497.109137 1500.105331
1505.056211 1507.900344 1510.642179 1513.548259 1516.245927 1518.946301
1521.597552 1525.213472 1526.865063 1528.421732 1530.011502 1531.467444
1532.990163 1535.690091 1537.053646 1538.330538 1539.525788 1541.807897
1542.92314  1543.911349 1544.939293 1545.850927 1546.776912 1547.645409
1549.296547 1550.086025 1550.856555 1551.592138 1552.378312 1553.099098
```

```
1553.820318 1555.443457 1555.935085 1556.39998  1556.864719 1557.31603
1593.875    1648.4  1740    1790    1810    1900];
%Mpa Plastic Stress
MnSn=[0 0.000148644 0.000237819 0.000326987 0.00040624  0.000505298
0.000594442 0.000703385 0.000921235 0.001030142 0.001148936 0.001277614
0.001416171 0.001544815 0.001841621 0.001989991 0.002158118 0.002326216
0.002504171 0.002691978 0.002889632 0.003284823 0.003482359 0.003699605
0.003926674 0.004173431 0.004676625 0.004923196 0.005179566 0.005455583
0.005701963 0.005967984 0.006243784 0.006785312 0.007051045 0.007326546
0.007601972 0.007887154 0.008162424 0.008722563 0.009007426 0.009292207
0.009567091 0.009861527 0.010155875 0.010450137 0.011038401 0.011332404
0.011645911 0.011949527 0.012262841 0.012898958 0.013202194 0.013515116
0.013837714 0.014150437 0.01447283  0.014795119 0.015449145 0.015761364
0.016102743 0.016424507 0.016736422 0.017077468 0.017720267 0.018080443
0.018421031 0.018761503 0.019101859 0.01942266  0.019762791 0.020442706
0.020782491 0.021112456 0.021481113 0.021820545 0.022169554 0.022518442
0.02320617  0.023564376 0.023912778 0.024280404 0.024628556 0.025005584
0.025710922 0.026087543 0.02645437  0.026811415 0.027534763 0.027910697
0.028257588 0.028633251 0.028979892 0.02934566  0.029701674 0.030413322
0.030768956 0.031124464 0.031470242 0.0318447   0.032190229 0.032535639
0.033216515 0.033571153 0.033906507 0.034241748 0.034567303 0.05 0.08 0.14
0.2 0.25 2];
%Plastic Strain
fprintf(fid,'** MATERIALS\r\n');
fprintf(fid,'**\r\n');
fprintf(fid,'*Material, name=Fe\r\n');
fprintf(fid,'*Density\r\n');
fprintf(fid,'7.60292e-06,\r\n');
fprintf(fid,'*Elastic\r\n');
fprintf(fid,'198000., 0.33\r\n');
fprintf(fid,'*Plastic\r\n');
for i=1:length(FeSs);
    fprintf(fid,'%6.2f,\t%6.8f\r\n',FeSs(i),FeSn(i));
end
fprintf(fid,'*Porous Metal Plasticity, relative density=1.\r\n');
fprintf(fid,' 1.1,  0.9, 1.21\r\n');
fprintf(fid,'*Void Nucleation\r\n');
fprintf(fid,' 0.11,  0.5, 0.04\r\n');
fprintf(fid,'*Material, name=Mn\r\n');
fprintf(fid,'*Density\r\n');
fprintf(fid,'7.60292e-06,\r\n');
fprintf(fid,'*Elastic\r\n');
fprintf(fid,'200000., 0.33\r\n');
fprintf(fid,'*Plastic\r\n');
for i=1:length(MnSs);
    fprintf(fid,'%6.2f,\t%6.8f\r\n',MnSs(i),MnSn(i));
end
% Define Step
fprintf(fid,'** ----------------------------------------------------------
------\r\n');
fprintf(fid,'**\r\n');
fprintf(fid,'** STEP: Step-1\r\n');
fprintf(fid,'**\r\n');
fprintf(fid,'*Step, name=Step-1, nlgeom=YES, inc=10000\r\n');
fprintf(fid,'*Static\r\n');
fprintf(fid,'1., 300., 0.003, 300.\r\n');
```

```
fprintf(fid,'**\r\n');
%---------------------------------
%Close The input file
fclose('all');
%---------------------------------
```

Appendix V MatLab code to apply boundary conditions to 2D RVE

```
fid=fopen('Mesh.inp','a');
% Define Sections, Assembly, Amplitude, Material
fprintf(fid,'\r\n');
fprintf(fid,'** Section: Section-Fe\r\n');
fprintf(fid,'*Solid Section, elset=PHASE2, material=Fe\r\n');
fprintf(fid,',\r\n');
fprintf(fid,'** Section: Section-2-Mn\r\n');
fprintf(fid,'*Solid Section, elset=PHASE1, material=Mn\r\n');
fprintf(fid,',\r\n');
fprintf(fid,'*End Part\r\n');
fprintf(fid,'**\r\n');
fprintf(fid,'**\r\n');
fprintf(fid,'** ASSEMBLY\r\n');
fprintf(fid,'**\r\n');
fprintf(fid,'*Assembly, name=Assembly\r\n');
fprintf(fid,'**\r\n');
fprintf(fid,'*Instance, name=PART-1-1, part=PART-1\r\n');
fprintf(fid,'*End Instance\r\n');
fprintf(fid,'**\r\n');
fprintf(fid,'*End Assembly\r\n');
fprintf(fid,'*Amplitude, name=Amp-1\r\n');
fprintf(fid,'0.,0.,300.,1.\r\n');
fprintf(fid,'**\r\n');
fprintf(fid,'**\r\n');
% Ferrite
FeSs=[444.095988    444.423576  446.506089  447.44946   448.09632
448.34174   448.692069  449.046936  449.46005   449.618676  449.618676
449.648 449.648 449.648 449.648 449.648 449.648 449.648 449.648 449.648
449.648 449.648 449.648 449.648 449.648 449.648 449.648 449.648 449.648
449.648 449.648 449.648 449.648 449.648 449.648 449.648 449.648 449.648
449.648 449.648 449.648 449.648 449.648 449.648 449.648 449.648 449.648
449.648 449.648 449.648 449.648 449.648 449.648 449.648 449.648 449.648
449.648 449.648 449.648 449.648 449.648 449.648 449.648 449.648 449.648
449.648 449.648 449.648 449.648 449.648 449.648 449.648 449.648 449.648
449.648 449.648 449.648 449.648 449.648 449.648 449.648 449.648 449.648
449.648 449.648 449.648 449.648 449.648 449.648 449.648 449.648 449.648
449.648 449.648 449.648 449.648 449.648 449.648 449.648 449.648 449.648
449.648 449.648 449.648 449.648 449.648 449.648 449.648 449.648 449.648
449.648 449.648 449.648 449.648 449.648 449.648 449.648 449.648 449.648
449.648 449.648 449.648 449.648 449.648 449.648 449.648 449.648 449.648
449.648 449.648 449.648 450.51837   451.535452  452.548519  452.9386
453.935664  454.22654   454.612707  454.90375   455.186115  455.348064
455.526522  455.526522  455.526522  455.526522  455.741994  455.92492
455.92492   456.070269  456.25327   456.54492   456.936516  457.32822
458.016428  458.299725  458.59188   458.884111  459.2808    459.6732
459.856872  460.22873   460.521392  460.81413   460.81413   460.81413
460.81413   460.81413   460.81413   460.81413   460.81413   460.81413
461.215674  462.316725  462.605661  462.899088  463.498056  463.791688
464.085396  464.37475   465.06297   465.56232   465.56232   465.56232
```

```
465.56232   465.56232   465.56232   465.56232   465.56232   465.56232
465.56232   465.56232   466.059022  466.480888  466.902898  466.913104
467.76513   468.626424  469.72274   469.85654   470.20556   470.67351
471.031749  471.614493  472.092006  473.07904   473.7954    475.045085
476.093184  476.617644  477.597614  478.14545   478.49067   479.26916
479.5268    479.79348   480.161847  480.478156  480.478156  480.478156
481.167 482.072916  482.655159  482.655159  482.655159  482.655159
482.655159  482.751097  484.190148  485.197604  486.897858  487.916642
488.399667  489.08857   489.08857   490.091679  490.889448  490.93872
490.93872   491.359902  491.839996  492.531545  493.699997  493.960544
493.960544  493.960544  494.431184  495.237608  496.400232  496.77886
496.77886   496.77886   496.77886   497.075954  497.672032  498.846922
499.543808  499.687055  499.843944  499.887036  500.689398  501.55848
501.55848   501.55848   501.55848   501.55848   501.55848   501.55848
501.717564  502.417344  502.463048  502.943584  502.943584  502.943584
502.943584  502.943584  502.943584  502.943584  502.943584  503.169196
505.134933  505.51512   506.439648  507.369442  507.626034  507.882626
508.41872   509.5265475 510.6405186 511.5331133 512.640649  513.5353382
514.5684417 515.7877534 516.7841848 518.0068766 519.0199716 519.9563173
520.7408527 521.398657  521.9133644 522.4280719 523.182915  524.0830323
524.5983549 525.4716786 526.827144  527.9507421 529.0852875 530.1016428
531.3882829 532.4027079 533.4135956 534.3193697 535.2165219 535.9984031
536.9018345 537.6209545 538.1424104 538.6638662 539.185322  539.7067778
540.2282337 540.7496895 541.4857715 542.0074341 542.5290967 543.0507593
543.5724219 544.0940845 544.6157471 545.1374097 545.6590723 546.1807349
546.7023975 547.2240601 547.7457227 548.2673852 548.7890478 549.3107104
549.832373  550.3540356 550.8756982 551.3973608 551.9190234 552.440686
552.9623486 553.4840112 554.3873725 554.9093945 555.4314165 556.9050054
558.7087689 560.2823871 561.6300924 562.9915396 563.8954784 564.4224835
564.9494886 565.4764938 566.0034989 566.7372738 568.058867  568.8692105
569.8031353 570.8560853 571.8069612 572.4604612 572.9900268 573.8760684
575.0826394 576.176753  577.1630351 578.0208699 579.0917416 579.9663778
580.8316016 581.7127448 582.4693602 583.3467263 584.4538339 585.348191
586.2382059 586.8767108 587.7678919 588.6598208 589.930132  590.8291323
591.4851416 592.39048   593.3017341 594.4557892 595.1082613 596.0269548
596.8080454 597.7229811 598.6438769 599.4318108 600.4793995 601.4026238
602.1923075 602.9876381 603.7834257 604.5848788 605.7617005 606.6893098
607.4927208 608.3018277 609.1166446 610.0522132 610.7320035 611.9418173
612.7589692 613.4398494 614.3842023 615.2133365 615.8951322 616.983612
617.803733  618.7569489 619.4454305 620.2775965 621.0996674 621.6608921
622.7754423 623.604188  624.4440596 625.2791236 625.8301768 626.9642167
627.8006798 628.5081101 629.2156915 630.0426267 630.7506797 631.3179397
632.461728  632.6203188 632.6481695 632.9424717 632.9645897 633.2694627
633.4543068 633.6119442 633.905867  1808.6395];
%Mpa Plastic Stress
FeSn=[0 5.97961E-05 0.000229199 0.000318871 0.000418498 0.000518114
0.000627681 0.000747194 0.000996135 0.00112556  0.001264922 0.001414216
0.001553538 0.001702789 0.001852018 0.002160355 0.002319459 0.002498421
0.002667411 0.002846311 0.00319408  0.003362953 0.003551659 0.00374033
0.003909111 0.004097714 0.004286282 0.004653391 0.004841854 0.005030282
0.005218674 0.005397118 0.005744001 0.005932259 0.006120481 0.006308668
0.006477015 0.006665135 0.00685322  0.007219388 0.007397475 0.007575531
0.007763444 0.007951322 0.008307204 0.008485098 0.00868272  0.008850669
0.009038343 0.009225981 0.009403712 0.009778817 0.009966316 0.010143915
0.010331346 0.010518743 0.010706104 0.011070864 0.011267976 0.011445344
0.01162268  0.011809835 0.011996954 0.012184038 0.01254826  0.012735241
```

```
0.012932026 0.013118935 0.013295975 0.013482816 0.013669623 0.014023477
0.014210182 0.014396853 0.014593311 0.01477009  0.014956656 0.015329684
0.01549652  0.015682951 0.015849728 0.016045901 0.016232229 0.016604782
0.016781206 0.016967397 0.017153554 0.017339676 0.01751597  0.017897835
0.018083818 0.018269767 0.018445898 0.018621997 0.018807846 0.018983882
0.019345636 0.019521577 0.019707259 0.019892906 0.020088287 0.020283631
0.02066444  0.020840149 0.021025586 0.021220746 0.021406113 0.021591445
0.021766992 0.02212774  0.022303193 0.022478614 0.022663748 0.022829365
0.023199468 0.023364997 0.023549966 0.023715437 0.023890611 0.024075483
0.024250594 0.024629896 0.024824354 0.025009054 0.02519372  0.025368635
0.025553234 0.025902909 0.0260777   0.026271876 0.026456309 0.026631004
0.026815371 0.027184002 0.027358569 0.027542802 0.027727001 0.027920857
0.02829877  0.028492516 0.028686224 0.028879895 0.029054167 0.029238087
0.029421974 0.029770298 0.029944415 0.03010883  0.030292557 0.030447248
0.030630912 0.030978816 0.031162383 0.031345916 0.031529415 0.031703226
0.03188666  0.03207006  0.032417463 0.032600766 0.032764746 0.032957629
0.033140833 0.033324003 0.033680607 0.033863679 0.034046717 0.03421046
0.034393434 0.034566748 0.034740031 0.035105754 0.035288565 0.035452104
0.035634852 0.035798334 0.036154057 0.036317455 0.036490436 0.036663386
0.036845913 0.037018802 0.037191661 0.037556488 0.037738851 0.037911586
0.038093885 0.038266559 0.038439202 0.038803574 0.03896654  0.039148646
0.03933072  0.03951276  0.039685189 0.039857588 0.04021187  0.04039375
0.040575597 0.040757411 0.040948758 0.041120939 0.041293091 0.041665984
0.041838042 0.04201007  0.042191624 0.042354038 0.042697887 0.042869768
0.043051165 0.04321344  0.043394775 0.043576077 0.043747806 0.044100713
0.044272353 0.044453496 0.044634606 0.044825213 0.045006256 0.045358719
0.045539665 0.045720579 0.045891941 0.046082308 0.046272639 0.04669124
0.046919494 0.047147696 0.047394856 0.047641955 0.047907994 0.048449353
0.048734161 0.049028378 0.049350968 0.04966397  0.050005316 0.050346545
0.051094945 0.051492601 0.051899561 0.052325272 0.052760256 0.053705221
0.05418681  0.054687039 0.05520588  0.055743304 0.056299281 0.056845533
0.057946549 0.058491903 0.059055749 0.059600499 0.060154336 0.060698487
0.061785902 0.062347895 0.062900213 0.06346158  0.063994586 0.064536652
0.065069087 0.066142434 0.06669266  0.067242585 0.06777358  0.068322911
0.069383475 0.069913335 0.070452203 0.070981498 0.071529069 0.072067068
0.072595509 0.073651553 0.074179158 0.074724981 0.075261264 0.07578802
0.076323732 0.0773574   0.077901493 0.078445289 0.078970371 0.079504382
0.080028908 0.080571549 0.081619208 0.082142627 0.08264742  0.083179472
0.083702074 0.084215243 0.0852957   0.085817198 0.086347566 0.08688679
0.08740746  0.08791873  0.088466231 0.089542107 0.090061396 0.090589519
0.091108264 0.091644928 0.092735559 0.093271351 0.093806855 0.094351142
0.094886069 0.09540259  0.095936955 0.096986738 0.097520257 0.098035421
0.09855935  0.099064952 0.099570299 0.100625289 0.101147864 0.101679168
0.10221019  0.102722944 0.103253412 0.104268608 0.104771333 0.105273805
0.105776025 0.106304876 0.107334885 0.107853966 0.108345949 0.108855567
0.109373859 0.109891883 0.110409638 0.11143543  0.111961298 0.112469077
0.112967697 0.113483863 0.11399087  0.115004113 0.115501471 0.115989707
0.116495445 0.116983196 0.117470709 0.117966842 0.118984915 0.119462609
0.119887035 0.120275934 0.120620513 0.12092965  0.121229863 0.121768254
0.121997644 0.122200522 0.122350449 0.122482719 0.122606155 0.122826539
0.122941119 0.123038062 0.123117371 0.123214296 0.123311212 0.123487399
0.123584288 0.123672361 0.123751621 0.123839679 0.12392773  0.124086201
0.12413902  0.124200637 0.124288656 0.124403069 0.12449987  0.124631856
0.124842997 0.12493096  0.125036504 0.125159625 0.125300317 0.125467362
0.125871673 0.126108909 0.126372439 0.126618338 0.126864176 0.127101177
0.127338122 0.127873236 0.128153837 0.128434359 0.12870604  0.129012687
```

```
0.129660719 0.129975826 0.130282084 0.130596995 0.130929294 0.131287703
0.131637246 0.132353428 0.132728782 0.133086547 0.133470347 0.133854
0.134228791 0.134995369 0.135395846 0.135787462 0.136178924 0.136570234
0.13696139  0.137777979 0.138177344 0.138593902 0.139001614 0.139417829
0.140241077 0.140648118 0.141072304 0.141479007 0.141894192 0.142317849
0.142732687 0.143579112 0.144002057 0.144416196 0.144838787 0.145261199
0.145692047 0.146527365 0.146949064 0.147379187 0.147817721 0.148264656
0.148694213 0.149132171 0.150007512 0.15045347  0.150890658 0.151327656
0.151790151 0.152226755 0.153107945 0.153552522 0.153996902 0.154441085
0.154902142 0.155345923 0.155798035 0.156710168 0.157161664 0.157629982
0.158089572 0.158523436 0.15945858  0.15991733  0.16038436  0.160851172
0.161292321 0.161758709 0.162216406 0.16315657  0.16362209  0.164095851
0.164560934 0.165025801 0.165507344 0.16644442  0.166908413 0.167372189
2];
%Plastic Strain
% Martensite
MnSs=[1059.387427   1071.700468 1079.481665 1086.574633 1092.237742
1098.441087 1104.75436  1111.796259 1125.46307  1131.860501 1137.748872
1144.010298 1150.622562 1156.675679 1169.96735  1176.421353 1183.569525
1190.560752 1197.78889  1205.229426 1212.796925 1227.280661 1234.268118
1241.736794 1249.312029 1257.282104 1272.676573 1279.881451 1287.123449
1294.644471 1301.136125 1307.906831 1314.677828 1327.216913 1333.085732
1338.958669 1344.625781 1350.285031 1355.627063 1365.81215  1370.794566
1375.608125 1380.245282 1385.035598 1389.669546 1394.432961 1402.98593
1407.347068 1411.828288 1416.062418 1420.292827 1427.943147 1432.016349
1436.095798 1440.177285 1444.070322 1447.969248 1451.782418 1458.383873
1461.879495 1465.545739 1468.983158 1472.281773 1475.741671 1481.310016
1484.719523 1487.931402 1491.08617  1494.185576 1497.109137 1500.105331
1505.056211 1507.900344 1510.642179 1513.548259 1516.245927 1518.946301
1521.597552 1525.213472 1526.865063 1528.421732 1530.011502 1531.467444
1532.990163 1535.690091 1537.053646 1538.330538 1539.525788 1541.807897
1542.92314  1543.911349 1544.939293 1545.850927 1546.776912 1547.645409
1549.296547 1550.086025 1550.856555 1551.592138 1552.378312 1553.099098
1553.820318 1555.443457 1555.935085 1556.39998  1556.864719 1557.31603
1593.875    1648.4  1740    1790    1810    1900];
%Mpa Plastic Stress
MnSn=[0 0.000148644 0.000237819 0.000326987 0.00040624  0.000505298
0.000594442 0.000703385 0.000921235 0.001030142 0.001148936 0.001277614
0.001416171 0.001544815 0.001841621 0.001989991 0.002158118 0.002326216
0.002504171 0.002691978 0.002889632 0.003284823 0.003482359 0.003699605
0.003926674 0.004173431 0.004676625 0.004923196 0.005179566 0.005455583
0.005701963 0.005967984 0.006243784 0.006785312 0.007051045 0.007326546
0.007601972 0.007887154 0.008162424 0.008722563 0.009007426 0.009292207
0.009567091 0.009861527 0.010155875 0.010450137 0.011038401 0.011332404
0.011645911 0.011949527 0.012262841 0.012898958 0.013202194 0.013515116
0.013837714 0.014150437 0.01447283  0.014795119 0.015449145 0.015761364
0.016102743 0.016424507 0.016736422 0.017077468 0.017720267 0.018080443
0.018421031 0.018761503 0.019101859 0.01942266  0.019762791 0.020442706
0.020782491 0.021112456 0.021481113 0.021820545 0.022169554 0.022518442
0.02320617  0.023564376 0.023912778 0.024280404 0.024628556 0.025005584
0.025710922 0.026087543 0.02645437  0.026811415 0.027534763 0.027910697
0.028257588 0.028633251 0.028979892 0.02934566  0.029701674 0.030413322
0.030768956 0.031124464 0.031470242 0.0318447   0.032190229 0.032535639
0.033216515 0.033571153 0.033906507 0.034241748 0.034567303 0.05 0.08 0.14
0.2 0.25 2];
%Plastic Strain
```

```
fprintf(fid,'** MATERIALS\r\n');
fprintf(fid,'**\r\n');
fprintf(fid,'*Material, name=Fe\r\n');
fprintf(fid,'*Density\r\n');
fprintf(fid,'7.60292e-09,\r\n');
fprintf(fid,'*Elastic\r\n');
fprintf(fid,'198000., 0.33\r\n');
fprintf(fid,'*Plastic\r\n');
for i=1:length(FeSs);
    fprintf(fid,'%6.2f,\t%6.8f\r\n',FeSs(i),FeSn(i));
end
fprintf(fid,'*Porous Metal Plasticity, relative density=1.\r\n');
fprintf(fid,' 1.1,  0.9, 1.21\r\n');
fprintf(fid,'*Void Nucleation\r\n');
fprintf(fid,' 0.11,  0.5, 0.04\r\n');
fprintf(fid,'*Material, name=Mn\r\n');
fprintf(fid,'*Damage Initiation, criterion=FLSD\r\n');
fprintf(fid,'1800.,1800.\r\n');
fprintf(fid,'*Damage Evolution, type=DISPLACEMENT\r\n');
fprintf(fid,'0.,\r\n');
fprintf(fid,'*Density\r\n');
fprintf(fid,'7.60292e-09,\r\n');
fprintf(fid,'*Elastic\r\n');
fprintf(fid,'200000., 0.33\r\n');
fprintf(fid,'*Plastic\r\n');
for i=1:length(MnSs);
    fprintf(fid,'%6.2f,\t%6.8f\r\n',MnSs(i),MnSn(i));
end
% Define Step
fprintf(fid,'** ----------------------------------------------------------
------\r\n');
fprintf(fid,'**\r\n');
fprintf(fid,'** STEP: Step-1\r\n');
fprintf(fid,'**\r\n');
fprintf(fid,'*Step, name=Step-1, nlgeom=YES, inc=10000\r\n');
fprintf(fid,'*Static\r\n');
fprintf(fid,'1., 300., 0.003, 300.\r\n');
fprintf(fid,'**\r\n');
%---------------------------------
% Import the BC
importBC('BC.rpt');
BCO=data;
BC=[0.1 0.1 0.1;0.1 0 0.1;0.1 0.1 0;0.1 0 0;0 0.1 0.1;0 0 0.1;0 0.1 0;0 0
0];
BC(1,4:6)=BCO(1,2:4);
BC(2,4:6)=BCO(3,2:4);
BC(3,4:6)=BCO(5,2:4);
BC(4,4:6)=BCO(7,2:4);
BC(5,4:6)=BCO(2,2:4);
BC(6,4:6)=BCO(4,2:4);
BC(7,4:6)=BCO(6,2:4);
BC(8,4:6)=BCO(8,2:4);
% Only 1 2 3 and 4 will be used, maximum deformation because it is tthe
% nearest face to the centre. Def taken should be Y and Z (5,6)

% For interpolation; Creating 2X2 matrices
```

```
% Deleted --------
n=1;
for z=2:-1:1;
    for y=2:-1:1;
        BCY(y,z)=BC(n,5);
        n=n+1;
    end
end
n=1;
for z=2:-1:1;
    for y=2:-1:1;
        BCZ(y,z)=BC(n,6);
        n=n+1;
    end
end

[BCGY,BCGZ]=meshgrid(1:2,1:2);
[YnodeG,ZnodeG]=meshgrid(1:1/225:2,1:1/225:2);
nodeY=interp2(BCGY,BCGZ,BCY,YnodeG,ZnodeG);
nodeZ=interp2(BCGY,BCGZ,BCZ,YnodeG,ZnodeG);
% Because the origin of 3D model and 2D model are opposite in the Z (X)
direction
% ONLY
nodeZ=-nodeZ;
% Create node number matrix N+1 X N+1
n=1;
for z=225:-1:1;
    for y=225:-1:1;
        nodeN(y,z)=n;
        n=n+1;
    end
end

% Change the node number off the surface with 0
n=1;
for z=224:-1:2;
    for y=224:-1:2;
       nodeN(y,z)=0;
       n=n+1;
    end
end

fprintf(fid,'**\r\n');
fprintf(fid,'** BOUNDARY CONDITIONS\r\n');
fprintf(fid,'**\r\n');
% Y Disp
fprintf(fid,'** Name: YZ Type: Displacement/Rotation Using
Analytical\r\n');
fprintf(fid,'Field: YZ\r\n');
fprintf(fid,'*Boundary, amplitude=Amp-1\r\n');
for z=225:-1:1;
    for y=225:-1:1;
        if nodeN(y,z)~=0
            fprintf(fid,'PART-1-1.%u, 2, 2,
%6.5E\r\n',nodeN(y,z),nodeY(y,z));
```

```
            fprintf(fid,'PART-1-1.%u, 1, 1,
%6.5E\r\n',nodeN(y,z),nodeZ(y,z));
        end
    end
end

fprintf(fid,'**\r\n');
fprintf(fid,'** OUTPUT REQUESTS\r\n');
fprintf(fid,'**\r\n');
fprintf(fid,'*Restart, write, frequency=0\r\n');
fprintf(fid,'**\r\n');
fprintf(fid,'** FIELD OUTPUT: F-Output-1\r\n');
fprintf(fid,'**\r\n');
fprintf(fid,'*Output, field\r\n');
fprintf(fid,'*Node Output\r\n');
fprintf(fid,'CF, COORD, RF, U\r\n');
fprintf(fid,'*Element Output, directions=YES\r\n');
fprintf(fid,'LE, PE, PEEQ, PEMAG, S, EVOL, IVOL\r\n');
fprintf(fid,'*Contact Output\r\n');
fprintf(fid,'CDISP, CSTRESS\r\n');
fprintf(fid,'**\r\n');
fprintf(fid,'** HISTORY OUTPUT: H-Output-1\r\n');
fprintf(fid,'**\r\n');
fprintf(fid,'*Output, history, variable=PRESELECT\r\n');
fprintf(fid,'*End Step\r\n');
%Close The input file
fclose('all');
%---------------------------------
```

Appendix VI MatLab code to apply boundary conditions to 3D RVE

```
% Import the BC
importBC('BC.rpt');
BCO=data;
BC=[0.1 0.1 0.1;0.1 0 0.1;0.1 0.1 0;0.1 0 0;0 0.1 0.1;0 0 0.1;0 0.1 0;0 0
0];
BC(1,4:6)=BCO(1,2:4);
BC(2,4:6)=BCO(3,2:4);
BC(3,4:6)=BCO(5,2:4);
BC(4,4:6)=BCO(7,2:4);
BC(5,4:6)=BCO(2,2:4);
BC(6,4:6)=BCO(4,2:4);
BC(7,4:6)=BCO(6,2:4);
BC(8,4:6)=BCO(8,2:4);
% For interpolation; Creating 3X3 matrices
% Deleted --------
n=1;
for x=2:-1:1;
    for z=2:-1:1;
        for y=2:-1:1;
            BCX(x,y,z)=BC(n,4);
            n=n+1;
        end
    end
end
n=1;
for x=2:-1:1;
    for z=2:-1:1;
        for y=2:-1:1;
            BCY(x,y,z)=BC(n,5);
            n=n+1;
        end
    end
end
n=1;
for x=2:-1:1;
    for z=2:-1:1;
        for y=2:-1:1;
            BCZ(x,y,z)=BC(n,6);
            n=n+1;
        end
    end
end

% Import the mesh
N=input('Choose No. of Element along RVE edge (8, 10, 15, 20, 30): ');
if N==8;
    importRVE('RVE8.INP');
elseif N==10;
    importRVE('RVE10.INP');
elseif N==15;
    importRVE('RVE15.INP');
elseif N==20;
    importRVE('RVE20.INP');
```

```
else
    importRVE('RVE30.INP');
end
node=data;
% Deleted --------
% Interpolation
[BCGX,BCGY,BCGZ]=meshgrid(1:2,1:2,1:2);
[XnodeG,YnodeG,ZnodeG]=meshgrid(1:1/(N):2,1:1/(N):2,1:1/(N):2);
nodeX=interp3(BCGX,BCGY,BCGZ,BCX,XnodeG,YnodeG,ZnodeG);
nodeY=interp3(BCGX,BCGY,BCGZ,BCY,XnodeG,YnodeG,ZnodeG);
nodeZ=interp3(BCGX,BCGY,BCGZ,BCZ,XnodeG,YnodeG,ZnodeG);
% Create node number matrix N+1 X N+1 X N+1
n=1;
for x=N+1:-1:1;
    for z=N+1:-1:1;
        for y=N+1:-1:1;
            nodeN(x,y,z)=node(n,1);
            n=n+1;
        end
    end
end

% Change the node number off the surface with NaN
n=1;
for x=N:-1:2;
    for z=N:-1:2;
        for y=N:-1:2;
            nodeN(x,y,z)=0;
            n=n+1;
        end
    end
end
if N==8;
    fid=fopen('RVE8.inp','a');
elseif N==10;
    fid=fopen('RVE10.inp','a');
elseif N==15;
    fid=fopen('RVE15.inp','a');
elseif N==20;
    fid=fopen('RVE20.inp','a');
else
    fid=fopen('RVE30.inp','a');
end
fprintf(fid,'**\r\n');
fprintf(fid,'** BOUNDARY CONDITIONS\r\n');
fprintf(fid,'**\r\n');
% X Disp
fprintf(fid,'** Name: X Type: Displacement/Rotation Using
Analytical\r\n');
fprintf(fid,'Field: X\r\n');
fprintf(fid,'*Boundary, amplitude=Amp-1\r\n');
for x=N+1:-1:1;
    for z=N+1:-1:1;
        for y=N+1:-1:1;
            if nodeN(x,y,z)~=0
```

```
                fprintf(fid,'PART-1-1.%u, 1, 1,
%6.5E\r\n',nodeN(x,y,z),nodeX(x,y,z));
            end
        end
    end
end
% Y Disp
fprintf(fid,'** Name: Y Type: Displacement/Rotation Using
Analytical\r\n');
fprintf(fid,'Field: Y\r\n');
fprintf(fid,'*Boundary, amplitude=Amp-1\r\n');
for x=N+1:-1:1;
    for z=N+1:-1:1;
        for y=N+1:-1:1;
            if nodeN(x,y,z)~=0
                fprintf(fid,'PART-1-1.%u, 2, 2,
%6.5E\r\n',nodeN(x,y,z),nodeY(x,y,z));
            end
        end
    end
end
% Z Disp
fprintf(fid,'** Name: Z Type: Displacement/Rotation Using
Analytical\r\n');
fprintf(fid,'Field: Z\r\n');
fprintf(fid,'*Boundary, amplitude=Amp-1\r\n');
for x=N+1:-1:1;
    for z=N+1:-1:1;
        for y=N+1:-1:1;
            if nodeN(x,y,z)~=0
                fprintf(fid,'PART-1-1.%u, 3, 3,
%6.5E\r\n',nodeN(x,y,z),nodeZ(x,y,z));
            end
        end
    end
end
fprintf(fid,'**\r\n');
fprintf(fid,'** OUTPUT REQUESTS\r\n');
fprintf(fid,'**\r\n');
fprintf(fid,'*Restart, write, frequency=0\r\n');
fprintf(fid,'**\r\n');
fprintf(fid,'** FIELD OUTPUT: F-Output-1\r\n');
fprintf(fid,'**\r\n');
fprintf(fid,'*Output, field\r\n');
fprintf(fid,'*Node Output\r\n');
fprintf(fid,'CF, COORD, RF, U\r\n');
fprintf(fid,'*Element Output, directions=YES\r\n');
fprintf(fid,'LE, PE, PEEQ, PEMAG, S, EVOL, IVOL\r\n');
fprintf(fid,'*Contact Output\r\n');
fprintf(fid,'CDISP, CSTRESS\r\n');
fprintf(fid,'**\r\n');
fprintf(fid,'** HISTORY OUTPUT: H-Output-1\r\n');
fprintf(fid,'**\r\n');
fprintf(fid,'*Output, history, variable=PRESELECT\r\n');
fprintf(fid,'*End Step\r\n');
fclose('all');
```

```
%==========
% Variables
% ---------
% BCO: Original BC
% BC : BC arranged similar to RVE arrangement, Consists of coordinates
(X,Y and Z) and X,Y and Z Disp.
% node: Node consists of number and coordinates(X,Y and Z) and X,Y and Z
Disp
```

Appendix VII Effect of some Gurson parameters

Effect of initial void in the material (f_o):

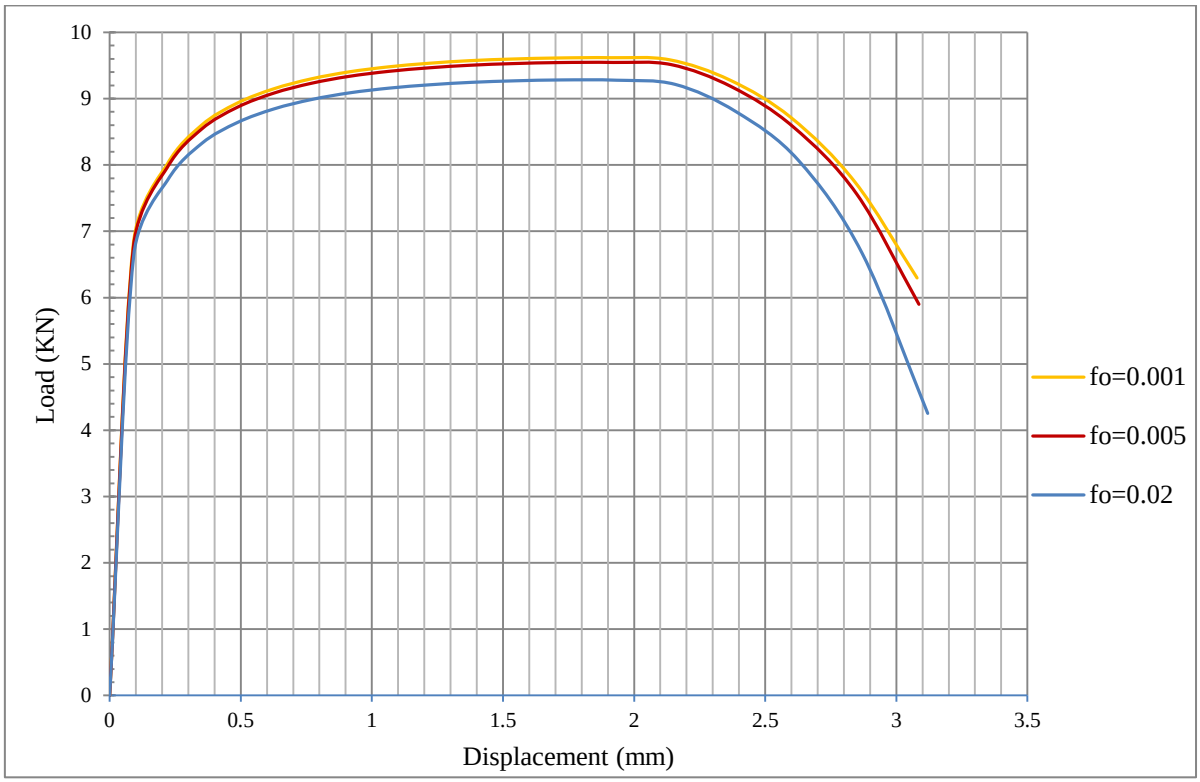

Effect of void nucleation amount in the material (f_N):

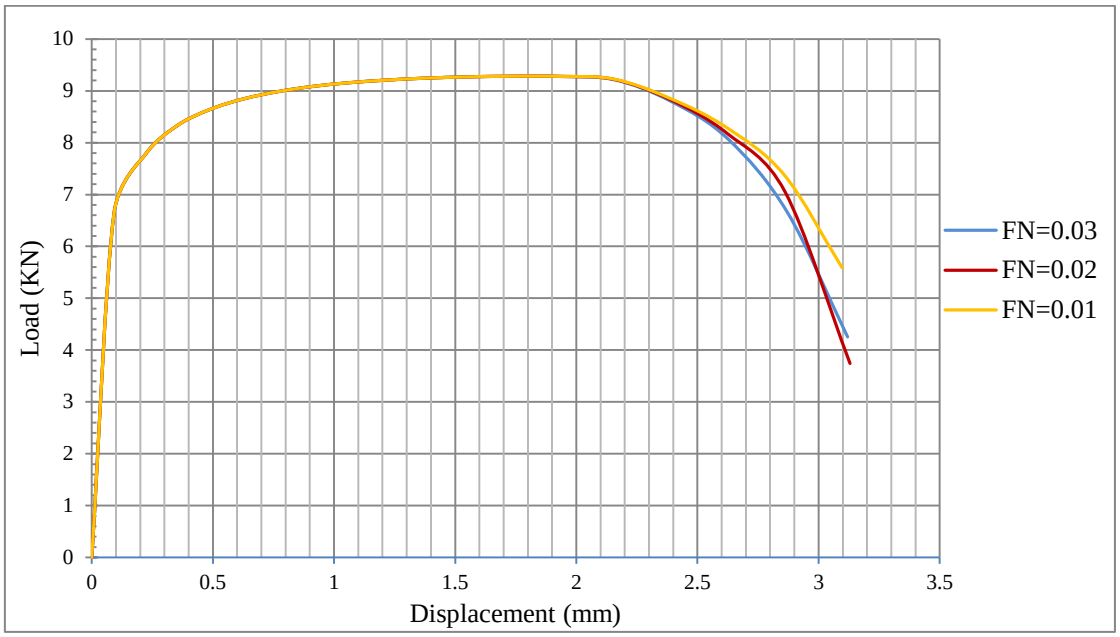

Effect of the standard deviation of the nucleation strain (S_N):

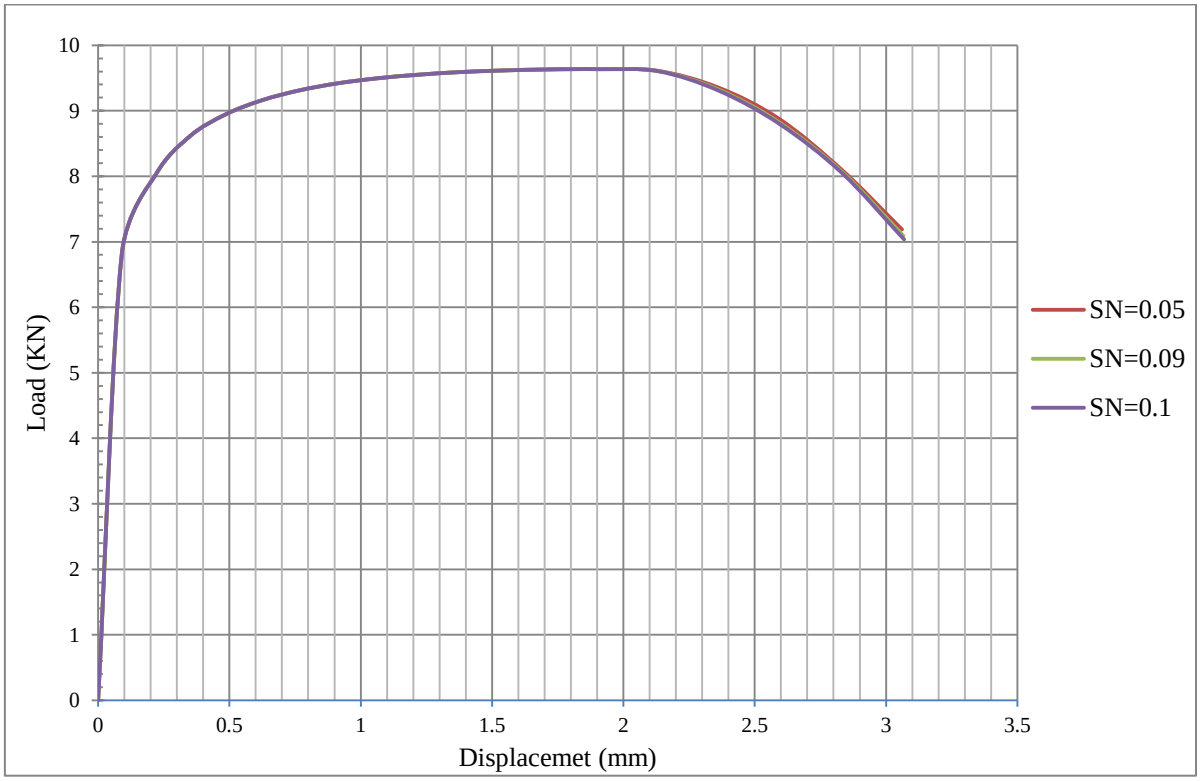

Appendix VIII Publications and Conferences List

1. Alharbi, K., et al., *A combined digital image correlation – finite element modelling approach to investigate damage formation in dual phase steels*, in *European Congress and Exhibition on Advanced Materials and Processes (EUROMAT2013)*. 2013: Sevilla, Spain.

2. Alharbi, K., et al., *DAMAGE FORMATION IN DUAL PHASE STEELS: Combined Approach of Digital Image Correlation and Microstructure Modelling*, in *7th European Conference on Steel and Composite Structures (EUROSTEEL2014)*. 2014: Napoli, Italy.

3. Alharbi, K., et al., *Damage in dual phase steel DP1000 investigated using digital image correlation and microstructure simulation.* Modelling and Simulation in Materials Science and Engineering, 2015. **23**(8): p. 085005.